UNIVERSITY OF SOUTHAMPTON

Faculty of Physical Sciences and Engineering

School of Physics and Astronomy

Progress towards atom interferometric measurements of gravity in a compact and integrated vacuum chamber

by

Chester H. Camm

Thesis for the degree of Doctor of Philosophy

August 2022

Abstract

Atom interferometry based gravity gradiometers are capable of operating with unparalleled sensitivity when compared to their classical counterparts. This makes them ideal candidates for field applications. The Phase Locked Atomic Interferometers for Gravity Gradiometry (PLAIN-GG) project aims to use two absolute gravimeters connected with a stabilised optical fibre link to achieve a lightweight gradiometer with a flexible baseline. This allows for a portable system without the sacrifice of sensitivity.

In this thesis we present the development of an atom interferometer for measurements of gravity using a novel, compact, and integrated vacuum chamber. We aim to use this chamber as the centre of the PLAIN-GG sensor head. Using absorption imaging, we characterise the atom number and temperature of the cold atom cloud as experimental variables are changed. When optimised, we measure the number of trapped atoms to be $\approx 1.5 \times 10^6$ and their temperature to be $\approx 7\,\mu$K. To demonstrate the viability of this chamber for use in inertial atom interferometry measurements, we find the atom ensemble to be detectable after a 120 ms free fall. We also briefly detail the preliminary work of the PLAIN-GG stabilised fibre link.

Declaration of authorship

I, Chester Hayden Camm, declare that the thesis entitled *Progress towards atom interferometric measurements of gravity in a compact and integrated vacuum chamber* and the work presented in the thesis are my own, and have been generated by me as the result of my own original research. I confirm that:

- This work was done wholly or mainly while in candidature for a research degree at this University;
- Where any part of this thesis has previously been submitted for a degree or any other qualification at this University or any other institution, this has been clearly stated;
- Where I have consulted the published work of others, this is always clearly attributed;
- Where I have quoted from the work of others, the source is always given. With the exception of such quotations, this thesis is entirely my own work;
- I have acknowledged all main sources of help;
- Where the thesis is based on work done by myself jointly with others, I have made clear exactly what was done by others and what I have contributed myself;
- None of this work has been published before submission;

Signed: _____

Date: _____

Acknowledgements

Firstly I would like to thank my supervisors, Matt Himsworth and Tim Freegarde, for providing me with this opportunity and for their invaluable guidance throughout. This has been an amazing journey for me both professional and personally, and the value of the lessons I have learnt are immeasurable.

I am lucky to have been surrounded by and worked alongside so many talented individuals during my PhD. I am extremely thankful, not just for your incredible professional expertise, but also for your friendship and support. A special thanks to Andrei Dragomir for showing me the ropes in the lab at the beginning of my PhD and for encouraging me to press ahead when my experiment refused to behave. A great many thanks to Jack Saywell and the newcomer Nikolaos Dedes for helping me wrap my brain around the theoretical side of this project. In particular, I am extremely grateful to Max Carey for your assistance throughout these years, and especially for helping me in the lab towards the end of the experiment. I would like to thank the research group as a whole for providing me with great company and insightful discussions during these four years. I hope we may continue these in the future despite how far we may scatter.

Thanks to all the Physics and Astronomy support staff for helping the lab run smoothly and for always being able to provide assistance in any niche technical issue I had. Especially, I would like to thank Gareth Savage and Leigh Allen for lending me their expertise in solving the many electrical problems I encountered.

I could not have accomplished this without the endless support from my friends and family. You have kept me sane these last few years and I will be forever thankful. I hope you know how much you mean to me and I look forward to many more wonderful years ahead. I am incredibly fortunate to be surrounded by so many I hold dear and that would never hesitate to offer help when I needed it. Thank you.

I, of course, owe a great deal to my parents for all they have done for me. Without your support I would never have started this, let alone finished it.

Words could never fully describe how truly grateful I am to you.

Thank you all for helping me along this journey.

"If you're not doing what you love, then you're the crazy one"

Angelo Niko Grubišić

Contents

List of figures

List of acronyms

50:50 BS 50:50 Beam Splitter 136, 137

AM amplitude modulation xv, 75, 80–83, 136

AOM acousto-optical modulator xvi, 5, 75, 76, 87, 92, 93, 99–103, 132–137, 143

CAD Computer Assisted Design xv, 78

CCD charge-coupled device 61, 62, 69, 90, 98

DBR distributed Bragg reflector 72, 99

EOM electro-optic modulator 75, 131–133

FM frequency modulation 72–75, 133, 135, 136

FWHM Full Width Half Maximum 96–99

GRACE-FO Gravity Recovery and Climate Experiment Follow-On 2

HeNe Helium Neon laser 5, 134–136, 142, 143

ICE Integrated Control Electronics 74

LC WP Liquid Crystal waveplate xv, xvi, 69, 71, 79–88, 91, 112

MOT magneto-optical trap xv, xvi, 3, 5, 6, 45, 51–54, 57–60, 62, 67–69, 71, 75, 77–80, 85–92, 95, 96, 98, 99, 101, 103–107, 111–116, 118, 121, 122, 124, 127, 130, 133, 146

ND filter neutral density filter 76, 77

OBE Optical Bloch Equation 19, 166

OSA optical spectrum analyser 132, 133

PBS polarising beam splitting cube 69–71, 75, 76, 84–86, 101, 132, 136

PD photodiode 5, 69, 71–74, 82–84, 92, 101, 124–126, 132, 135, 136

PID proportional-integral-derivative 5, 135–143

PLAIN-GG Phase Locked Atomic Interferometers for Gravity Gradiometry iii, xv, xvi, 4–6, 42, 67, 68, 77, 130, 131, 134, 135, 142, 143, 145–147, 180

PM polarisation maintaining 69, 74, 76, 101, 132

RF radio-frequency 74–76, 87, 100–102, 131–133, 135, 137, 143

RWA rotating wave approximation 15, 16

SAS saturated absorption spectroscopy 72–74, 132, 133

SNR signal-to-noise ratio 41, 59, 107, 108, 122, 124, 126, 127

TA tapered amplifier 131–133

TDSE time-dependent Schrödinger equation 11, 14, 16, 18, 30, 163, 164, 167, 168, 171

TNE Transient Nematic Effect xv, 81–84, 112

TOF time-of-flight xvi, 62, 63, 68, 90, 91, 95, 107, 108, 111–115, 126, 127, 133

TTL transistor–transistor logic 67, 74, 75, 80, 81, 87, 103, 133

Chapter 1

Introduction

The simplest measurement of gravity can be dropping an inertial test mass and measuring its position over time. However these measurements have a fundamental problem of the equivalence principle. Einstein's equivalence principle indicates it is impossible to distinguish between linear and gravitational acceleration. In reality this manifests as mechanical noise affecting a gravimeter's measurements of local gravity. However, since the attraction due to gravity falls off the further away from the object, if measurements were to be taken at two points—one further from the gravitational source than the other—then the gravitational acceleration and linear acceleration can be distinguished from each other. By measuring the difference of gravity between these two points any noise common to both points is also rejected—a feature that makes this type of measurement ideal for noisy environments. These devices are called gravity gradiometers [1, 2].

Baron Loránd von Eötvös is regarded as the father of gravity gradiometry [3]. In 1890 he adapted the Coulomb balance to create the 'torsion balance', the first gravity gradiometer. Eötvös also lends his name to the unit used to measure a gravitational gradient; the 'Eotvos', or E, where $1\,\mathrm{E} = 10^{-9}\,\mathrm{s}^{-2}$. The torsion balance was constructed of two known masses, held at different heights, separated by a horizontal beam. This beam was then suspended by a thin string. If the gravitational force on both masses is unequal a torque is exerted on the beam. This deflects the beam and the angle of deflection can be measured. The torsion balance could reach a sensitivity of 1 E after a lengthy measurement time [4]. This basic design was improved upon for many years until other implementations became more sensitive and practical. These include accelerometers on a spinning disk [5, 6] to a superconducting mass on a spring [7] and micro-fabricated gradiometers [8]. Gravity gradiometers have also found

use in space; for example in 2018 the Gravity Recovery and Climate Experiment Follow-On (GRACE-FO) mission was launched [9]. Its mission is to track the movement of the Earth's water in order to help measure and assess climate change [10]. GRACE-FO consists of two identical satellites following one another in orbit. As they orbit the Earth the changes in gravity—the gravity gradient—will alter the distance between the satellites. When the trailing satellite then travels over an area of higher gravity it will 'catch up' with the leading satellite. By measuring the distances between the satellites the gravity gradient can be detected. GRACE-FO has a sensitivity of $\approx 10^{-6}\,\mathrm{E}/\sqrt{\mathrm{Hz}}$ with a baseline length of 220 km [11].[1] For further reading, Veryaskin [4] provides a good summary and history of gravity gradiometry techniques and systems.

Gravity measurements, due to its ability to detect invisible density changes provides an invaluable tool for a wide range of fields including civil engineering, archaeology, inertial navigation, geophysics, and geodesy. Because a gravitational field cannot be shielded, measurements of gravity are able to overcome certain limitations that restrict other measurement techniques, such as radar, which are limited by resolution, range, and by absorption of their transmissive signal [14]. However, to compete with these tools the gravimeter must be suitably sensitive. Ideally, 1 E of sensitivity is required for applications such as civil engineering, however sensitivities on the order of $< 10\,\mathrm{E}$ are suitable [15].

A classical system, made from bulk material and using manufactured inertial test masses, is prone to wear and degradation. This can affect measurements and give classical gravity gradiometers a limited lifetime. Atoms are not susceptible to this macroscopic wear and degradation; making them the ideal candidates for use as inertial test masses. Furthermore, atom interferometry can be used to increase the sensitivity of measurements as opposed to simply dropping the atoms. [16]. This is a technique where pulses of laser light are used to impart specific quantum states onto the atom ensembles—most commonly, lasers that excite Raman transitions are used. The evolution of the atom's quantum state depends on the acceleration it undergoes and by measuring the atom's final state we are able to find measurements of gravity. This is explained in more detail in Chapter 3. For these quantum gravity gradiometers to maintain the common noise rejection, it is required that the phase of the light pulses used to interact with the atomic test masses are phase correlated at both test mass locations. To provide this, line of sight is required and the atom clouds are usually in the same vacuum chamber.

[1] The per $\sqrt{\mathrm{Hz}}$ in the unit implies the precision scales inversely with the square root of the measurement time; i.e. the measurement gets more sensitive the longer the measurement is performed for [12, 13]. For example, a $1\,\mathrm{E}/\sqrt{\mathrm{Hz}}$ sensitivity provides 1 E at 1 s and 0.1 E at 100 s.

Snadden et al. [17] were the first to create a quantum gravity gradiometer in 1998 [4]. They used two magneto-optical traps (MOTs), one on top of the other separated by 1.09 m, in two separate vacuum chambers. Line of sight of Raman beams was achieved through windows on these chambers. In this design they were able to reach a sensitivity of 100 E. While not the most sensitive it showed there to be potential for future quantum gravity gradiometers.

To increase the sensitivity most designs use a large single vacuum chamber and an 'atom fountain'. Here a 2D MOT is used to cool and then eject atoms in a continuous beam on a vertical trajectory. During this trajectory the atoms are in free fall and by using two trajectories offset from each other the gravity gradient can be measured. This has the benefit of longer measurement times since the atoms are launched upwards and travel twice the distance compared to dropping the atom ensembles. This increases sensitivity and is a commonly used technique as a result [18, 19]. This however requires a large enough single vacuum chamber to accommodate the fountain's trajectory.

Since Snadden et al. [17], quantum gravity gradiometry has become more refined and found many uses. Due to their unparalleled sensitivity quantum gradiometers found their use mainly in fundamental science [20]. These include measuring the gravitational constant G, [21], mapping Earth's gravity field [22], and testing the equivalence principle [23]. Unfortunately, due to the large vacuum chambers required for these measurements, current quantum gravity gradiometers are bulky and heavy; this limits their practicality outside of the lab. Currently, classical gravity gradiometers remain the only suitable solution for field use [14]. Bongs et al. [24] gives a good overview of the challenges atom interferometers are confronted by to become more practical than their classical counterparts in field applications. In recent years, there has been much progress in developing portable quantum gravity gradiometers [25, 26, 27]. Most notably—and recently—this includes a successful measurement performed outside of the laboratory environment [28]. However, these devices remain fundamentally limited by a trade-off between sensitivity and portability [15].

Despite gradiometers theoretically being best suited for field applications, absolute quantum gravimeters have found more success outside the lab. [29, 30, 31, 32] Currently, the most sensitive gravity gradient measurement performed with a portable atom interferometer was with an absolute gravimeter in an elevator shaft [33]. Bidel et al. [33] was able to achieve a precision of 4 E using a baseline of 45.8 m. Notably, this system was then able to perform a survey of absolute gravity onboard a ship [34].

1.1 The PLAIN-GG project

In order to create a practical quantum gravity gradiometer we decided to take a fundamentally different approach. Rather than have both atom ensembles in one vacuum chamber, where we are restricted by geometry and necessary encumbrance, the Phase Locked Atomic Interferometers for Gravity Gradiometry (PLAIN-GG) project will attempt to use two separate vacuum chambers with one atom cloud in each. This would allow free translation of the chambers relative to each other and relieve of the weight and bulk from requiring one large chamber. Chapters 5 and 6 detail the progress made to building these sensor heads.

However this presents another problem; we no longer have line of sight for the interaction beams to maintain their phase coherence. We can use an analogy for the laser light being a ruler that measures the atom's position relative to the phase of the light. When moving the atom clouds into separate chambers we now have two rulers that are free to move independently of each other. We now require a method to stabilise these separated rulers so they move together and maintain the phase coherence of the interaction light between both atom ensembles. To do this we plan to adapt a method used in distributing optical phase in atomic clocks [35]. Foreman et al. [36] demonstrated transfer instability of 5×10^{-15} at 1 s for 86 km of optical fibre and 6×10^{-18} at 1 s for a 7 km fibre. This instability is suitable for distributing signals for the most precise atom clocks over a much larger distance than required for our system. Section 7.2 details the progress made towards the construction of this stabilisation system. An aim to determine the success of this stability mechanism is to ensure that the fibre arms are not the main source of noise in the system. If the dominant noise source is the mirrors in the vacuum chambers then this noise is able to be successfully 'shared' between both sensor heads through a rigid structure; being a gradiometer, any measurements would then be unaffected by this common noise.

Figure 1.1 shows the initial design of the proposed system named PLAIN-GG. This approach can also provide additional benefits. The ability to control the phase relation between the two atom clouds enables investigation into the regime between uncorrelated accelerometers, and fully coherent single chamber quantum gravity gradiometers. This is a largely unexplored region and further demonstrates novelty of this approach. The flexible optical fibre link between both atomic test masses also provides the ability to have a variable baseline. This may be useful in applications where different levels of sensitivity are required. Furthermore, this opens up possibilities of probing the gravity gradient along multiple axes.

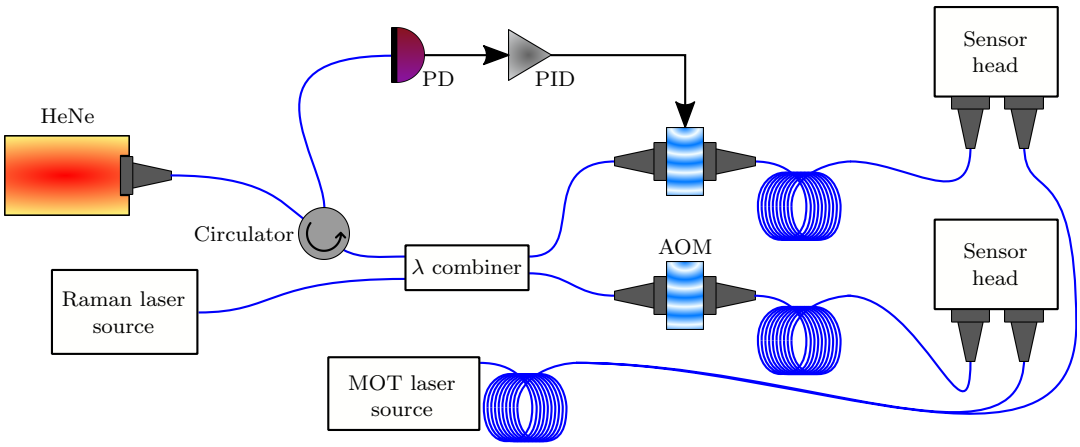

Figure 1.1: Design of the PLAIN-GG. Light from the Helium Neon laser (HeNe) is sent through an optical fibre Michelson interferometer. Along the arms of the interferometer are acousto-optical modulators (AOMs), one of which is modulated with a proportional-integral-derivative (PID) feedback loop. At the ends of the interferometer arms are the sensor heads which is where the cold atom physics takes place. These contain retro-reflecting mirrors that the HeNe's light reflects off of and then re-enters the optical fibre interferometer. The HeNe's light is then shone onto a photodiode (PD) which detects phase changes in the interferometer. The PID feedback loop then corrects for any changes in phase between the two fibre interferometer arms. Raman interaction light also passes through the fibre interferometer in order to be phase stabilised. The MOT light necessary for the cooling and trapping of the atoms does not pass through the optical fibre interferometer as the AOMs would shift the light's frequency.

For a gravity gradiometer to measure a 10 kg object 1 m away with a 1 m baseline a sensitivity of 1 E is required. A device with 30 E of sensitivity is able to detect objects of masses > 300 kg under the same conditions. While a device with this level of sensitivity may not be capable of detecting small objects, it should still be suitable for measuring larger structures. Therefore, we have chosen 30 E as a reasonable initial sensitivity aim of the PLAIN-GG project.

1.2 Thesis overview

In Part I we introduce the theoretical background for atom interferometry and gravity gradient measurements with atom interferometry. We begin in Chapter 2 by introducing Raman transitions, this is the tool which we use to perform

the atom interferometry. Through the use of Raman transitions we are able to transform a multi-level atom into an ideal two-level system with long state lifetimes. Chapter 3 then describes how we use pulses of light that drive Raman transitions to build an atomic Mach-Zehnder interferometer. We then describe how this technique can be used to make inertial measurements; and in particular, measurements of local gravity. By using two atom interferometers we then describe how noise insensitive measurements of the gravity gradient can be performed. To begin realising such an interferometer, we require an ensemble of atoms which are able to maintain coherent quantum states for long time periods. Chapter 4 describes how this can be achieved through cooling and trapping of atoms within a MOT. This chapter also includes details of how we are able to measure the number of atoms trapped by the MOT and the cloud's average temperature with absorption imaging.

Part II contains the experimental work performed. Chapters 5 and 6 contain the majority of the experimental work in this thesis. In these chapters we describe the apparatus used for performing the cold atom experiments (Chapter 5) and the results using that apparatus (Chapter 6). Here we also describe the novel vacuum chamber which we design the optical system around. This vacuum chamber is the first commercially available compact vacuum chamber with integrated optics designed for inertial measurements with atom interferometry. We aim to use this vacuum chamber as the basis for the PLAIN-GG sensor head design. Showing the viability of this chamber for use in atom interferometry is a foundational step towards realising the PLAIN-GG project.

In Chapter 7 we describe the progress made towards realising a Raman laser system and plans for observing Raman transistions in the apparatus described in Chapter 5. Here we also describe the preliminary work and results in building the optical fibre interferometer for stabilising the Raman light in the PLAIN-GG system.

Part I

Theoretical background

Chapter 2

Coherent manipulation of atoms

In this chapter we will explore the theoretical background behind turning a three-level atom into a much simpler two-level atom by driving stimulated Raman transitions between the two hyperfine ground states of ^{85}Rb. A stimulated Raman transition is a two-photon process which by simultaneous absorption and stimulated emission, coherent population transfer between two energy states is induced. This is performed through a virtual intermediate level which is far detuned from a real atomic energy level. Usually the transition between the two real energy levels, where coherent population transfer is achieved between, is single-photon forbidden. This creates a system where state lifetimes are longer than the interferometer period. The Raman transition is also capable of imparting momentum to the interacting atoms; we will see this couples the internal and external energy states.

This technique provides the means to coherently manipulate the state of an atom. Therefore, it is an important foundational step in performing atom interferometry: the tool we will be using to take measurements of gravity [37].

After describing the theory underpinning Raman transitions, the realities of using such a technique on an actual atom, ^{85}Rb, will then be discussed. The experimental work on implementing the Raman transitions is described in Chapter 6.

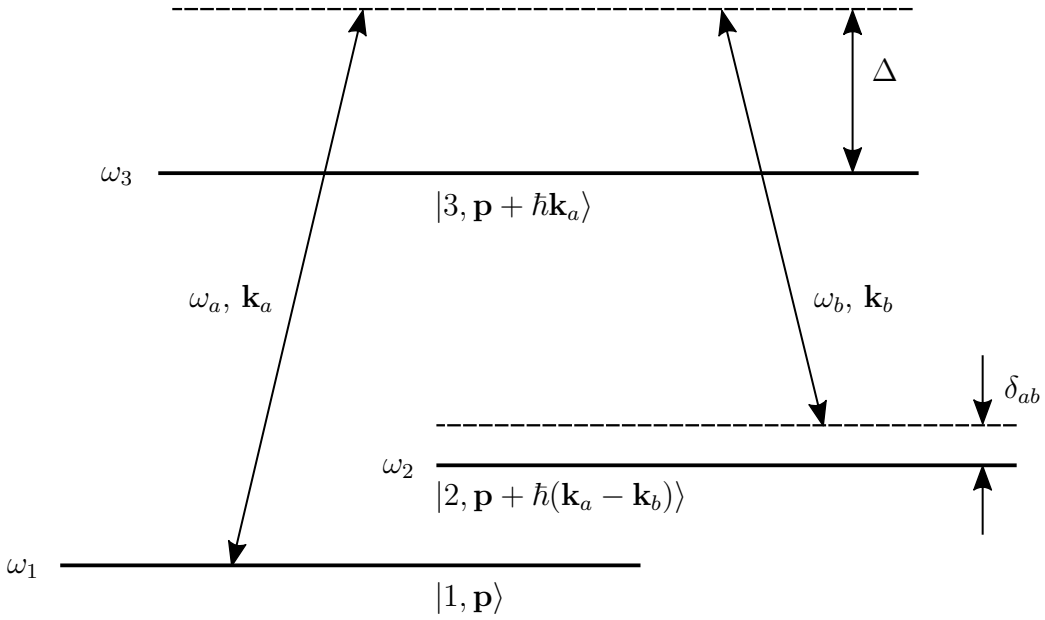

Figure 2.1: Energy level diagram of three-level atom interacting with two lasers of frequencies ω_a and ω_b, and respective wavevectors $\mathbf{k}_a$ and $\mathbf{k}_b$. Frequency is increasing in the 'upwards' direction such that $\omega_1 < \omega_2 < \omega_3$. Atomic states $|1, \mathbf{p}\rangle$ and $|3, \mathbf{p} + \hbar\mathbf{k}_a\rangle$ are coupled by monochromatic light of frequency ω_a and wavevector $\mathbf{k}_a$. Likewise, states $|2, \mathbf{p} + \hbar(\mathbf{k}_a - \mathbf{k}_b)\rangle$ and $|3, \mathbf{p} + \hbar\mathbf{k}_a\rangle$ are coupled by light of frequency ω_b and wavevector $\mathbf{k}_b$. The 'detunings' Δ and δ_{ab} represent frequency differences between the atomic transitions and the coupled light beams.

2.1 Raman transitions

Consider a three-level atom, seen in Figure 2.1, with two lower energy states, $|1\rangle$ and $|2\rangle$, and an upper state, $|3\rangle$, separated by their respective frequencies: ω_1, ω_2, and ω_3. The lower energy states represent two hyperfine levels of the ground level of an atom; therefore no single-photon electric dipole transition can couple them, including spontaneous decay. The upper energy level is an excited state that can spontaneously decay to either $|1\rangle$ or $|2\rangle$. Two lasers, counter-propagating along the $\hat{\mathbf{z}}$ axis with frequencies ω_a and ω_b, interact with the atom. The total field is given by

$$\mathbf{E} = \frac{1}{2}\mathbf{E}_a e^{i(\mathbf{k}_a \cdot \mathbf{z} - \omega_a t + \phi_a)} + \frac{1}{2}\mathbf{E}_b e^{i(\mathbf{k}_b \cdot \mathbf{z} - \omega_b t + \phi_b)} + c.c., \tag{2.1}$$

where $\mathbf{E}_{a,b}$ are the amplitudes of each beam, $\mathbf{k}_{a,b}$ are the beam's wavevectors, $\phi_{a,b}$ are the phases of each laser, and the *c.c.* represents the complex conjugate

of both terms. Since the beams are counter-propagating: $\mathbf{k}_a \approx -\mathbf{k}_b$.[1]

Laser A, with frequency ω_a, couples $|1\rangle$ to $|3\rangle$; likewise laser B, with frequency ω_b, couples $|2\rangle$ to $|3\rangle$. However both are greatly detuned from single-photon resonance by $\Delta \equiv (\omega_{31}) - \omega_a = (\omega_{32}) - \omega_b - \delta_{ab}$, where $\omega_{31} = \omega_3 - \omega_1$ and $\omega_{32} = \omega_3 - \omega_2$. The beams also have a small two-photon Raman detuning between the ground states $\delta_{ab} \equiv \omega_{ab} - \omega_{21} = (\omega_a - \omega_b) - (\omega_2 - \omega_1)$. If Δ is sufficiently large, no transition will be driven to state $|3\rangle$ and we can assume its population to be negligible. We will describe these quantities in more detail in Section 2.1.2.

In Figure 2.1 we have chosen a momentum inclusive basis: $|1\rangle \equiv |1, \mathbf{p}\rangle$, $|3\rangle \equiv |3, \mathbf{p} + \hbar\mathbf{k}_a\rangle$, and $|2\rangle \equiv |2, \mathbf{p} + \hbar(\mathbf{k}_a - \mathbf{k}_b)\rangle$, where $\mathbf{p}$ is the initial momentum of the atom. This choice of basis will become clear in Section 2.1.1.

We can write the atomic wavefunction as

$$|\Psi(t)\rangle = c_1(t)\,|1, \mathbf{p}\rangle + c_2(t)\,|2, \mathbf{p} + \hbar(\mathbf{k}_a - \mathbf{k}_b)\rangle + c_3(t)\,|3, \mathbf{p} + \hbar\mathbf{k}_a\rangle\,, \tag{2.2}$$

where $c_{1,2,3}(t)$ are the state's time-dependent amplitudes. The wavefunction evolves according to the time-dependent Schrödinger equation (TDSE):

$$i\hbar\frac{\partial}{\partial t}\,|\Psi(t)\rangle = \hat{H}\,|\Psi(t)\rangle\,, \tag{2.3}$$

where $\hat{H}$ is the Hamiltonian. The Hamiltonian is the sum of the atomic Hamiltonian, $\hat{H}_A = \sum_n \hbar\omega_n\,|n\rangle\,\langle n| + \hat{\mathbf{p}}^2/2m$, and the interaction Hamiltonian, $V = -\hat{\mathbf{d}} \cdot \mathbf{E} = -e\hat{\mathbf{r}} \cdot \mathbf{E}$, where $\hat{\mathbf{p}}$ is the momentum operator which describes transitions between states, m is the atomic mass, $\hat{\mathbf{d}}$ is the electric dipole moment operator, e is the electric charge, and $\hat{\mathbf{r}}$ is the operator for the position of the electron relative to the atomic nucleus centre of mass. The Hamiltonian for the three level system is:

$$\hat{H} = \frac{\hat{\mathbf{p}}^2}{2m} + \hbar\omega_1\,|1\rangle\,\langle 1| + \hbar\omega_2\,|2\rangle\,\langle 2| + \hbar\omega_3\,|3\rangle\,\langle 3| + V \tag{2.4}$$

The interaction Hamiltonian represents the potential the atom is experiencing. In this case, this represents the state couplings by the laser. We write the interaction Hamiltonian as [38, 39]

$$\begin{aligned} V &= \hat{V}_{13}^*\,|3\rangle\,\langle 1| + \hat{V}_{23}^*\,|3\rangle\,\langle 2| + \hat{V}_{13}\,|1\rangle\,\langle 3| + \hat{V}_{23}\,|2\rangle\,\langle 3| \\ &= \frac{\hbar\Omega_{a1}^*}{2}\left(e^{-i(\mathbf{k}_a\cdot\mathbf{z} - \omega_a t + \phi_a)} + e^{i(\mathbf{k}_a\cdot\mathbf{z} - \omega_a t + \phi_a)}\right)|3\rangle\,\langle 1| \\ &\quad + \frac{\hbar\Omega_{b2}^*}{2}\left(e^{-i(\mathbf{k}_b\cdot\mathbf{z} - \omega_b t + \phi_b)} + e^{i(\mathbf{k}_b\cdot\mathbf{z} - \omega_b t + \phi_b)}\right)|3\rangle\,\langle 2| + c.c., \end{aligned} \tag{2.5}$$

[1] For ^{85}Rb (we see later that this is our atom of choice): $\mathbf{k}_a - \mathbf{k}_b/\mathbf{k}_a \approx 3\,\text{GHz}/400\,\text{THz} \approx 8 \times 10^{-6}$. Therefore this assumption is valid.

where we have introduced the single-photon *Rabi frequency* [40]:

$$\Omega_{Ln} = -\frac{\langle n|\,\hat{\mathbf{d}}\cdot\mathbf{E}_L\,|3\rangle}{\hbar}, \tag{2.6}$$

for coupling of state $|n\rangle$ to $|3\rangle$ by laser $L = a, b$. The Rabi frequency is the rate which the population will oscillate periodically between the coupled states when driven with a (resonant) laser. This behaviour is called 'Rabi flopping' [41]. In Section 2.2 we describe this phenomenon in more detail.

2.1.1 Momentum transfer

The Hamiltonian, through Equation 2.5, includes $e^{i\mathbf{k}_{a,b}\cdot\mathbf{z}}$ terms in its matrix elements. We shall assume that $\mathbf{k}_{a,b}$ is aligned parallel with z; the terms now become $e^{ik_{a,b}z}$. As we will see this leads to a momentum transfer from the light to the atom in quanta of $\pm\hbar k_{a,b}$ in the z direction. Physically this is due to conservation of momentum during absorption and stimulated emission of the laser photons; each photon carries $\hbar k_{a,b}$ momenta.

To see this analytically we begin by re-writing the completeness relation $\mathbb{I} = \int_{-\infty}^{\infty} \mathrm{d}p\,|p\rangle\,\langle p|$, where $|p\rangle$ is the momentum state wavefunction, as:

$$\mathbb{I}e^{\pm ik_{a,b}z} = \int_{-\infty}^{\infty} \mathrm{d}p\, e^{\pm ik_{a,b}z}\,|p\rangle\,\langle p|\,. \tag{2.7}$$

Similarly using the completeness relation, we define the momentum state wavefunction as [38, 40]

$$|p\rangle = \int_{-\infty}^{\infty} \mathrm{d}z\,|z\rangle\,\langle z|p\rangle = \frac{1}{\sqrt{2\pi\hbar}}\int_{-\infty}^{\infty} \mathrm{d}z\, e^{ipz/\hbar}\,|z\rangle\,. \tag{2.8}$$

Substituting this into Equation 2.7 gives

$$\begin{aligned} e^{\pm ik_{a,b}z} &= \frac{1}{\sqrt{2\pi\hbar}}\int_{-\infty}^{\infty}\mathrm{d}p\int_{-\infty}^{\infty}\mathrm{d}z\, e^{i(p\pm\hbar k_{a,b})z/\hbar}\,|z\rangle\,\langle p| \\ &= \int_{-\infty}^{\infty}\mathrm{d}p\,|p\pm\hbar k_{a,b}\rangle\,\langle p| \end{aligned} \tag{2.9}$$

Here we can see that the $e^{\pm ik_{a,b}z}$ part of the Hamiltonian acts on the momentum term of wavefunction in such a way to impart $\pm\hbar\mathbf{k}_{a,b}$. This motivates the choice of momentum inclusive basis seen in Figure 2.1 and equation 2.2.

If we assume the atom is in initial state $|1,\mathbf{p}\rangle$ the incident light from laser A, with wavevector $\mathbf{k}_a$, will drive the transition to the upper state. The absorption

of the photon will also impart momentum giving the new state $|3, \mathbf{p} + \hbar\mathbf{k}_a\rangle$. While in this upper state the atom undergoes stimulated emission driven by the second laser beam B, with wavevector $\mathbf{k}_b$, propagating in the opposite direction. This imparts more momentum in the same direction as the momentum from the absorption of the first photon; leading to the final state $|2, \mathbf{p} + \hbar(\mathbf{k}_a - \mathbf{k}_b)\rangle$.[2] We can see here that the *internal* atomic states have been coupled to the atom's *external* states. Here we can define the effective wavevector $\mathbf{k}_{\text{eff}} = \mathbf{k}_a - \mathbf{k}_b$, where for counter-propagating beams $\mathbf{k}_{\text{eff}} \approx 2\mathbf{k}_a$.[3] We can then re-write states $|2\rangle$ and $|3\rangle$ as $|2, \mathbf{p} + 2\hbar\mathbf{k}_{\mathbf{eff}}\rangle$ and $\left|3, \mathbf{p} + \frac{1}{2}\hbar\mathbf{k}_{\mathbf{eff}}\right\rangle$ respectively.

2.1.2 Evaluating the three-level Hamiltonian

In this section we will see how our three-level Raman system has an inertial-dependent phase term. This phase term will be key for the application of the atom interferometry in Chapter 3. Currently the total three-level Hamiltonian can be written as

$$\hat{H} = \begin{pmatrix} E_1 & 0 & \hat{V}_{13} \\ 0 & E_2 & \hat{V}_{23} \\ \hat{V}_{13}^* & \hat{V}_{23}^* & E_3 \end{pmatrix}, \tag{2.10}$$

where the diagonal terms, $E_n = \hbar\omega_n + \mathbf{p}_n^2/2m$, represent the energy and momenta of each state, the off-diagonal terms represent the interaction part of the Hamiltonian seen in Equation 2.5.[4] Since a (direct) transition cannot be driven between states $|1\rangle$ and $|2\rangle$ their interaction elements on the Hamiltonian are zero.[5] The interaction terms are given by:

$$\hat{V}_{13} = \frac{\hbar\Omega_{a1}}{2}\left(e^{-i(\omega_a t+\phi_a)} + e^{i(\omega_a t+\phi_a)}\right) \tag{2.11}$$

$$\hat{V}_{23} = \frac{\hbar\Omega_{b2}}{2}\left(e^{-i(\omega_b t+\phi_b)} + e^{i(\omega_b t+\phi_b)}\right), \tag{2.12}$$

with Rabi frequencies defined in Equation 2.6. We have assumed that laser A *only* couples to the $|1\rangle \Leftrightarrow |3\rangle$ transition, and laser B *only* couples to the $|2\rangle \Leftrightarrow |3\rangle$ transition. This allows us to ignore any Ω_{b1} and Ω_{a2} terms.[6]

[2] Here we can see the atom has gained $+\hbar\mathbf{k}_{a,b}$ momentum. If the atom began in the $|2, \mathbf{p} + \hbar(\mathbf{k}_a - \mathbf{k}_b)\rangle$ state it would return to the $|1, \mathbf{p}\rangle$ state via the same process, 'gaining' $-\hbar\mathbf{k}_{a,b}$ momentum.

[3] In the case of co-propagating beams $\mathbf{k}_{\text{eff}} = 0$ however in this thesis we will only be dealing with counter-propagating beams. The reason for this is that the coupling of internal states to external momentum states is essential for atom interferometry, we will see this in Chapter 3.

[4] It may be helpful to note that $\hat{V}_{13}^* = \hat{V}_{31}$, $\hat{V}_{23}^* = \hat{V}_{32}$, and vice-versa.

[5] i.e. $\langle 1|\,\hat{\mathbf{d}}\cdot\mathbf{E}\,|2\rangle = \langle 2|\,\hat{\mathbf{d}}\cdot\mathbf{E}\,|1\rangle = 0$ as the transition is dipole forbidden.

[6] In reality the light would still interact; however rather than drive transitions it would contribute towards an AC Stark shift. A full treatment including these absent terms can be

By substituting the atomic wavefunction, Equation 2.2, and the three-level Hamiltonian, Equation 2.10, into the TDSE, Equation 2.3, we arrive at the following coupled differential equations:

$$i\hbar\frac{\partial}{\partial t}c_1(t) = E_1c_1(t) + \hat{V}_{13}c_3(t) \tag{2.13a}$$

$$i\hbar\frac{\partial}{\partial t}c_2(t) = E_2c_2(t) + \hat{V}_{23}c_3(t) \tag{2.13b}$$

$$i\hbar\frac{\partial}{\partial t}c_3(t) = E_3c_3(t) + \hat{V}^*_{13}c_1(t) + \hat{V}^*_{23}c_2(t) \tag{2.13c}$$

These equations are non-trivial to solve. To simplify this system we make the transformation $|\Psi'(t)\rangle = \hat{T}\,|\Psi(t)\rangle$, where the diagonal unitary matrix $\hat{T} = \mathbb{I}\cdot e^{iE_nt/\hbar}$ and $\langle n|\Psi'(t)\rangle = b_n(t) = c_n(t)e^{iE_nt/\hbar}$ [38].[7] This has the effect of performing substitutions that factor out the fast oscillations of the atomic states. We can see this by performing this substitution on the TDSE—a detailed derivation can be found in Appendix A.1.1—to obtain the transformed Hamiltonian:

$$\hat{H}' = \hat{T}\hat{H}\hat{T}^\dagger - i\hbar\hat{T}\frac{\partial}{\partial t}\hat{T}^\dagger = \begin{pmatrix} 0 & 0 & \hat{V}'_{13} \\ 0 & 0 & \hat{V}'_{23} \\ \hat{V}'^*_{13} & \hat{V}'^*_{23} & 0 \end{pmatrix}, \tag{2.14}$$

where the new elements are

$$\hat{V}'_{13} = \frac{\hbar\Omega_{a1}}{2}\left(e^{\frac{i}{\hbar}(E_1-E_3)t - i(\omega_at+\phi_a)} + e^{\frac{i}{\hbar}(E_1-E_3)t + i(\omega_at+\phi_a)}\right) \tag{2.15}$$

$$\hat{V}'_{23} = \frac{\hbar\Omega_{b2}}{2}\left(e^{\frac{i}{\hbar}(E_2-E_3)t - i(\omega_bt+\phi_b)} + e^{\frac{i}{\hbar}(E_2-E_3)t + i(\omega_bt+\phi_b)}\right). \tag{2.16}$$

We now (re)introduce the single-photon detuning for each laser[8]

$$\Delta = \omega_a - (E_3 - E_1)/\hbar \tag{2.17}$$

$$= \omega_b - (E_3 - E_2)/\hbar + \delta_{ab} \tag{2.18}$$

found in Dunning [40].

[7] I realise that it may be confusing to have quantities $b_2(t)$ and Ω_{b2} in close proximity to each other. Remember that these are not labelled similarly for any other reason than convention (and some aesthetics). The notation of laser B and the state amplitudes b_n are independent of each other.

[8] It is also perfectly valid to define this as if Δ were 'below' $|3\rangle$ in Figure 2.1. There would simply be just a change of sign (can be interpreted as the 'atom' rotating in the opposite direction) for the terms in this section.

where the two-photon detuning is

$$\delta_{ab} = \omega_a - \omega_b - (E_2 - E_1)/\hbar \tag{2.19}$$

$$= (\omega_a - \omega_b) - \left(\omega_2 + \frac{(\mathbf{p} + \hbar\mathbf{k}_{\text{eff}})^2}{2m\hbar}\right) + \left(\omega_1 + \frac{\mathbf{p}^2}{2m\hbar}\right) \tag{2.20}$$

$$= [(\omega_a - \omega_b) - (\omega_2 - \omega_1)] - \mathbf{k}_{\text{eff}} \cdot \mathbf{v} - \frac{\hbar k_{\text{eff}}^2}{2m} \tag{2.21}$$

$$= \delta_L - \delta_{\text{Doppler}} - \delta_{\text{recoil}}. \tag{2.22}$$

Here we have defined separate contributions to the detuning: the laser detuning $\delta_L = (\omega_a - \omega_b) - (\omega_2 - \omega_1)$, the Doppler shift of the atom relative to the lasers $\delta_{\text{Doppler}} = \mathbf{k}_{\text{eff}} \cdot \mathbf{v}$, and the recoil shift $\delta_{\text{recoil}} = \hbar k_{\text{eff}}^2/2m$. For this thesis the Doppler contribution will be particularly important in Chapter 3.

Using these definitions of the detunings, Equations 2.15 and 2.16 become

$$\hat{V}'_{13} = \frac{\hbar\Omega_{a1}}{2}\left(e^{i(\Delta-2\omega_a)t-i\phi_a} + e^{i\Delta t+i\phi_a}\right) \tag{2.23}$$

$$\hat{V}'_{23} = \frac{\hbar\Omega_{b2}}{2}\left(e^{i(\Delta-\delta_{ab}-2\omega_b)t-i\phi_b} + e^{i(\Delta-\delta_{ab})t+i\phi_b}\right). \tag{2.24}$$

Here we can see that the more off resonant the lasers are from the transitions the faster the terms oscillate. In particular the 'off-resonant' terms, $e^{i(\Delta-2\omega_a)t}$ and $e^{i(\Delta-\delta-2\omega_b)t}$, will always oscillate much faster than their 'resonant' counterparts, $e^{i\Delta t}$ and $e^{i(\Delta-\delta)t}$.[9] These rapidly oscillating terms will average out and are negligible. This is called the rotating wave approximation (RWA). Under this approximation the three-level Hamiltonian becomes

$$\hat{H} = \frac{\hbar}{2}\begin{pmatrix} 0 & 0 & \Omega_{a1}e^{i\Delta t+i\phi_a} \\ 0 & 0 & \Omega_{b2}e^{i(\Delta-\delta)t+i\phi_b} \\ \Omega_{a1}^* e^{-i\Delta t-i\phi_a} & \Omega_{b2}^* e^{-i(\Delta-\delta)t-i\phi_b} & 0 \end{pmatrix}. \tag{2.25}$$

2.1.3 Effective two-level atom

Now we have simplified the three-level Hamiltonian, in this section we will see how we can turn this three-level system into a two-level system where

[9] From Figure 2.1 we can see that $\omega_a \gg \Delta$. In a real system the sign of Δ can change, however it is unimportant as, for rubidium, ω_a is on the scale of THz whereas Δ is usually on the scale of GHz. If we used a definition where $\Delta = \omega_{31} - \omega_a$, a factor of $-2\omega_{31}$ and $-2\omega_{32}$ would neatly fit into the terms of this substitution. The approximation we make here would remain valid as the difference between the upper and lower energy levels is also much greater than Δ.

population is only transferred coherently between $|1\rangle$ and $|2\rangle$. This is seen when the single-photon detuning is sufficiently large: $|\Delta| \gg |\Omega_{a1}|, |\Omega_{b2}|, |\delta_{ab}|$. Under this condition any transfer of population to $|3\rangle$ is negligible, including any associated spontaneous decay [39].[10]

We begin by solving the TDSE for $|\Psi'(t)\rangle$ and the transformed RWA Hamiltonian found in Equation 2.25. This gives the following equations:

$$i\hbar\frac{\partial}{\partial t}b_1(t) = b_3(t)\frac{\hbar}{2}\Omega_{a1}e^{i\Delta t+i\phi_a} \tag{2.26a}$$

$$i\hbar\frac{\partial}{\partial t}b_2(t) = b_3(t)\frac{\hbar}{2}\Omega_{b2}e^{i(\Delta-\delta_{ab})t+i\phi_b} \tag{2.26b}$$

$$i\hbar\frac{\partial}{\partial t}b_3(t) = b_1(t)\frac{\hbar}{2}\Omega^*_{a1}e^{-i\Delta t-i\phi_a} + b_2(t)\frac{\hbar}{2}\Omega^*_{b2}e^{-i(\Delta-\delta_{ab})t-i\phi_b}. \tag{2.26c}$$

Remembering that $b_n(t) = c_n(t)e^{i\omega_n t}$, the amplitudes $b_1(t)$ and $b_2(t)$ oscillate much slower than $b_3(t)$. Therefore we can treat them as being constants and integrate Equation 2.26c, remembering that $\Delta \gg \delta_{ab}$, to obtain:

$$b_3(t) = b_1(t)\frac{\Omega^*_{a1}}{2\Delta}e^{-i\Delta t-i\phi_a} + b_2(t)\frac{\Omega^*_{b2}}{2\Delta}e^{-i(\Delta-\delta_{ab})t-i\phi_b}. \tag{2.27}$$

Substituting this result into Equations 2.26 gives

$$i\hbar\frac{\partial}{\partial t}b_1(t) = \frac{\hbar}{2}\left(b_1(t)\frac{|\Omega_{a1}|^2}{2\Delta} + b_2(t)\frac{\Omega_{a1}\Omega^*_{b2}}{2\Delta}e^{i(\delta_{ab}t-\phi_L)}\right) \tag{2.28a}$$

$$i\hbar\frac{\partial}{\partial t}b_2(t) = \frac{\hbar}{2}\left(b_1(t)\frac{\Omega^*_{a1}\Omega_{b2}}{2\Delta}e^{-i(\delta_{ab}t-\phi_L)} + b_2(t)\frac{|\Omega_{b2}|^2}{2\Delta}\right) \tag{2.28b}$$

$$i\hbar\frac{\partial}{\partial t}b_3(t) = b_1(t)\frac{\hbar}{2}\Omega^*_{a1}e^{-i\Delta t+i\phi_a} + b_2(t)\frac{\hbar}{2}\Omega^*_{b2}e^{-i(\Delta+\delta_{ab})t+i\phi_b}, \tag{2.28c}$$

where we have defined the effective laser phase $\phi_L = \phi_b - \phi_a$.[11] This represents the phase of the 'standing wave' the two counter-propagating lasers create. We will address this in more detail in Chapter 3.

We can see that the populations of states $|1\rangle$ and $|2\rangle$ now no longer depend on b_3, the population of $|3\rangle$. We have therefore uncoupled the ground states from the excited state of the three-level atom. By inspection we can see that the effective two-level Hamiltonian is

$$\hat{H} = \frac{\hbar}{2}\begin{pmatrix} 2\Omega_1^{\mathrm{AC}} & \Omega_R e^{+i(\delta_{ab}t+\phi_L)} \\ \Omega_R^* e^{-i(\delta_{ab}t+\phi_L)} & 2\Omega_2^{\mathrm{AC}} \end{pmatrix}, \tag{2.29}$$

[10] By this we have also assumed that the population of $|3\rangle$ starts at zero i.e. $b_3(t=0) = 0$.

[11] The choice of sign for the definition of ϕ_L is arbitrary. Defining $\phi_L = \phi_a - \phi_b$ is perfectly reasonable.

where we have defined the two-photon Raman Rabi frequency

$$\Omega_R = \frac{\Omega_{a1}\Omega_{b2}^*}{2\Delta}, \tag{2.30}$$

and the AC Stark shift $\Omega_{1,2}^{\mathrm{AC}} = |\Omega_{a1,b2}|^2/4\Delta$ of each state. The Raman Rabi frequency is analogous to the single photon Rabi frequencies except it is now describing the coupling strength between the two ground states: a previously forbidden transition. In reality this transition is still forbidden by any other means than the Raman lasers driving the transition; therefore we have also effectively eliminated any spontaneous decay in the atomic system. The expression for the Stark shift we have here is slightly incomplete. It would take on a slightly different form that includes both laser contributions to each level; which would only add towards the light shift of each level. A full treatment including these terms can be found in Dunning [40]. However for this thesis these terms are largely ignored. We can apply another transformation to the Hamiltonian to simplify these Stark shift terms. The transformation $I \cdot e^{i\left(\Omega_1^{\mathrm{AC}}+\Omega_2^{\mathrm{AC}}\right)t/2}$ turns the diagonal elements of the Hamiltonian into terms representing the difference in the Stark shifts $\delta_{\mathrm{AC}} = \Omega_2^{\mathrm{AC}} - \Omega_1^{\mathrm{AC}}$:

$$\hat{H}' = \frac{\hbar}{2}\begin{pmatrix} -\delta_{\mathrm{AC}} & \Omega_R e^{+i(\delta_{ab}t-\phi_L)} \\ \Omega_R^* e^{-i(\delta_{ab}t-\phi_L)} & \delta_{\mathrm{AC}} \end{pmatrix}. \tag{2.31}$$

We can make a final transformation in order to remove time dependence from the Hamiltonian. We do this by transforming into a frame rotating around the z axes at rate δ_{ab}. This is expressed by the operator [38][12]

$$\hat{R} = \begin{pmatrix} e^{-i\delta_{ab}t/2} & 0 \\ 0 & e^{i\delta_{ab}t/2} \end{pmatrix}. \tag{2.32}$$

This transformation results in the rotating frame Hamiltonian

$$\hat{H}_R = \frac{\hbar}{2}\begin{pmatrix} \delta & \Omega_R e^{-i\phi_L} \\ \Omega_R^* e^{+i\phi_L} & -\delta \end{pmatrix}, \tag{2.33}$$

where we have defined the total detuning into $\delta = \delta_{ab} - \delta_{\mathrm{AC}}$. We have now arrived at a time-independent[13] two-level Hamiltonian of a three-level atom undergoing Raman transitions between its two ground levels. We will use this Hamiltonian to build an atom interferometry 'tool-kit'.

[12]This is constructed using a matrix exponential of the Pauli spin matrix, $\hat{\sigma}_z$, and the identity $\exp(i\alpha\hat{\sigma}) = I\cos(\alpha) + i\hat{\sigma}\sin(\alpha)$.

[13]We will see later on in Chapter 3 that we can 'nudge' some necessary time-dependence back and solve for a very simple case.

2.2 The Bloch sphere and Rabi oscillations

In Equation 2.6 we introduced the concept of the Rabi frequency and proceeded to use it extensively. Here we describe the importance of this quantity and its relation to atom interferometry. In order to do so we first introduce the Bloch sphere [42]: a method to visually and intuitively represent the state and evolution of a two-level atom. A different method of deriving the equations in this section using the density matrix can be found in Appendix A.2. The Bloch sphere figures were generated using the QuTiP package [43, 44].

Following from Equation 2.33, we now attempt to show the dynamics of the two-level atom. However rather than arriving at a set of differential equations through solving the TDSE we find a much more useful[14] 'time-propagator' operator[38, 45]. Section A.3.1 shows the following steps in more explicit detail. Assuming that the Hamiltonian is time-independent,

$$|\Psi(t)\rangle = \exp\left[\frac{-i}{\hbar}\hat{H}\cdot(t-t_0)\right]|\Psi(t_0)\rangle \tag{2.34}$$

is a solution to the TDSE.[15] We can call the exponential a new time-propagator operator that takes $|\Psi(t=t_0)\rangle$ to the new state at arbitrary time t:

$$\hat{U}(t,t_0) = \exp\left[\frac{-i}{\hbar}\hat{H}\cdot(t-t_0)\right]. \tag{2.35}$$

Before we plug the rotating frame Hamiltonian (Equation 2.33) into this operator, let us first represent it in terms of the field vector,

$$\mathbf{\Omega} = \Omega_R\cos(\phi_L)\hat{\mathbf{x}} + \Omega_R\sin(\phi_L)\hat{\mathbf{y}} + \delta\hat{\mathbf{z}}, \tag{2.36}$$

and the vector of Pauli matrices, $\hat{\sigma} = (\hat{\sigma_x}, \hat{\sigma_y}, \hat{\sigma_z})^\mathsf{T}$:

$$\hat{H}_R = \frac{\hbar}{2}\begin{pmatrix}\delta & \Omega_R e^{-i\phi_L}\\ \Omega_R e^{i\phi_L} & -\delta\end{pmatrix} = \frac{\hbar}{2}\mathbf{\Omega}\cdot\hat{\sigma}. \tag{2.37}$$

This allows us to use the identity $\exp[i\alpha\hat{\mathbf{n}}\cdot\hat{\sigma}] = I\cos(\alpha) + i\hat{\mathbf{n}}\cdot\hat{\sigma}\sin(\alpha)$ on the time-propagator operator, where $\alpha = -\sqrt{\Omega_R^2+\delta^2}(t-t_0)/2$ and $\hat{\mathbf{n}} = \mathbf{\Omega}/\sqrt{\Omega_R^2+\delta^2}$. We arrive at a matrix with the form

$$\hat{U} = \begin{pmatrix}C^* & -iS^*\\ -iS & C\end{pmatrix}, \tag{2.38}$$

[14] At least in my opinion.

[15] Valid for any time-independent Hamiltonian... not just the one we happen to have also made time-independent.

where the elements C and S are

$$C = \cos\left(\frac{\sqrt{\Omega_R^2 + \delta^2}}{2}(t - t_0)\right) + \frac{i\delta}{\sqrt{\Omega_R^2 + \delta^2}} \sin\left(\frac{\sqrt{\Omega_R^2 + \delta^2}}{2}(t - t_0)\right) \quad (2.39)$$

$$S = e^{i\phi_L} \frac{\Omega_R}{\sqrt{\Omega_R^2 + \delta^2}} \sin\left(\frac{\sqrt{\Omega_R^2 + \delta^2}}{2}(t - t_0)\right). \quad (2.40)$$

We can see that $\hat{U}$ is a function of t, t_0, Ω_R, δ, and ϕ_L. By adjusting these parameters we can provide different 'pulses' of light to the atom - controlling its state. To show the effect of these on the atomic state we will introduce the state vector

$$\mathbf{R} = u\hat{\mathbf{x}} + v\hat{\mathbf{y}} + w\mathbf{z}, \quad (2.41)$$

where u, v, and w are the Optical Bloch Equations (OBEs):

$$u = \langle\Psi|\,\hat{\sigma}_x\,|\Psi\rangle = c_1 c_2^* + c_1^* c_2 \quad (2.42a)$$

$$v = \langle\Psi|\,\hat{\sigma}_y\,|\Psi\rangle = i\,(c_1 c_2^* - c_1^* c_2) \quad (2.42b)$$

$$w = \langle\Psi|\,\hat{\sigma}_z\,|\Psi\rangle = |c_1|^2 - |c_2|^2 \quad (2.42c)$$

The state vector, $\mathbf{R}$, can be plotted on a unit sphere. On this sphere the poles would represent the 'pure states', in this case $|1\rangle$ and $|2\rangle$ in the $+\hat{\mathbf{z}}$ and $-\hat{\mathbf{z}}$ directions respectively. Any mixed state will have components along the equator where the angle of the vector along the $\hat{\mathbf{x}}$–$\hat{\mathbf{y}}$ plane is the global phase.[16] This is representation is the *Bloch sphere* picture. We can also represent the field vector, $\mathbf{\Omega}$, on the Bloch sphere.

Figure 2.2 shows these vectors on the Bloch sphere and how $\mathbf{\Omega}$ affects the state of $\mathbf{R}$ and therefore $|\Psi\rangle$. We can see that the atomic state 'orbits' around the field vector, and thus the state population to oscillate. It can be seen that $\mathbf{\Omega}$ causes a 'torque' on $\mathbf{R}$: $\dot{\mathbf{R}} = \mathbf{R} \times \mathbf{\Omega}$. This relation is shown more rigorously in Appendix A.2. The frequency of this oscillation is the (effective) Rabi frequency, $\Omega_{\text{eff}} = |\mathbf{\Omega}| = \sqrt{\Omega_R^2 + \delta^2}$, which is also described by the magnitude of the field vector. Any detuning 'lifts' the field vector off the sphere's equator and increases its magnitude. This can be seen in Figure 2.2b as $\mathbf{\Omega}$ protrudes out of the Bloch sphere; $\mathbf{R}$ has 'rotated' around the field vector by a larger angle over the same period as in Figure 2.2a. However due to the smaller angle between $\mathbf{R}$ and $\mathbf{\Omega}$, the atomic state doesn't ever fully reach the other state. It can be seen that the 'amplitude' of the state population oscillations is decreased in this scenario,

[16] It may be worth noting, to clear up any confusion, that these dimensions are not the same spatial coordinates *we* physically occupy. These are just the dimensions of this particular representation.

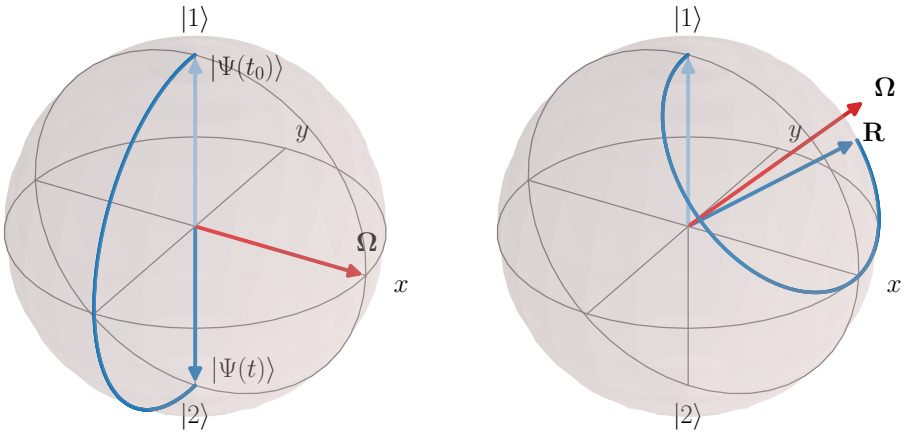

(a) $\delta = 0$ (b) $\delta = \Omega_R$

Figure 2.2: Visual representation of the light field, $\mathbf{\Omega}$, and the atomic state, $|\Psi\rangle \equiv \mathbf{R}$, using Equations 2.36 and 2.41, shown by the blue and red arrows respectively. The faded blue arrow represents the initial state of the atom—here the atom starts with $c_1(t_0) = 1$. The blue line represents the path the state vector, $\mathbf{R}$, has taken over the period $t = \pi/\Omega_R$. (a) shows the case where $\delta = 0$ and (b) where $\delta = \Omega_R$. The trajectories and vector positions calculated by applying Equation 2.38 to the initial atomic state for each time step.

whilst the frequency is increased. Figure 2.3 shows this sinusoidal oscillation called *Rabi oscillations* or *Rabi flopping* [41]. Here we can also see the effect of detuning on the Rabi oscillations. This and many of the graphs throughout this thesis were generated with the matplotlib python package [46].

If we increase the duration of the light pulse, the atomic state will continue to rotate around $\mathbf{\Omega}$. After a period of $t = 2\pi n/\Omega_{\text{eff}}$, where n is an integer, the atomic state will have oscillated back to its initial state.[17] In the case for $\delta = 0$, the state will continue to 'flop' sinusoidally between the two pure states as the light pulse is increased. During the time between the atom being in either $|1\rangle$ or $|2\rangle$ the atom will be in a superposition of those states.

If we time a resonant ($\delta = 0$) light pulse duration to be half-way between a full oscillation, $t = \pi/\Omega_R$, we will have completely swapped the atomic state population. Similarly, by timing the pulse to stop 'in-between' the two states we can engineer a coherent superposition of the two states. For equal state probabilities we would time the pulse so that the atom stops at the midpoint: $t = \pi/2\Omega_R$. This forms the basic tools for coherently manipulating the atomic state for atomic interferometry: π (mirror) pulses and $\pi/2$ (beam-splitter) pulses

[17] i.e. $|\Psi(t_0)\rangle = |\Psi(n2\pi/\Omega_{\text{eff}})\rangle$ where n in an integer.

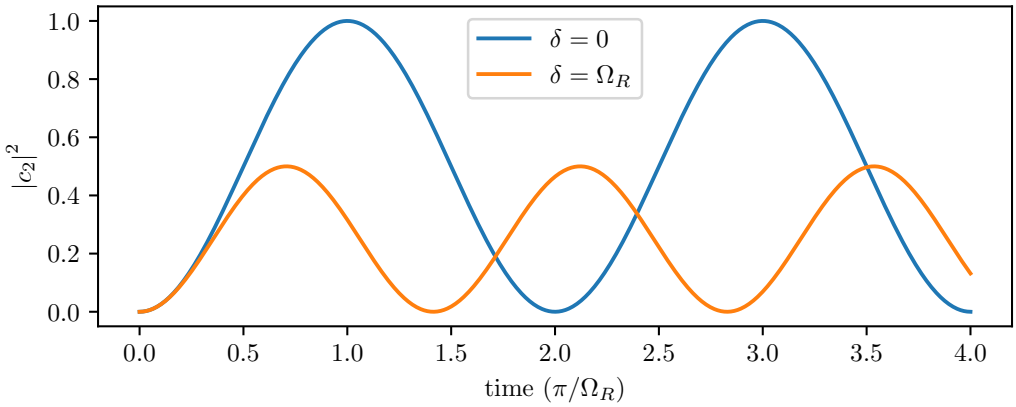

Figure 2.3: Simulation of Rabi oscillations of an atomic state by resonant and detuned light. The time axis is scaled to the period of half a resonant Rabi flop. This simulation was achieved by numerically computing the effect of Equation 2.38 on the atomic state at each time.

respectively. This will be discussed in more detail in Chapter 3. Therefore any system that can undergo Rabi oscillations by Raman transitions can be an atomic interferometer.

2.2.1 Dephasing in an ensemble

As we can see in Figures 2.2 and 2.3 a detuning changes the path taken on the Bloch sphere. The larger the detuning, the smaller the amplitude of the Rabi oscillations and the higher the oscillation's frequency.

In an atomic ensemble, where the atoms have a temperature and a distribution of velocities, each atom will see a slightly different Doppler shifted laser. This would mean that each atom, while beginning in the same state, would oscillate as if seeing a slightly different detuning from its different speed neighbour. When measuring the atomic state of the ensemble, it would be impossible to select individual atoms; the measured signal would be the average state of the ensemble. Figure 2.4 shows the effect of this dephasing in the ensemble.

As we increase the temperature of the ensemble, a larger portion of the atoms contribute to a detuned signal. This acts to 'dephase' the overall Rabi oscillations of the ensemble from an atom that experiences no Doppler shift. This is seen by the oscillations damping until eventually the ensemble resembles a steady state. The hotter the ensemble the faster the damping rate. As a larger proportion of atoms are contributing to a detuned signal their average also has a smaller

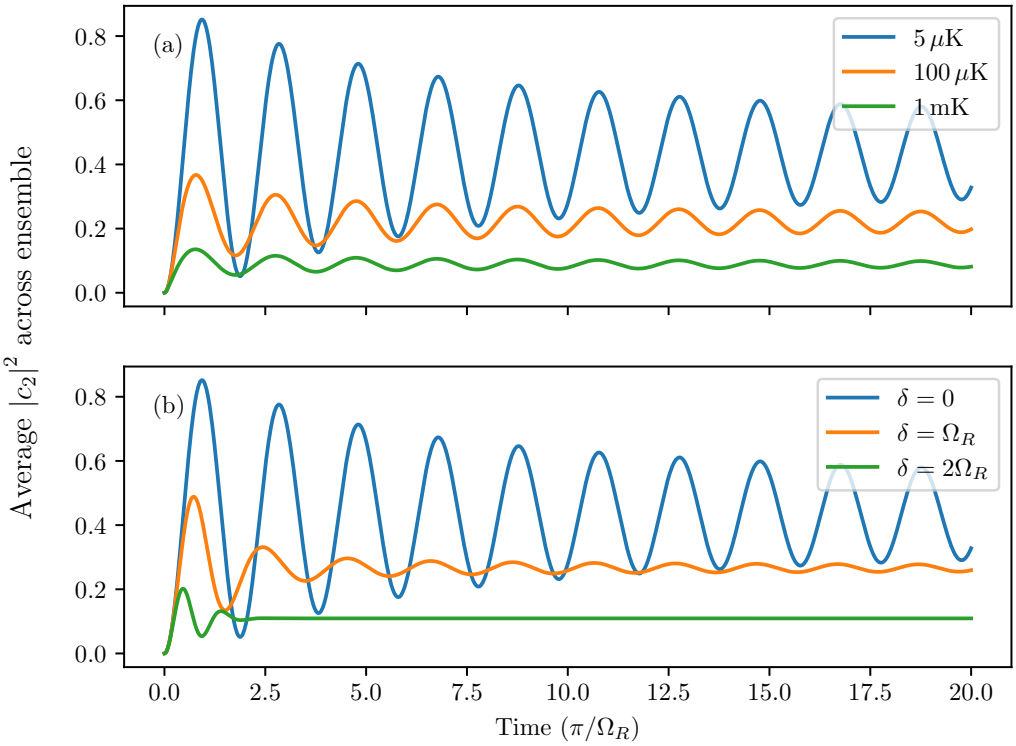

Figure 2.4: Simulation of Raman dephasing in ensemble of atoms. This simulation is illustrative and is not to make any useful experimental predictions. Graph (a) shows how changes in the temperature of the ensemble affects the overall phase, decay rate, and amplitude of the ensemble average population. Similarly graph (b) shows how laser detuning affects this in a 5 μK ensemble. The simulations used 1000 atoms with velocities distributed by the one-dimensional Maxwell-Boltzmann distribution. Using Equation 2.38, the progression of each atom's state population was calculated with the detunings determined through the atom's Doppler shift.

amplitude. This is seen by a decreased signal when the ensemble has reached a steady state. To minimise these effects in an experiment it is important to cool the atoms as much as possible.

The same effect occurs due to laser detuning. Now a much smaller portion of the atoms experience resonant light, again due to their Doppler shift. So a greater fraction of the atoms are contributing to the detuned signal. In an experiment this can be used as a method for spectroscopy, as it allows probing of the Raman linewidth.

This is also a reason why a large Ω_R is beneficial experimentally. Increasing $\mathbf{\Omega}$

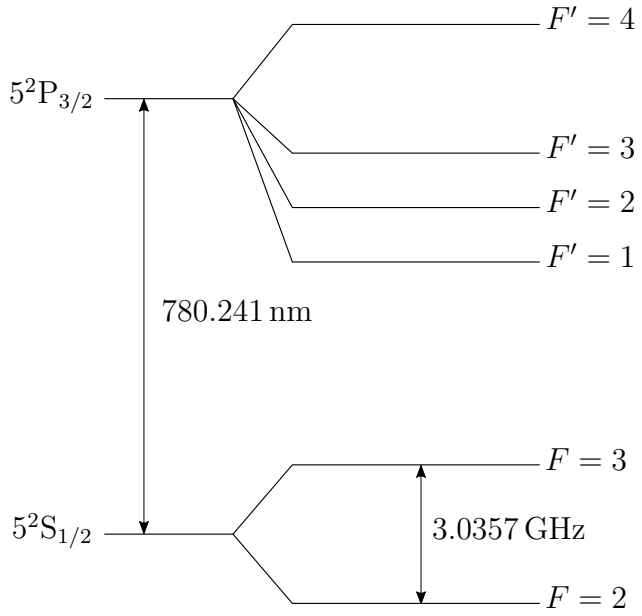

Figure 2.5: ^{85}Rb D_2 hyperfine structure. For more detail please refer to Steck [49] where the data presented here was taken from.

in the 'resonant' $\hat{\mathbf{x}}$–$\hat{\mathbf{y}}$ plane decreases this dephasing effect. A large part of the work by Saywell [38] is to confront and alleviate the difficulties that effects such as this present in an atomic interferometer.

We have not included any spontaneous emission in the atomic model of this chapter. The reasons for this is that we are transitioning between atomic states whose single-photon transitions are forbidden.[18] Carey [47] and Fox [48] include spontaneous decay in their discussion.

2.3 Rubidium-85

In our experiments we use ^{85}Rb, atomic number 37, the hyperfine structure of which can be seen in Figure 2.5. These transitions, named the D_2 line, conveniently sit around 780 nm. This wavelength is convenient because laser diode technology at that wavelength is well developed due to its application in commercial CD drives. Rubidium also has a high vapour pressure at room temperature, enabling vapour cells for absorption spectroscopy to be used for laser locking.

[18] Remember this is an assumption made at the beginning of this chapter. We are using a two-photon Raman transition to 'bypass' the single-photon forbidden transition.

Rubidium has two distinct fine-structure atomic transitions from the $\left|5^2\mathrm{S}_{1/2}\right\rangle$ ground state to the excited $\left|5^2\mathrm{P}_{1/2}\right\rangle$ (D_1) and $\left|5^2\mathrm{P}_{3/2}\right\rangle$ (D_2) states at 795 nm and 780 nm respectively [49].[19] ^{85}Rb has a nuclear spin angular momentum of $I = 5/2$; therefore, the ground state has hyperfine states $|F = 2, 3\rangle$, the D_1 line hyperfine states to be $|F' = 2, 3\rangle$, and the D_2 hyperfine states as $|F' = 1, 2, 3, 4\rangle$.[20] Any transition between these states must conserve angular momentum. This leads to only certain transitions being permitted by the selection rule $\Delta F = F' - F = 0, \pm 1$ [48]. Another reason we choose to use the D_2 line is that there is a closed transition (only one decay route back to the initial state) of $|F = 3\rangle \Leftrightarrow |F' = 4\rangle$. The D_1 line has no such transitions. This closed transition is integral to the convenient cooling and trapping of rubidium. This and the previous factors allow us to cool and trap rubidium with relative ease: a topic we will detail in Chapter 4.

Rubidium has two abundant isotopes; ^{85}Rb and 87 with relative abundances of 72.17% and 27.83% respectively [50]. A reason we choose the ^{85}Rb isotope over ^{87}Rb is due to the hyperfine splitting frequency of its ground states. In ^{85}Rb the splitting is about 3.0 GHz and around 6.8 GHz in ^{87}Rb. This puts different bandwidth requirements of equipment to use the different isotopes, with ^{85}Rb having a lower bandwidth requirement. The equipment used currently in the lab in designed for ^{85}Rb and while there is scope to use ^{87}Rb we currently do not have the required equipment.

2.3.1 Multiple Raman routes

At the beginning of the chapter we introduced the electric dipole matrix, $\hat{\mathbf{d}} = e\hat{\mathbf{r}}$, whose elements represent the strength of an external field on the atom's electron. Revisiting the single-photon Rabi frequency, which represents the coupling strength of a transition by the external field,

$$\Omega^{(L)}_{|F,m_F\rangle,|F',m'_F\rangle} = -\frac{1}{\hbar}\left\langle F', m'_F\right| \hat{\mathbf{d}} \cdot \mathbf{E}_L \left|F, m_F\right\rangle, \tag{2.43}$$

where $|F, m_F\rangle$ is the starting ground state, and $|F', m'_F\rangle$ is the excited state.[21] Here we have also introduced the magnetically sensitive Zeeman sub-levels, m_F,

[19] The notation used for the fine structure is $n\,^{2S+1}L_J$, where n is the principle quantum number (electron energy level), S is the electron spin, L is the orbital angular momentum, and $J = L + S$ is the total electron angular momentum. Rather than numbers, it is convention to use the 'names' of the electron orbitals for L; the first few are S = 0, P = 1, and D = 2.

[20] The total atomic angular momentum F has integer values satisfying $|J - I| \leq F \leq J + I$.

[21] This is the case for absorption of a photon, the complex conjugate of the Rabi frequency would represent stimulated emission.

where there are $2F+1$ levels of each state $|F\rangle$.[22] For the rubidium transitions we can write the single-photon Rabi frequencies as the vectors

$$\mathbf{\Omega}_{a1} = \left(\Omega^a_{|2,m_F\rangle,|1,m'_F\rangle}, \Omega^a_{|2,m_F\rangle,|2,m'_F\rangle}, \Omega^a_{|2,m_F\rangle,|3,m'_F\rangle}, \Omega^a_{|2,m_F\rangle,|4,m'_F\rangle}\right) \tag{2.44a}$$

$$\mathbf{\Omega}_{b2} = \left(\Omega^b_{|3,m_F\rangle,|1,m'_F\rangle}, \Omega^b_{|3,m_F\rangle,|2,m'_F\rangle}, \Omega^b_{|3,m_F\rangle,|3,m'_F\rangle}, \Omega^b_{|3,m_F\rangle,|4,m'_F\rangle}\right). \tag{2.44b}$$

For ^{85}Rb the only possible paths for the Raman transitions to be mediated by are the $|F'=2,3\rangle$ states. While the Raman light may fulfil the large Δ condition for all F' levels, transitions between $|F=2\rangle$ to $|F'=4\rangle$ are forbidden. Similarly, $|F=3\rangle$ cannot transition to $|F'=1\rangle$. These components in the above vector are therefore zero.[23]

Extending this formalism to the Raman Rabi frequency, Equation 2.30, results in [38, 40]:

$$\begin{aligned}\Omega_R &= \frac{|\mathbf{\Omega}_{a1}\cdot\mathbf{\Omega}_{b2}|}{2\Delta} \\ &= \frac{1}{2\Delta}\left|\Omega^a_{|2,m_F\rangle,|2,m'_F\rangle}\Omega^b_{|3,m_F\rangle,|2,m'_F\rangle}\right. \\ &\qquad \left. +\Omega^a_{|2,m_F\rangle,|3,m'_F\rangle}\Omega^b_{|3,m_F\rangle,|3,m'_F\rangle}\right|.\end{aligned} \tag{2.45}$$

We have applied our model to a real atom where $|1\rangle = |F=2\rangle$ and $|2\rangle = |F=3\rangle$. Our model slightly breaks down here as $|3\rangle$ is equivalent to two states $|F'=2,3\rangle$. Therefore the Raman transitions take both paths simultaneously.

2.3.2 Raman polarisations

When a transition occurs between the hyperfine F levels, in addition to obeying $\Delta F = 0, \pm 1$ they must also satisfy the selection rule $\Delta m_F = m'_F - m_F = 0, \pm 1$. In the presence of a weak magnetic field, the m_F levels of their respective F levels become non-degenerate; this Zeeman splitting is given by $\Delta E = \mu_B g_F B m_F$, where μ_B is the Bohr magneton, g_F is the Landé g-factor for a given F level, and B is the magnetic field strength [41]. Whereas a transition to a different F state is driven by the laser's wavelength, the transition between m_F levels is determined by the laser's polarisation relative to the applied magnetic field. The magnetic field applies a quantisation axis to the atom. We will take the magnetic field to be acting in the $\hat{\mathbf{z}}$ direction: $\mathbf{B} = B\hat{\mathbf{z}}$.

To discuss polarisations we take the atom's perspective, at some positive $\hat{\mathbf{z}}$ position looking towards the laser source at the origin. The polarisation of a

[22] These states have values given by the integers that satisfy $-F \leq m_F \leq F$.

[23] i.e. $\Omega^a_{|2,m_F\rangle,|4,m'_F\rangle} = \Omega^b_{|3,m_F\rangle,|1,m'_F\rangle} = 0$

laser beam propagating in the negative $\hat{\mathbf{z}}$ direction would still be determined whilst looking towards the origin in a positive $\hat{\mathbf{z}}$ position i.e. $\pi^{0,+,-} = -\pi^{0,+,-}$, and $\pm\sigma^{+,-} = \mp\sigma^{-,+}$.

For linearly polarised light propagating perpendicular to $\hat{\mathbf{z}}$, its polarisation can be parallel with $\hat{\mathbf{z}}$. We call this polarisation π^0 which drives a transition where $\Delta m_F = 0$. If this linearly polarised light propagates in the $\hat{\mathbf{z}}$ direction, with its polarisation parallel to either $\hat{\mathbf{x}}$ or $\hat{\mathbf{y}}$ directions it will drive a $\Delta m_F = \pm 1$ transition. These polarisations are called π^- and π^+ respectively.

To drive a $\Delta m_F + \pm 1$ transition with a particular sign, we require circularly polarised light propagating along the quantisation axis $\hat{\mathbf{z}}$. Left-circularly polarised light, σ^+, with the polarisation rotating anti-clockwise drives a $\Delta m_F = +1$ transition, whereas right-circularly polarised light, σ^-, with the polarisation rotating clockwise drives a $\Delta m_F = -1$ transition.[24]

Only particular combinations of polarisations for the two counter-propagating beams give valid Raman transitions.[25] These are all perpendicularly polarised combinations[26] which have routes through an $m'_F = \pm 1$ state. However, when being driven to the ground state the total change $\Delta m_F = 0$. Following from the previously described transitions, the linearly polarised case $\pi^+ - \pi^-$, named lin-perp-lin, takes a route through $m'_F = \pm 1$. For left-circularly polarised light, $\sigma^+ - \sigma^+$, the $m'_F = +1$ route is taken. Similarly the right-circularly polarised configuration, $\sigma^- - \sigma^-$, takes the $m'_F = -1$ route.

The reason only certain combinations of polarisations can achieve Raman transitions is that, rather than the transitions being forbidden by selection rules, the dipole matrix elements (in Equation 2.45) cancel out. It is particularly worth noting that the polarisations $\sigma^\pm - \sigma^\mp$ cannot facilitate Raman transitions. As we will see in Chapter 4 this is the required configuration for the atom trapping beams. This polarisation requirement must be considered in any experiment involving Raman transitions and motivates design choices in Chapter 5.

[24] Linear polarisations can be constructed using a superposition of circular polarisations: $\pi^+ = (\sigma^+ + \sigma^-)/\sqrt{2}$ and $\pi^- = (\sigma^+ - \sigma^-)/\sqrt{2}$.

[25] There are other combinations that provide Raman transitions with beams that are not counter-propagating [40]. However we are only interested in the counter-propagating case as they are useful for atom interferometry.

[26] It may be more intuitive to see that these light beams are perpendicularly polarised by looking towards the laser source, as opposed to the fixed viewpoint we have set previously.

Chapter 3

Atom interferometry

Broadly speaking, atom interferometry—a form of matter-wave interferometry—is a technique where matter behaves as a wave to perform interferometry. This is analogous to optical interferometry where constructive and deconstructive interference causes fringes to be observed. Depending on the nature of the experiment, these fringes can be used to perform measurements with precision smaller than the travelling wave's wavelength.

Perhaps the most famous example, especially in popular science, is Young's double slit experiment [51]. Waves diffracting through two thin slits would interfere at a distance after propagating. Here an 'interference pattern' would be observed. This pattern could only be explained through the properties of waves. The wavelength of a matter-wave is given by the de Broglie wavelength relation $\lambda_{\mathrm{dB}} = h/p$, where p is the momentum of the particle.

We are able to appropriate the optical Mach-Zehnder interferometer configuration for atom interferometry [37, 52]. Here the 'roles' of light and matter are swapped; the matter becomes the propagating wave and light is used as the mirrors and beamsplitters. We can construct this interferometer using timed pulses of light. A beamsplitter, $\pi/2$, pulse followed by a mirror, π, pulse and finally another beamsplitter pulse: identical to the typical optical Mach-Zehnder. Figure 3.1 shows this matter-wave interferometry sequence. Likewise, to any optical interferometer, a measurement with the interferometer requires determination of the phase difference of the interferometer arms. For an atomic interferometer we imprint this phase onto the atomic state population.

We begin this chapter by creating the 'tool-kit' to construct the interferometry sequence. This tool-kit will be used as the basis for all numerical simulations in this chapter. We then explore how this can be used to make inertial measurements of

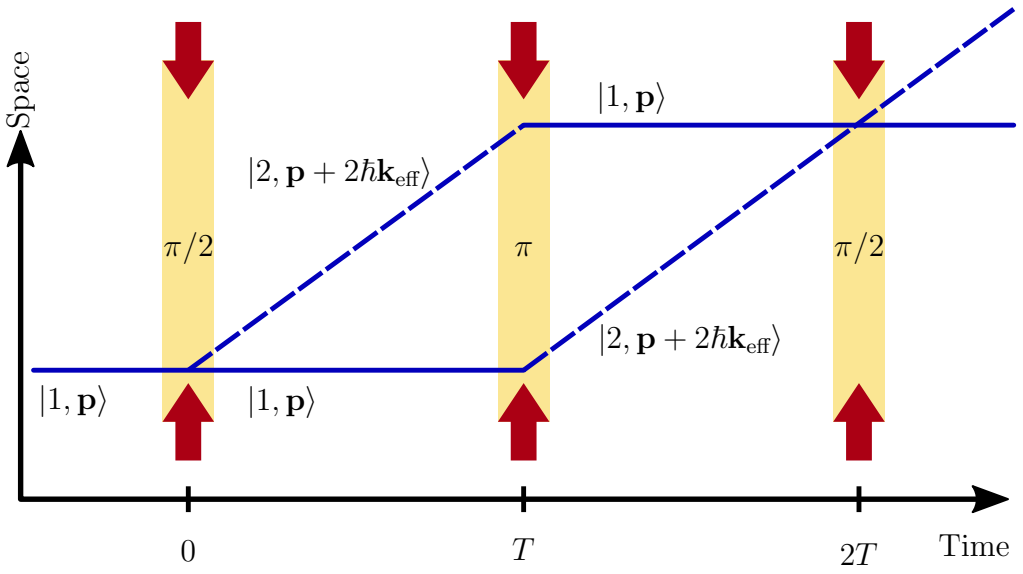

Figure 3.1: Spatial and temporal representation of Mach-Zehnder matter-wave interferometry sequence. The solid lines represent trajectories where the atom is in the ground state, $|1\rangle$, and has not gained any momentum from the light pulses. The dashed lines represent trajectories where the atom is in the excited state, $|2\rangle$, and has gained momentum, $2\hbar\mathbf{k}_{\text{eff}}$, from the two light pulses. The light pulses are applied in a beamsplitter–mirror–beamsplitter ($\pi/2$–π–$\pi/2$) sequence chronologically; and applied along the spatial axis that is being investigated. Here we have used the two arrows to indicate that the pulses are comprised of two counter-propagating beams. For symmetry of the interferometer the pulses are each separated by time T. The final output of the interferometer is the state population, where these two populations are determined by the phase accumulated during the interferometry sequence.

local gravity, and some of the challenges in making such a measurement. Finally we discuss the benefits of using a gradiometer and how such a measurement can be achieved.

3.1 Interferometry tool-kit

Following from the results in Chapter 2, we can build the beamsplitter and mirror pulses, also called $\pi/2$ and π–pulses respectively. These are pulses of counter-propagating Raman beams along the axes we wish to make a measurement along. In the ideal case the pulses are resonant, $\delta = 0$, and maintain the same phase, ϕ_L, at each pulse. We also set $t_0 = 0$ for the purposes of each pulse. We will see later how this is not the case when making measurements, however we will assume this holds true while we build the pulses.

To construct a π–pulse we use Equation 2.38 with $t = \pi/\Omega_R$ (half the period of a full Rabi oscillation). This results in

$$\hat{U}_\pi = \begin{pmatrix} 0 & -ie^{-i\phi_L} \\ -ie^{i\phi_L} & 0 \end{pmatrix}. \tag{3.1}$$

Hence the two-level atom wavefunction is transformed into

$$|\Psi\rangle_\pi = \begin{pmatrix} c_1(t_\pi) \\ c_2(t_\pi) \end{pmatrix} = -i \begin{pmatrix} e^{-i\phi_L} c_2(t_0) \\ e^{i\phi_L} c_1(t_0) \end{pmatrix}. \tag{3.2}$$

As expected for a mirror pulse, the state populations become swapped. We know this intuitively from the Bloch sphere picture presented in Section 2.2. We can also see that this facilitates the mirror function in Figure 3.1. It is important to remember, as we showed in Section 2.1.1, that the internal states are coupled to the external momentum states. When we swap the states we also swap their momenta and therefore direction in the interferometer.

We construct a beamsplitter pulse in the same way. Using the time propagator matrix, Equation 2.38, with $t = \pi/2\Omega_R$ we obtain:

$$\hat{U}_{\pi/2} = \frac{1}{\sqrt{2}} \begin{pmatrix} 1 & -ie^{-i\phi_L} \\ -ie^{i\phi_L} & 1 \end{pmatrix}, \tag{3.3}$$

transforming the waveform into

$$|\Psi\rangle_{\pi/2} = \frac{1}{\sqrt{2}} \begin{pmatrix} c_1(t_0) - ie^{-i\phi_L} c_2(t_0) \\ c_2(t_0) - ie^{i\phi_L} c_1(t_0) \end{pmatrix}. \tag{3.4}$$

From this equation it is slightly less intuitive what happens. Returning to the Bloch sphere picture, when the atom is in a pure state a beamsplitter pulse will put the atom in an equal superposition of both states. This effect of the beamsplitter pulse on the momentum states can be seen in Figure 3.1. Similarly when the atom is in a superposition, the pulse will attempt to return the atom to the other basis state.[1] An important feature to note is that this depends on the angle between the state vector and the laser phase, ϕ_L. This fact allows us to map the atomic phase onto its state populations.

A change in the atom's phase, relative to the laser phase, during the sequence would be reflected onto the final atomic state. Currently, the $\pi/2$–π–$\pi/2$ sequence will simply return the atomic state to its initial state. The atomic phase accumulation occurs during the time between the interferometry pulses. This stage of the interferometry determines what the interferometer is sensitive to—what is being measured. We call this period of the sequence free evolution.

3.1.1 Free evolution operator

When we approach the time between the interferometry pulses, the free evolution time, the assumption—made in Equation 2.34—that the Hamiltonian is time-independent breaks down. Here we need to introduce time dependence into the Hamiltonian. Thankfully when setting the Rabi frequency to zero, i.e. no laser, the Hamiltonian only has diagonal elements—this makes the TDSE much simpler to solve. A more detailed description of the following steps can be found in Appendix A.3.2. We introduce time dependence into the Hamiltonian through the Doppler shift in Equation 2.22:

$$\delta_{\text{Doppler}}(t) = \mathbf{k}_{\text{eff}} \cdot \mathbf{v}(t) = \mathbf{k}_{\text{eff}} \cdot (\mathbf{v}_0 + \mathbf{a}t)\,, \tag{3.5}$$

where $\mathbf{v}_0$ is the initial velocity of the atom, and $\mathbf{a}$ is the acceleration experienced by the atom in time t. The Doppler shift the atom experiences–hence the detuning—is dependent on its velocity, and therefore its acceleration. This changes the phase the atom's state accrues compared to the laser's phase. Solving the TDSE with the diagonalised rotating frame Hamiltonian, Equation 2.33, results in the following differential equations:

$$i\hbar\frac{\partial}{\partial t}\begin{pmatrix} c_1(t) \\ c_2(t) \end{pmatrix} = \frac{\hbar}{2}\begin{pmatrix} \delta(t)c_1(t) \\ -\delta(t)c_2(t) \end{pmatrix}. \tag{3.6}$$

[1] This follows that a beamsplitter pulse is 'half' a mirror pulse, both in period and function.

This has solutions

$$c_1(t) = c_1(t_0)\exp\left[-\frac{i}{2}\int_{t_0}^{t+t_0}\delta(\tau)\,\mathrm{d}\tau\right] \tag{3.7a}$$

$$c_2(t) = c_2(t_0)\exp\left[+\frac{i}{2}\int_{t_0}^{t+t_0}\delta(\tau)\,\mathrm{d}\tau\right]. \tag{3.7b}$$

Therefore the transformed wavevector is

$$|\Psi(t)\rangle_{\mathrm{FE}} = \begin{pmatrix}\exp\left[-\frac{i}{2}\mathbf{k}_{\mathrm{eff}}\cdot\left(\mathbf{v}_0 t + \frac{1}{2}\mathbf{a}\left[t^2+2tt_0\right]\right)\right]c_1(t_0)\\ \exp\left[+\frac{i}{2}\mathbf{k}_{\mathrm{eff}}\cdot\left(\mathbf{v}_0 t + \frac{1}{2}\mathbf{a}\left[t^2+2tt_0\right]\right)\right]c_2(t_0)\end{pmatrix}. \tag{3.8}$$

As expected, only the phase of the atomic population changes. Importantly, this phase change depends on the acceleration, or forces, the atom experiences. We can write the free evolution 'operator' to be

$$\hat{U}_{\mathrm{FE}} = \begin{pmatrix}e^{-\frac{i}{2}\mathbf{k}_{\mathrm{eff}}\cdot\left(\mathbf{v}_0 t+\frac{1}{2}\mathbf{a}\left[t^2+2tt_0\right]\right)} & 0\\ 0 & e^{+\frac{i}{2}\mathbf{k}_{\mathrm{eff}}\cdot\left(\mathbf{v}_0 t+\frac{1}{2}\mathbf{a}\left[t^2+2tt_0\right]\right)}\end{pmatrix}. \tag{3.9}$$

Assuming the pulse lengths to be small compared with t, for the first period of free evolution (between the first beamsplitter pulse and the mirror pulse) $t = T_1$. For the second period of free evolution we want to begin where the previous free evolution ended (i.e. $t_0 \equiv T_1 + t_0$) and end after a period of T_2: $t = T_2$. For the purposes of this thesis we will only consider the case for equal periods of free evolution, $T = T_1 = T_2$. It is also worth noting that in previous parts of the interferometry sequence we have taken t_0 to be at the start of that interferometry pulse, however here t_0 is the start of the interferometry *sequence* when the atoms have initial velocity $\mathbf{v}_0$. We will see later that under this restriction the static terms in the detuning cancel out for the final interferometer phase shift.[2] To simplify the algebra we will only consider the $\delta_{\mathrm{Doppler}}$ terms in our calculations. We will see that the time independent velocity term vanishes as would the other terms we are neglecting to show.

3.1.2 Total interferometer phase shift

Now we have the individual components of the interferometer we can construct the entire interferometry sequence:

$$|\Psi\rangle_{\mathrm{final}} = \hat{U}_{\pi/2}\hat{U}_{\mathrm{FE}}\hat{U}_{\pi}\hat{U}_{\mathrm{FE}}\hat{U}_{\pi/2}\,|\Psi(t_0)\rangle\,. \tag{3.10}$$

[2]The recoil shift, δ_{recoil}, also vanishes if we consider v_0 to be the average of the initial and final velocities [53].

Maintaining the assumptions made previously (resonant laser, constant laser phase, and small $1/\Omega_R$ compared to T) and the initial state $|\Psi(t_0)\rangle = (1,0)^\intercal$, we find the final state of the atom to be

$$|\Psi\rangle_{\text{final}} = \begin{pmatrix} -\cos\left(\frac{1}{2}\phi_{T_1} - \frac{1}{2}\phi_{T_2}\right) \\ e^{i\phi_L}\sin\left(\frac{1}{2}\phi_{T_2} - \frac{1}{2}\phi_{T_1}\right) \end{pmatrix}, \tag{3.11}$$

where the terms [38]

$$\phi_{T_1} = \mathbf{k}_{\text{eff}} \cdot \left(\mathbf{v}_0 T_1 + \frac{1}{2}\mathbf{a}\left[T_1^2 + 2T_1 t_0\right]\right) \tag{3.12a}$$

$$\phi_{T_2} = \mathbf{k}_{\text{eff}} \cdot \left(\mathbf{v}_0 T_2 + \frac{1}{2}\mathbf{a}\left[T_2^2 + 2T_1 T_2 + 2T_2 t_0\right]\right) \tag{3.12b}$$

are the phase terms originating from the first and second period of free evolution respectively. We can see that the final populations depend on the difference of phase accumulated during each free evolution period. The full calculation can be found in Appendix A.3.3.

Many analogies can be made of matter-wave interferometers [54]. The periods of free evolution can be interpreted as the atom 'winding up' and then back down like a coil, where Equations 3.12 are the angles through which the coil has been wound. The difference in how far the atom has been 'rotated' each way is the final phase term of the interferometer—which is then mapped onto the atomic state populations. We will return to this analogy later as we have neglected yet to involve the dynamics of the laser.

Figure 3.2 shows the state of the atom during a Mach-Zehnder interferometry sequence on the Bloch sphere. Here we can see the effect of each interferometry stage on the internal state of the atom. In particular the phase of the atom can be seen clearly along the equator of the Bloch sphere.[3] This is particularly useful in showing geometrically how the difference in free evolution phases determines the final atomic state. We can see that if $\phi_{T_1} = \phi_{T_2}$ the atomic state returns to the initial state. Likewise, if $\phi_{T_2} - \phi_{T_1} = \pi$ we obtain an inversion of the initial state.

We obtain the final result of the interferometer as the population of the excited atomic state

$$P_2 = \frac{1}{2} - \frac{1}{2}\cos(\Phi), \tag{3.13}$$

where Φ is the total phase shift of the interferometer. When the periods of free evolution are equal, $T = T_1 = T_2$, the total phase shift is

$$\begin{aligned} \Phi &= \phi_{T_2} - \phi_{T_1} \\ &= \mathbf{k}_{\text{eff}} \cdot \mathbf{a}T^2. \end{aligned} \tag{3.14}$$

[3] These phases have been calculated in Appendix A.3.4.

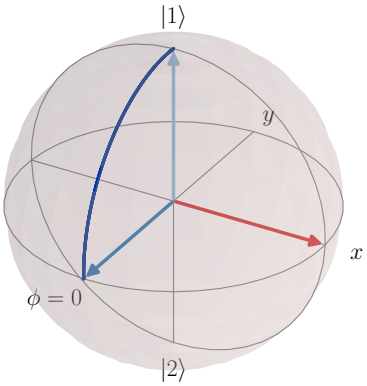

(a) First beam-splitter pulse

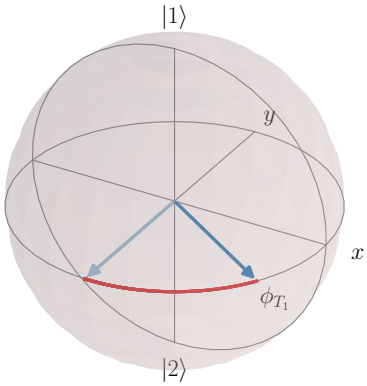

(b) Free evolution

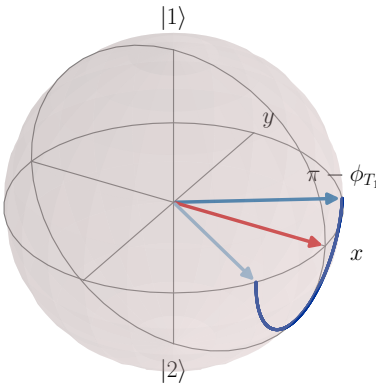

(c) Mirror pulse

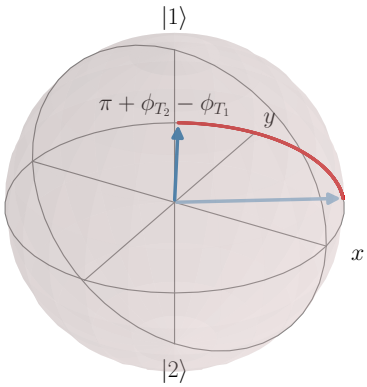

(d) Second free evolution

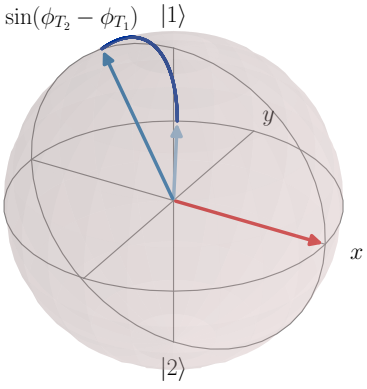

(e) Final beam-splitter. Amplitude rather than phase shown here.

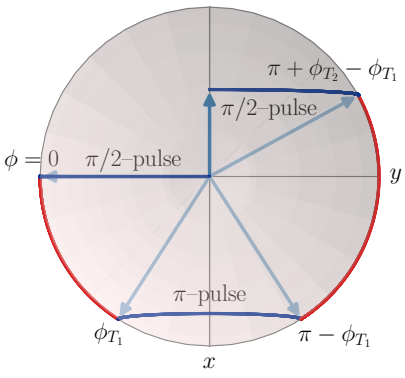

(f) Top-down view of entire sequence

Figure 3.2: Bloch sphere representation of Mach-Zehnder interferometry sequence. The blue arrows represent the starting point (faded) of the atomic state vector, $\mathbf{R}$, and end state with similarly blue trajectories. The red arrows represent the laser vector $\mathbf{\Omega}$. The red trajectories represent the phase accumulated during free evolution. For each phase term we have neglected to include the $\phi_L - \pi/2$ terms as here we are mostly interested in the interaction of ϕ_{T_1} and ϕ_{T_2}. Adapted from Saywell [38].

We can see that $\mathbf{k}_{\text{eff}}T^2$ is the space-time area enclosed by the interferometer, seen more clearly in Figure 3.1. The phase shift due to acceleration is proportional to this factor.[4]

The output of the interferometer being dependent on acceleration allows us to use this as an inertial sensor. This technique has found applications in measuring acceleration [58, 59], rotations [60, 61, 62, 63], and gravity [1, 16, 52]. In this thesis we are particularly interested in measuring gravity and gravity gradients. By directing the Raman beams vertically, aligning $\mathbf{k}_{\text{eff}}$ vertically, the acceleration we measure can be local gravity, $\mathbf{g}$. Therefore Equation 3.14 becomes $\Phi = -k_{\text{eff}}gT^2$.

3.2 Gravity

So far we have neglected to involve the aspects of the laser in the interferometry sequence. Let us imagine an atom falling under earth's gravity, seen in Figure 3.3. If we wish to interact with this atom using resonant light we would need to continually 'chirp' the laser's frequency to match the atom's Doppler shift. This is no different during the interferometry sequence. When the atom is falling due to gravity during the interferometry sequence the acceleration it experiences is constant.[5] Therefore with a constant laser phase, $\phi_{T_1} = \phi_{T_2}$ and the atom will always return to its initial state. However, the laser phase *does not* remain constant. This adds extra phase terms to the interferometry sequence and affects the final output of the interferometer. Figure 3.4 shows an example of this effect on the Bloch sphere. In this diagram, even when $\phi_{T_1} = \phi_{T_2}$, the atom does not return to its initial state. To return the atom back to its initial state, we must maintain constant laser phase. This is done by phase-continuously chirping the Raman laser frequency at each stage of the interferometry sequence to match the atom's Doppler shift.[6] When these are matched the atom will once again return to its initial state.

This is analogous to the phase difference accrued between two oscillators of different frequencies. As the atom becomes Doppler shifted it sees the laser frequency shift, and hence phase. The longer there is a frequency difference the more phase will be accrued between them. In order to not gain any relative phase the laser frequency must stay the same as the atoms, requiring a chirp.

[4] The phase shift of some gyroscope schemes can be proportional to T^3 [55, 56, 57].

[5] We will assume that the interferometry sequence period ($2T$) is sufficiently shot that any effect from the gravity gradient is negligible.

[6] Chirping also maintains resonance with the atom. Off-resonant interactions lead to decreasing fringe amplitudes [64]. This is the same effect seen in Section 2.2.1.

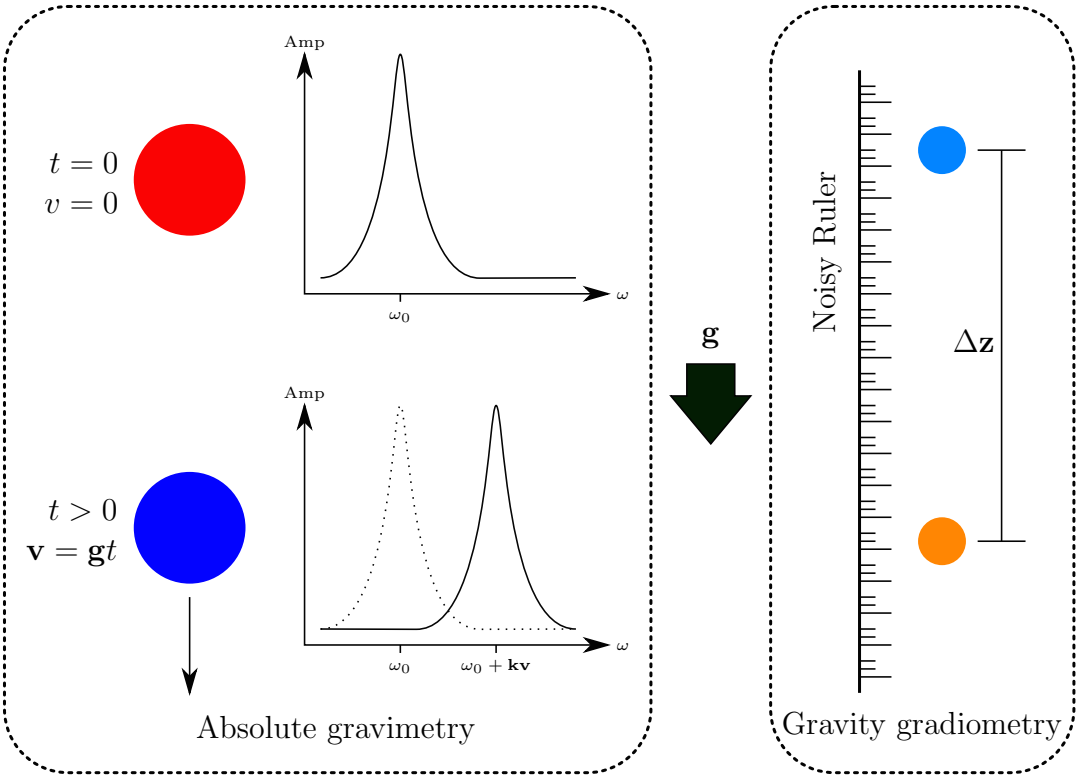

Figure 3.3: Concept of classical gravity measurement. The left side shows an example of a classical absolute gravity measurement. The right side shows an example of a classical gravity gradiometry measurement. In the centre is the acceleration due to gravity, $\mathbf{g}$, common to both diagrams. The coloured balls represent the atomic test masses. The atoms in the left side are the same atom at different times. The atoms on the right side are different atoms at different heights, separated by $\Delta\mathbf{z}$. The graphs on the left represent atomic spectral lines that become Doppler shifted.

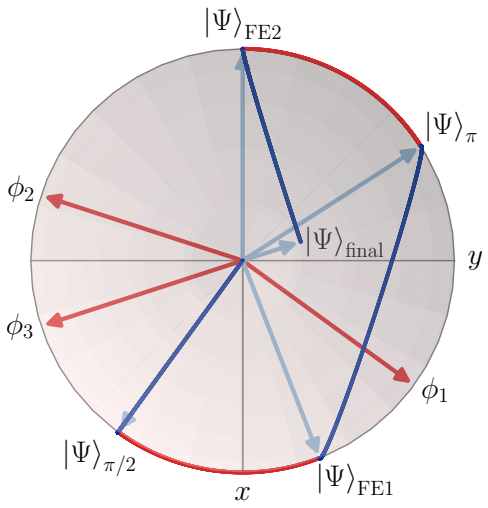

Figure 3.4: Top-down view of Mach-Zehnder interferometry sequence with changing laser pulse phases. The phases ϕ_1, ϕ_2, and ϕ_3 are the laser phases for the $\pi/2$, π, and the final $\pi/2$ pulses respectively. The atomic state is also labelled at each stage, represented by a blue arrow. The laser vector $\mathbf{\Omega}$ is represented by the red arrows. The trajectories of the atomic state are represented by the blue and red lines for pulses and free evolution respectively. Here the phase accrued during free evolution is the same for both periods.

We can build up a picture of the phase accrued by iterating the chirp rate. This can then be used to find the chirp rate which matches the atom's Doppler shift.

In the frame of the atom, there is no phase difference gained through free evolution. The Doppler shift is experienced through interaction with the laser pulses. Here we can define the phase of each pulse as [65]

$$\phi_n = \omega_n t_n - k_{\mathrm{eff}} g t_n^2 + \phi_n^0, \tag{3.15}$$

where ω_n is the frequency of the pulse, t_n is the time at which the laser is pulsed, and ϕ_n^0 is the phase of the light pulse at the atom's position at $t = 0$. The pulses are numbered $n = 1, 2, 3$ corresponding to the $\pi/2$, π, and the final $\pi/2$ pulses respectively. The laser's frequency can be defined by the chirp rate β:

$$\omega_n = \omega_0 + \beta(t_n - t_0), \tag{3.16}$$

where ω_0 is the initial (unchirped) laser frequency and t_0 is the time when the chirp is started. Performing the interferometry steps (with a free evolution stage which accrues zero phase) we obtain a final phase of

$$\Phi = \phi_1 - 2\phi_2 + \phi_3 \tag{3.17}$$

$$= (\beta - k_{\mathrm{eff}} g)\, T^2 + \Delta\phi^0, \tag{3.18}$$

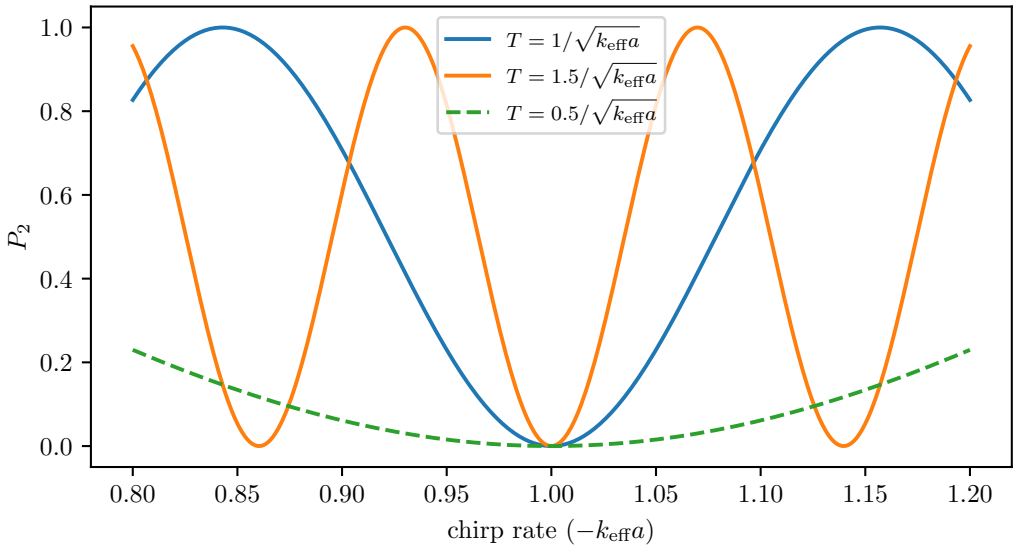

Figure 3.5: Simulation of interferometry sequence measuring gravity. Laser phases defined in Equation 3.15 and $\phi_{T_1} = \phi_{T_2} = 0$. Horizontal axis scaled by $-k_{\text{eff}}a$, in experiments chirp rate is usually measured in MHz/s. Multiple dwell times, T, have been plotted to illustrate their effect on the fringe periodicity.

where $\Delta\phi^0 = \phi_1^0 - 2\phi_2^0 + \phi_3^0$ is the initial phase difference between the pulses.[7]

This provides us two experimentally controllable variables: β and $\Delta\phi^0$.[8] Scanning across these results in interferometer fringes. Using Equation 3.18 g can be found to high precision.[9] Figure 3.5 shows a simulated example of this when scanning β with $\Delta\phi^0 = 0$

There are a couple methods to obtain a gravity measurement from this. For example Peters et al. [1, 16] uses a coarse 'guess' of β that corresponds roughly to g and then varies $\Delta\phi^0$ to fine tune. Bidel et al. [33, 34] simply varies β to obtain fringes (similarly to Figure 3.5). Hauth et al. [29] uses a hybrid of the two methods, first obtaining a best guess β and then tuning $\Delta\phi^0$ to the fringe maxima. The chirp rate is then varied to track the fringe and the absolute local gravity is calculated.[10]

[7] It is worth noting that this is insensitive to ω_0 and t_0. This implies that the timing when the chirp is initiated or even the chirp 'offset' is unimportant.

[8] Usually in experiments only one laser phase is modulated, this tends to be the final interferometer pulse, ϕ_3^0.

[9] Might be worth remembering that $k_{\text{eff}} = 4\pi/\lambda$.

[10] The sensitivity of an interferometer can be increased by operating on the side of a fringe [66]. This is due to the sides of the fringes having a steeper slope than the maxima/minima and hence are more sensitive to phase fluctuations.

3.2.1 Phase noise

An accelerometer is also sensitive to mechanical vibrations due to the laser phase being affected by movements of equipment—usually vibrations from a retro-reflecting mirror. Such vibrations are indistinguishable from absolute gravity as they modulate the laser's phase and hence effect the atom's phase during the interferometry sequence. This has the effect of 'scrambling' the measured fringe. As a result, the accelerometer apparatus is usually supported by sophisticated vibration isolation/damping stages [30, 33, 67]. Classical accelerometers have also found use in compensating for these vibrations [34, 68], creating 'hybrid' accelerometers.[11] We have seen how the dynamics of the laser phase are used for inertial measurements. Therefore any instability in the laser phase would affect measurements. In a matter-wave interferometer the mechanism by which vibrational noise affects the measurement is though the laser phase.

Even within a vibrationless environment laser phase fluctuations would still be present. Any Raman laser system involves electronic frequency (and phase) manipulation. Inevitably any electronic noise present in these control systems is imprinted onto the laser phase.

There are many other contributions to the interferometric phase noise and degradation of the interferometer fringe. For example magnetic field noise, aberrations in wave-front uniformity, and non-uniform beam intensity. These are discussed in detail in works such as Hinton [15], Schmidt [64], and Zhu [69]. We have chosen to focus on the noise inherent to the laser itself in this thesis as it is most relevant to the benefits of gradiometry.

Sensitivity function

Any discussion of phase noise would be incomplete without inclusion of the sensitivity function. With this we can quantify the effect the noise has on the interferometer. A detailed derivation of the following can be found in Cheinet et al. [70]. Here we only state the main results.

So far we have approximated each Raman laser pulse to be instantaneous. This of course is not possible in a physical system.[12] The laser pulses have a period

[11] This arrangement also allows the classical accelerometer to compensate for the slow repetition rate of current matter-wave accelerometers.

[12] Not just because of physical limitations but we require, by definition, the laser pulse durations to be scaled by the Rabi frequency, $\approx 1/\Omega_R$. Usually the Rabi frequency is on the order of $< 100\,\mathrm{kHz}$ [65].

defined by the Rabi frequency. The period of a $\pi/2$ pulse is $\tau_R = \pi/2\Omega_R$, therefore a π pulse length is $2\tau_R$. Here we can adjust T to be between when the laser pulses are switched on and off. The means the entire interferometry sequence has a period of $2(T + 2\tau_R)$. We will also redefine $t = 0$ to be the centre of the π pulse. This divides the interferometry sequence evenly into two segments. The initial time is then $t_i = -(T + 2\tau_R)$ and the final time $t_f = T + 2\tau_R$.

Consider a laser phase fluctuation, $\delta\phi_L$, at time t, this fluctuation changes the transition probability, Equation 3.13, by δP. The sensitivity function is defined as:

$$g_s(t) = 2 \lim_{\delta\phi_L \to 0} \frac{\delta P(\delta\phi_L, t)}{\delta\phi_L}. \tag{3.19}$$

Considering the effect of $\delta\phi_L$ on δP during each section of the interferometry sequence leads to [69]

$$g_s(t) = \begin{cases} \sin(\Omega_R(t+T)) & -T - 2\tau_R < t < -T - \tau_R \\ -1 & -T - \tau_R < t < -\tau_R \\ \sin(\Omega_R t) & -\tau_R < t < \tau_R \\ 1 & \tau_R < t < T + \tau_R \\ \sin(\Omega_R(t-T)) & T + \tau_R < t < T + 2\tau_R \end{cases} \tag{3.20}$$

Outside the interferometer any laser phase fluctuations have no impact on the interferometer phase, Φ. Therefore $g_s(t) = 0$ during the period outside t_i and t_f.

Using this we can evaluate the influence of the laser phase noise on the interferometric phase:

$$\delta\Phi = \int_{-\infty}^{+\infty} g_s(t)\,\mathrm{d}\phi_L(t) = \int_{-\infty}^{+\infty} g_s(t)\frac{\mathrm{d}\phi_L(t)}{\mathrm{d}t}\,\mathrm{d}t. \tag{3.21}$$

It is more useful now to look in the frequency domain. The Fourier transform of the sensitivity function is given by

$$G(\omega) = \int_{-\infty}^{+\infty} e^{-i\omega t} g_s(t)\,\mathrm{d}t, \tag{3.22}$$

$$= \frac{4i\Omega_R}{\omega^2 - \Omega_R^2} \sin\left(\frac{\omega(T+2\tau_R)}{2}\right)\left[\cos\left(\frac{\omega(T+2\tau_R)}{2}\right) + \frac{\Omega_R}{\omega}\sin\left(\frac{\omega T}{2}\right)\right] \tag{3.23}$$

where ω is the frequency of the phase noise component. The root mean squared standard deviation of the interferometric phase noise is

$$\left(\sigma_\Phi^{\mathrm{RMS}}\right)^2 = \int_0^{+\infty} |H(\omega)|^2 S_{\phi_L}(\omega)\,\mathrm{d}\omega, \tag{3.24}$$

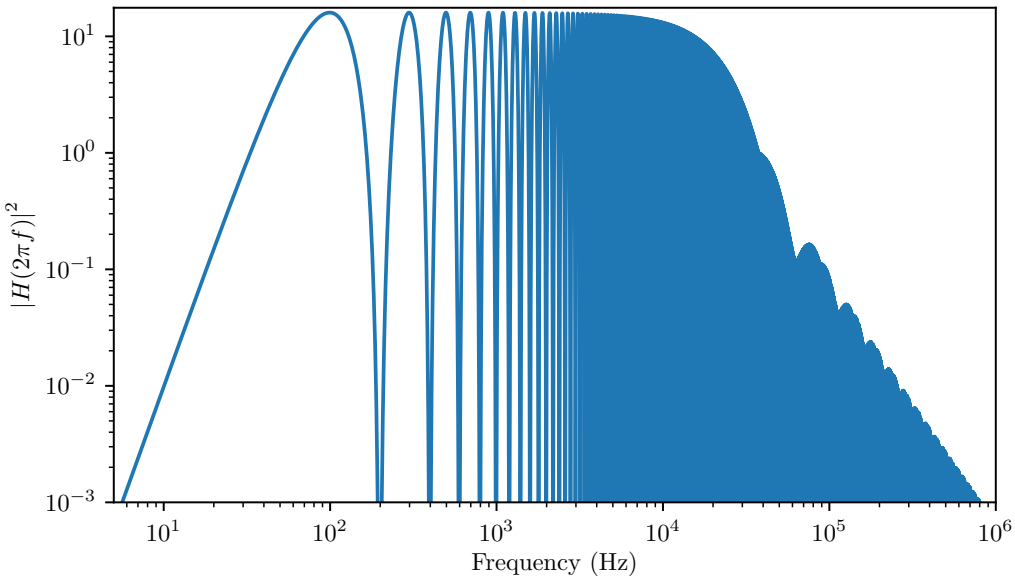

Figure 3.6: Interferometer transfer function for $T = 5\,\text{ms}$ and $\tau_R = 20\,\mu\text{s}$. The frequency term here refers to the frequency within a power spectral density. Here we can observe areas of 'gain' or increased sensitivity to noise (where the transfer function > 1), and other areas where there is an attenuation effect.

where $|H(\omega)|^2 = \omega G(\omega)$ is the transfer function of the interferometer, and $S_{\phi_L}(\omega)$ is the power spectral density of the laser phase. Here we can see the interaction between the laser phase fluctuations and the noise response of the interferometer.

The transfer function behaves as a filter to the interferometric noise. Figure 3.6 shows an example of a transfer function curve. Regular oscillations lead to zeroes at $f_k = k/(T + 2\tau_R)$, where k is an integer. These points represent frequencies where the laser phase noise is 'synchronised' to the interferometer operation; fluctuating the same for each pulse of the interferometer, cancelling out any effect on the interferometric phase [69]. The second feature to note is the low pass filtering effect with corner frequency $f_0 = (\sqrt{3}/3)(\Omega_R/2\pi)$ and slope $\approx 2/(\omega/\Omega_R)^2$. This is due to fast oscillations averaging out their effect. The transfer function provides a useful tool for determining the optimum parameters to run the interferometer with to minimise fringe noise. The interaction between the laser phase noise power spectral density and the transfer function allow us to effectively ignore high frequency noise; and focus efforts in minimising lower frequency noise.

The Allan variance[13] of the interferometer signal over the period τ is

$$\sigma_\Phi^2(\tau) = \frac{1}{\tau}\sum_{n=1}^{\infty} |H(2\pi n f_c)|^2 S_{\phi_L}(2\pi n f_c), \tag{3.25}$$

where the cycling frequency $f_c \approx 1/(T + 2\tau_R)$. Here we can see that the interferometer is only sensitive to noise at multiples of this frequency. In the case of laser phase noise the sensitivity function is given by

$$\sigma_\Phi^2(\tau) = \left(\frac{\pi}{2}\right)^2 \frac{S_{\phi_L}}{\tau}\frac{T}{\tau_R}. \tag{3.26}$$

Here we can see that the sensitivity of interferometer depends on the Raman pulse length. While longer pulses would give a more sensitive interferometer they also reduce signal strength due to atom loss from the velocity dependence of the beams. Reduced signal strength also reduces the signal-to-noise ratio (SNR). This becomes a balancing act to find optimal experimental parameters.

3.2.2 Gravity gradiometry

Another analogy we can use is that the Raman laser is being used as a ruler, the wave-fronts of the light being the regular tick marks of the ruler. We can say that during the interferometry sequence we measure the position of the atom relative to this ruler, as the laser phase is imprinted onto the atom. As we have discussed in the above section, if we have an unstable ruler our measurement will lose precision. If however we are measuring the distance between two stable points, as seen in Figure 3.3, this differential measurement is unaffected by the instability of the ruler. Likewise if we have two gravimeters using exactly the same Raman laser beam, a differential measurement would be insensitive to the common laser phase noise. This is the benefit of using gradiometry for noisy applications.

A measurement of the gravity gradient is a differential measurement of gravity divided by the separation between the two measurement locations [12]

$$\Delta g = \frac{g_{\text{upper}} - g_{\text{lower}}}{z_{\text{upper}} - z_{\text{lower}}}, \tag{3.27}$$

where $g_{\text{upper,lower}}$ are the absolute gravity measurements for the upper and lower sensors at positions $z_{\text{upper,lower}}$. This is found through the difference in the

[13]The Allan variance is similar to the variance however measured over different time periods τ [71, 72].

interferometric phase shifts

$$\Delta\Phi = \Phi_{\text{upper}} - \Phi_{\text{lower}} \tag{3.28}$$

$$= k_{\text{eff}}\Delta g T^2 \left(z_{\text{upper}} - z_{\text{lower}}\right) + \left(\Delta\phi^0_{\text{upper}} - \Delta\phi^0_{\text{lower}}\right). \tag{3.29}$$

We have (re)introduced the laser phase term $\Delta\phi^0$ for the upper and lower measurements. This laser phase term is where we will absorb any noise terms in the experiment. As mentioned previously if this noise is common to both interferometers then $\Delta\phi^0_{\text{upper}} = \Delta\phi^0_{\text{lower}}$ and their term vanishes. This 'common mode' noise rejection is why gravity gradiometers are well suited to practical applications.

Figure 3.7 shows a simulation of an example gradiometric measurement. We introduce a random vibrational noise, common to both interferometers, in Figure 3.7b. To make any sense of the noisy data it can be displayed in a Lissajous plot. To extract the phase differential a parametric ellipse can be fitted to this data [20]:[14]

$$x(t) = A\sin(t) + B \tag{3.30a}$$

$$y(t) = C\sin(t + \Delta\Phi) + D, \tag{3.30b}$$

where A and C represent the amplitudes of the measured interferometric fringes, and B and D are the coordinates for the centre of the ellipse. Here we see that the phase scrambling due to (common) noise does not impede the gradiometric measurement. It may also be interesting to note that, since now only the phase relationship matters between the two interferometers, an accurate frequency chirp is also no longer required. Experimentally the chirp is now only necessary to maintain resonance. The scrambling by the vibrational noise can probe the phase relationships of the two interferometers.[15]

Equation 3.29 also allows us to see the stability required for phase noise not common mode to both interferometers. This is of particular interest in this thesis as the final goal of the PLAIN-GG project is to actively maintain the phase correlation of the Raman beams. For 30 Eotvos of sensitivity ($= 30 \times 10^{-9}\,\text{s}^{-2}$), with 780 nm light, $T = 40$ ms (the maximum time for the chamber described in Chapter 5), and a baseline separation of 4 m, we obtain a phase stability requirement of ≈ 3 mrad during the period of the interferometer. This is achievable with Raman laser stability [30] and optical stability methods [36]. This is for a single-shot of data. In an actual experiment many data-points would be collected and averaged relaxing this requirement. It is also possible to improve this sensitivity requirement using techniques such as large momentum transfer and composite pulses [74, 75, 76].

[14] There are also more complicated methods using Bayesian estimators [73].

[15] Perhaps in very stable environments a chirp would still be required.

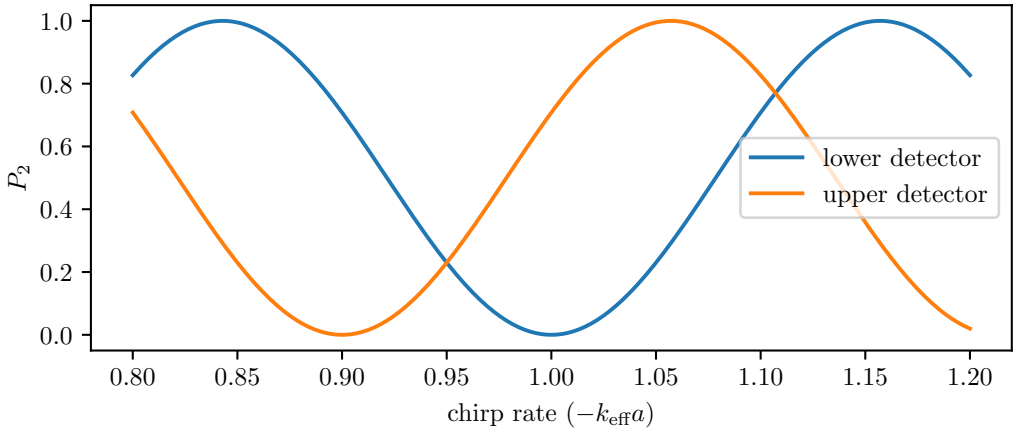

(a) Fringe data

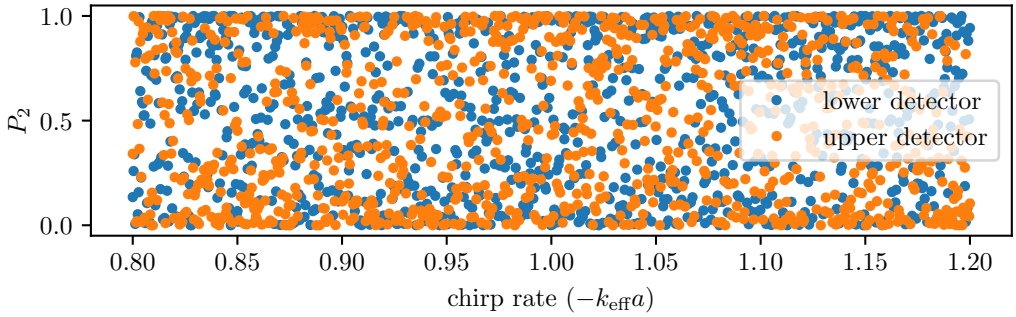

(b) Noisy fringe data

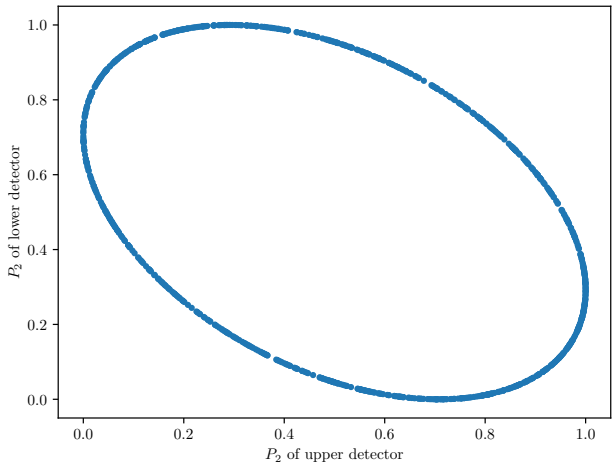

(c) Lissajous plot of noisy fringe data

Figure 3.7: Simulation of gravity gradiometer with random common mode noise added to acceleration detected. Here the 'upper detector' measures an acceleration 10% smaller than the 'lower detector'. The chirp rates in (a) and (b) are scaled to the gravitational acceleration experienced by the lower detector.

In this chapter we have taken a simplified approach to the effect of gravity gradients on the interferometer sequence. In reality they also induce phase shifts on each interferometer [12]. We have also assumed no rotations, such as those induced by Earth's rotation. Wu [77] includes this in their model.

Chapter 4

Atom trapping

In order to implement the atom interferometry technique described in Chapter 3, we need the ability to coherently manipulate atoms. At room temperature, collisional decoherence events are common and prevent any coherent states to survive long enough to be useful. By sufficiently reducing the temperature of the atoms we can prevent these events. Isolation from the environment is also a necessary measure against decoherence. By trapping and cooling atoms to sub-Kelvin temperatures, we are able to observe coherent effects on a macroscopically sized sample of atoms.

In this chapter we introduce how laser cooling and trapping of atoms, specifically ^{85}Rb, can be achieved. We then describe methods used to characterise, and therefore optimise, a MOT. The treatment given here closely follows that in Foot [41] and Himsworth [78].

4.1 Scattering force

The central idea behind laser cooling is that radiation has momentum: $\mathbf{p} = \hbar\mathbf{k}$, where $\hbar$ is the reduced Planck constant, and $\mathbf{k}$ is the light's wave-vector. During light-matter interaction, the light is able to impart its momentum onto the atom. This happens in two ways: the absorption of the photon imparts a momentum 'kick' in the direction of the light beam, $\hat{\mathbf{k}}$; and spontaneous emission imparts another kick in a random direction. Under steady illumination from the light, the atoms undergo successive absorption and emission events: receiving successive kicks. These kicks average out to slow down the atom. Therefore the magnitude of this 'scattering' force is the product of the photon momentum and the atom's

scattering rate[1]

$$F_{\text{scatt}} = \hbar k R_{\text{scatt}}, \tag{4.1}$$

where the scattering rate is the product of the transition linewidth and the population of the excited state:

$$R_{\text{scatt}} = \Gamma \rho_{22} = \frac{\Gamma}{2} \frac{\Omega^2/2}{\delta^2 + \Omega^2/2 + \Gamma^2/4}, \tag{4.2}$$

where Γ is the transition linewidth, ρ_{22} is the excited state population[2], Ω is the single photon Rabi frequency, and δ is the detuning. Here the detuning is the sum of the laser detuning and the Doppler shift: $\delta = \omega - \omega_0 + kv$, where ω is the laser frequency, ω_0 is the transition frequency. The Doppler shift, kv, is the product of the atom's velocity, v, and the laser's wave-vector. The Rabi frequency, Ω, and the transition linewidth, Γ, are related to the light intensity, I, and the transition's saturation intensity, I_{sat}, by

$$\frac{I}{I_{\text{sat}}} = \frac{2\Omega^2}{\Gamma^2}. \tag{4.3}$$

The scattering force is therefore

$$F_{\text{scatt}}(\delta) = \hbar k \frac{\Gamma}{2} \frac{I/I_{\text{sat}}}{1 + I/I_{\text{sat}} + (2\delta/\Gamma)^2}. \tag{4.4}$$

This is only be useful for slowing atoms travelling towards the laser source [79]. By employing multiple pairs of beams in counter-propagating directions we can attempt to cool atoms along all axes.

4.2 Optical molasses

Atoms in a gas will have a distribution of velocities in all directions. To slow the atoms down—cooling them— we direct counter propagating beams of equal intensity and same frequency at the atoms along all three axes.[3] Since the atoms are provided with equal and opposite forces, it can be seen that there is no net force. However, this is only true for stationary atoms.[4] Atoms moving along beam axis will experience a Doppler shift of the light, imbalancing these

[1] Since we are only talking about forces in the direction of the light beam $\hat{\mathbf{k}}$, we will drop the vector notation for simplicity.

[2] This is the same quantity as in Equation A.6.

[3] This also has the effect of creating standing waves which we will discuss in Section 4.6.

[4] This is the aim anyway, as a stationary atom is a cold atom indeed.

forces. We can detune the laser light to selectively interact with atoms of certain velocities along $\hat{\mathbf{k}}$. If we detune the light to red ($\delta_{\text{laser}} = \omega - \omega_0 < 0$) then only atoms moving towards the light will become resonant and receive a kick 'backwards'. Blue detuning the light ($\delta_{\text{laser}} > 0$) will have the opposite effect and kick atoms already travelling in the direction of the light further in that direction.

Consider a single atom moving along an axis. The force on the atom is the sum of the scattering forces from the counter-propagating lasers:

$$F_{\text{molasses}} = F_{\text{scatt}}(\delta_{\text{laser}} + kv) + F_{\text{scatt}}(\delta_{\text{laser}} - kv) \tag{4.5}$$

$$\approx 4\hbar k^2 \frac{I}{I_{\text{sat}}} \frac{2v\delta_{\text{laser}}/\Gamma}{\left[1 + I/I_{\text{sat}} + (2\delta_{\text{laser}}/\Gamma)^2\right]^2} \tag{4.6}$$

$$\approx -\alpha v, \tag{4.7}$$

where α is the damping coefficient given by:

$$\alpha = 4\hbar k^2 \frac{I}{I_{\text{sat}}} \frac{-2\delta_{\text{laser}}/\Gamma}{\left[1 + (2\delta_{\text{laser}}/\Gamma)^2\right]^2}. \tag{4.8}$$

We have neglected the term $I/I_{\text{sat}} \ll 1$ in the denominator as we are dealing with intensities far below saturation in this treatment [41]. We have assumed that the Doppler shift is small compared to δ_{laser} and Γ. Figure 4.1 shows these forces on the atom. At low velocities, $|kv| \ll \Gamma$, we see that a force is exerted on the atom dampening its movement in either direction. This is analogous to a particle moving in a viscous sticky liquid, such as treacle, where $F \propto v$. This analogy leads to this technique often being called 'optical molasses' [80].

The negative sign in Equation 4.8 is due to the necessity of red, or negative, detuning: to exhibit damping α must be positive. Figure 4.1 shows two regimes of detuning which have slightly differing effects on the atoms. The $\delta_{\text{laser}} = -\Gamma/2$ case shows a steeper gradient, hence larger α, about $|kv| = 0$. This would slow the atoms more then the $\delta_{\text{laser}} = -3\Gamma/2$ light, which has a flatter gradient about the origin. However this is able to cool a larger range of velocities, leading to more atoms being cooled. There is then a trade-off between the size of an atom trap and its loading rate.

If we extend this model to have counter-propagating beams along all 3 axes we can begin to cool atoms in all directions. Equation 4.7 and Figure 4.1 imply that the atom will eventually reach rest. Sadly this is physically unrealistic and we have not taken into account heating from fluctuations in the forces on the atom. An absorption event is always followed by an spontaneous emission event; while this eventually averages to zero force, the fluctuations lead to a cooling

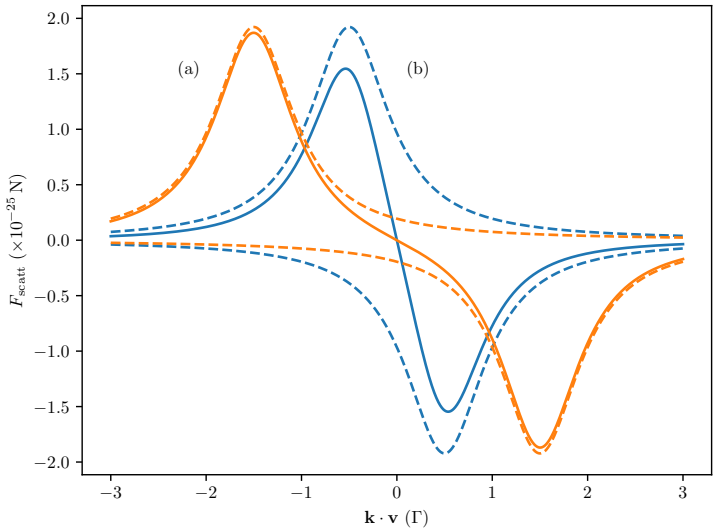

Figure 4.1: Scattering forces on an atom from two counter-propagating beams. Plot (a) has laser detuning $\delta = -3\Gamma/2$ and (b) has $\delta = -\Gamma/2$. The dashed lines describe the force from the individual beams and the solid lines are the sum of the forces on the atom. The positive forces are generated by the $+k$ beam and the negative forces are generated by the $-k$ beam.

limit. This is called the Doppler cooling limit and will be discussed in more detail in Section 4.6.

4.3 Trapping force

Due to the optical Earnshaw theorem [81] the scattering force is not enough to trap and cool atoms.[5] A spatially dependent force is needed in addition to the velocity dependent scattering force. This is introduced though the Zeeman shift:

$$\Delta E = \mu_B g_F m_F B, \tag{4.9}$$

where μ_B is the Bohr magneton, g_F is the Landé g-factor for a given hyperfine F level, B is the magnetic field strength, and m_F is the Zeeman sub-level that is being shifted. We will assume the magnetic field only has components in the $\mathbf{z}$ direction. The important factor to note here is that the Zeeman shift

[5]Briefly, the optical Earnshaw theorem determines that the scattering force alone cannot trap atoms within the beam overlap region. This is because there cannot be a 'sink' of optical fields. It may be enough to cool the atoms however they would eventually move out of the beams and be lost to the environment.

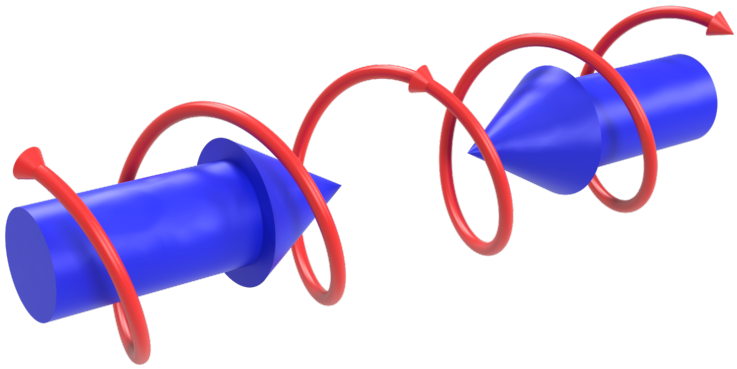

Figure 4.2: Diagram showing how light polarisation depends on magnetic field vector. The helix in red is the electric field vector as the beam moves from left to right. We have chosen to show σ^- polarisation here. The large blue arrows inside the helix is the magnetic field direction. If we look at the diagram from its centre, between the two blue arrows, we can understand how to interpret it. When the magnetic field is pointing in the same direction of the light (left hand side of the image) the observer sees σ^- polarisation. When looking at towards the right hand side of the image, where the magnetic field is anti-parallel to the direction of light, we see the light to be σ^+. Inspired by Figure 5.2 in Himsworth [78].

is proportional to the strength of the magnetic field. We can then engineer a magnetic field that shifts the atomic energy levels differently depending on the atom's position. This is achieved through a quadrupole magnetic field, created using magnetic coils in an anti-Helmholtz configuration, providing a magnetic field gradient with a field strength of zero in its centre. The field gradient provides a spatial dependence to the Zeeman splitting.

The now non-degenerate m_F sublevels have transitions that are sensitive to the light's polarisation. We will use the same notation and perspective as in Section 2.3.2 to describe these polarisations. We take the atom's perspective looking in the negative magnetic field direction. When the laser's electric field vector is rotating anti-clockwise it is σ^- polarised and drives $\Delta m_F = -1$ transitions. Likewise, when the electric field vector rotates clockwise it is σ^+ polarised and drives $\Delta m_F = +1$ transitions. Note we have not specified the direction the light beam in these definitions. When driving these transitions, the apparent polarisation is determined by the direction of light when compared to the direction of the magnetic field. Figure 4.2 shows an example of how the apparent polarisation is dependent on the direction of the magnetic field. Here we can see how the same circularly polarised light can change apparent polarisation when the magnetic field direction is flipped—as would happen in

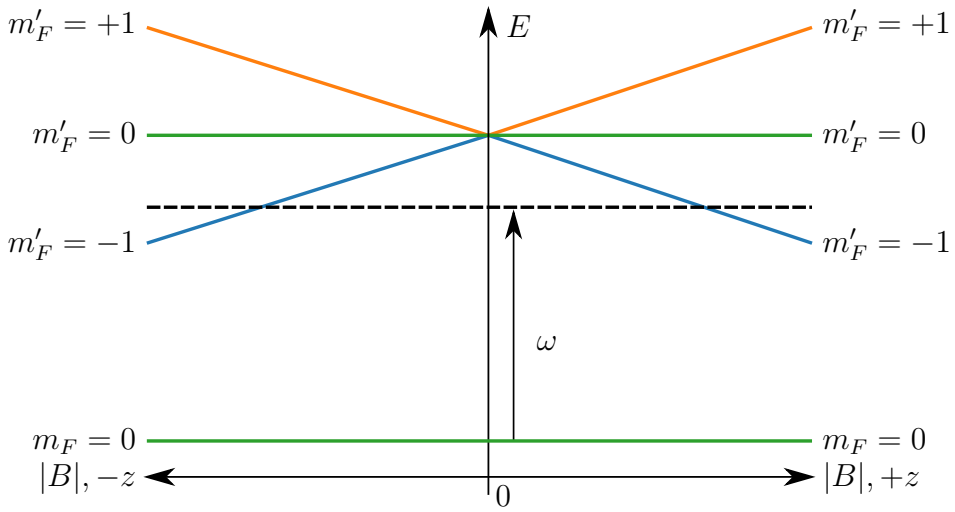

Figure 4.3: Energy level diagram showing the spatial dependence of the Zeeman effect in a quadrupole magnetic field. This uses a simplified atom with $F = 0$ and $F' = 1$. The arrow labelled ω is a red detuned laser frequency (with respect to $m'_F = 0$). It can be seen that this laser is only resonant with $m'_F = -1$ when the atom is at particular locations on the **z** axis. To interact with the $m'_F = +1$ state ω would need to be blue detuned.

the middle of the quadrupole field.

Considering that the scattering force requires red detuned light to cool atoms, we see from Equation 4.9 that the $m_F < 0$ sublevels would become resonant in a large enough magnetic field. Figure 4.3 shows how the transition frequencies change spatially in the magnetic field. We can see here that for red detuned light σ^- polarisation is required to drive a transition in this regime. This light must also be directed towards the origin. The direction of the magnetic field here is left ambiguous; only the magnitude is shown. As previously implied, if the magnetic field points towards the origin point then the incoming light must be σ^-. If the magnetic field is directed away from the origin, the incoming light would need to be σ^+.

We implement this effect into the scattering force by adjusting the detuning term $\delta = \delta_{\text{laser}} + kv + \beta z$, where β is the frequency shift per unit length caused by the magnetic field gradient $\frac{\mathrm{d}B}{\mathrm{d}z}$:

$$\beta = \frac{\Delta E}{\hbar} = \frac{\mu_B g_F m_F}{\hbar} \frac{\mathrm{d}B}{\mathrm{d}z}. \tag{4.10}$$

Following the same two beam addition as with the molasses force, Equation 4.7,

we arrive at [41]

$$F_{\mathrm{MOT}} = F_{\mathrm{scatt}}(\delta_{\mathrm{laser}} + kv - \beta z) + F_{\mathrm{scatt}}(\delta_{\mathrm{laser}} - kv + \beta z) \tag{4.11}$$

$$= -\alpha v - \frac{\alpha\beta}{k} z. \tag{4.12}$$

This shows there is a new position-dependent 'spring' force proportional to β centred around the origin. This extra force is able to overcome the limitations described by the optical Earnshaw theorem to contain the atoms within the overlapping region of the beams. We have chosen the subscript 'MOT' as this is the force the MOT takes advantage of.

From Equation 4.12 we can see that atoms entering the trapping region would be slowed down (cooled) and 'pushed' towards the centre of the trap. For an atom to escape the trap, it would need a large enough velocity so that it could not be slowed sufficiently to then be brought towards the centre.

4.4 The magneto-optical trap

By directing counter-propagating laser beams along all three Cartesian axes within the quadrupole magnetic field, we can take advantage of the trapping cooling forces in Equation 4.12 in all three dimensions. Figure 4.4 shows the arrangement of a typical MOT. In this diagram, for the purposes of labelling polarisations, we take the perspective of the laser source; σ^- polarised light now has a clockwise rotating electric field vector. Likewise, σ^+ polarised light has an anti-clockwise rotating vector. These beams would still drive the $\Delta m_F = -1$ and $\Delta m_F = +1$ transitions respectively.

Here we have displayed the direction of the magnetic field vertically to be towards the centre of the trap. The requires that the beams travelling between the magnetic coils have σ^- polarisations, and for the horizontal beams to be σ^+. If the magnetic field were inverted, so that it travelled vertically away from the centre, the polarisations would need to be reversed. This is an important feature of the MOT to keep in mind during construction. It is also worth noting that these polarisations oppose the requirements for Raman transitions described in Section 2.3.2: in the notation described there the MOT requires $\sigma^+ - \sigma^-$ polarised light for all its beams.

Different geometries of MOT exist that differ from this typical six beam configuration. MOT geometries to enable miniaturised systems are of particular note [82]. For example, pyramidal [83] and tetrahedral [84] MOTs require only

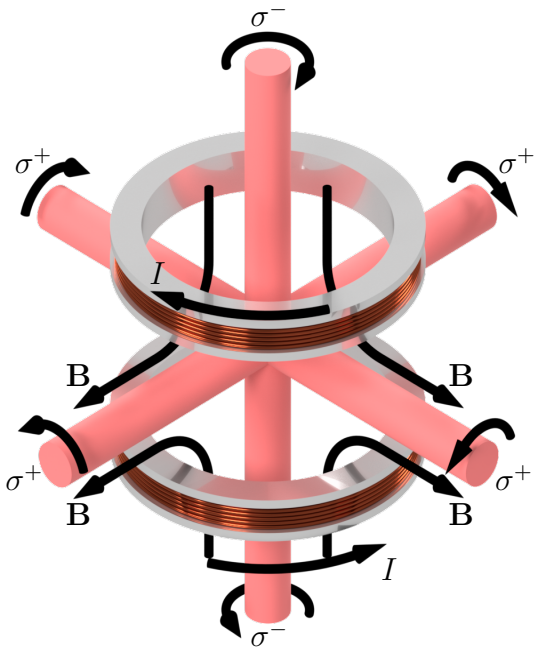

Figure 4.4: Typical six beam MOT configuration. Two coils of wire, with current I in anti-Helmholtz configuration, generate a quadrupole magnetic field. Six counter-propagating laser beams, with labelled polarisations, point towards the central point of the quadrupole magnetic field.

a single laser beam to generate a cold atom cloud and can be micro-fabricated. We can generate a six beam MOT with a single laser beam in a similar way by arranging five mirrors and a $\lambda/4$ waveplate [85], seen in Figure 4.5.[6] Here we take the perspective of the laser source when labelling polarisations. Upon reflection with a mirror, σ^- polarised light will gain a π phase shift and change polarisation to σ^+. For the central mirror a $\lambda/4$ waveplate is used to counteract this effect and provide σ^- polarisation. The side mirrors are angled at 45° so that beams are generated that counter-propagate along all the three Cartesian axes with σ^+ polarisation. Using a quadrupole magnetic field, this matches the design of the six beam MOT in Figure 4.4. Because this MOT design only requires a single laser source, lowering the number of required components, it is a good candidate for a compact and portable MOT system. This is the design we use in Chapter 5 to generate the MOT.

[6]This arrangement is also often also called a pyramidal MOT.

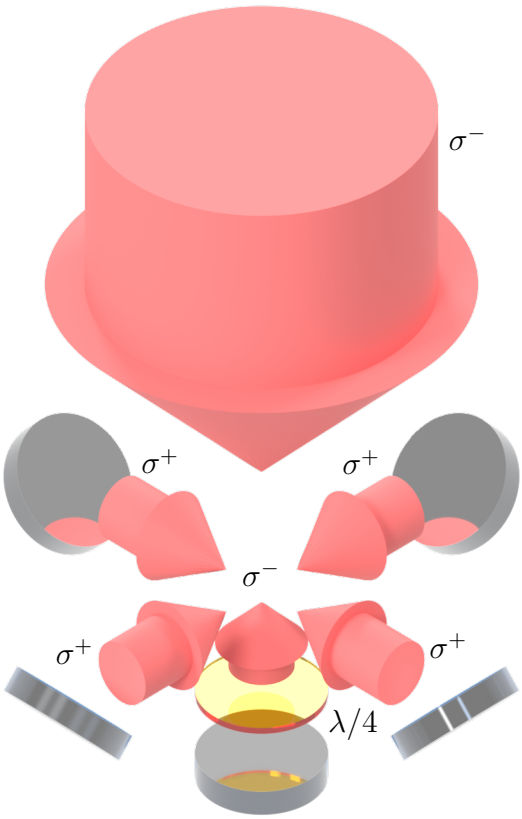

Figure 4.5: MOT generated with a single beam incident on five mirrors. A beam with a large enough diameter is able to illuminate all five mirrors and generate the required beams for a MOT seen in Figure 4.4. A $\lambda/4$ waveplate is placed in front of the central mirror to create the correct polarisation for the reflected beam.

4.5 Repump laser

For a ^{85}Rb MOT we drive the $F = 3 \Rightarrow F' = 4$ transition to cool the atom. We choose this transition as it can only decay back to the starting $F = 3$ state. Such a transition is called a 'closed' transition. This enables successive atom-laser interactions without the atom being pumped into a dark state.

Unfortunately, this is not always the case. Each transition has a Lorentzian shaped absorption probability,[7] therefore there is a non-zero probability of exciting the $F = 3 \Rightarrow F' = 3$ transition. This probability is increased by the red detuning of the laser shifting the laser frequency closer to resonance. For

[7]For rubidium, transitions to the D_2 line have line-widths of $\Gamma = 2\pi \times 6.0666\,\text{MHz}$ [49, 86].

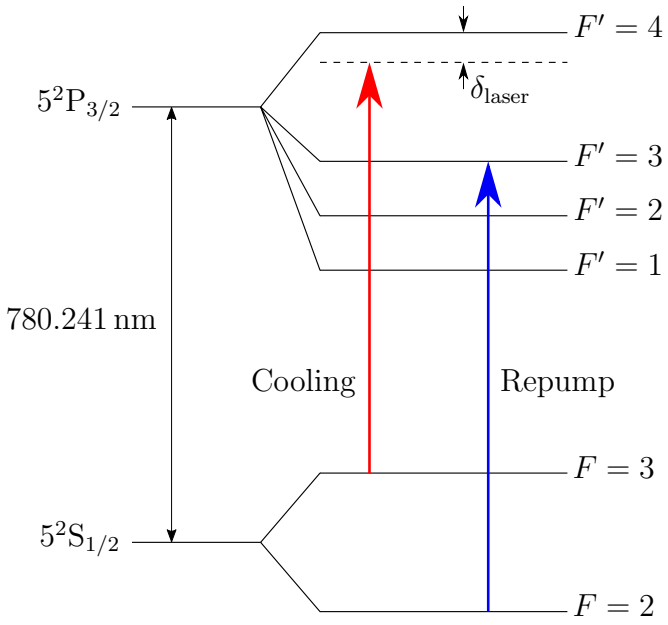

Figure 4.6: ^{85}Rb D_2 hyperfine structure and MOT beam transitions.

$\delta_{\text{laser}} = -3\Gamma$, there is a $\approx 1\%$ chance of exciting the atom to the $F' = 3$ state.[8] This is then able to decay to either $F = 2, 3$ states. In the case where the atom decays to the $F = 2$ state, the cooling laser, driving the $F = 3 \Rightarrow F' = 4$ transition, can no longer interact with the atom. To remove the atom from this 'dark' state we need another laser. We use a 'repump' laser resonant with the $F = 2 \Rightarrow F' = 3$ transition to pump out of the dark state. The atom then can again decay to either $F = 2, 3$ states and this repeats until it decays to the $F = 3$ state. Here the atom once again interacts with the cooling laser once again. Figure 4.6 shows this pumping scheme on the ^{85}Rb D_2 line.

For the remainder of this thesis, we shall refer to the transition $F = 3 \Rightarrow F' = 4$ as the cooling transition and the laser that drives it as the cooling laser. Similarly, we shall call the $F = 2 \Rightarrow F' = 3$ transition the repump transition and its accompanying repump laser.

[8] There is also a chance of exciting the $F = 2$ state however it is significantly lower. This state also has the same decay routes and so we can ignore its effect.

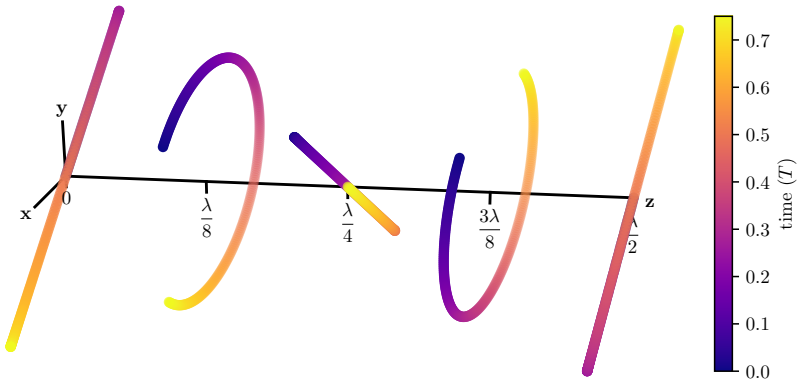

Figure 4.7: Simulation of the polarisation gradient caused by two counter-propagating, perpendicularly polarised, linearly polarised beams. The data-points shown are the electric field vector sum along the $\hat{\mathbf{x}}$–$\hat{\mathbf{y}}$ plane at each time at the marked points on the $\mathbf{z}$ axis. The beam travelling in the positive $\hat{\mathbf{z}}$ direction is polarised along the $\mathbf{y}$ axis. The beam travelling in the negative $\hat{\mathbf{z}}$ direction is polarised along the $\mathbf{x}$ axis. Time is in units of the time period of the beam frequencies.

4.6 Sub-Doppler cooling

As previously mentioned, fluctuations in the laser field lead to the Doppler cooling limit, described by [41]

$$T_D = \frac{\hbar\Gamma}{2k_B}, \tag{4.13}$$

where k_B is Boltzmann's constant.[9] For rubidium this limit is $T_D \approx 145\,\mu\text{K}$. However, researchers found during experiments that colder atoms could be achieved [88]. A method of achieving this is polarisation gradient cooling.

Consider two counter-propagating beams travelling along the $\mathbf{z}$ axis. One is linearly polarised along the the $\mathbf{y}$ axis, we shall call this π^+ polarised. Likewise the other beam is linearly polarised along the $\mathbf{x}$ axis with π^- polarisation. This combination of polarisations, $\pi^- - \pi^+$, is often referred to as lin-perp-lin. The superposition of these two perpendicularly polarised beams leads to a standing wave of polarisations (not a standing wave of intensity). This polarisation standing wave leads to spatial periodic changes in the polarisation. Figure 4.7 shows this polarisation gradient. Travelling along the $\mathbf{z}$ axis, the polarisation switches from linearly polarised, to circular, and back to linear. The circular polarisations shall be taken when looking in the negative $\hat{\mathbf{z}}$ direction.[10] Therefore,

[9] A more rigorous treatment can be found in Castin et al. [87].
[10] We are not particularly interested in the linearly polarised points.

the polarisation at $y = \lambda/8$ is σ^+, and σ^- at $y = 3\lambda/8$. We see here that every $\lambda/4$ the polarisation swaps to its orthogonal counterpart, and this periodic pattern repeats every $\lambda/2$.[11] An atom travelling along the beam paths would experience a regular polarisation inversion [89].

So far, we have largely considered the atom to be a two level system. The Zeeman structure in the energy levels of alkali atoms allows the polarisation gradient cooling effect to happen. Consider an atom with a fine lower (ground) level with angular momentum $J = 1/2$, and an upper level with $J' = 3/2$. Conveniently, this describes the fine structure of the ^{85}Rb D_2 line we are interested in. These levels have $2J + 1$ sub-levels fulfilling $-J \leq m_J \leq J$ with integer spacing between each m_J sub-level. Therefore, the ground level has $m_J = -1/2, 1/2$ sub-levels and the upper level with $m_{J'} = -3/2, -1/2, 1/2, 3/2$. When exciting the $J = 1/2 \Rightarrow J' = 3/2$ transition, polarisation determines the sub-level being pumped into with selection rule $\Delta m_J = 0, \pm 1$.[12] When being driven with σ^+ a $\Delta m_J = +1$ transition is driven, and σ^- drives a $\Delta m_J = -1$ transition. Linear polarisations drive $\Delta m_J = 0$ transitions. The coupling strengths between the lower m_J states and the upper $m_{J'}$ states are then also determined by the polarisations.

In the presence of σ^+ light, the $m_J = +1/2$ state has a higher coupling strength than the $m_J = -1/2$ level, with ratios given by the Clebsh-Gordan coefficients [89]. The opposite is true for σ^- light. The light shift is proportional to the coupling strength of the transition. For a red-detuned beam, the light shift acts to increase the transition frequency. As the atom moves through the polarisation gradient, it periodically experiences positions where the $m_J = 1/2$ state has a larger shift than the $m_J = -1/2$ state and vice versa. Figure 4.8 shows this spatial light shift oscillation. As the atom enters the σ^+ polarised region, the $m_J = 1/2$ level is shifted further than the $m_J = -1/2$ level. This pumps the atom out of the $m_J = -1/2$ state into the excited level. Here the atom is able to spontaneously decay. As determined by the Clebsh-Gordan coefficients, the atom will preferentially decay into the lower energy state, in this case the $m_J = 1/2$, where it will radiate more energy than it absorbed. In the scenario where it decays to the higher (original) energy state, this process will happen again until it decays into the lower (dark) state. The atom then moves into the σ^- region, where this process happens again for the $m_J = 1/2$ state; the state the atom was just pumped into. These successive events continue to radiate energy away from the atom, cooling it down.

[11] The actual polarisations are not important, particularly as the polarisations repeat spatially. Phase shifting our view along the **z** axis by $\lambda/4$ would appear to give us the opposite polarisations stated here.

[12] This is not strictly the case for $\Delta J = 0$ because $\Delta m_F = 0$ is forbidden [41].

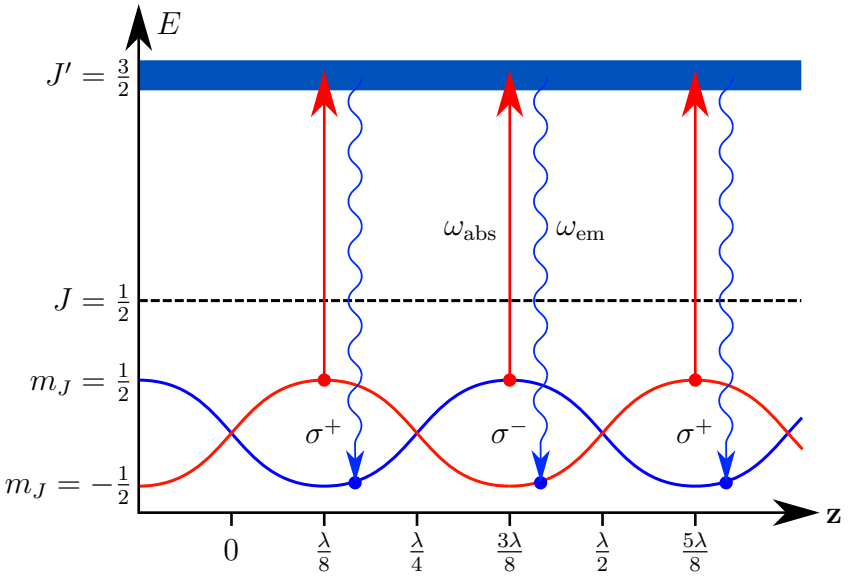

Figure 4.8: Energy level diagram demonstrating the Sisyphus cooling effect. Under the polarisation gradient seen in Figure 4.7, an atom is periodically pumped into alternating m_J sub-levels. The thick dark blue bar represents the upper level's $m_{J'}$ states. The black dotted line represents the unperturbed (prior to the light shift) energy level of the ground state. The red and blue sinusoidal lines shows the shifting energy levels of the $m_J = -1/2$ and $m_J = 1/2$ states respectively. The red vertical arrow is the driving laser with frequency ω_{abs}, and the squiggly blue arrow is the emitted photon of frequency ω_{em}.

This is analogous to rolling a ball up a hill, where potential energy is gained, for it to suddenly appear back at the bottom of the hill. Any potential energy gained is lost. This mechanism is also called the Sisyphus effect, named after the mythological Greek king who was sentenced to roll a boulder up a hill for eternity, only for it to roll back to the bottom when he reached the top.

Eventually the atom slows enough that the energy loss is equal to the recoil the atom experiences from spontaneous emission. This leads to the recoil limit [41]

$$T_{\text{r}} = \frac{h^2}{k_B m \lambda^2}, \tag{4.14}$$

where h is the Planck constant, and m is the mass of the atom. For ^{85}Rb D_2 transitions, $T_{\text{r}} \approx 370\,\text{nK}$. Typically, temperatures on the order of a few μK can be realistically achieved [90, 91]. Performing this cooling technique requires isolation from magnetic fields which would act to perturb the m_J sub-levels. For this reason, we observe temperatures closer to the Doppler limit when using the MOT, as the magnetic Zeeman shift is much stronger than the Stark/light shift. This effect it usually used as a separate cooling stage after initially cooling

atoms in the MOT. Somewhat ironically, in the experiment we call this the molasses stage.

We also find that reaching the sub-Doppler cooling limit becomes impossible in practice. During the molasses cooling stage, the temperature of the atoms follow [41, 89]

$$T \propto \frac{I}{|\delta|}. \tag{4.15}$$

Here we can see that to obtain the coldest atoms we should use the largest detuning and the lowest laser power. However, it is easy to see that both these adjustments would decrease the strength of any interaction the laser has with the atoms, limiting this effect. We observe a limit—above the recoil limit—which the atoms can be cooled to which further reductions of laser power and increase of detuning lead to hotter atoms [92]. Furthermore, as the atoms get colder, the radius of their position wavefunction expands—since the de Broglie wavelength is inversely proportional to the inverse square root of temperature. Eventually, the 'size' of the atoms increase such that it can no longer distinguish the differences in the polarisation gradient and the Sisyphus cooling method ceases to function properly. Practically, the limit to the Sisyphus cooling effect is closer to a few μK in rubidium. In order to get atoms colder—approaching the recoil limit and below—techniques such as evaporative cooling are required which lead towards creating a Bose-Einstein condensate.

It may be worth noting that this picture is incomplete; in practice we use circularly polarised beams in 3D. We have presented a 1D picture using linearly polarised beams. However, this model is sufficient to understanding this mechanism to achieving sub-Doppler temperatures. Dalibard & Cohen-Tannoudji [89] include the circularly polarised case in their approach. A treatment in 3D can be found in Gajda & Mostowski [93] and in Castin & Mølmer [94].

4.7 Magneto-optical trap optimisation

The signal strength obtained out a matter-wave interferometer, or any cold atom experiment, is proportional to the number of atoms seen at the detector. Furthermore, in the classical limit the signal-to-noise ratio is proportional to the square root of the number of atoms. Therefore, it is important to obtain the largest number of atoms possible. We achieve this by varying experimental parameters such as laser power and frequency. However, in order to measure their effect we require a measurement tool. This can be achieved through fluorescence or absorption imaging. For reasons that will be made clear in Chapter 5, we

only use absorption imaging.

As described in Section 2.2.1, it is also important to obtain the coldest atoms possible.[13] Here we detail how a temperature measurement is achieved through the use of absorption imaging. Temperature is dependent on experimental parameters used during the molasses stage of the experiment. In this section we will explain how the size of a cold atom cloud grows within a MOT, how we determine the size of an atom trap, and finally how we determine the temperature of the atom cloud.

4.7.1 Loading rate

When the MOT beams and magnetic field are switched on (and aligned properly) the atoms with sufficiently low velocities that pass into the beam intersection begin to be cooled and trapped. The number of atoms captured by the MOT increases over time. However, after a period of time the number of atoms reaches a steady state. This steady state is an equilibrium of the MOT cooling and trapping more atoms, and atoms being lost from the trap to the environment. Atoms are lost through collisions with other atoms in the trap and with background atoms [95]. The rate of change of the number of trapped atoms is described by [96]

$$\frac{\mathrm{d}N(t)}{\mathrm{d}t} = R - \gamma_L N(t) - \beta \frac{N(t)^2}{V}, \tag{4.16}$$

where N is the total number of atoms in the trap at time t, R is the capture rate, γ_L is the loss rate of the trap, β is the loss rate due to two-body collisions of atoms within the trap, and V is the trapping volume. The loss rate, γ_L, is determined by collisions with the background vapour. We can assume the trap to be low density and therefore neglect the rightmost term in the equation. We then obtain

$$\frac{\mathrm{d}N(t)}{\mathrm{d}t} = R - \gamma_L N(t), \tag{4.17}$$

which has the solution

$$N(t) = \frac{R}{\gamma_L}\left(1 - e^{-\gamma_L t}\right). \tag{4.18}$$

We can see that the atom number reaches a steady state R/γ_L. This steady state—the total atom number—can be calculated by [97]:

$$N = \frac{R}{\gamma_L} = 0.1\frac{A}{\sigma}\left[\frac{v_\mathrm{c}}{v_\mathrm{thermal}}\right]^4, \tag{4.19}$$

[13] This also has implications for SNR for matter-wave interferometers. We discuss this in Chapter 6.

where A is the surface area of the trap volume, $\sigma \approx 10^{-13}\,\mathrm{cm}^2$ [98] is the collision cross section, the capture velocity v_c is the maximum velocity for an atom to be captured by the trap, and $v_\mathrm{thermal} = (8k_BT/\pi m)^{1/2} \approx 270\,\mathrm{ms}^{-1}$ is the average speed of the background atoms. The capture velocity is [95]

$$v_\mathrm{c} = \sqrt{\frac{\hbar k \Gamma r}{2m}}, \tag{4.20}$$

where r is the radius of the trap.

The loading rate of the trap can be a dominant limiting factor in the repetition rate of experiments involving cold atoms. The initial rate atoms begin filling the trap is determined by R as seen in Equations 4.16 and 4.17. The loading rate can be expressed as

$$R = 0.5nV^{2/3}v_c^4\left(\frac{m}{2k_BT}\right)^{3/2} \tag{4.21}$$

where n is density of background rubidium atoms, k_B is the Boltzmann constant, and T is the temperature of the background atoms [99]. We can immediately see that by increasing the size and capture velocity of the trap that we can increase the loading rate. The loss rate, γ_L, is also dependent on the background vapour pressure. The loss rate can be expressed as [99]

$$\gamma_L = n\sigma\sqrt{\frac{3k_BT}{m}}. \tag{4.22}$$

We can see here that whilst we may initially gain many atoms due to a larger background pressure, this also increases the rate of loss by the same mechanism. So as a higher atom flux entering the trapping volume makes a faster growing trap, it also decreases the total number of atoms able to trap and how fast it can reach that number. In order to circumvent this effect, some experiments rely on a '2D' MOT to load a large amount of atoms directly into the typical six-beam '3D' MOT [100, 101]. Often the trap lifetime, τ, is discussed rather than the loading rate where $\tau = 1/\gamma_L$.

4.7.2 Absorption imaging

By imaging the shadow of the cold atoms we can obtain information about the density of the cold atom cloud [102]. Therefore the number of atoms can be determined. Beer's law describes the attenuation of light through a non-saturable absorptive medium [41]

$$\frac{\mathrm{d}I(\omega)}{\mathrm{d}z} = -\sigma(\omega)\rho I \Rightarrow I(\omega) = I_0 e^{-\sigma(\omega)n}, \tag{4.23}$$

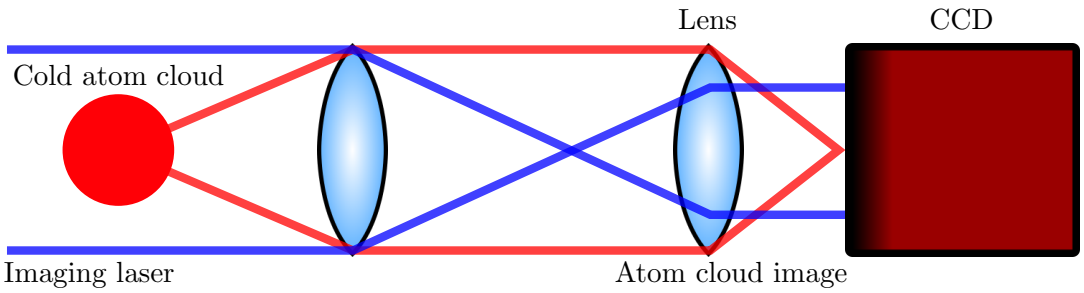

Figure 4.9: Typical absorption imaging arrangement (not to scale). The collimated resonant imaging laser has a larger diameter than the atom cloud. The laser is absorbed by the cold atom cloud and the image of the shadow is detected by the charge-coupled device (CCD). The red lines represent the image of the (shadow of the) cold atoms detected by the CCD. The fluorescence can be used to focus the lens arrangement to be able to target the CCD correctly.

where $I(\omega)$ is the intensity of light, of frequency ω, after passing through a medium of density ρ with absorption cross section σ, and I_0 is the intensity of light before passing through the medium [103]. We will assume I_0 is far below the saturation intensity I_{sat}. Here the column density, $n = \int_{-\infty}^{\infty} \rho(x, y, z)\, \mathrm{d}z$, gives the per unit area density of the medium. For a cloud of atoms with resonant light, $\sigma(\omega_0) = \sigma_0 = \frac{\hbar\omega_0\Gamma}{2I_{\text{sat}}}$, where c is the speed of light in a vacuum. To obtain the largest absorption, and hence the best data, we assume that the light used is resonant with the desired transition: $I \equiv I(\omega_0)$. Therefore the final atom number over a measurement area, A, is:

$$N = nA = \frac{\ln\left(\frac{I_0}{I}\right)}{\sigma_0} A. \tag{4.24}$$

Figure 4.9 shows the experimental arrangement for an absorption imaging system. In this arrangement each pixel of the CCD is a separate measurement, where A is equal to the area of each pixel. Therefore the total atom number of the imaged atom cloud is the sum of the atom numbers across all pixels:

$$N_{\text{total}} = \frac{A}{\sigma_0} \sum_{\text{pixels}} \ln\left(\frac{I_0}{I}\right). \tag{4.25}$$

Experimentally this requires two images to be taken; one with the cold atoms present, I, and another without the cold atoms, I_0. The laser intensity must be kept constant for both exposures and must be resonant with a transition. If the laser is not resonant less absorption would be seen as σ is dependent on detuning. A third dark image—where no light is present—should also be taken

to subtract any offsets from the illuminated images. However we did not do this during experimentation and may have introduced some of the systematic effects seen in Chapter 6.

This also requires the atoms to not be fluorescing during imaging. We have assumed that any fluorescence collected by the CCD is negligible due to the beam being weak[14] and the detector is sufficiently far away that the solid angle is small. Under normal operation atoms in a MOT fluoresce due to the interaction with the trapping beams. To image correctly, the trapping beams must be switched off when the imaging beam is switched on.

4.7.3 Temperature measurement

There are many different methods of measuring the temperature of the atoms in the MOT [88, 104]. The easiest to implement is often release and recapture.[15] This involves releasing the cold atom cloud from the MOT forces after reaching a steady state, then attempting to trap the same cloud after a variable time. The ratio between the number of atoms in the steady state and the 'recaptured' atoms is measured across a range of delay times, and a fit is used to obtain the temperature. However, this method is more prone to systematic errors [78, 82, 105] and requires the ability to measure the atom number during trapping—which is only possible through fluorescence measurements. We see in Chapter 5 it is not trivial to measure the fluorescence of our cold atom cloud. Rather, we must rely on absorption imaging to recover information from the cloud in our experiment. Here we will discuss the cloud expansion through a time-of-flight (TOF) technique for measuring temperature. We have chosen this method mainly due to the restrictions imposed by our vacuum chamber. This is discussed in more detail in Chapter 5.

Any group of particles in thermal equilibrium have a velocity distribution determined by the Maxwell-Boltzmann distribution

$$P(v) = \left(\frac{m}{2\pi k_B T}\right)^{\frac{3}{2}} \exp\left[\frac{-mv^2}{2k_B T}\right], \tag{4.26}$$

where m is the mass of the particle, k_B is the Boltzmann constant, T is the temperature of the distribution, and v is the speed of the particle. Similarly,

[14] When compared to I_{sat}.

[15] Very little adjustment needs to be made to the typical MOT setup. The camera used to image the fluorescence of the atoms can be replaced with a suitable sensor to collect the fluorescence instead.

in an ideal trap, we can assume a Gaussian distribution for the density of the particles before release:

$$n_0(\mathbf{r}) = \left(\frac{1}{2\pi\sigma^2}\right)^{\frac{3}{2}} \exp\left[\frac{-\mathbf{r}^2}{2\sigma^2}\right], \tag{4.27}$$

where $\mathbf{r}$ is the radial position of the particle, and $\sigma = \sqrt{k_B T/m}$ is the rms radius of the initial cloud.

As the cloud is released from the trap it will expand in accordance to its velocity distribution.[16] The expansion of the radius of the cloud is described by [107]

$$\sigma^2(t) = \sigma^2(0) + \frac{k_B T}{m} t^2, \tag{4.28}$$

where $\sigma(t)$ is the rms radius of the cloud at time t, and hence $\sigma(0)$ is the initial rms radius.[17] A detailed derivation of Equation 4.28 can be found in Weiss et al. [108]. To obtain the temperature, T, from this equation, multiple measurements must be made of cloud's radius at different points in time while no external forces–such as those from a magnetic or optical field—act on the atoms. A suitable imaging system is required to perform these measurements. This can be fluorescence or, as previously discussed, absorption imaging.

As shown in Section 4.1, when the atoms interact with the laser a force is applied to the atoms—this acts to heat the atoms [102]. This prevents a continual measurement of the cloud expansion as the previous light interactions would affect subsequent measurements. Since interaction with the laser field disturbs the atoms, it is not possible to obtain all the measurements for Equation 4.28 at once. Multiple 'runs' are required where the time between releasing the atoms and making a measurement, t, are varied. This allows a picture of how the cloud's radius develops over time to be built up, without the laser interfering with measurements. By fitting Equation 4.28 to this data, the temperature can be obtained. It is important to note that the magnetic field must be switched off during the TOF to remove any state-dependent forces.

[16] The cloud will also fall due to gravity... unless your lab is in orbit [106].

[17] It may be helpful to note how this relates the size of the cloud to the speed of the atoms: $v^2 = 2k_B T/m$.

Part II

Experimental work

Chapter 5

Experimental apparatus

This chapter describes the experimental apparatus and methods for the cold atom experiments; the results of which are shown in Chapter 6. Our aim is to build towards a gravimeter for use in the PLAIN-GG system. This will form one of the two gravimeters for the PLAIN-GG gradiometer. We use a novel compact vacuum chamber design that includes integrated optics for the cold atom experiments. We characterise the MOT generated within this vacuum chamber and work towards detecting atoms after they undergo free fall. As will be seen in Chapter 7, we have yet to observe Raman transitions and hence have not made a gravimeter. However, detecting the cold atom ensemble after its free fall is a vital step to realising a gravimeter through atom interferometry, and shows the viability of this compact chamber as a gravimeter.

The apparatus is comprised of three main parts: the cooling laser source (described in Section 5.2), the laser switching system (Section 5.3), and the sensor head (Section 5.1). The cooling laser source supplies laser power of the desired frequencies through optical fibre to the laser switching system. The laser switching system turns on and off the laser beams supplied through optical fibre to the vacuum chamber, where the MOT and absorption imaging system is located. The experiment is coordinated with a SpinCore[1] PulseBlasterUSB—which we will refer to as the *pulseblaster*—by sending transistor–transistor logic (TTL) signals to components of the experiment at specific times.

Fibre deployment of the laser beams to the sensor head is required by the design of the PLAIN-GG project. While we focus on the development of this chamber during this thesis, the progress made is with the goals of the PLAIN-GG project in mind.

[1] `www.spincore.com`

We begin this chapter by describing the apparatus used for the cold atom experiments within the vacuum chamber; the vacuum chamber is then described. This is followed by the method used to perform absorption imaging of the cold atom cloud. This absorption imaging is then used extensively throughout the MOT characterisation, including for the TOF temperature measurements of the cold atom cloud where we also detail an additional cooling stage, the molasses stage. Finally, we describe the method for detecting atoms at the bottom of the chamber.

5.1 Sensor head

Figure 5.1 shows the optical arrangement of the PLAIN-GG sensor head. This is designed around the constraints of the compact vacuum chamber, the design of which is detailed in Section 5.4. The main constraint this optical system is designed around is that the chamber has only one window for optical access. Inside the vacuum chamber are mirrors arranged to generate the MOT beams from a single laser beam, and mirrors to allow for the detection of atoms once they have fallen to the bottom of the vacuum chamber (the detection area). Attached to the outside of the chamber are components that are arranged to direct and detect light going into the chamber in order to generate a MOT, to image the cold atom cloud with absorption imaging, and to detect the cold atoms at the bottom of the chamber. Figure 5.2 shows some images of this setup in the lab.

We are restricted in analysing the cold atoms due to the chamber only having one window. Through this window atom trapping, imaging, and detection after falling due to gravity must be achieved and is what led to this optical design. Fluorescence imaging is difficult because it would require the MOT laser beams to be illuminating the atoms. The intense MOT beams would then be incident on the camera sensor and over-expose the image. Furthermore, the closest position for a fluorescence collecting lens would be $\approx 100\,\text{mm}$ from the atoms—this would give a small solid angle and decrease the fluorescence signal strength. For these reasons we have decided to use absorption imaging as the sole method for imaging the cold atom cloud. During absorption imaging, the MOT beams are shut off when using the imaging beam so they do not over-expose the camera. The intensity of the absorption beam can be controlled to provide the desired signal strength.

As described in Figure 4.5, we use a single collimated beam to illuminate all the MOT mirrors. The beam is aligned to be perpendicular to the central

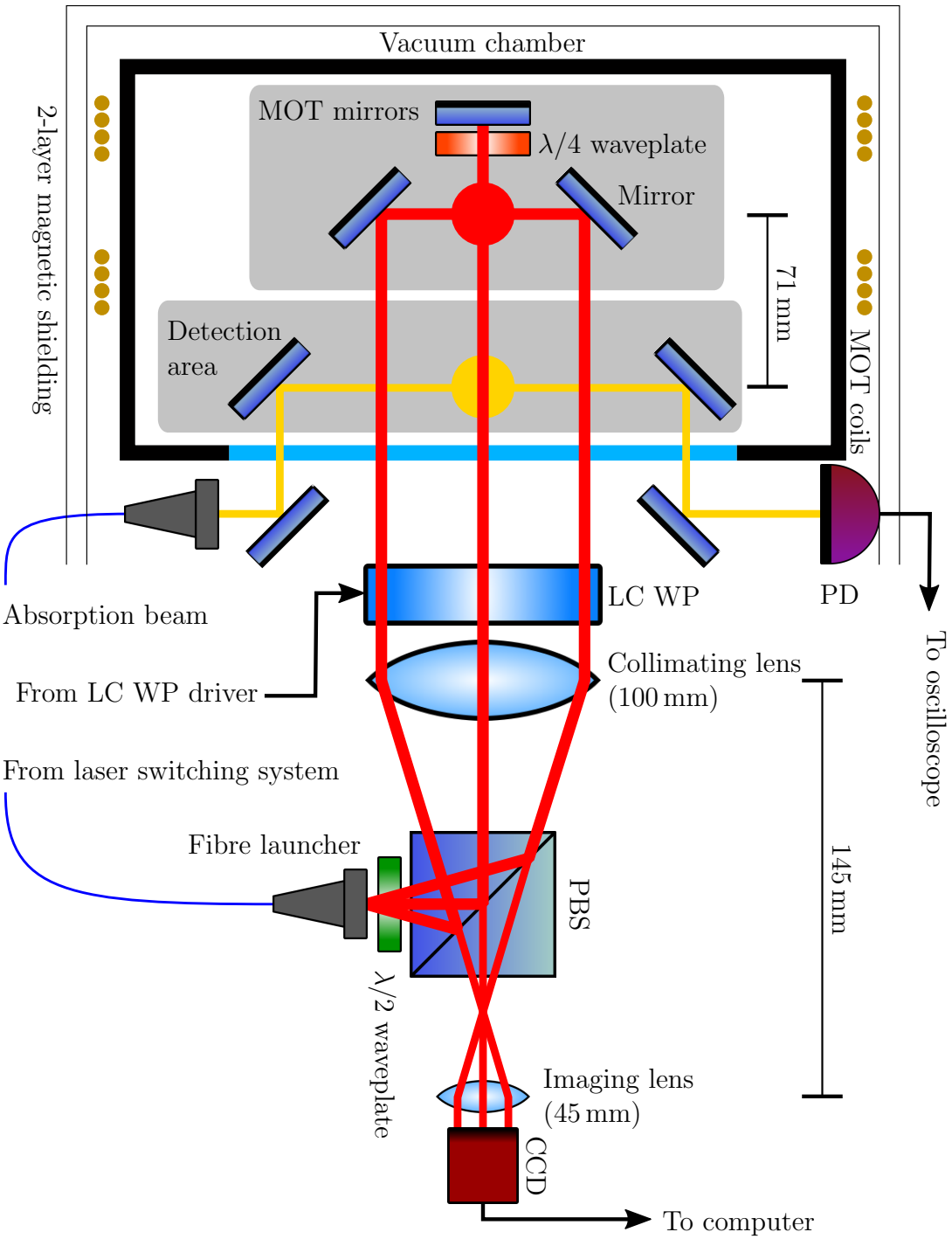

Figure 5.1: Optical arrangement of sensor head for absorption imaging and absorption detection (see Chapter 6). The red circle represents the cold atom cloud formed by the MOT, with corresponding lasers. The yellow circle represents the cold atom cloud after falling 71 mm, with corresponding absorption beam. The blue lines represent optical fibre, the fibre from the switching system is polarisation maintaining (PM) and the fibre from the absorption beam is non-PM. The light blue line at the base of the vacuum chamber is the chamber window. The optical path for imaging the cold atom cloud is not pictured here, the imaging path requires focusing the collimating lens on the cold atom cloud.

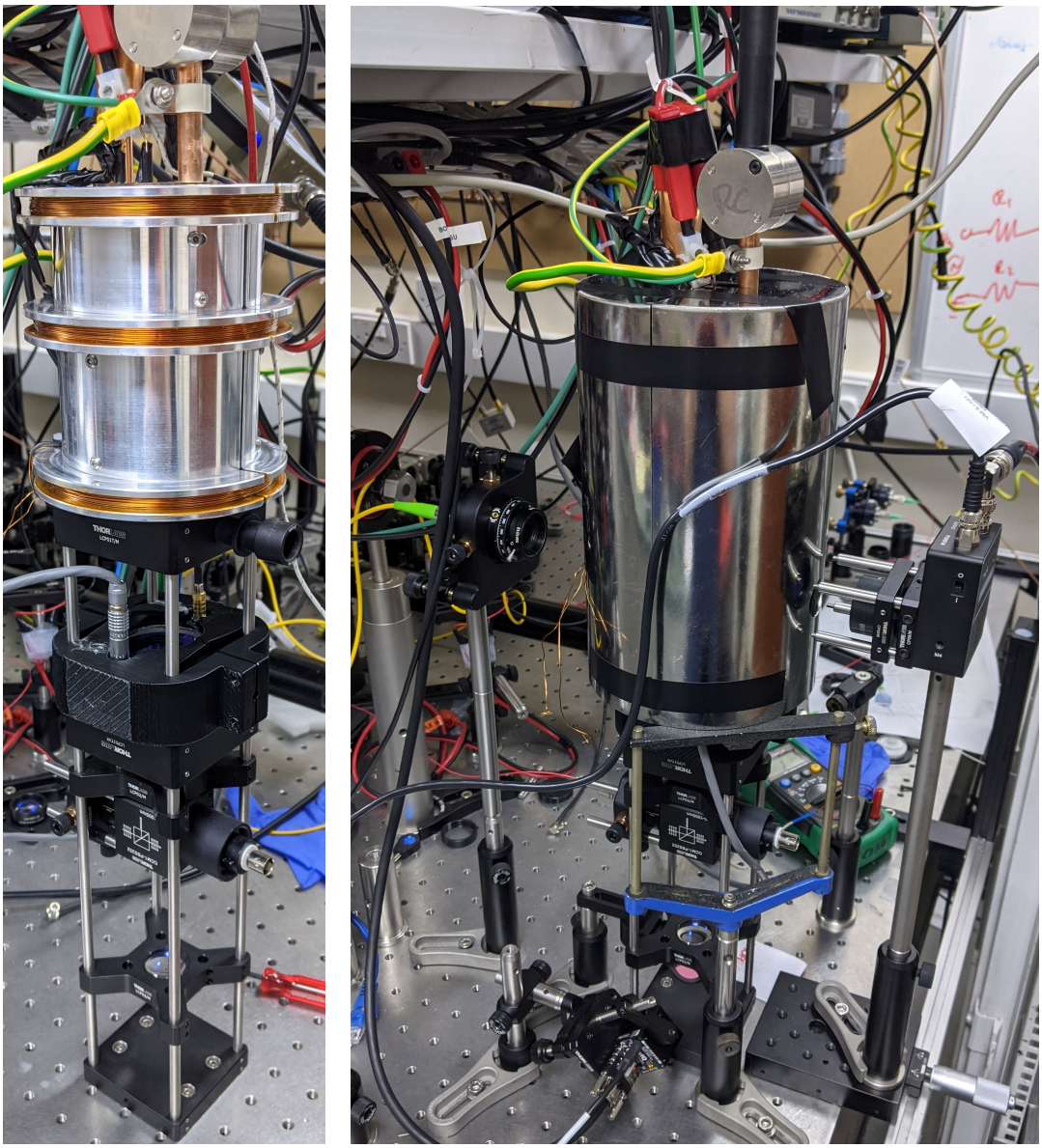

(a) (b)

Figure 5.2: Photos of sensor head lab setup. (a) shows the setup before the magnetic shields, camera, and detection area optics have been positioned. (b) shows the full setup in the lab. The additional magnetic coil seen is not used currently. An additional photodiode is also seen attached to the unused polarising beam splitting cube (PBS) port in Figure 5.1, this was used for debugging purposes.

retro-reflecting mirror.[2] We then take advantage of the retro-reflected beams in order to image the shadow of the atom cloud. This requires a second lens, to image the reflected beam, and a camera in order to record the images for analysis. To provide access to both light input and output we use a PBS and waveplates to direct the beams correctly. To ensure proper alignment and structural rigidity, we used a cage mount system to attach the optics to the vacuum chamber, which has M4 screw holes to allow for a cage mount adapter. The absorption beam is reflected by two 15 mm × 15 mm prisms, which are attached using epoxy resin onto a modified cage mount lens holder. This allows the 7 mm diameter absorption laser beam to pass into and across the vacuum chamber. It is then reflected back out of the vacuum chamber and directed onto a PD by the second periscope.

To illuminate the entire MOT area, we used a 100 mm focal length lens with a 2 inch diameter, which allows the laser beam's diameter to first expand to the desired diameter of 30 mm before collimation. The fibre launcher was mounted on a 3-axis translation stage in order to properly align the light to the collimating lens. The $\lambda/2$ waveplate allows control over the ratio between the orthogonally polarised cooling and repump laser light intensity. Upon retro-reflection, the light that passes through the PBS is then re-collimated by the smaller imaging lens before being detected by a camera. This is the optical path the light takes when performing the absorption imaging.

In Chapters 2 and 4 we discussed how the Raman transitions and the MOT require different polarisations of light to function. In order to fulfil these polarisation requirements, we use a Liquid Crystal waveplate (LC WP), with its fast axis aligned at 45° to the laser beam's linear polarised axis, which acts as a variable retarder. Using electronic control, the LC WP is able to change between $\lambda/4$ and $\lambda/2$ retardations. When used as a $\lambda/4$ waveplate we obtain correct polarisations for a MOT, and the $\lambda/2$ configuration provides the lin-perp-lin polarisations for Raman transitions. During absorption imaging it was found that switching from $\lambda/4$ to $\lambda/2$ configurations was also required to obtain a clear image of the atom cloud (see Section 5.6). The use and development of the LC WP is described in more detail in Section 5.5. We choose to use a LC WP, as opposed to a Pockels cell to avoid requiring high voltage equipment and the LC WP has a smaller form factor.

In order to provide the magnetic quadrupole field necessary for the MOT, we attach a pair of electromagnetic coils to the outside of the vacuum chamber in an

[2] A MOT can still be achieved with small misalignments, however the highest quality atom cloud is usually generated with this perpendicular alignment. Another reason for wanting this alignment is that it allows the laser beams to be retro-reflected, a later requirement for both the Raman beams and the stabilisation laser.

anti-Helmholtz configuration. These coils were made from 200 turns of 0.56 mm diameter copper wire. The coils were 7 mm thick, had an inner diameter of 76 mm, were separated by 44 mm, and housed in a mount attached to the cage mount system the optics were mounted on. These were manufactured by the University of Southampton Physics mechanical workshop. In Figure 5.2a a third magnetic coil at the bottom of the chamber can be seen. This coil was originally intended to be used for a quantisation field, however this coil is unused in the work presented in this thesis.

To provide isolation from any external magnetic fields, which may affect the Raman transitions, we use 2 layers of μ-metal as magnetic shielding. These layers were each made of two halves which have gaps to fit around the ion pump tube—to isolate the atoms from the strong magnetic field caused by the pump—and the dispenser electrodes. The shields also extend below the vacuum chamber slightly and have holes to allow optical access through periscopes to the detection area. Currently we do not include any magnetic coils to adjust or bias the residual magnetic field within the shielding.

5.2 Cooling laser source

Figure 5.3 shows the laser source system that the subsequent laser control system relies upon. This system frequency stabilises the two lasers, the repump and cooling lasers, to the desired frequencies for laser cooling. The repump laser is spectroscopically locked through frequency modulation (FM) to the repump transition.[3] The cooling laser is phase locked via a beat-note with the repump laser. We use this to arbitrarily set the cooling lasers frequency detuning from the cooling transition.[4] Bjorklund [109] and Appel et al. [110] have detailed descriptions of FM and phase locking mechanisms respectively.

This lasers used are two Vescent[5] 780 nm distributed Bragg reflector (DBR) lasers. These are used for both the cooling and repump beams. The repump beam passes through a Vescent D2-210-Rb SAS spectroscopy module—in order to FM lock [109] the repump laser—the beam is then coupled into an optical fibre. The cooling beam is coupled into an optical fibre. The two laser beams exit the rack through separate fibre mating sleeves for easy deployment of the light. The laser beams are also combined in-fibre and connected to a Vescent D2-160 PD to obtain a beat note for phase locking [110] the cooling laser. The

[3] $F = 2 \Rightarrow F' = 3$
[4] $F = 3 \Rightarrow F' = 4$
[5] `www.vescent.com/`

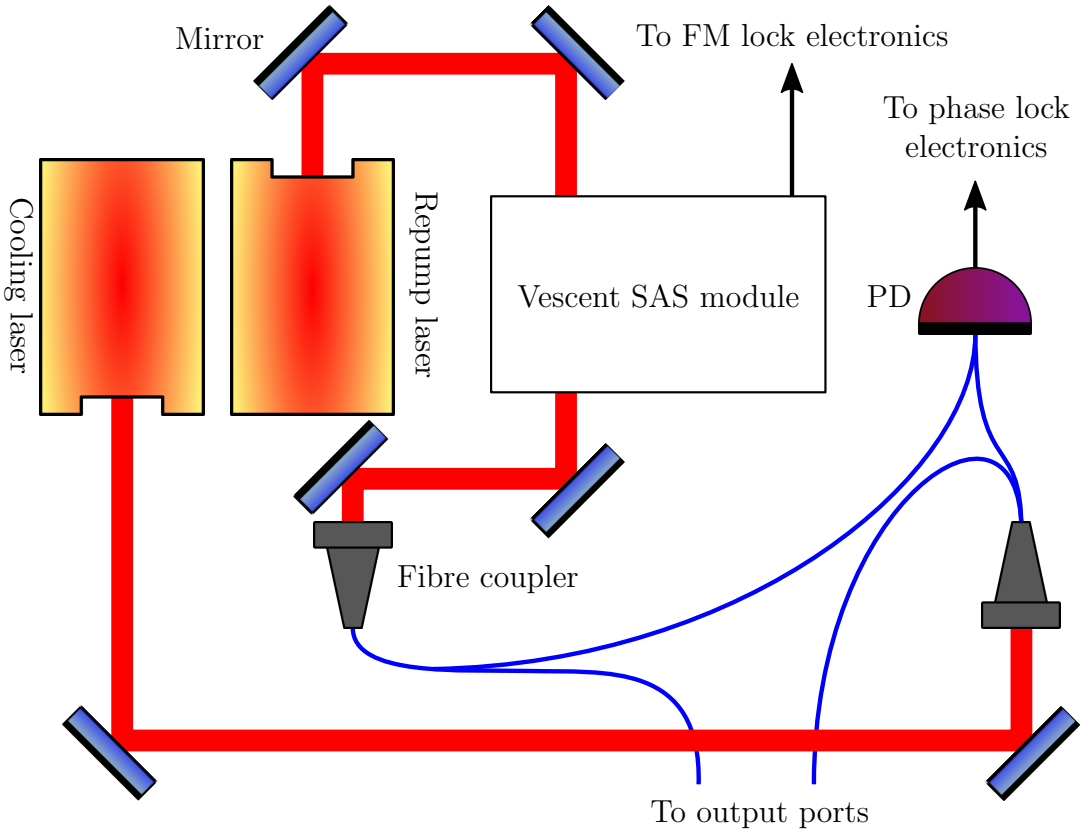

Figure 5.3: Cooling laser source optical arrangement. The red lines represent laser light originating from their respective lasers. The blue lines represent optical fibre. The repump beam first passes through a saturated absorption spectroscopy (SAS) module and is then fibre coupled. The cooling beam is fibre coupled. Both fibre coupled beams are sent to individual outputs and are also combined onto a PD to obtain a beat note. This system was designed and built by members of the Quantum Control group at the University of Southampton.

fibres used inside the rack are *not* PM fibres.[6]

To maintain stability of the optical components, the laser system is encased within a server rack and actively temperature controlled by a Eurotherm 3216 temperature controller. The optics are placed on an optical breadboard within the rack. The optical breadboard is heated, from the underside, by electric heating elements to 25°C. A PT100 sensor attached to the top of the breadboard monitors the temperature.

The lasers are controlled by Vescent Integrated Control Electronics (ICE) modules. Both lasers are temperature controlled by an ICE-QT1 and powered by an ICE-PB1. The repump laser is controlled, and FM locked, by an ICE-CS1 which the SAS module (D2-210-Rb) is connected to. The cooling laser is controlled, and phase locked, by an ICE-CP1 which the D2-160 PD is connected to. This allows the cooling laser to be set to an arbitrary frequency offset from the repump transition. To be precise, the repump laser is locked to the cross-over resonance [41] between the $F = 2 \Rightarrow F' = 1, 3$ transitions and the *actual* repump transition peak is very weak in comparison [111]; this cross-over peak is $-46.4\,\mathrm{MHz}$ from the repump transition. This doesn't affect the quality of the trap as having exact resonance with the repump transition is not too important [78]; the repump interacts with only $\approx 0.5\%$ of the atoms at a time, therefore a $\approx 7\,\Gamma$ detuning from resonance—decreasing the excitation probability by $\approx 95\%$—will still drive a sufficient amount of atoms to out of the dark state. The ICE-CP1 accepts an external frequency reference: allowing the cooling frequency offset to be determined by an external oscillator, a feature integral to the design of the experiment. This phase locking component is also capable of multiplying this external reference frequency by a range of powers of 2, relaxing the requirement for high frequency radio-frequency (RF) components.

We control the phase lock's offset frequency using a MOGLabs[7] XRF agile RF synthesiser—we shall refer to this device as the *Moglabs RF source*. This allows us to change the cooling laser's frequency during the experiment to desired values, coordinated by TTL signals from the pulseblaster. We use this method to turn the cooling laser into a multi-purpose laser throughout the experiment.

In this configuration, we are able to use $\approx 50\,\mathrm{mW}$ out of the cooling laser fibre out of the available $\approx 93\,\mathrm{mW}$ power from the laser aperture. The repump laser produces $\approx 57\,\mathrm{mW}$ of light, after the SAS module we couple the remaining $\approx 53\,\mathrm{mW}$ and are able to use $\approx 33\,\mathrm{mW}$ out of the fibre.

[6] This system was originally designed for use in another project.

[7] `www.moglabs.com`

5.3 Laser switching system

Figure 5.4 shows the experimental arrangement of the laser switching system for controlling the lasers used throughout the experiment. In order to provide the fastest possible time for shuttering the light (both on and off) we use AOMs as shutters. We use AOMs rather than Pockels cells, electro-optic modulators (EOMs), or mechanical shutters as they provide a fast response, variable optical attenuation, and were readily available to use. The AOMs used are both Gooch & Housego[8] M080-2B/F-GH2 AOMs. The repump beam's AOM is driven by an AA Opto-Electronic[9] MODA80-B4-33. The cooling beam's AOM is driven by the Moglabs RF source to allow analogue control of the laser beam's power. Since we can set the cooling laser's frequency arbitrarily, any frequency shift caused by the AOM can be disregarded. Therefore, a zero frequency shift arrangement similar to the repump beam is unnecessary and would waste laser power.

The power to both these AOMs is digitally controlled by two Mini-Circuits[10] ZX80-DR230-S+ RF switches, thereby switching the laser beams coupled into the fibre on or off. The RF switches are controlled by TTL signals from the pulseblaster. We use this switch on the cooling beam's AOM, despite being able to modulate the AOM's amplitude freely, to help development of the control software. The pulseblaster also coordinates the amplitude modulation (AM) and the FM of the Moglabs RF source, and hence the AM and the FM of the cooling laser.

Due to imperfections in the polarisation optics, some laser power is transmitted through the PBSs that should be reflected. We use this to fibre couple the weak undiffracted beam from the cooling laser to use as a resonant absorption beam—not to be confused with the absorption *imaging* beam—for detecting atoms after free fall. This is explained in detail in Section 5.8. We use the undiffracted beam from the AOM in order to have the absorption beam on while the cooling or imaging light is off. This also prevents coupling of the repump light: since the cooling and repump beams are coupled into the same fibre, they are effectively co-propagating and would also couple into the other fibre together.

Using this system we are able to obtain $\approx 14.8\,\mathrm{mW}$ of cooling and $\approx 5.3\,\mathrm{mW}$ of repump laser power at the end of the output fibre. As seen in Section 5.1, we cannot use all this available power in the MOT due to the beams being orthogonally linearly polarised. The absorption beam power is decreased by the

[8] www.gandh.com
[9] www.aaoptoelectronic.com
[10] www.minicircuits.com

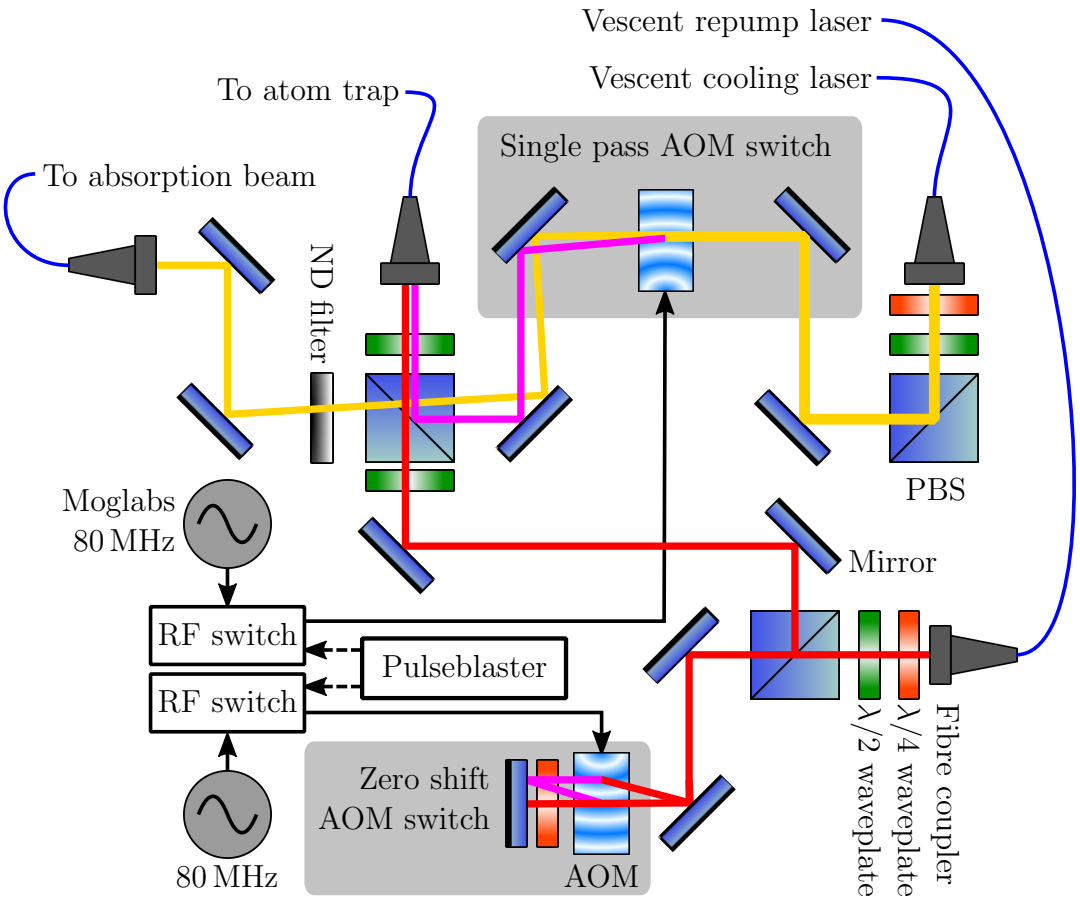

Figure 5.4: Design of laser switching system. The function of the absorption beam is detailed in Chapter 6. The fibres travelling from the cooling laser source and to the absorption beam are non-PM, and the fibre travelling to the trap is PM. The cooling laser beam passes through an AOM, the diffracted order is coupled into the fibre that leads to the atom trap. The cooling laser beam's undiffracted order is also fibre coupled after passing through a neutral density filter (ND filter). The repump laser beam passes twice through an AOM so that no net frequency shift is gained, it is then coupled into the same fibre as the diffracted cooling beam.

ND filter to provide $\approx 0.4\,\mu$W out of the fibre; this gives an $I/I_{\text{sat}} \approx 1 \times 10^{-5}$ which we would assume to be within the weak probe limit [111].

This system provides very flexible solid state laser control, primarily of the cooling laser. The cooling laser power and frequency can be controlled through software commands requiring no manual manipulation or realignment, providing us with the ability to automate experimentation through software. The experiments and data collected with the cold atom experiments are performed in this manner, allowing a large amount of data to be taken without human interference. This helps to keep the lab environment stable and to perform experiments in quick succession.

5.4 Vacuum chamber

Bidel et al. [33] demonstrated a compact vacuum chamber capable of absolute gravimetry [34]. This chamber used a 6 cm falling distance ($\approx$ 110 ms) and achieved a sensitivity of $42\,\mu\text{Gal}/\sqrt{\text{Hz}}$ ($1\,\mu\text{Gal} = 10^{-8}\,\text{m/s}^2$).[11] They showed it was possible for a small vacuum chamber to be capable of atom interferometric inertial measurements. This is the basis for the design of the vacuum chamber used for the PLAIN-GG project.

In order for the optical fibre interferometer (seen in Figure 1.1 and detailed in Section 7.2) to stabilise the Raman beams, we require a retro-reflecting mirror that both the optical interferometer and the Raman beams use to share any phase noise. The chamber also requires suitable distance to drop the cold atom ensemble over: we have decided to use a 71 mm falling distance ($\approx$ 120 ms) to slightly increase the drop time used in Bidel et al. [33, 34]—slightly increasing sensitivity—while maintaining a compact design. Figure 5.5 shows the design of this vacuum chamber. To create a compact laser cooling system, we mount five MOT mirrors into the vacuum chamber: one central mirror and four tilted at 45° to the central mirror arranged with equal spacing around the central mirror. This central mirror will act as the retro-reflecting mirror for the Raman lasers and the stabilisation laser for the PLAIN-GG project. This mirror arrangement allows a single laser beam, as described in Section 4.4, to illuminate all the MOT mirrors and form a cold atom cloud—removing the need for more optical components and keeping the system compact. The chamber is then mounted so that the MOT mirrors are above the chamber window. After the cold atom ensemble is released from the MOT, the cold atoms fall due to gravity down

[11] Note that these are the units for an *absolute* gravimeter, as opposed to the Eotvos for a differential gravimeter.

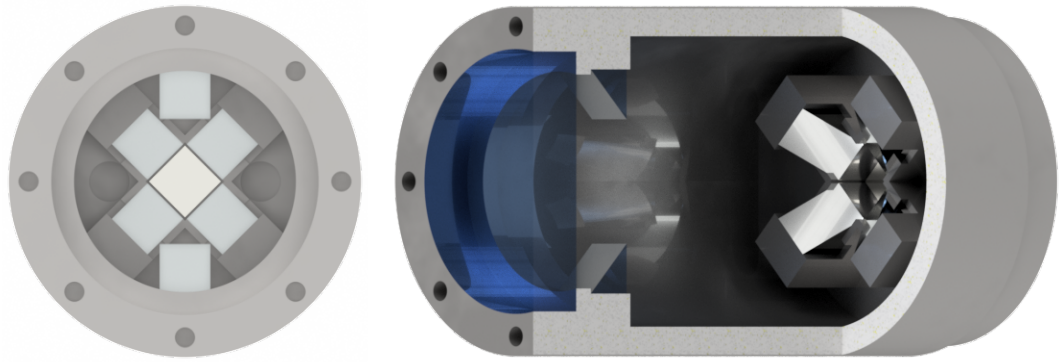

Figure 5.5: Computer Assisted Design (CAD) rendering of the vacuum chamber. The image on the left is looking through the window towards the mirrors, with the window removed for clarity. The image on the right is a cut-out view to see the inside of the vacuum chamber from a side angle.

towards the single window of the chamber. Between the MOT mirrors and the window, two more mirrors are placed at a distance of 71 mm from the MOT mirrors; these act to direct any light for detecting the atoms at the bottom of the chamber—this may be through an absorption beam or through detecting fluorescence. In order not to obscure the MOT light, these detection mirrors are orientated at 45° to the MOT mirrors. Right angled prisms are used for the side mirrors and the mirrors at the bottom of the chamber, the central retro-reflecting mirror is a flat square mirror. A $\lambda/4$ waveplate is placed in front of this retro-reflecting mirror to create correct polarisations for the reflecting MOT beam, seen clearer in Figure 5.1.

All the prisms inside the chamber are 10 mm × 10 mm dielectric coated prisms and the central mirror is a square 10 mm × 10 mm dielectric coated mirror. The window is 12 mm thick anti-reflective coated BK7 glass with a diameter of 53 mm, the window recess lip has a diameter of 44 mm.[12] Around the recess for the window are M4 screw holes for mounting a cage mount adapter onto the chamber. The chamber has a 70 mm outer diameter and is 120 mm tall.

Next to the MOT mirrors are two small 8 mm diameter holes which lead to a small area where the Rubidium dispensers are positioned—these can be seen in the left image of Figure 5.5. Two SAES[13] Rubidium dispensers, fitted in a V formation in order to share a single electrical (ground) connection, provide the atomic vapour used in the experiments. By passing an electrical current

[12] From our investigations discussed in Section 5.6, we suspect that this anti-reflective coating is only on the outer surface of the window.

[13] `www.saesgetters.com`

through these dispensers, heating causes Rubidium to be released into the vacuum chamber. This rear section of the vacuum chamber is also where two ports for vacuum pumps are located.

The chamber pressure is maintained by a single small MA353G ion pump. To maintain portability, we power this ion pump with a Ferrovac[14] LSA3 battery powered ion pump controller. When the dispensers are active, the pressure tends to settle at $\approx 2 \times 10^{-9}$ mbar. When the dispensers are not in use, the chamber pressure idles at pressures $< 10^{-9}$ mbar and has gone as low as 2×10^{-10} mbar. These pressures will change according to the temperature of the chamber; due to several heating effects from the system described later in this chapter, the chamber is usually at $\approx 25°$C. When the chamber has reached temperatures of $\approx 45°$C, by leaving on the MOT coils on permanently, the idle pressure has been $\approx 2.5 \times 10^{-9}$ mbar and reached $\approx 6.5 \times 10^{-9}$ mbar when using the dispensers.

5.4.1 Manufacture

These chambers were manufactured by Teledyne e2v[15] as off-the-shelf products, ready for use in cold atom experiments on delivery, making these chambers the first commercial vacuum chambers purpose built for atom interferometry with integrated optics. Teledyne e2v handled the machining, assembly, bake-out, pumping to vacuum, and dispenser activation prior to delivery.

A particular feature of this chamber is the vacuum pumping process. Two tubes are used to connect the chamber to vacuum pumps, one connecting to a small and lightweight ion pump, and another to the roughing and turbo pump. Once the chamber has reached sufficient vacuum—and dispensers activated—the tube to the roughing and turbo pump is deformed to seal it off, permanently disconnecting the two pumps and leaving only the ion pump connected. This process allows the chamber to be more portable at the cost of the inability to pump the chamber back to a sufficient vacuum if the pressure increases beyond the level the ion pump can handle.

5.5 Liquid crystal waveplate

In order to trap atoms, and later perform Raman transitions for gravimetry, we require to be able to switch quickly between $\lambda/4$ (MOT) and $\lambda/2$ (Raman)

[14] www.ferrovac.com
[15] www.teledyne-e2v.com

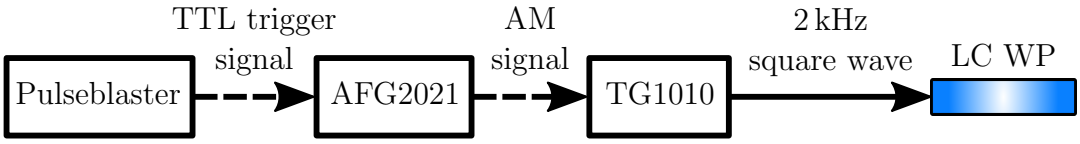

Figure 5.6: LC WP driver built from the pulseblaster and two arbitrary function generators. The pulseblaster is used to control the timing of the switching by triggering the AFG2021. The AFG2021 is programmed with the desired waveform to perform AM on the TG1010's 10 V (20 Vpp) 2 kHz square wave that drives the LC WP.

retardances. Clearly it is impractical and not fast enough to mechanically switch between two different waveplates before the atoms would fall and hit the vacuum chamber window, and it is not possible, with our current optical configuration of the vacuum chamber, to fulfil both these requirements with static waveplates. To solve this we use a LC WP which is able to vary its retardance by altering the driving voltage supplied to it.

The LC WP functions by orientating the nematic liquid crystals to an applied electric field [112, 113]. Without a force from the electric field, the crystals relax to a default alignment determined by the manufacturing process. The balance between this 'relaxation force' and the electric field strength determines the orientation the crystals will move towards. This orientation determines the magnitude of the waveplate's birefringence and hence its retardance. However, the viscous nature of the nematic liquid crystals prevent them from changing their orientation too fast and they asymptotically approach the desired orientation [114, 115]. This limits the switching times between different retardances. This switching is also faster when going from low to high voltage compared to high to low voltage, as the torque on the nematic liquid crytals is higher from the electric field compared to relaxing back to their original position. Since we only care about the switching times from $\lambda/4$ to $\lambda/2$ retardance (MOT to Raman), as this must be done quickly before the atoms fall too far, we can choose suitable voltages for this.

We use a Meadowlark[16] liquid crystal variable retarder for the LC WP. It is driven by a 2 kHz square wave of amplitudes in the range 0-10 V. The amplitude of this square wave determines the retardance of the LC WP. Through AM of the square wave, we can arbitrarily select the desired retardance during the experiment. Figure 5.6 shows the experimental setup used to control the retardance of the LC WP. This is built from two arbitrary function generators: a Tektronix[17]

[16] `www.meadowlark.com`
[17] `www.tek.com`

AFG2021 and an AimTTi[18] TG1010. This allows arbitrary control of the LC WP's driving voltage and hence arbitrary control of the LC WP's retardance. Before the AFG2021 detects a TTL trigger signal from the pulseblaster, it provides a constant chosen voltage to the TG1010 which corresponds to a desired retardance for the LC WP. After receiving the TTL trigger signal from the pulseblaster, the AFG2021 outputs the programmed arbitrary waveform to the TG1010 which changes the LC WP's retardance correspondingly. Once the waveform has been completed, the AFG2021 returns to outputting the initial 'idling' voltage and awaits the next TTL trigger.

To provide the fastest switching times between retardances, the waveform we use to AM the LC WP's driving voltage takes advantage of the Transient Nematic Effect (TNE) [116, 117, 118]. This effect describes the ability for the LC WP to reach a desired retardance faster, when the desired retardance's corresponding voltage is higher than the current voltage driving the LC WP, by supplying a greater voltage than the desired retardance's corresponding voltage. Figure 5.7 shows this TNE pulse waveform that the AFG2021 outputs for AM after triggering. The TNE pulse works by applying a large initial voltage, the TNE voltage, to rapidly accelerate the nematic liquid crystals to the desired orientation. Once the crystals have reached the desired position, the voltage is dropped to the voltage corresponding to the desired retardance. This prevents the crystals from rotating further and maintains the desired retardance for the chosen period. The allows us to gain the benefits of the faster response times from the TNE without over-shooting the desired retardance. Since we only require the switching time from $\lambda/4$ to $\lambda/2$ retardance to be fast, the initial voltage is chosen so that the LC WP sits at $\lambda/4$ retardance. Hence we call this the $\lambda/4$ voltage, and similarly the $\lambda/2$ voltage is when the LC WP is at $\lambda/2$ retardance. The TNE voltage is the voltage used for the period of rapid acceleration called the TNE interval; this is usually set to the highest voltage possible (10 V in this case) in order to minimise the TNE interval. It is possible to decrease the time changing from $\lambda/2$ to $\lambda/4$ retardances by applying 0 V to the LC WP for a small interval, applying the TNE but in reverse, however it is unnecessary to optimise this response time for this system.

The LC WP is also able to be heated. The viscosity of the nematic liquid crystals decreases with increasing temperature; therefore, we also can achieve faster switching times by heating the LC WP. We use a Meadowlark D5020 liquid crystal digital interface controller for temperature control.[19] We are able to safely heat the LC WP up to 50°C and this is the temperature we heat the

[18] `www.aimtti.com`

[19] This controller is capable of controlling the retardance of the LC WP as well, it however lacks sufficient timing controls that we require.

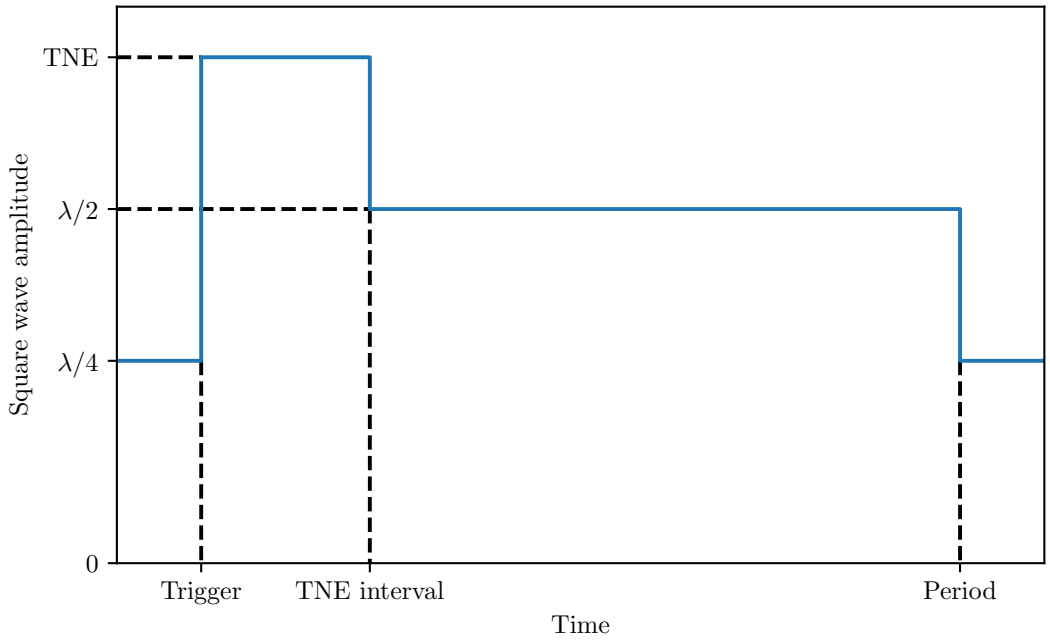

Figure 5.7: TNE pulse waveform example for AM of the LC WP's driving square wave. Here the features of the pulse are labelled. The TNE interval and period are taken with respect to the trigger. This is the shape of the pulse that would be used for AM of the LC WP's driving square wave.

LC WP for operation.

The Meadowlark LC WP has a quoted response time of $\approx 5\,\text{ms}$ from low to high voltage and $\approx 20\,\text{ms}$ for high to low voltage. This is the response time when naïvely stepping the voltage from one to the other. Figure 5.8 shows the LC WP response using basic and TNE AM waveforms. This was measured by placing a PD in the camera's position in Figure 5.1. For demonstration purposes the pulse period is different in both cases and can be set arbitrarily for different usages. The main focus of this comparison is the difference in rise times from $\lambda/4$ to $\lambda/2$ retardances between using the TNE pulse and a basic stepping pulse. We see that the basic stepping pulse has a rise time of $\approx 90\,\text{ms}$ whereas the TNE pulse has a rise time equal to the TNE interval $\approx 1.5\,\text{ms}$. We have at times measured TNE pulse rise times $\approx 0.75\,\text{ms}$. We can see that the TNE pulse significantly improves the switching response time and we will use this waveform whenever using the LC WP to switch retardances from $\lambda/4$ to $\lambda/2$. After the AM pulse, the LC WP takes $\approx 100\,\text{ms}$ to return to the $\lambda/4$ retardance for both pulses. A $90\,\text{ms}$ response time for the basic switching waveform is impractical to be used when the cold atom cloud's drop time in the vacuum chamber is $120\,\text{ms}$. This would mean a maximum of $T = 15\,\text{ms}$ for the atom interferometery and limit

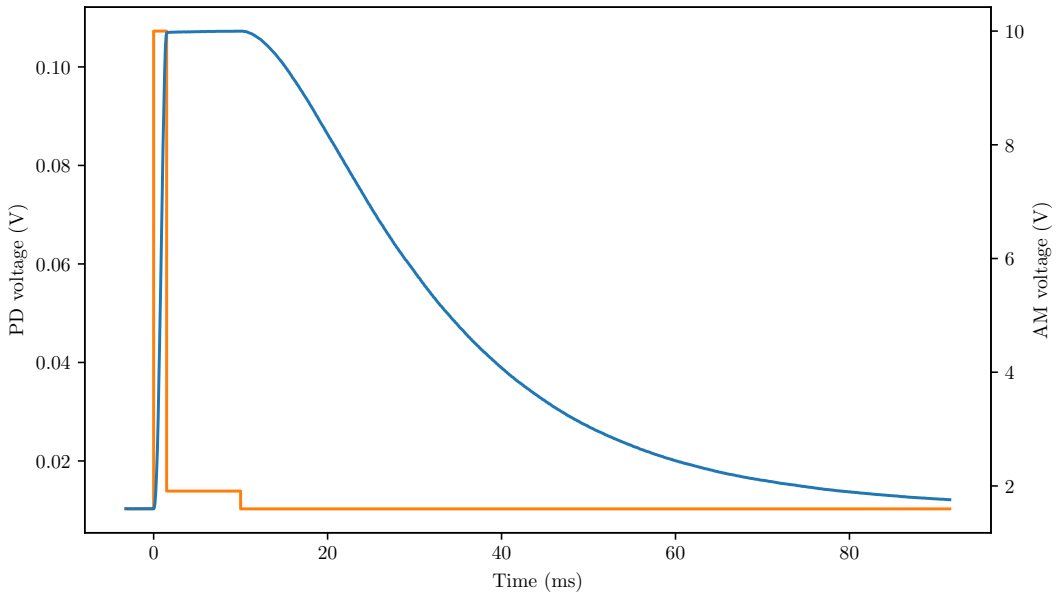

(a) TNE operation.

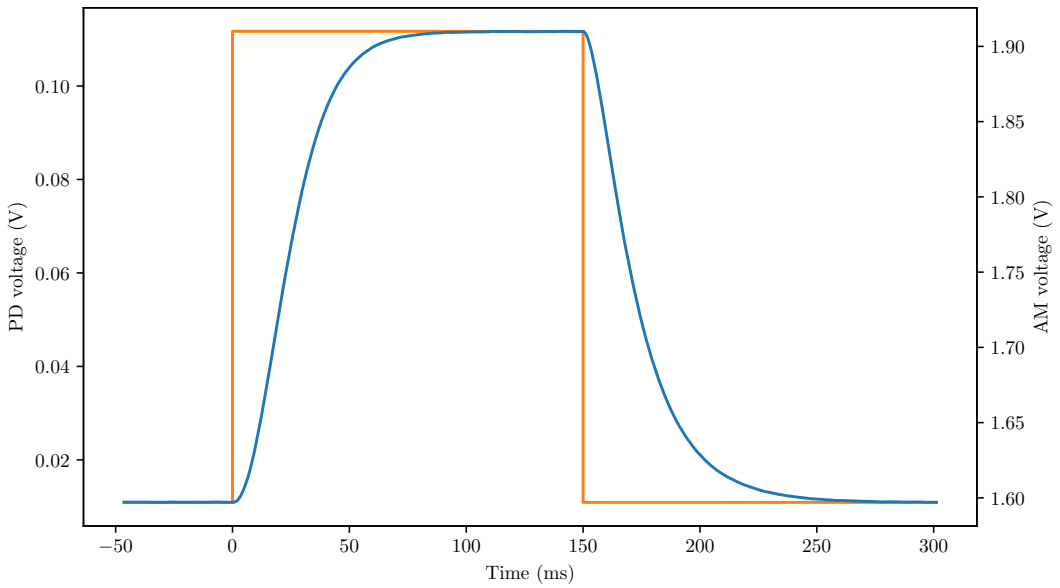

(b) Basic stepping operation.

Figure 5.8: Graphs comparing (a) TNE operation and (b) basic stepping waveforms. The blue lines represent the intensity of the light detected by a PD at the camera position in Figure 5.1, represented on the left axis. The orange lines represent the AM signal used to control the LC WP, represented on the right axis. Note that the axis scales are not the same between the two graphs. Both measurements were taken with the LC WP heated to 50 °C. The low PD level is $\lambda/4$ retardance and the high PD level is $\lambda/2$ retardance. The parameters used here were: $\lambda/4$ voltage = 1.597 V, $\lambda/2$ voltage = 1.91 V, TNE voltage = 10 V, and TNE interval = 1.494 ms. The period used for the TNE pulse was 10 ms and the basic pulse had a 150 ms period.

our sensitivity—for comparison, Bidel et al. [33] uses $T = 48\,\text{ms}$. Therefore, the TNE pulse should be used as it provides a significant decrease of response time.

The TNE parameters were found by iterating the variables in the order: $\lambda/4$ voltage, TNE interval, and $\lambda/2$ voltage while looking at the PD signal. The TNE voltage was always fixed at the maximum 10 V. When iterating these variables, we took advantage of the non-linearity of the LC WP's retardance response to voltage in order to find points of inflection. This non-linearity occurs because particular voltages correspond to particular angles of the nematic liquid crystals, and as they rotate the retardance the crystals provide changes from 0 to λ periodically. This is seen in our setup, where the detected laser beam's power depends on the light's polarisation entering the PBS, as an oscillating signal when sweeping the voltage from 0 V to 10 V at the camera's position. In our experimental setup, these points of inflection corresponded to either $\lambda/4$ or $\lambda/2$ retardances—the minima and maxima respectively. If the $\lambda/4$ voltage was set too low, it would pass through this point of inflection and would need to be adjusted. Similarly if the TNE interval were set too high, it would pass a different point of inflection and need to be reduced—since this point can be clearly seen in the time domain it is very simple to set the TNE interval. If the $\lambda/2$ voltage was set too high, it would also pass an inflection when the LC WP is relaxing back to the $\lambda/4$ operation.

A frustrating aspect of the LC WP is that it required regular recalibration: where the TNE pulse's parameters (apart from the TNE voltage) would need to be adjusted. Over time the voltages required to maintain proper polarisations shifted slightly. The TNE interval depends on the voltage difference between the TNE voltage and the $\lambda/4$ and $\lambda/2$ voltages. A larger difference means a faster response time can be achieved—a behaviour described by the TNE. For example if $\lambda/4$ voltage = 9 V and the TNE voltage = 10 V, the response time would be slower compared to if the $\lambda/4$ voltage = 1 V. While the nematic liquid crystals have a larger angle to rotate, they experience a larger torque initially and since the $\lambda/2$ voltage tends to be close to the $\lambda/4$ voltage the nematic liquid crystals don't need to rotate such a large angle. Since the TNE interval—and hence the response time—depend on these voltages this also shifts slightly as the voltages shift. We are unsure of what causes these small shifts as they happen over long time-scales; and since the rest of the experiment can still function with small changes in polarisations, it was not a priority to investigate. This instability is possibly caused by general wear and tear from use, fluctuations of the temperature of the LC WP, or inherent instability of the LC WP.

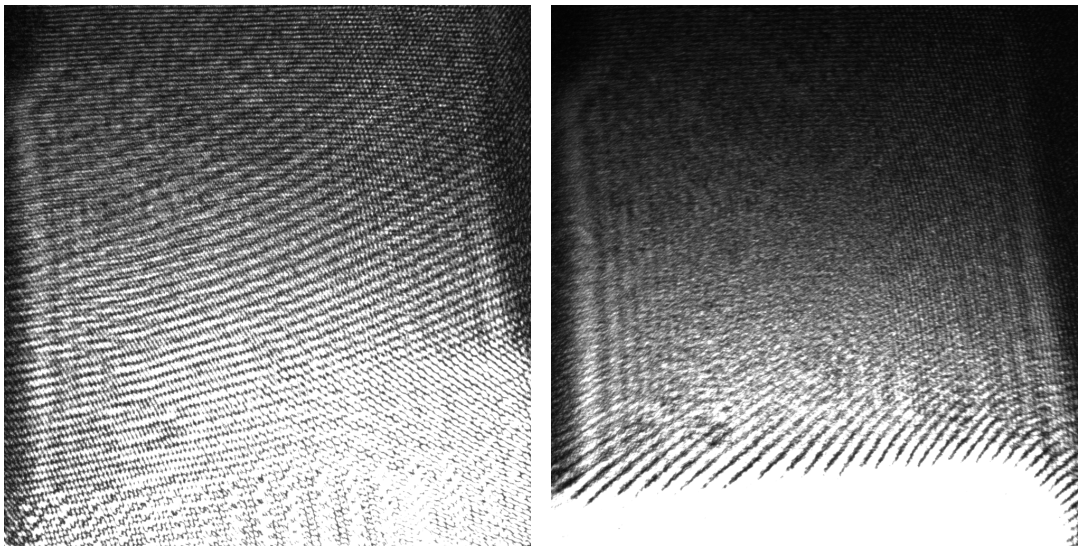

(a) $\lambda/4$ waveplate (b) $\lambda/2$ waveplate

Figure 5.9: Images of chamber mirrors with different LC WP settings. The main mirror visible in the centre of the image is a side mirror, with the central mirror at the bottom of both images. Due to the polarisation changing the intensity of light detected at the camera, both images were taken with different laser intensities to properly expose the camera. The most notable fringes that are present in (a) but not in (b) are the large pitched fringes on the side mirror and the 'cross-stitched' pattern on the central mirror. These fringes would be observed to move on short timescales. It may be worth noting that these are not absorption images but are single exposures of the camera.

5.6 Absorption imaging

During development, we discovered interference fringes present on any absorption images we recorded when using a $\lambda/4$ waveplate for atom trapping. We determined this is due to reflections from the *inner* surface of the vacuum chamber window—the interface between the glass and the vacuum—and the fraction of useful reflected light from the MOT mirrors that passes through the PBS. The outer surface of the window—the interface between the air and the window, which adds a π phase shift on reflection—could not create this effect as the light it reflects is orthogonally polarised to the useful light. However, these fringes vanished when using a $\lambda/2$ waveplate with its fast and slow axes in the same orientation as the $\lambda/4$ waveplate. This showed that the LC WP could be used to remove these fringes in the absorption images. The LC WP hence became an integral part of the imaging system. Figure 5.9 shows images of the chamber windows with and without using the LC WP to switch retardances. Here we

can see the fringes present in both images, and how the $\lambda/2$ case has much less pronounced fringes on the mirror's image. Despite absorption imaging removing features common to the images used, the fringes present in the $\lambda/4$ case remain in the final absorption image; in particular the 'cross-stitch' interference pattern seen on the central mirror, and the prominent fringes on the side mirror. The absorption imaging is unable to remove these features because the interference fringes are very sensitive to any vibration or change in polarisation—they can be seen slowly moving and shifting—and in the areas of deconstructive interference there is simply no light for the camera to detect. When using the $\lambda/2$ retardance for absorption imaging, no such disruptive interference patterns are seen in the final image. Changing the LC WP's retardance to $\lambda/2$ also allows more light to pass through the PBS towards the camera. This increases the brightness of the images and providing increased flexibility of the imaging laser beam's power. It is unclear where the fringes in the $\lambda/2$ case arise from, in particular those seen surrounding the central mirror at the bottom of the image, these may be caused by other reflections from interfaces. Thankfully, these fringes remain static—during the imaging period—and are able to be 'subtracted' by the absorption imaging technique and do not effect our results.

While this interference fringe problem was improved by the LC WP switching, it would be preferable if the fringes were not present at all. A possible solution to this is to alter the design of the vacuum chamber to tilt the window by a small angle. This would direct any unwanted reflections from the window away from the absorption imaging camera.

When imaging the atoms trapped by the MOT with the camera in Figure 5.1, the laser light reflecting off the central mirror would pass through the cold atoms twice. We will assume that this, and the reflected light from the side mirrors, does not create any additional effects that would change the absorption cross section, σ. Therefore, the absorption detected from the light reflecting off the central mirror would indicate a cloud twice as large. To compensate for this we make a small adjustment to Equation 4.25:

$$N_{\text{retro}} = \frac{A}{2\sigma_0} \sum_{\text{pixels}} \ln\left(\frac{I_0}{I}\right) = \frac{1}{2} N_{\text{total}}. \tag{5.1}$$

We will use this equation to determine the atom number when imaging the central mirror and Equation 4.25 when imaging the trap from the side mirrors. The camera we are using has a pixel area of $A = 5.3\,\mu\text{m} \times 5.3\mu\text{m} = 2.8 \times 10^{-11}\,\text{m}^2$,[20] and the absorption cross sectional area is $\sigma_0 \approx 1.2457 \times 10^{-13}\,\text{m}^2$ [49].

In order to obtain the absorption images, we require a coordinated sequence of

[20] We see in Section 6.2.1 that the effective pixel size due to the imaging optics is $10.6\,\mu$m.

Parameter	Time	Description
t_{MOT}	2 s	Atom trapping time
Cooling rise time	10 μs	Rise time of cooling AOM
Cooling fall time	6 μs	Fall time of cooling AOM
Repump rise time	10 μs	Rise time of repump AOM
Repump fall time	10 μs	Fall time of repump AOM
Repump pump time	100 μs	Pumping during imaging sequence
Cooling to imaging time	15 μs	To decrease power to imaging power
Imaging to cooling time	15 μs	To increase power to cooling power
Imaging exposure time	45 ns	To expose camera
LC WP rise time	1.4 ms	To swap to $\lambda/2$ retardance
LC WP fall time	110 ms	To decay to $\lambda/4$ retardance
Camera delay	85 μs	Time between trigger and exposure
Camera reset time	72.5 ms	Delay between successive images

Table 5.1: Table showing the imaging sequence's calibration parameters. These values were measured and saved to properly coordinate the imaging sequence seen in Figure 5.10. The rise and fall times are used to ensure laser beams or devices are in their desired state before the next event can occur.

events; these include atom trapping, turning off the MOT lasers (and possibly the MOT coils), switching the LC WP to the correct polarisation, beginning the camera exposure, exposing the camera, retrieving the recorded image, performing a second 'background' exposure, retrieving the background image, and finally applying Equations 4.25 and 5.1 to the recorded images. The timings are handled by the pulseblaster which sends TTL signals to the relevant devices. Figure 5.10 shows the sequence used to image the atoms. Table 5.1 shows the parameters used to coordinate the imaging sequence properly. The AOM rise and fall time here are much longer than the typical response time of an AOM—typically these are ≈ 100 ns. This is due to the RF signal being switched by the RF switches which have a slower response time. We also see that the camera has a limited frame rate, requiring ≈ 75 ms between each image—this is possibly caused by the software used to record the images rather than the camera's hardware. This and the LC WP fall time limit how fast the background image can be taken after the atom's image. The cooling laser's frequency is changed ≈ 1 ms before it is used as an imaging beam to ensure the locking system has enough time to successfully change the lock-point.

After the experimental sequence is performed, two images recorded by the camera are sent to a computer for analysis. Here we use the first image recorded to provide values of I and the second background image for I_0. After applying Equation 4.25 for an image of the side mirrors or Equation 5.1 for an image of the

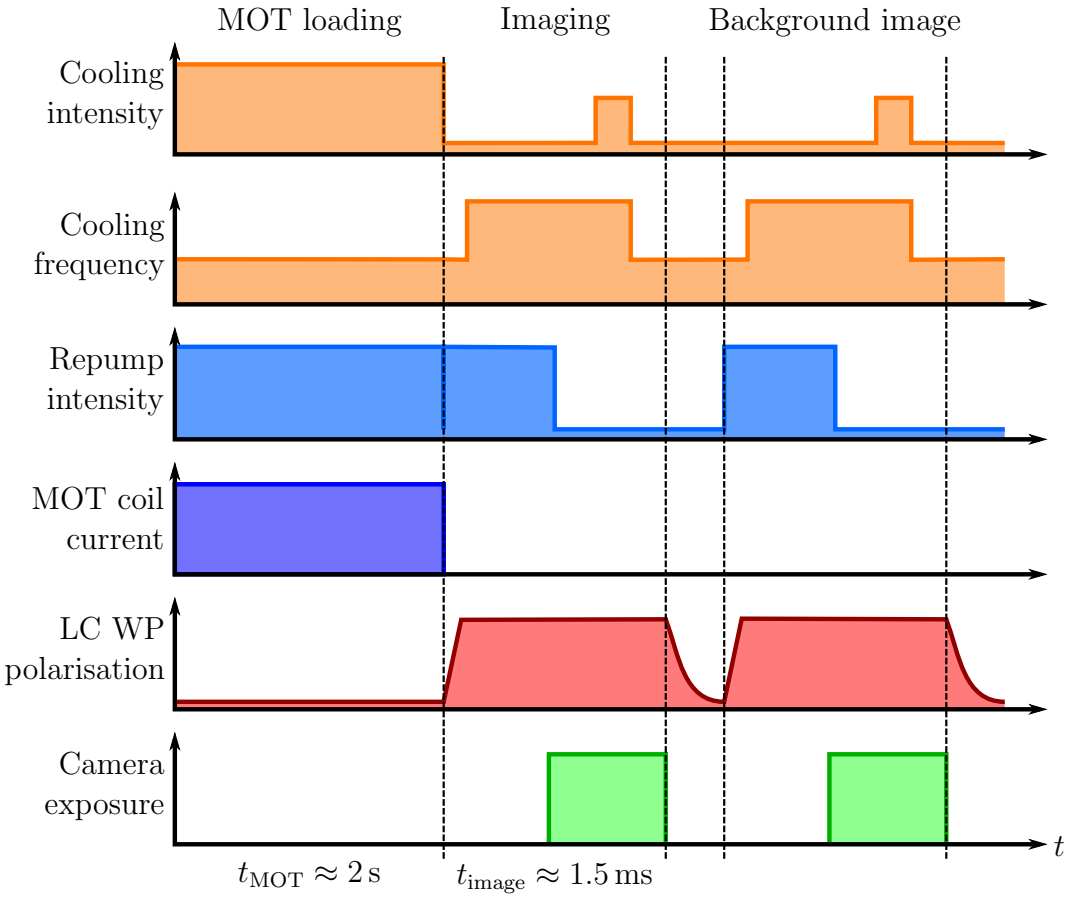

Figure 5.10: Representation of the absorption imaging timing sequence, not to scale. After the atoms are released from the MOT, the LC WP first begins to switch its retardance from $\lambda/4$ to $\lambda/2$. This is the longest period in the imaging sequence, apart from the LC WP decay, which limits the delay between recording the absorption image and switching off the MOT. During the imaging sequence, the repump is briefly switched on to pump any atoms out of the dark $F = 2$ state; the frequency of the cooling laser is also changed to be resonant with the cooling transition—turning the cooling laser into the imaging laser—the camera is then triggered. Due to uncertainty in the delay between the camera being triggered and beginning the exposure, we allow an exposure much larger than the time the imaging laser will be exposing the camera for; this allows much more precise control of the exposure period. After the first exposure, the image recorded is sent a computer. This period is lengthy and allows time for the LC WP to decay back to $\lambda/4$ retardance to be ready for the background imaging. To minimise any differences between the two images, apart from the cold atoms being present, the background imaging sequence is perform exactly as the first imaging sequence. t_{image} is the time including the rise time of the LC WP and the exposure period.

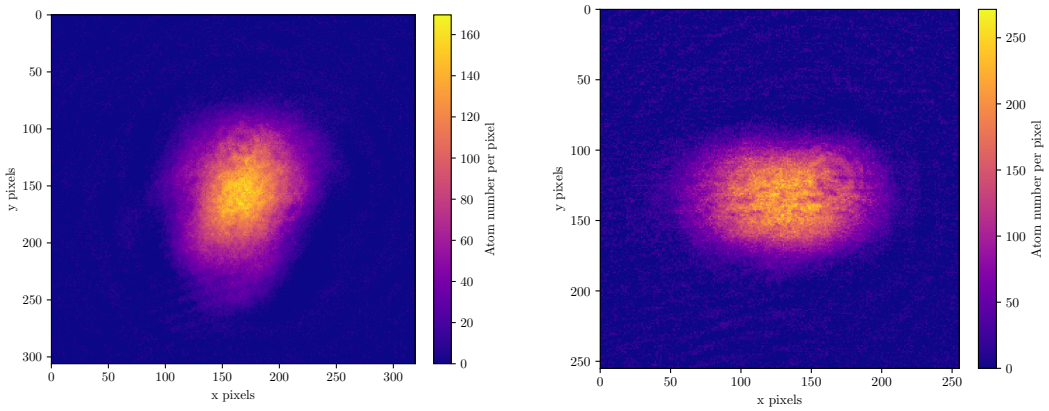

(a) Central mirror.

(b) Side mirror.

Figure 5.11: Examples of absorption images of the cold atom cloud from imaging the central mirror (a) and a side mirror (b). The atom number for (a) was found using Equation 5.1, and Equation 4.25 was used for (b). The total atom number in (a) is 1.3×10^6 atoms and in (b) is 1.6×10^6 atoms. The discrepancy between the measured atom numbers could be explained by these measurements being taken on different occasions with slightly different experimental parameters.

central mirror to each pixel, we obtain an image of the cold atoms. Figure 5.11 show examples of these images, showing the cold atom cloud's profile from both angles. The side angle shows the cloud looks 'squashed', this is most likely due to the up-down MOT forces being stronger from both the construction of the quadrupole magnetic field, and because the cooling beam's Gaussian intensity profile indicates a higher intensity of light on the central MOT mirror compared to the side mirrors. We found that $\approx 0.87\,\mathrm{mW}$ of imaging laser power yielded the best absorption imaging measurements without over-exposing the camera. The intensity of this beam is therefore $\approx 0.12\,\mathrm{mW/cm^2}$ which is much less than the saturation intensity of $I_{\mathrm{sat}} \approx 3.90\,\mathrm{mW/cm^2}$.

In Section 4.7.2 we mentioned how we neglected to incorporate a dark image subtraction into our calculations. If we estimate that this dark image has a uniform pixel value of 1, we then obtain atom numbers $\approx 2.5\%$ larger than we originally calculated. This percentage doubles to $\approx 5\%$ for a pixel value of 2, and a pixel value of 10 raises this significantly to $\approx 35\%$. The dark areas of the images, where only scatter from the inside of the vacuum chamber, can give us an estimate of this value; we find this to be a pixel value of 5, which gives an estimated adjustment to our atom numbers of $\approx 15\%$. We will not be incorporating this adjustment into the atom numbers given throughout this thesis, however it is worth keeping in mind that the atom numbers shown may be slightly larger because of this.

5.6.1 An imaging problem

The first image, collecting values of I, is consistently brighter than the background I_0 image. This means that a *negative* atom number is calculated in places where no (or little) absorption is detected; this is obviously unrealistic. This brightening is caused by a 'pre-exposure' of the image by the high intensity MOT laser beams being incident on the CCD sensor before the image exposure. It is possible to apply this pre-exposure effect to the background image in attempt to have equal brightness. However, this requires an pre-exposure period of $\approx 1\,\mathrm{s}$, in which case the fluctuations of laser power act to ruin the absorption image. Taking a 'blank' image before imaging the cold atom cloud in order to remove the brightening effect is also not possible due to the lengthy reset time seen in Table 5.1. Performing this blank image while the MOT lasers are active also does not remove the brightening effect.

To prevent this affecting our overall atom number, and because the negative numbers are present only on pixels that detect no absorption, we decided to ignore any negative atom number and reset any of these measurements to zero. While this does not solve the actual problem, this occurs on the pixels that do not detect any cold atoms and would not contribute to any measurements. Because of this, it is possible that the atom number we detect is much lower than the actual value. However, the absorption imaging can still reliably show any relative changes in atom number and shape; this makes this system still appropriate for characterising the MOT and making progress towards realising an atom interferometer. To further reduce the effect of noisy pixels on the image, any measurements of total atom number use a cropped image to focus on the atom cloud.

5.7 Molasses stage

In order to cool the cold atom cloud closer to the sub-Doppler cooling limit, we perform an additional cooling stage after the MOT. This *molasses* stage takes advantage of the Sisyphus effect described in Section 4.6 to cool down the atoms to orders of magnitude below the Doppler cooling limit. This is required in order to obtain the coldest and most dense sample of atoms for atom interferometry, and to detect the atoms at the bottom of the chamber. Here we use the absorption imaging system to employ the TOF technique (Section 4.7.3) to measure the temperature of the atoms.

Figure 5.12 shows the experimental sequence used for performing the molasses

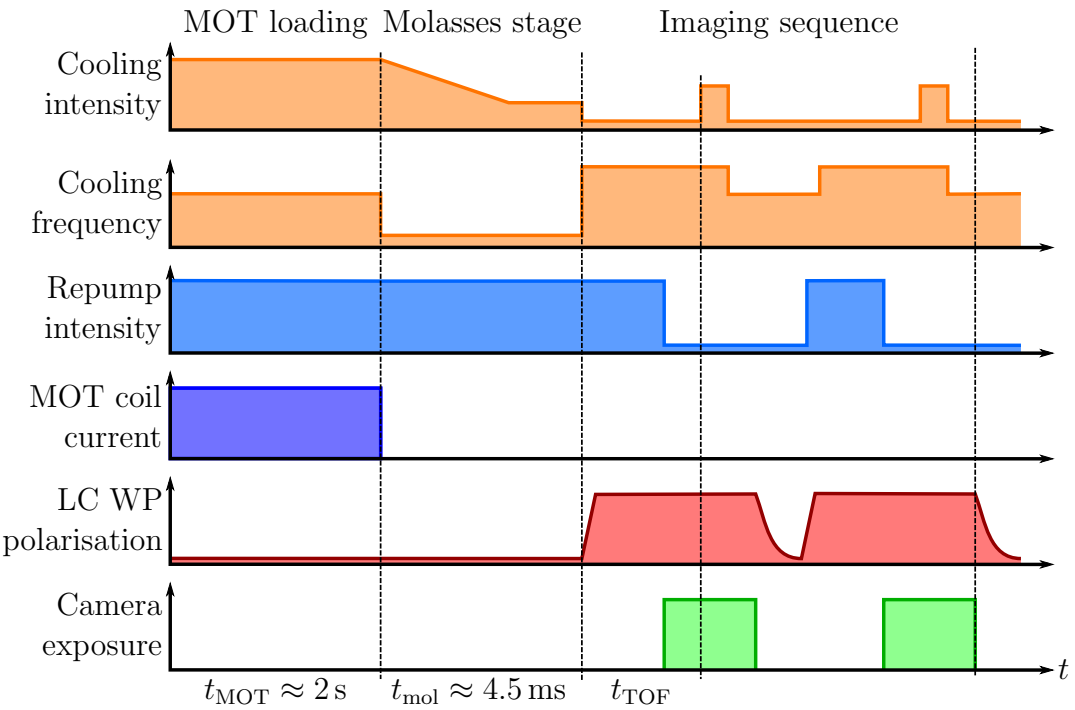

Figure 5.12: Representation of the molasses and TOF timing sequence, not to scale. After the MOT loading time the molasses stage occurs. During the molasses stage the MOT coil current is turned off, the repump light is left on, the intensity of the cooling beam is gradually decreased, and the cooling laser's frequency is detuned further from resonance. Once the molasses stage had finished, the absorption imaging sequence is used to image the size of the atom cloud. The TOF time, t_{TOF}, is measured from the end of the molasses period, t_{mol}, to when the imaging laser is turned on.

stage and TOF technique. We follow the results from Ji et al. [90] where they found the most effective molasses stage method was to gradually decrease the cooling laser's intensity, and quickly increase its frequency detuning. After the period where the cooling laser's intensity is ramped down—which lasts $\approx 3\,\mathrm{ms}$—we then maintain this lower power for $\approx 2.5\,\mathrm{ms}$ to further cool the atoms. After performing this sequence, absorption images of the atom cloud are obtained. From these images the size of the atom cloud can be measured. By repeating these measurements several times and varying t_{TOF}, we can build up a picture of how the cloud expands over time. We can then apply Equation 4.28 to this data to find the temperature of the cold atom cloud.

Since we are mostly interested in the vertical temperature of the atom cloud—as this temperature relates to the performance of the gravimeter—we aim the camera at one of the chamber's side mirrors. This allows us to see both the

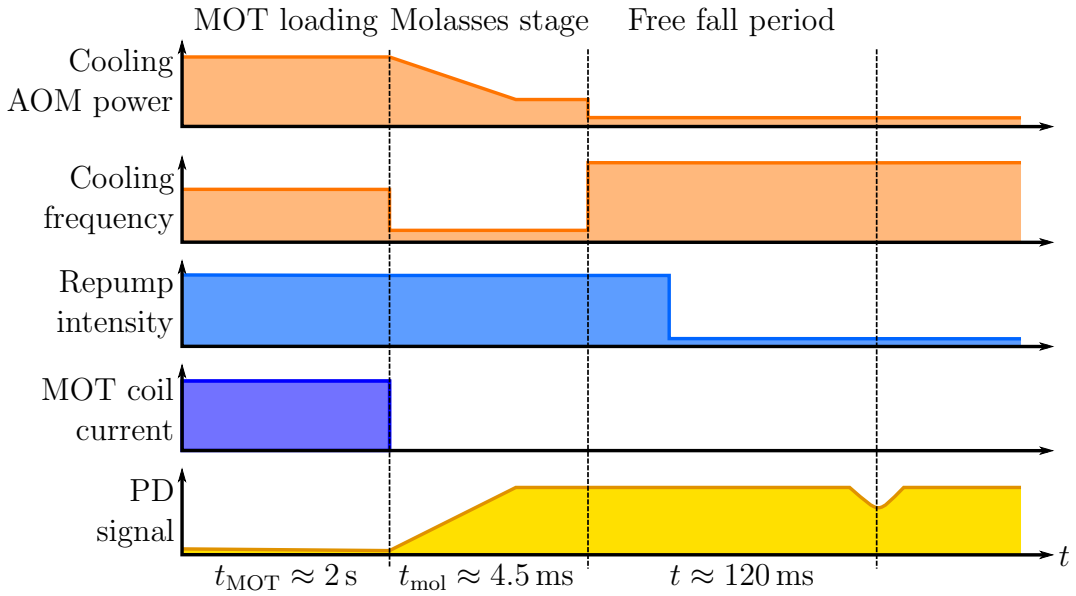

Figure 5.13: Representation of the experimental sequence for detecting atoms at the bottom of the vacuum chamber, not to scale. After the molasses stage, the atoms are allowed to fall to the bottom of the chamber. During this time the cooling laser's frequency is shifted to resonant with the cooling transition. After the atom ensemble has fallen the 71 mm distance between the MOT mirrors and the detection mirrors, a dip in the signal where the the atom ensemble has fallen into the beam and absorbing light is detected.

vertical and horizontal size of the atom cloud as it expands, and hence measure temperature in both directions.

5.8 Detection area atom detection

For a gravimeter to function, the atom ensemble must be detected after falling for a distance. Here is where the population of states would be measured after atom interferometry. While we have not implemented the atom interferometry, we must be able to detect atoms after they have been released from the MOT and fallen to the bottom of the chamber if the sensor head is to be used as an inertial sensor

To detect the atoms at the bottom of the chamber, we use a resonant absorption beam that passes through the area where the atoms fall through and is then detected by a PD. Figure 5.13 shows the experimental sequence for this detection. Since the absorption beam is the undiffracted cooling laser's beam (see

Figure 5.4), its power is related to the cooling beam's AOM. When the cooling beam is switched off using the AOM, the absorption beam is at maximum power. We also employ a 100 μs state preparation time where the repump is used to pump all the atoms into the $F = 3$ ground state to increase the absorption detected at the bottom of the chamber.

Chapter 6

Finding a needle in a haystack

This chapter shows the results of the cold atom experiments using the apparatus described in Chapter 5. As we mentioned in that chapter, in order for the experiment to demonstrate the ability to be used as an atom interferometer, we must be able to detect the cold atom ensemble after it has undergone free fall. To be able to detect the atom ensemble, it must be denser than the surrounding background rubidium gas. Intuitively, this provides two foci of optimisation: increasing the atom number and decreasing the cloud's temperature (or size after TOF).

We begin this chapter by characterising how the experimental variables affect the number of atoms trapped in the MOT. This is followed by measurements of the temperature of the cold atom cloud and characterisation of the molasses stage. Detection of the atom ensemble after free fall is then shown—where we find the proverbial needle.

6.1 Magneto-optical trap characterisation

We create the MOT in the vacuum chamber by directing the cooling and repump lasers at the MOT mirrors after collimation. Using a large enough diameter beam we are able to illuminate all the MOT mirrors with a single laser beam containing both MOT lasers with the correct polarisation of the cooling beam. We then run electrical current through the MOT coils such that they generate a quadrupole magnetic field. The polarity of this field is chosen to match the polarisation requirements described in Section 4.4. Rubidium vapour is introduced into the vacuum chamber by running 4 A through the chamber's

Rubidium dispensers. These dispensers are left on consistently while performing any experiments. Prior to the development of the absorption imaging system, we were able to detect the presence of cold atoms by imaging their shadow in the reflected MOT laser beams when attempting to trap the atoms. This gave a signal not ideal for characterisation, due to the cooling beam being detuned from resonance; however, it was enough to help detect the presence of the cold atoms.

The design of the vacuum chamber presents some constraints and additional challenges to optimising the MOT when compared with less restrictive chambers. Due to the MOT mirrors being fixed inside the chamber, the only variables we have control over are those concerning the laser and magnetic field: laser intensity, laser frequency, and the magnetic field gradient. While we technically have some control of the alignment of the laser and since the Raman beams (which would take the same optical path as the MOT beams) require retro-reflection, we will only use MOT beams that are retro-reflected along the main chamber axis.

The first aspect of the system to characterise and optimise is the absorption imaging system—as our measurements of the cold atom cloud are dependent on this system. In Section 4.7.2, we assumed to use resonant light to image the atoms to ensure the correct absorption cross section. Because we have arbitrary control over the cooling laser's frequency, we are able to ensure this assumption remains correct. Figure 6.1 shows how the atom number measured by the absorption imaging is affected by different detunings of the imaging and cooling beams. We also see in this graph how different cooling beam detunings affect the trap's atom number. The data were taken in a random order to remove any time-based biases—this will be the case for all similar measurements in this thesis—and the imaging and cooling frequencies were varied on separate occasions; which is why the maximum atom number for both series is different. We have plotted a Lorentzian distribution as this is the line shape we would expect from an atomic transition:

$$y(x) = A\frac{\gamma^2}{(x - x_0)^2 + \gamma^2} + y_0, \tag{6.1}$$

where A is the amplitude of the curve, the scale parameter $\gamma = \text{FWHM}/2$, x_0 is the position of the curve's peak, and y_0 is an offset fitting parameter to take into account erroneous atom number measurements from noise. We fit this Lorentzian to the measured atom number from varying the imaging beam's frequency as we expect the cold atom's transition linewidths to exhibit more ideal Lorenzian distributions as opposed to the Doppler broadened Voigt distributions. When the absorption light is not resonant, due to the atomic transition probabilities being Lorenzian shaped, less light is scattered from the

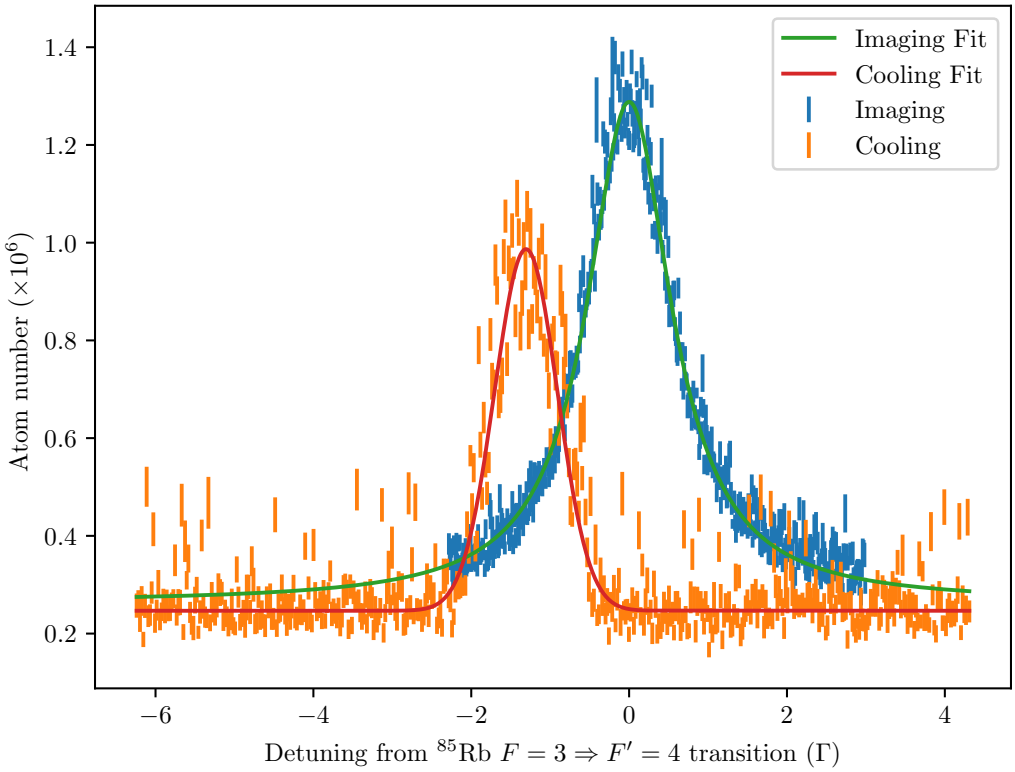

Figure 6.1: Figure showing atom number as the frequency of the imaging and cooling lasers, blue and orange respectively, are varied. A Lorentzian curve is fitted to the imaging laser's frequency with a Full Width Half Maximum (FWHM) of $1.3 \pm 0.01\,\Gamma$. A Gaussian curve is fitted to the cooling laser's detuning with a FWHM of $1.1 \pm 0.01\,\Gamma$ and centred at $-1.31 \pm 0.004\,\Gamma$. The x axis is scaled by assuming the centre-point of the Lorentzian is resonance and dividing the frequency used to define the laser's set point by Γ.

beam. This increases the light detected on the CCD, therefore decreasing the total atom number measured.

For the cooling laser's frequency we fit the Gaussian distribution

$$y(x) = A \exp\left(\frac{-(x - x_0)^2}{2\sigma^2}\right) + y_0, \tag{6.2}$$

where the standard deviation $\sigma = \text{FWHM}/2\sqrt{2}$. We use a Gaussian here because we are primarily interested in the centre of this peak, as this determines the best laser detuning to obtain the largest atom number. A theoretical model for this line shape can be derived through the the scattering force (Equation 4.4). As the detuning of the cooling laser is changed, the range of atomic velocities that can be effectively cooled through the scattering force changes. At small red detunings, very low velocities can be trapped; these atoms are already very cold and there are proportionally few of them. As the detuning is increased to the red, it eventually reaches a point where the maximum number of atoms can be effectively cooled and trapped. Continuing beyond this point, the MOT begins to attempt to trap faster moving atoms; however, because the capture velocity (Equation 4.20) remains constant the MOT is unable to trap the atoms that are faster then the maximum capture velocity.

The important features we wished to use this data for is to find the centres of each of the peaks as this provides the frequencies to set their corresponding lasers to. Hence, we shall use a detuning of $\delta_{\text{cooling}} = -1.31\,\Gamma$ for the cooling beam for our measurements. From Equation 4.7, this detuning corresponds to a maximum force around a velocity of $\approx 1\,\text{ms}^{-1}$; from Equation 4.20, this indicates we have a MOT with trapping radius of $\approx 0.1\,\text{mm}$. We would expect, with the size of the laser beams and the MOT mirrors, a trapping radius of at least 2.5 mm with a maximum radius of 5 mm. This would correspond to a maximum capture velocity of $\approx 7\,\text{ms}^{-1}$. Our measurements of the atom numbers give total atom numbers between 1-2 $\times 10^6$ usually, with the highest total atom number measured being $\approx 4 \times 10^6$. Using Equation 4.19, with $A = 4\pi r^2$ and $r = 5\,\text{mm}$, gives an expected atom number of $N \approx 2 \times 10^8$. Using a trapping radius of $r = 1.5\,\text{mm}$, gives $N \approx 1.6 \times 10^6$ which is much closer to our measured value; implying this is our actual trapping radius.[1] This difference could be caused by the previously mentioned pre-exposure issue decreasing the number of atoms seen, or because we are unable to use the entire trapping area. This smaller trap size could be caused because we are illuminating the MOT mirrors unevenly due to the laser's Gaussian intensity profile, therefore we do not have the ideal six beam MOT in our experiment. Using a top-hat beam shaper could fix this and provide a larger trap.

[1] A trapping radius of $r = 0.1\,\text{mm}$ gives $N \approx 30$ which clearly is not the system we have here.

The FWHM of the Lorentzian distribution is slightly larger than the expected Γ; here we have observed a FWHM of $1.3 \pm 0.01\Gamma$. If this were caused by Doppler broadening, this would suggest that the temperature of the atoms are on the order of $\approx 20\,\text{mK}$. This is significantly hotter that we would expect from atoms in a MOT—we see in Section 6.3 that we measure temperatures closer to $100\,\mu\text{K}$. The Vescent 780 nm DBR laser we are using has a quoted linewidth of $\approx 200\,\text{kHz}$, this addition to the natural linewidth Γ could explain this broadening.

For completeness, in our system the phase lock offset frequency that matches resonance—hence the frequency we will set the imaging laser's frequency to—is $\delta_{\text{imaging}} = 2873.6 + 80\,\text{MHz} = 2953.6\,\text{MHz}$; the additional 80 MHz term is the frequency shift caused by the AOM. Taking into account the AOM shift and the repump to the crossover peak $-46.4\,\text{MHz}$ from resonance, the predicted offset is $\approx 2949\,\text{MHz}$ [49]. This is very close to our measured value with a $\approx 5\,\text{MHz}$ difference. Since the error signal generated appears to blur the $F = 2$ transition lines together, forming an error signal that spans $\approx 90\,\text{MHz}$, this sub Γ discrepancy could be explained by an offset in the repump's lock-point from the cross-over's resonance.

The errors for each data set were found by taking a series of atom number measurements and finding the standard error, with the average of the atom number measurements used as the data point's centre. This is the method we will use to determine our errors in similar measurements. The data points where there are no cold atoms present in the image are dominated by noise on the pixels or fluctuations of the imaging laser beam power. This appears to add an offset to the measurements. Ideally, this offset would be cancelled out by the noise having an equal chance to imitate a 'negative' atom number. However due to the pre-exposure problem described in Section 5.6, this balance is disrupted and we only obtain the noise that results in a positive atom number. Here we can see an offset of $y_0 \approx 2.5 \times 10^5$. This could also indicate that the total atom number we measure is larger than the actual atom number. However, because we crop the absorption image tightly to focus on the cold atom cloud as a way to compensate for the pre-exposure problem, when the cold atom cloud is present in the absorption image the noise that causes this offset no longer dominates the measured value. Therefore, we have decided *not* to subtract this value as this offset may not be present or as large in the presence of actual absorption features. We would also expect, from the pre-exposure problem, to obtain atom numbers which are *lower* than the actual value—further reducing the need for subtracting this offset. The atom numbers measured can then be interpreted similar to a lower bound for the total atom number. Other factors that could account for this offset issue is that we neglected to obtain a 'dark' exposure to subtract from the two exposures used for the absorption imaging. While we expect this effect to be small it may be significant enough to have

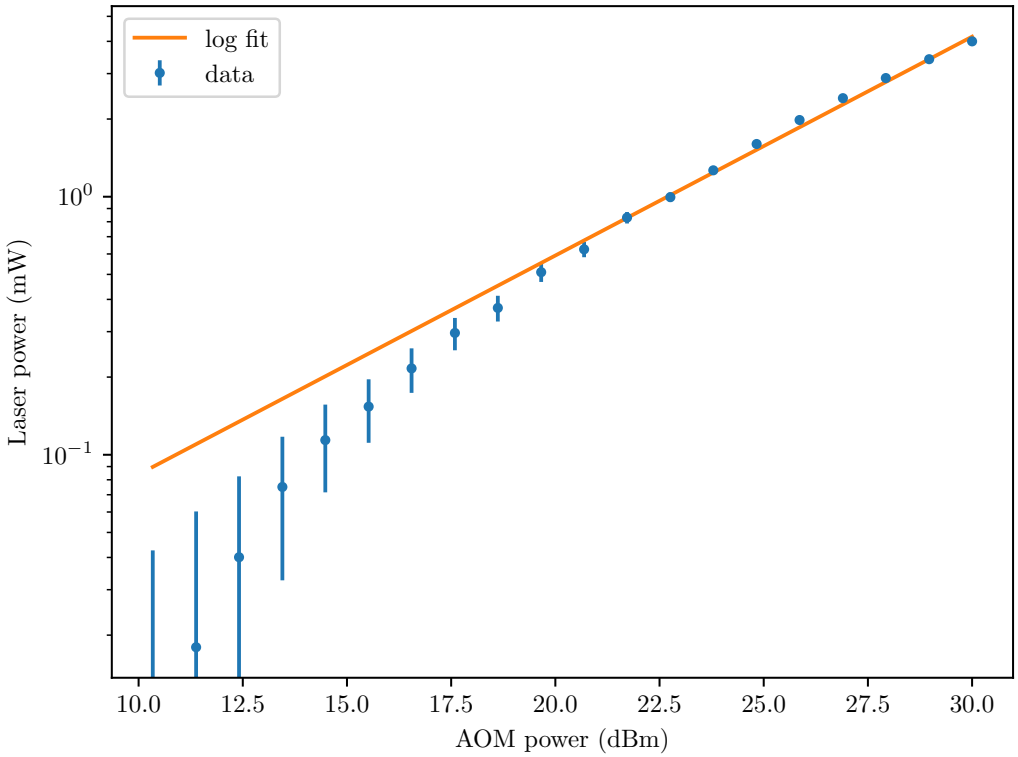

Figure 6.2: Cooling AOM power calibration. An exponential curve has been fitted to this dataset in order to convert between AOM power and laser power.

effected our results. Furthermore, the effect of many beams interacting with the atoms during absorption imaging may not be a negligible effect. Since the absorption cross section, σ_0, is proportional to the scattering rate [49], the atoms are scattering (and hence absorbing) light from the other five beams rather than the one we are using for imaging. This would lead to less absorption detected and therefore less atoms detected. While this does not change the observed offset detected, it may mean that there are many more atoms present then measured.

To finish optimising the absorption imaging system we determine the best laser beam power to use. We do not control the laser beam's power directly; we control it by altering the RF power supplied to the laser beam's corresponding AOM. Therefore, we must first understand the relation between the AOM's RF power and the laser beam's power entering the vacuum chamber. Figure 6.2 shows how the cooling AOM's RF power is related to the cooling laser's power. Here we fit the function

$$\log_{10}\left(\frac{y(x)}{y_{\text{ref}}}\right) = mx + \frac{y_0}{y_{\text{ref}}}, \tag{6.3}$$

where m is a scale constant, y_0 is an offset parameter, and the reference constant

$y_{\text{ref}} = 1\,\text{mW}$. This function is chosen to allow us to convert continuously between AOM power and laser power. From the fit we find $m = 0.085 \pm 0.002\,\text{dBm}^{-1}$, $y_0 = -1.92 \pm 0.06\,\text{mW}$. This was measured by placing a PD in the beam path, varying the AOM's RF power, and measuring the voltage detected for each RF power. We have assumed a linear voltage response to the laser power which was measured by placing a ThorLabs[2] power monitor sensor immediately after the PBS. The scale begins at $\approx 10\,\text{dBm}$ as the PD was unable to detect any difference in laser power below this point. This issue in detection at low powers also leads to the discrepancy in the fit in this regime. During the experiment, this isn't very useful as we control the AOM through its RF power. As a result, following data were taken using the decibel scale and the calibration applied afterwards; this calibration spaces the data points logarithmically. Scaling data by this calibration then hides some information at the lower powers, however nothing of interest tends to occur there. Somewhat often realignment was required to correct for drifts and to maintain reliable optical powers during the course of the experimentation.

The MOT laser beams are delivered to the vacuum chamber optics (Figure 5.1) by a PM fibre from the laser switching system (Figure 5.4) in *orthogonal* linear polarisations. This prevents all of the power from both the cooling and repump lasers reaching the MOT mirrors after passing through the PBS. The $\lambda/2$ waveplate between the fibre and the PBS allows us to control the power ratio of the two MOT beams. This makes it difficult to properly characterise the role each laser plays in the MOT. The lowest powers we found to generate an atom cloud were 3 mW of cooling and 0.3 mW of repump. This was found by carefully rotating the $\lambda/2$ waveplate and monitoring the atom number. Once the maximum atom number was found the power of each beam after reflecting off the PBS was recorded. When more laser power was available we found 4 mW of cooling and 0.5 mW of repump was optimum. These powers are quite less then the maximum power available out the fibres; however, since the cooling and repump beams have orthogonal polarisations, this maximum fibre output power was only available when extinguishing the other beam. This is unsuitable for trapping and hence a balance between the two beams is required. Overall, because we were always working with the maximum available laser power, any attempt to characterise the laser power's effect on atom number indicated that higher powers would result in more atoms trapped. This would of course reach a limit where losses would become dominant, however we never reached that point. For completeness, Figure 6.3 shows how varying the power of the cooling beam affects atom number. After setting the laser powers with the $\lambda/2$ waveplate, the laser powers are controlled by controlling the power to their respective AOMs. In the current laser control system, we do not have analogue control over the

[2] `www.thorlabs.com`

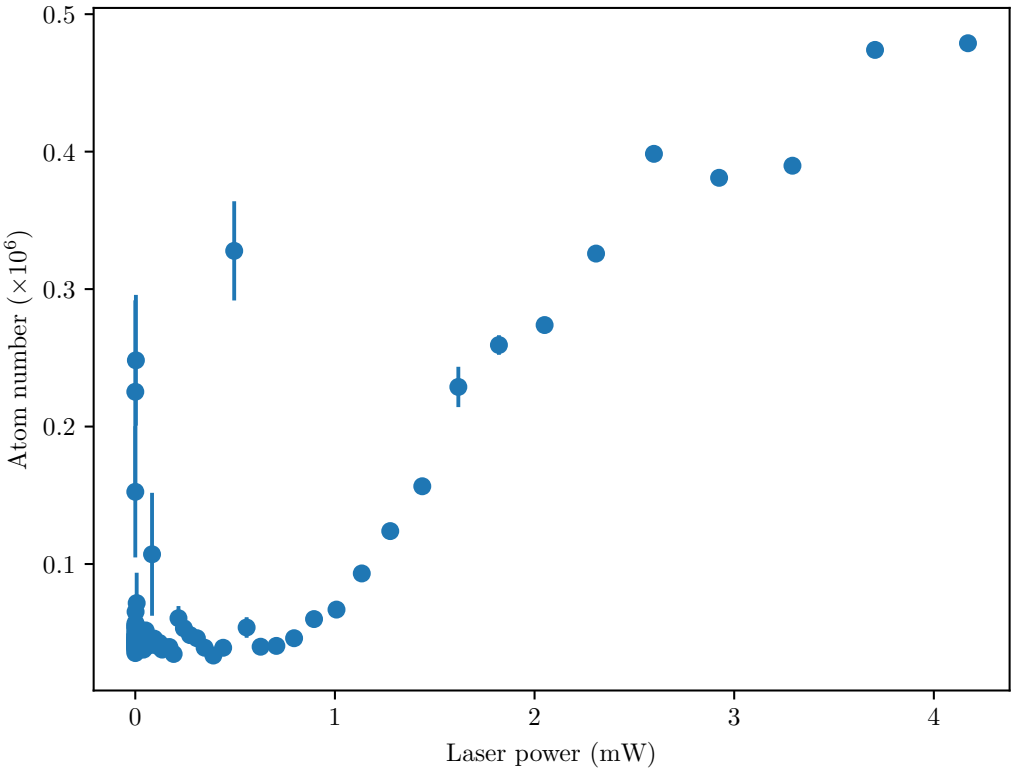

Figure 6.3: Scan of cooling laser power against atom number. The power shown is the cooling AOM's RF power.

repump AOM's power, we only have analogue control of the cooling AOM.

For measurements of atom number, where a series of measurements have been made to find the average value and the standard error, there are data points with large error bars that do not appear to follow the general trend of the data. This can occur when, occasionally, the camera is knocked out of synchronisation with the rest of the experiment. In this scenario the camera misses a TTL trigger from the pulseblaster and hence does not take an image, or the computer does not successfully receive the recorded image from the camera. On subsequent triggers the recorded images become muddled; where the I_0 images are recorded as I images and vice verse. Because of the method we use to record many absorption images in sequence, this affects only that particular data point. Usually this loss of synchronisation occurs after the first few measurements; the erroneous measurements then tend to give vastly different values. This shifts the average value of the collected data points and the increased range of measured values then increases the standard error when compared to measurements that remain synchronised.

We have seen in Equation 4.12 that the MOT force depends on the magnetic field gradient. Figure 6.4 shows how this magnetic field gradient affects the MOT's atom number. From the Gaussian fit, the maximum atom number is found at $13.2 \pm 0.3\,\mathrm{G/cm}$ which corresponds to a coil currents of $\approx 1.3\,\mathrm{A}$ and $\approx 1\,\mathrm{A}$ for the bottom and top coils respectively. We choose a Gaussian here in order to find the centre of this distribution. The measurements of magnetic field gradient were performed by taking measurements of the magnetic field strength with a Hall probe along the central axis of the magnetic field coils. The coils used were exact duplicates of the ones used in the MOT, including the metal support structure. Since it is impossible to measure the magnetic field inside the vacuum chamber, we assume any difference caused by interactions with the structure of the chamber is negligible. The atom numbers were measured separately by using the same coil currents used that generated the measured magnetic field gradients.

We observe larger atom numbers here than generally seen throughout the rest of the data, this is most probably because the data gathered here was done over a shorter amount of time. This prevented the vacuum chamber from heating up and increasing the pressure within the vacuum chamber. The lower pressure decreases the losses from the MOT and therefore increases the steady state population of the MOT. For the longer time-scale experiments, where there a significantly larger number of datapoints, this heating effect becomes significant and the increased pressure decreases the atom number in the MOT.

Figure 6.5 shows the atom number as a function of the time the MOT is active

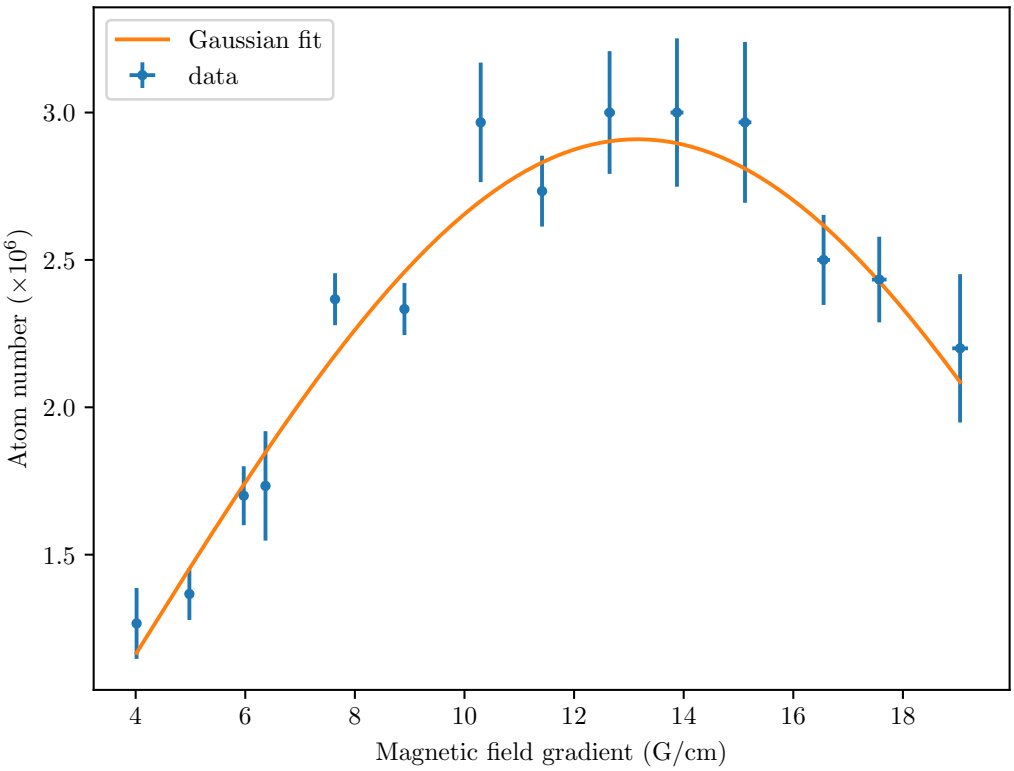

Figure 6.4: Graph showing how the MOT's atom number is related to the magnetic field gradient. The Gaussian fit (Equation 6.2) shows the maximum atom number is at $13.2 \pm 0.31\,\mathrm{G/cm}$.

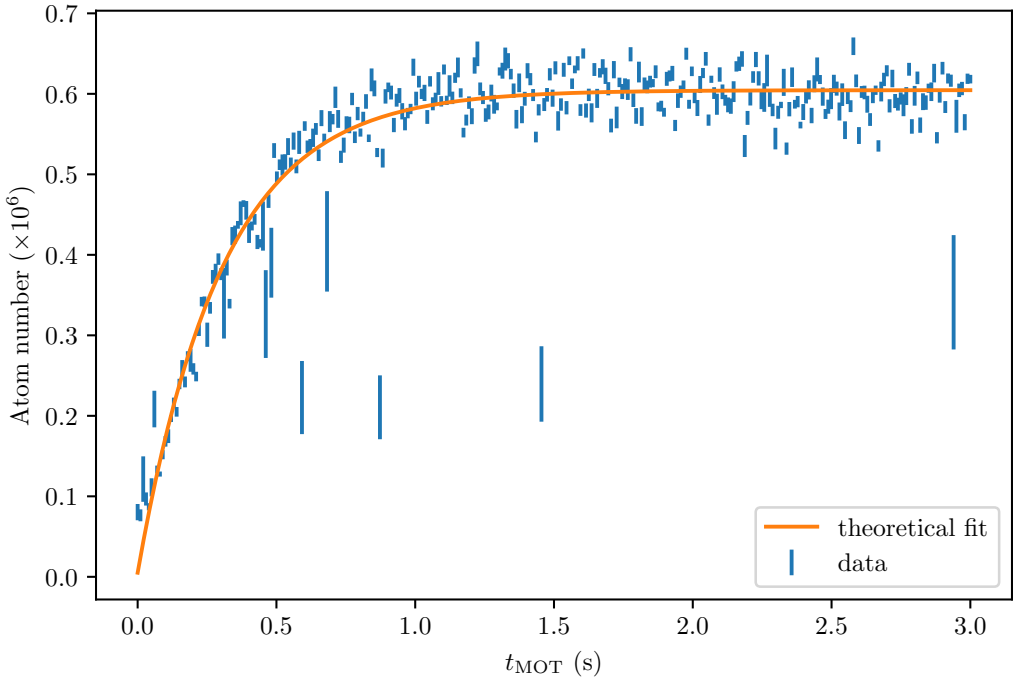

Figure 6.5: Atom number as the time the MOT is active for, t_{MOT}, is varied. Equation 6.4 has been fitted to the data. From the fit the rise time is $\approx 0.3\,\mathrm{s}$.

for, t_{MOT}. From this we can find the loading rate of the MOT. We have fitted a slightly modified version of the theoretical model in Equation 4.18 to the data:

$$N(t) = \frac{R}{\gamma_L}(1 - e^{-\gamma_L(t-t_0)}) + y_0, \tag{6.4}$$

where t_0 is a time offset fitting parameter. Here we find the loading rate of the trap to be $R = 1.96 \pm 0.004 \times 10^6\,\mathrm{s}^{-1}$ and the loss rate $\gamma_L = 3.29 \pm 0.085\,\mathrm{s}^{-1}$. Since with absorption imaging we are unable to view the trap directly as the MOT loads—a feat fluorescence imaging is capable of—this measurement was performed by varying the MOT trapping time, t_{MOT}, and then performing the absorption imaging.

Figure 6.6 shows the time between switching on the Rubidium dispenser and creating a trap with the maximum atom number. This was performed by continually attempting to trap atoms in the MOT then performing the absorption imaging measurement, as a result we were unable to use our usual method of obtaining errors. Before the dispensers have been switched on, we observe noisy measurements where the measured atom number is dominated by noise on the pixels and fluctuations in laser power. After the dispensers have been turned on, there is a quick rise in the measured atom numbers. Here the Rubidium vapour

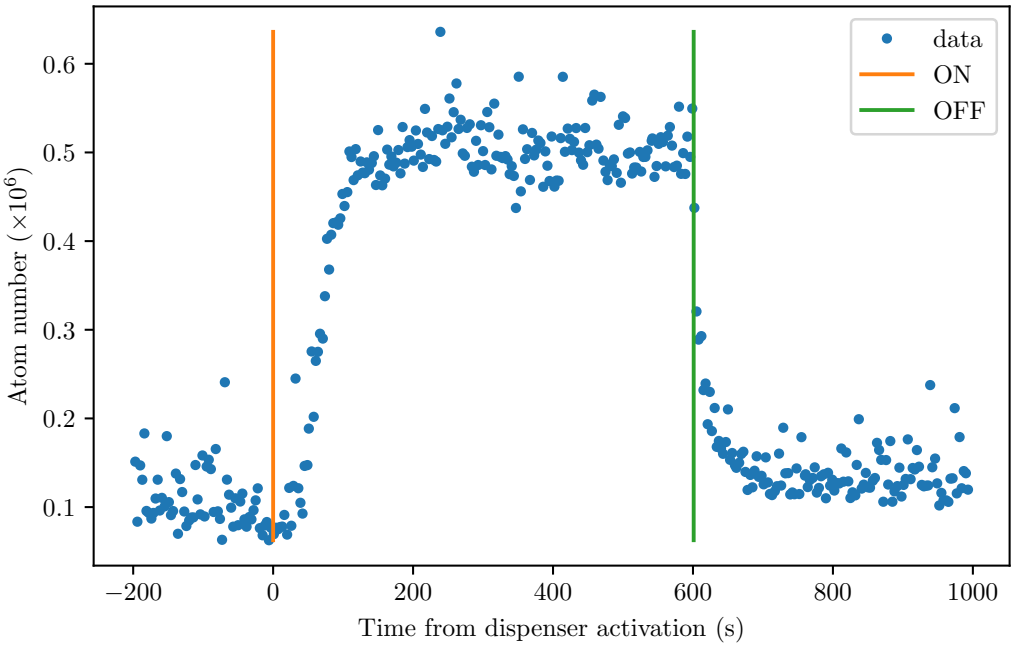

Figure 6.6: Figure showing time required between dispenser activation and saturation. The vertical lines shows the times when the dispensers were turned on and off.

begins entering the MOT's trapping region and we begin detecting the cold atom cloud. As more vapour is added to the chamber and more vapour is able to enter the trapping volume, the atom number rises as there are more Rubidium atoms available to trap. The atom number then reaches a stable value as the chamber reaches an equilibrium between the rate the dispensers are releasing atoms to the environment and the rate the ion pump is removing Rubidium from the chamber. The number of atoms entering the trapping area during this event appears to follow a sigmoidal function, beginning slowly then after a short time quickly increasing the atom number before slowing down again closer to the equilibrium. The slow start could be explained by both the dispensers needing a short time to heat up enough to properly emit atoms and it can take some time before the atoms are able to travel from the dispensers to the area within the MOT mirrors. Once the dispensers are turned off, this equilibrium is disturbed as the vapour is pumped away by the ion pump. This leaves fewer and fewer atoms available for the MOT to trap which decreases the measured atom number. Because the ion pump relies on atoms entering it through ballistic collisions to be pumped out of the environment, some atoms remain in the chamber. Over time these atoms eventually make their way into the pump however on short time scales we are still able to trap some of them. This can be seen here as the measurements reach a new stable atom number measurement that is slightly

larger than what was measured before the dispensers were turned on.

We can see that the chamber becomes saturated with Rubidium vapour at $\approx 180\,\mathrm{s}$. The time for the chamber to pump away the Rubidium vapour is $\approx 100\,\mathrm{s}$. Because of this we make sure to leave the dispensers on for 3 minutes before beginning any experiments involving the MOT.

6.2 Temperature measurement

In order to detect the cold atom ensemble after it has fallen to the bottom of the chamber (the detection area), we require that the atoms within it are distinguishable from the background vapour. For this to be the case, the density of the cold atoms must be higher than the background vapour's density by an appreciable amount in order to obtain a reasonable SNR. Since the cold atom cloud's density after some TOF is related to its temperature (Equation 4.28), we can find a maximum temperature requirement for the cold atom cloud to be detected at the bottom of the chamber.

The density of the background atoms is

$$\rho_{\mathrm{b}} = \frac{P}{k_B T_{\mathrm{b}}}, \tag{6.5}$$

where P is the pressure of Rubidium in the vacuum chamber, k_B is Boltzmann's constant, and $T_{\mathrm{b}} \approx 300\,\mathrm{K}$ is the temperature of the background atoms. The radius of the cold atom cloud, $\sigma(t)$, is described by Equation 4.28; assuming the cloud is spherical, its density is

$$\rho_{\mathrm{cloud}} = \frac{N}{\frac{4}{3}\pi\sigma^3(t)}, \tag{6.6}$$

where N is the cloud's atom number and t is the expansion time of the cloud.

The SNR is found by calculating the ratio between the number of atom contributing to the signal, and the number of atoms contributing towards the noise. Assuming the cold atom cloud is cold enough that its transition linewidth is not Doppler broadened, the SNR is

$$\mathrm{SNR} = \frac{\rho_{\mathrm{cloud}}}{\rho_{\mathrm{b}} \frac{\Gamma}{\Delta\omega_{\mathrm{D}}}/2}, \tag{6.7}$$

where Γ is the transition linewidth, and $\Delta\omega_{\mathrm{D}} \approx 0.5\,\mathrm{GHz}$ is the Doppler broadened transition linewidth. The factor of 2 arises from the background atoms having

equal populations in its ground states, and the cold atoms begin prepared into one state. For the atom cloud to be detectable, for a certain SNR, its density must be larger than this portion of background atoms:

$$\rho_{\text{cloud}} > \rho_{\text{b}} \frac{\Gamma}{\Delta\omega_{\text{D}}} \frac{\text{SNR}}{2}. \tag{6.8}$$

Rearranging this gives the cold atom's maximum temperature to be

$$T < m \frac{\left[2N / \left(\frac{4}{3}\pi \text{SNR} \rho_{\text{b}} \frac{\Gamma}{\Delta\omega_{\text{D}}}\right)\right]^{2/3} - \sigma^2(0)}{k_B t^2}. \tag{6.9}$$

For a SNR = 2, assuming a conservative $N = 1 \times 10^6$ atoms, a maximum chamber pressure $P = 1 \times 10^{-8}$ mbar $= 1 \times 10^{-6}$ Pa, an initial radius $\sigma(0) = 0.25$ mm, and a free fall time $t = 120$ ms, a minimum temperature of $T < 13\,\mu$K is required. Considering similar experiments are able to reach temperatures of $\lesssim 5\,\mu$K [33, 91, 119], temperatures $< 13\,\mu$K are certainly feasible.

6.2.1 Camera calibration

In Section 4.7.3 we described a TOF method for measuring the temperature of the cold atom cloud. This involves taking measurements of the size of the cloud during its expansion. While the absorption imaging system is capable of making these measurements, we must first calibrate the imaging optics so we know how much distance each pixel represents. We can then take images of the cold atom cloud, measuring the size of the cloud at each time, to find the temperature of the cloud.

The lens system in Figure 5.1 consists of the Ximea MQ013RG-E2 camera (which has pixels of dimensions $5.3\,\mu\text{m} \times 5.3\,\mu\text{m}$), a 45 mm lens, and a 100 mm lens; with 145 mm spacing between the two lenses, and the camera is placed 45 mm away from the smaller lens so that it is at the lens' focus. By imaging an object of known size, we can calibrate the scale of the camera's pixels. For this we use a Edmund Optics[3] 1951 USAF test target which has features with standardised dimensions. This target is placed 100 mm away from the 100 mm lens in the imaging system so that the target is at the focal point of the lens. Figure 6.7 shows the image of the test target taken with this imaging system.

From this image of the test target, we can measure how many pixels the features span. We use the group 2 element 6 line series for this which has line spacings of 0.14 mm. Figure 6.8 shows the horizontal and vertical pixel profiles of this

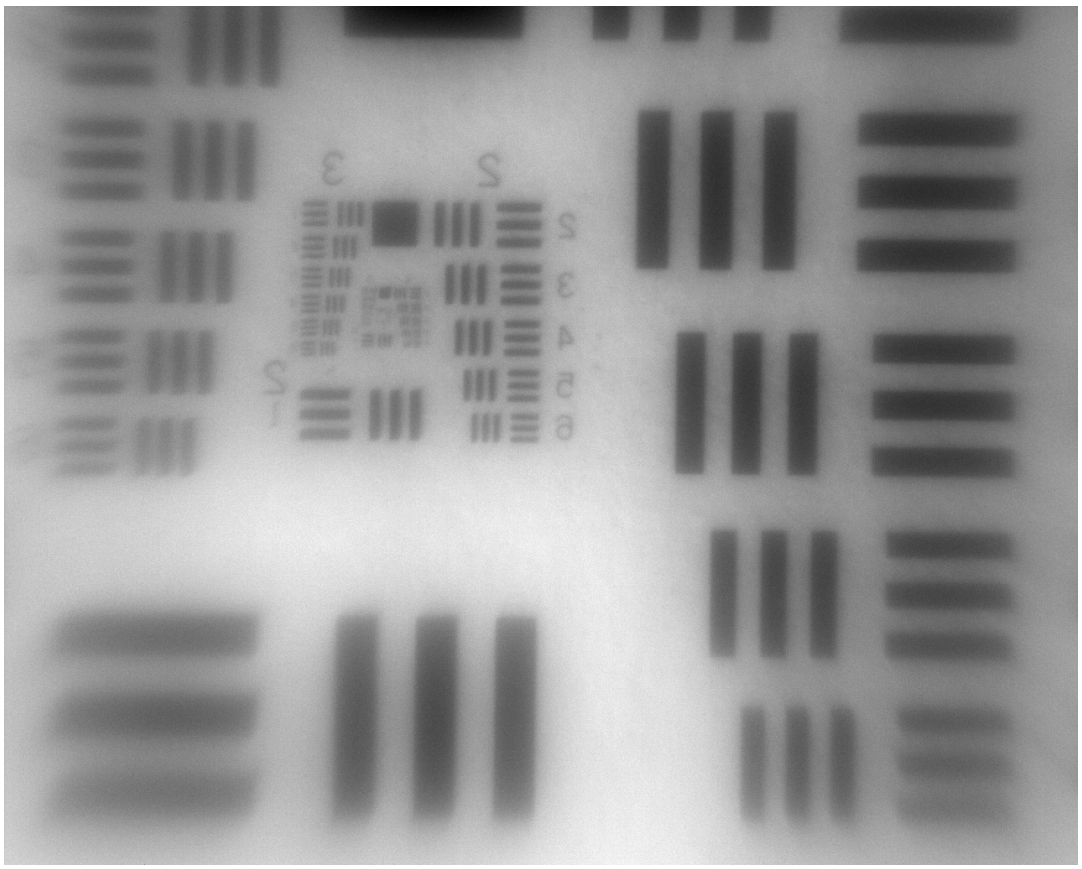

Figure 6.7: Figure showing image of Edmund Optics 1951 USAF test target taken with Ximea MQ013RG-E2 through a 45 mm and 100 mm lens system. This image appears to be inverted along its horizontal axis; to improve contrast and remove shadows the test target was imaged from behind. It can be seen that the focus deteriorates towards the edges of the image; the centre of the image was prioritised for sharpness.

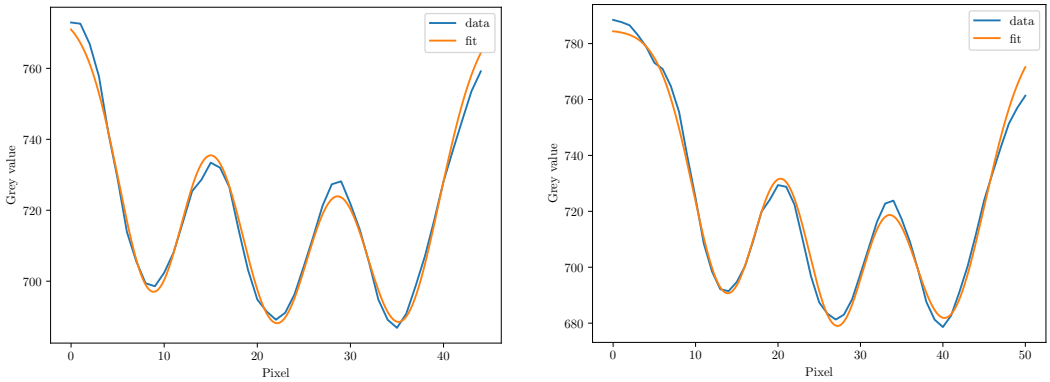

(a) Horizontal pixel profile.

(b) Vertical pixel profile.

Figure 6.8: Figure showing pixel calibration of the absorption imaging system. Data is gathered from the 'group 2, element 6' lines of Figure 6.7. The blue line is the average pixel data of a series of slices of the line widths and spacings. The orange line is a triple Gaussian fit (Equation 6.10). Lower grey values correspond to darker points of the image, and larger grey values correspond to brighter points on the image. From the fits we find the three lines to be 13.2 ± 0.1 pixels apart for both the horizontal and vertical profiles.

line series. These data were gathered by taking an average of pixel slices across the lines' lengths from Figure 6.7. To find the line spacing, we have fitted a triple Gaussian distribution to the datasets:

$$\begin{aligned} y(x) = A_1 \exp\left(\frac{-(x - x_0 - \Delta x)^2}{2\sigma_1^2}\right) \\ + A_2 \exp\left(\frac{-(x - x_0)^2}{2\sigma_2^2}\right) \\ + A_3 \exp\left(\frac{-(x - x_0 + \Delta x)^2}{2\sigma_3^2}\right) + y_0, \end{aligned} \tag{6.10}$$

where $A_{1,2,3}$ is the amplitude for the three single Gaussian distributions, similarly $\sigma_{1,2,3}$ are the standard deviations for the individual Gaussian distributions, and Δx is the separation between each Gaussian peak. Once again, this distribution is chosen as we are only interested in the separation between the lines of the image. From this fit, we find $\Delta x = 13.2 \pm 0.1$ pixels for both the horizontal and vertical lines. This gives the distance each pixel represents to be $10.6 \pm 0.1\,\mu$m along both axes. From the lenses used we would expect that each pixel represents $5.3\,\mu\text{m} \times 100/45 = 11.8\,\mu$m. This small discrepancy could be from the lenses possibly not being positioned exactly 145 mm which would alter the magnification

[3] `www.edmundoptics.co.uk`

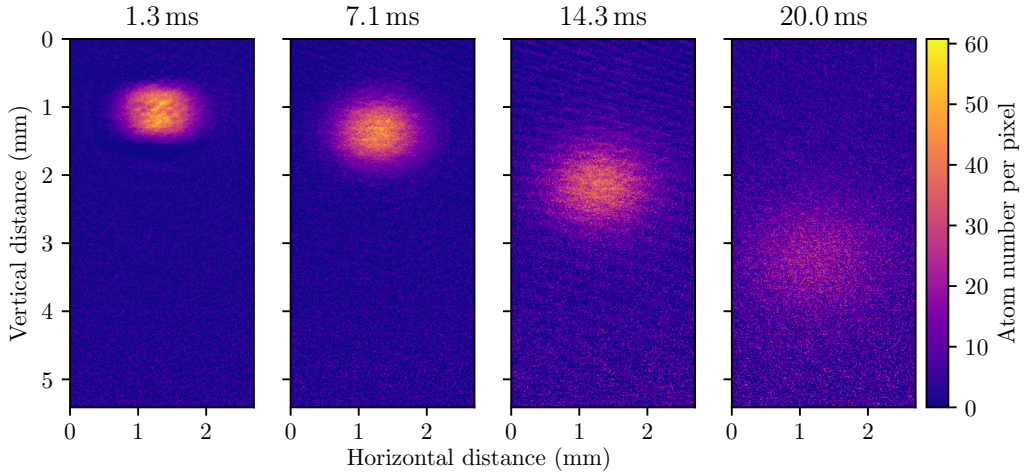

Figure 6.9: Absorption images of the atom cloud at varying TOFs. The TOFs are indicated above the image. The sample of atoms in these images had a temperature of $\approx 6.5\,\mu$K.

slightly. We confirmed the validity of this calibration by measuring the MOT mirrors in the vacuum chamber as they are of known size, 10 mm × 10 mm, and finding the mirrors to be correctly sized on the images when using this calibration. Using this calibration of the pixel size, accurate measurements of the cold atom cloud's size can be achieved. Since the atoms fall over a relatively short distance, we will assume this calibration is valid even as the atoms move out of the focal plane of the lens system.

6.2.2 Time-of-flight measurements

Figure 6.9 shows absorption images of the atom cloud expanding—and falling due to gravity—on a side MOT mirror. This image series was collected by performing the sequence described in Section 5.7 multiple times and varying the TOF, t_{TOF}, for each sequence. The atom clouds in this series of images were cooled with the molasses stage after being prepared in the MOT. From these images, it can be seen that as the cloud expands it starts to become too diffuse for the absorption imaging to detect it clearly.

We can see in the 1.3 ms image of Figure 6.9 (and in Figure 5.11), the shape of the cold atom cloud does not follow an ideal Gaussian distribution. However, as described in Section 4.7.3, the velocity distribution still follows a Gaussian distribution. As the cloud expands, the shape of the cloud becomes dominated by the motion of the atoms and hence the Gaussian velocity distribution begins

to shape the cloud. Therefore, in the larger t regime—which provides us with the information to find the cloud's temperature—the shape of the cloud follows a Gaussian distribution more closely. This can be seen clearer in the $\geq 7.1\,\text{ms}$ images in Figure 6.9. While trapping, due to the magnetic field having different strengths along the MOT's 'major' axis compared to the other axes, the atom cloud is not symmetrical or Gaussian.

To find the rms radius of the atom cloud, we fit the 2-dimensional Gaussian as we would expect the cloud to follow a Gaussian distribution:

$$z(x,y) = A\exp\left(-\frac{(x-x_0)^2}{2\sigma_x^2} - \frac{(y-y_0)^2}{2\sigma_y^2}\right) + z_0, \tag{6.11}$$

where x_0 and y_0 are the coordinates of the centre of the cloud, z_0 is an offset, and $\sigma_{x,y}$ is the rms radius of the cloud along its respective axis. From this fit we can simultaneously obtain the radii of both the cloud's dimensions, allowing us to find both the vertical and horizontal temperatures. We assume that both of the horizontal temperatures—for Figure 6.9 this includes the direction facing towards the camera and the direction horizontal across the page—are equal due to any cooling forces on the atoms being equal in both these directions. We then use a modified version of Equation 4.28 to find the temperature:

$$\sigma^2(t) = \begin{cases} \sigma^2(0) + k_B T(t+t_0)^2/m & t+t_0 \geq 0 \\ \sigma^2(0) & t+t_0 < 0 \end{cases} \tag{6.12}$$

where t_0 is a time offset. This time offset allows us to account for us being unable to take measurements at TOFs less than the minimum time for an absorption image to be taken—this is mostly governed by the TNE interval. This is seen during the experiment by the atom cloud remaining static until TOFs greater than this minimum time are reached; this is visible in Figure 6.9 by the first image having a TOF of 1.3 ms. We fix the $t+t_0 < 0$ value to be the initial radius to prevent unrealistic behaviours of the parabola which may occur more often with this time offset adjustment. This is done with the experiment primarily to allow for a variable time delay for the initial image; this is mainly dependent on the LC WP's rise time changing when recalibrating. This allowed us to more easily create an automated data collection procedure. Since the temperature measurement is dependent on the rate at which the cloud expands, the time offset does not affect the temperature measurement.

Figure 6.10 shows two examples of TOF measurements of atom clouds with different temperatures. Equation 6.12 has been fitted to each data set in order to measure the temperature. For the data with the hotter atom cloud (the MOT series), we can see that the data points begin to level off and the fit deviates. This is because at these later times the hot cloud has already dispersed too much

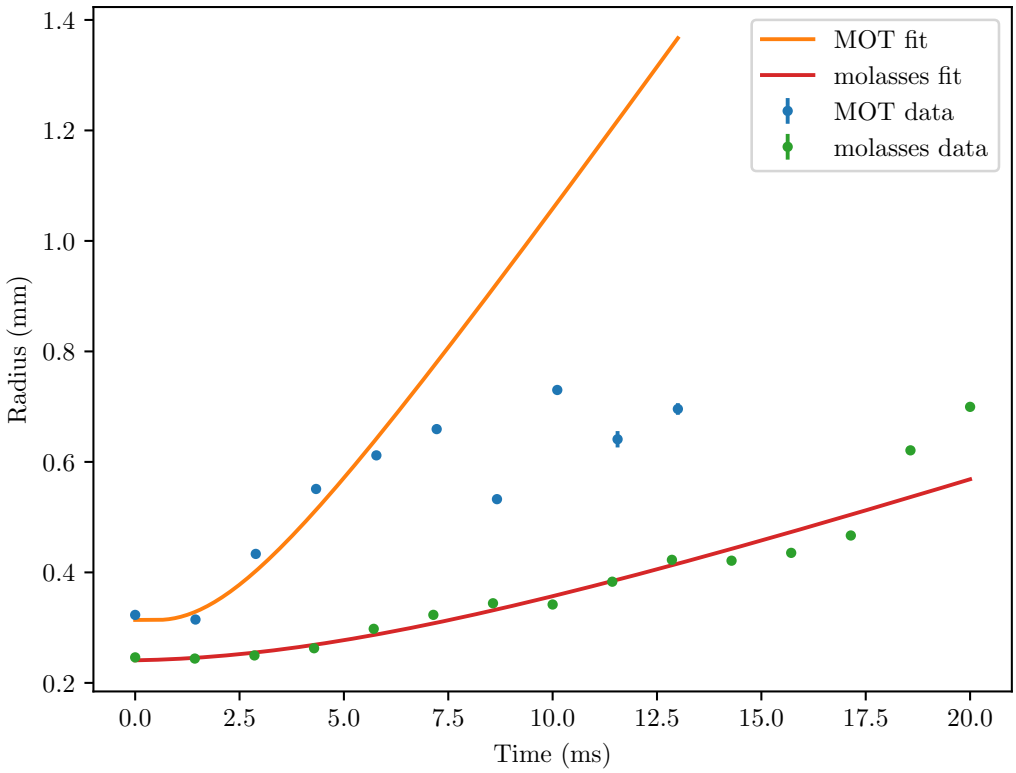

Figure 6.10: Examples of typical TOF measurements of the cold atom cloud before the molasses cooling stage (MOT series) and after the molasses cooling stage (molasses series). From the fits, the MOT series has a temperature of $T = 116.2 \pm 38.8\,\mu$K, and the molasses series has a temperature of $T = 6.5 \pm 1.2\,\mu$K.

to be detectable on the absorption images—this can be seen in the 20 ms image from Figure 6.9. This can also be seen as clouds of radius of ≈ 0.7 mm are the maximum size we are able to measure; hotter atoms would reach this size quicker than colder clouds. In this scenario the Gaussian fit tends to start fitting to noise. The errors of the radii are derived from the covariance of the fitting parameters of the Gaussian fit; however, because Gaussians are well known for being able to fit well to most distributions, the Gaussian is also able to fit well to noise. This rarely occurs when an atom cloud is present as the absorption signal from the atom cloud is larger than any noise signal. In the cases where the Gaussian does preferentially fit to noise, because we take many TOF data points to create a picture of how the cloud expands, this erroneous radius measurement makes little contribution to the final temperature measurement. It is worth noting that these datapoints, while unphysical, are still being used in the fitting algorithm as when we are automating data collection it is difficult to automatically discern which data is erroneous or not. For a colder atom cloud, the Gaussian fit is able to track the expansion to longer time scales. While the colder clouds will eventually become too diffuse to detect on the absorption image, this tends to happen beyond or at the longest TOF time period we use for measurements. Due to this fitting behaviour, measurements of higher temperature atom clouds tend to have a greater uncertainty than measurements of colder atom clouds for the same set of TOFs. For measurements performed later in this chapter (Section 6.3), we perform the measurements with consistent TOFs where this behaviour presents itself in our measurements of hotter clouds. Since the atom cloud diffuses at the same size regardless of how far the cloud has fallen, we can rule out this diffusion occurring due to the cloud falling out of the focal plane of the imaging system.

We focus mainly on the vertical temperature of the atom cloud as it is the temperature that most effects the number of atoms detected at the bottom of the chamber. In most cases, we find that the vertical and horizontal temperatures are similar to each other.

6.3 Molasses stage characterisation

During the molasses stage, as seen in Figure 5.12, the cooling laser beam's power is ramped down from the power used for the MOT to a chosen power and its frequency is further detuned from resonance. After this period where the cooling beam's power is decreased, it maintains that lower power for a small period while the detuning remains constant. The repump laser's frequency is unchanged and its power remains on during the cooling's ramp period, after which the

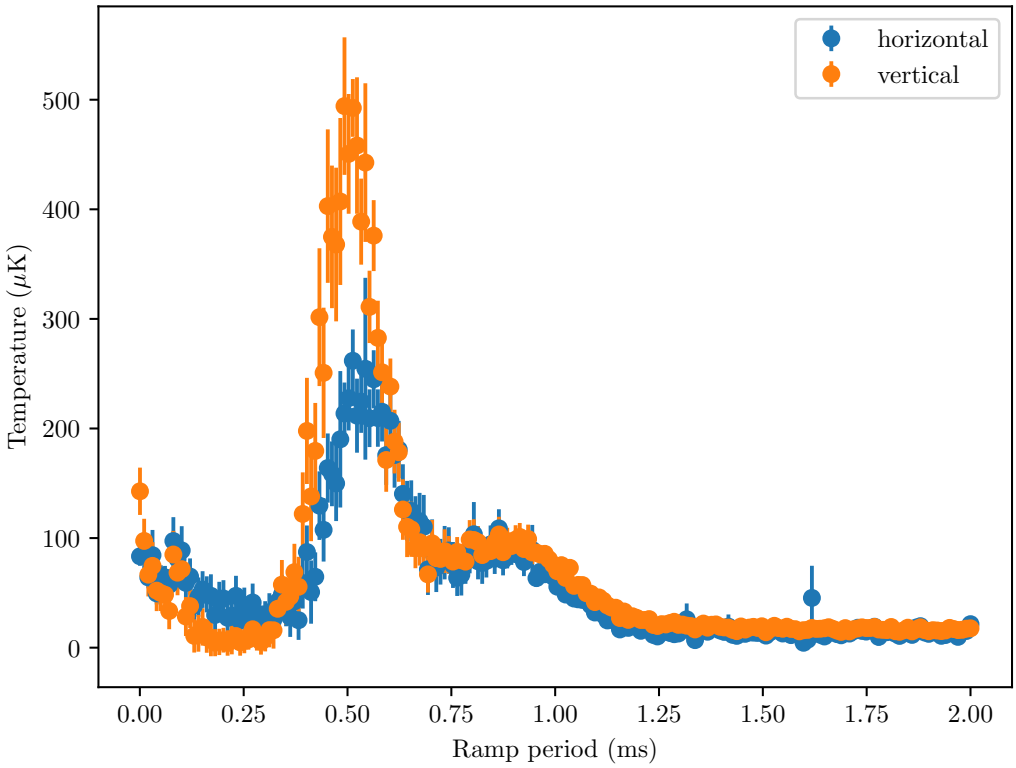

Figure 6.11: Temperature of the cold atom cloud as the molasses ramp period is changed. It is worth noting that this is not the temperature of the atoms at each point of the ramp.

repump laser beam's power is shut off. This sequence has several variables we can control and vary to characterise their effect on the atom cloud's temperature and atom number: the ramp period, the cooling laser beam's final power after the ramp, the cooling laser's frequency during the molasses stage, and the period the cooling beam remains at the lower power level after the ramp for. Before the molasses stage, typical temperatures of the atom cloud are $\approx 150\,\mu$K; after the molasses cooling stage, temperatures of the atom cloud tend to be $\approx 7\,\mu$K with the lowest temperatures measured to be $\approx 5\,\mu$K. Similar to the atom number measurements for the MOT characterisation, temperature measurements are taken in a random order and multiple temperature measurements are used to find an average value for each data point. From these multiple measurements, both the standard error and the error from the TOF fitting are used to find the error of each data point.

Figure 6.11 shows how the atom cloud's temperature is dependent on the ramp period of the molasses stage. We can see here that temperatures in both the horizontal and vertical directions tend to be similar to each other. At ramp

periods $\lesssim 0.3\,\text{ms}$, the atoms appear to undergo rapid cooling. However, at slightly longer ramp periods the atoms experience a large heating effect. This heating effect heats the cold atoms to much higher temperatures than the atoms are cooled to within the MOT. A possible explanation for this effect is that if the light shift is decreased too rapidly,[4] the m_J state the atom is preferentially pumped into has a smaller energy difference from the upper J level than when the atom was pumped into the initial m_J state. For example, let us say the atom begins in the $m_J = +1/2$ state at time t_0, the atom then moves into an area of σ^- polarisation. Here the atom will be preferentially pumped into the $m_J = -1/2$ state. Usually this would cool the atoms; however, if the light shift has decreased such that the $m_J = -1/2$ state is at a higher energy level than the $m_J = +1/2$ state was at t_0 then the energy lost through spontaneous emission will be less than the energy that was absorbed. This means that the atom will continue to radiate less energy than it absorbs, therefore heating the atom. However, this would appear to contradict the cooling effect seen at short periods as this heating effect should be present at these very short periods. We would usually expect to see the decay of the magnetic field to be a limiting factor in the rate we can cool the atoms during the molasses stage. This would be indicated by an initial constant temperature as the atoms still mainly experience the MOT forces rather than the sub-Doppler Sisyphus cooling effect; however we do not see this behaviour here. This heating effect appears to become less dominant at periods of $\gtrsim 0.75\,\text{ms}$. Here the effect of the molasses stage appears to not cool the atoms below the temperature the MOT cools the cloud to, this MOT temperature can be seen at the 0 ms ramp period. At ramp periods $\gtrsim 1\,\text{ms}$, the Sisyphus cooling effect becomes dominant and the atoms begin to reach minimum temperatures at $\approx 1.5\,\text{ms}$ ramp periods; longer periods have little or no further cooling effect.

Figure 6.12 shows this molasses ramp period's effect on the cloud's total atom number. Because we are not trapping any more atoms from the background atmosphere during the molasses stage—only further cooling the ones we have already trapped and cooled with the MOT—this and subsequent atom number graphs can be seen to describe how many atoms are lost during the molasses stage. Here we can see a general trend where the atom loss reaches a minimum at a ramp period of $\approx 3\,\text{ms}$. Shorter ramp periods lose atoms likely due to only a small velocity selection being able to be successfully cooled in this time. It is possible that this is not detected during the temperature measurement because these hotter atoms would have dispersed into the background during these measurements and therefore not contributed to the shape of the atom

[4]The light shift is a proportional to the square of the Rabi frequency; and the Rabi frequency is proportional to the magnitude of the electric field. i.e. the light shift is proportional to the square of the magnitude of the electric field.

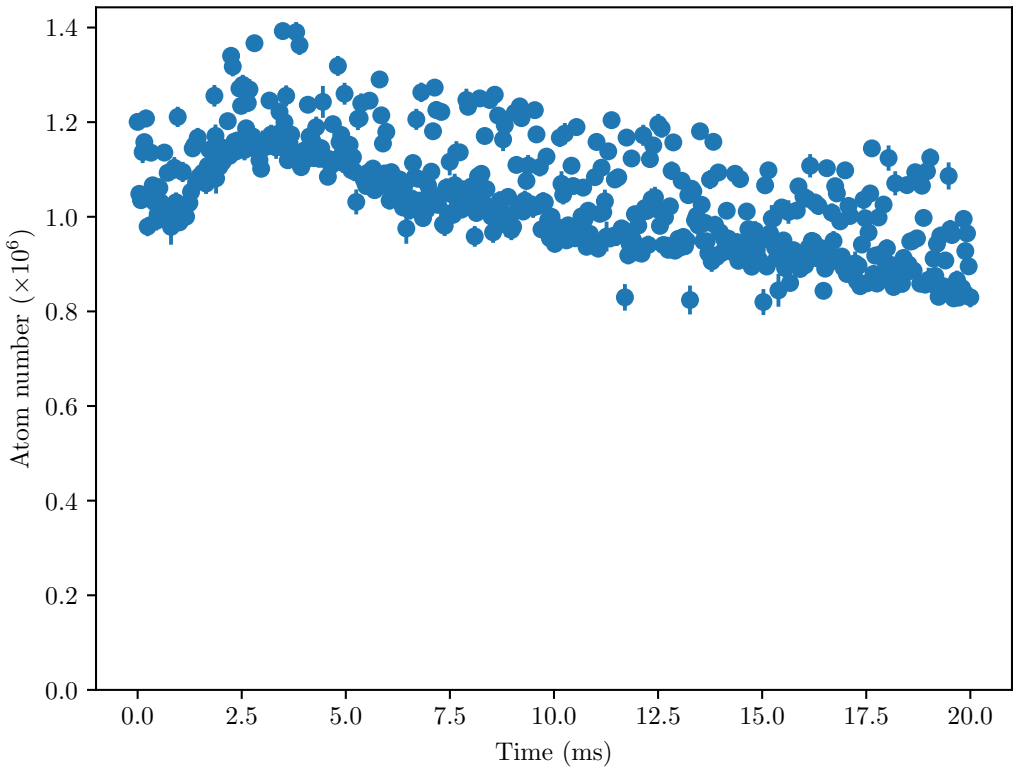

Figure 6.12: Total atom number of the cold atom cloud as the molasses ramp period is varied. It is worth noting that this is not the cloud's atom number at each point of the ramp.

cloud. At the longer time periods, the usual loss rates of the MOT due to collisions with the background atoms (and with other atoms within the cloud) act to remove atoms from the cloud. Because we find the coldest and most numerous atom cloud with a ramp period of 3 ms, this is the ramp period we use during the experiment.

There is also a large amount of noise present in Figure 6.12. It is unclear what causes this instability as we would expect the data points of the noise to also have much larger error bars—as seen in previous atom number measurements. This noise doesn't appear to be randomly distributed and lies within a consistent boundary. These two factors could indicate that the 'noisy' data points are not caused from instabilities in the experiment and could be replicated. Repeat measurements of this data set returned results with similar distributions of data. This apparent noise effect may be caused by a long period of instability within the experiment from an unknown source. It is unlikely that an atom loss mechanism has such strong frequency dependence.

Figure 6.13 shows how the temperature of the atom cloud changes as the final power of the cooling beam's power ramp is varied. The laser's power is ramped linearly from the power used for the MOT to the power indicated on the graph. We can see more clearly that the horizontal temperatures are consistently lower than the vertical temperatures, however they both follow the same general trend. Here we see that as the power is decreased, we have a mostly linear trend towards a minimum temperature at $\approx 0.5\,\mathrm{mW}$. This agrees with the theoretical prediction in Equation 4.15. As the power is decreased, the energy difference between the m_J states is decreased and the atom radiates less energy every emission event, allowing the atom to cool down further. Further reductions in the laser power are less effective at cooling and lead to an increase in temperature; this could be a similar effect that is seen when the ramp period is too small. A smaller ramp power imitates a faster ramp as the gradient of the ramp can be the same. This characteristic temperature behaviour for a change in laser power can also be seen in Lett et al. [92].

Figure 6.14 shows the dependence of the cloud's total atom number on the power of the laser at the end of the ramp. Here we see the same large 'noisy' distribution seen in Figure 6.12; this is also most likely due to the same effect. Because changing the ramp powers can imitate a different ramp period, if this effect is not due to instability within the system, we would also expect to observe it here. Also by this logic, it is subject to the same atom loss mechanisms as the ramp period. We see in Figure 6.11, that there is a significantly larger range of temperatures when compared to Figure 6.13. This could explain why the changing ramp power does not appear to affect the total atom number, as we are sampling a very small section of the ramp periods. From these results, we

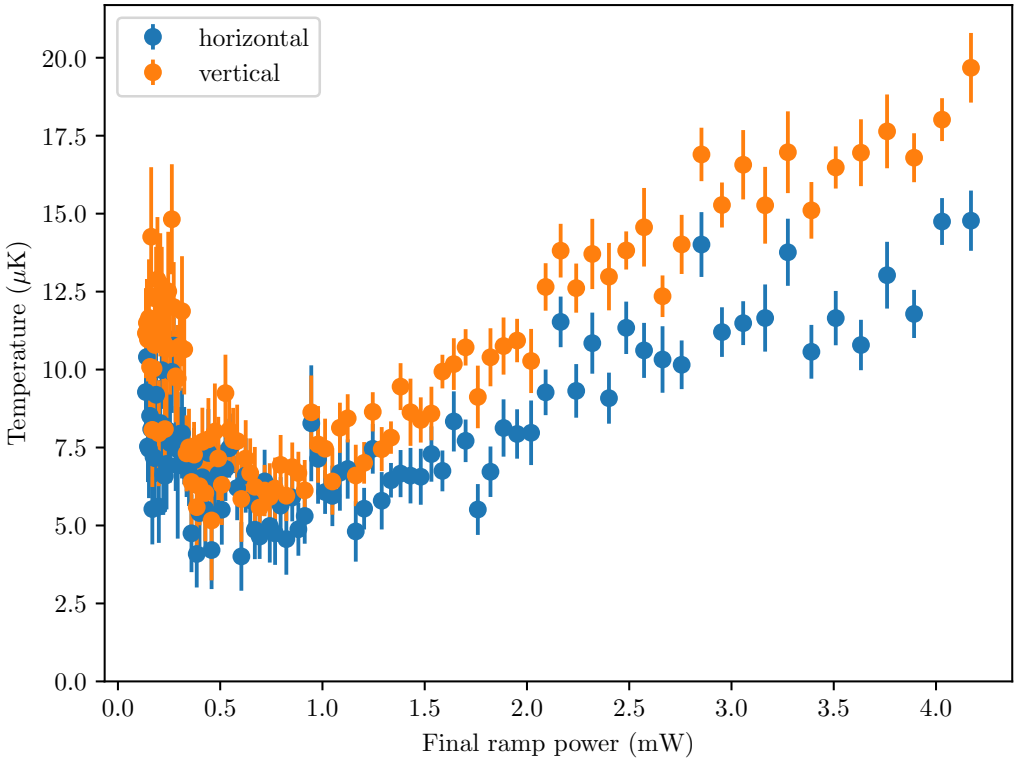

Figure 6.13: Temperature of the cloud as the cooling beam's power ramp end point is varied during the molasses stage.

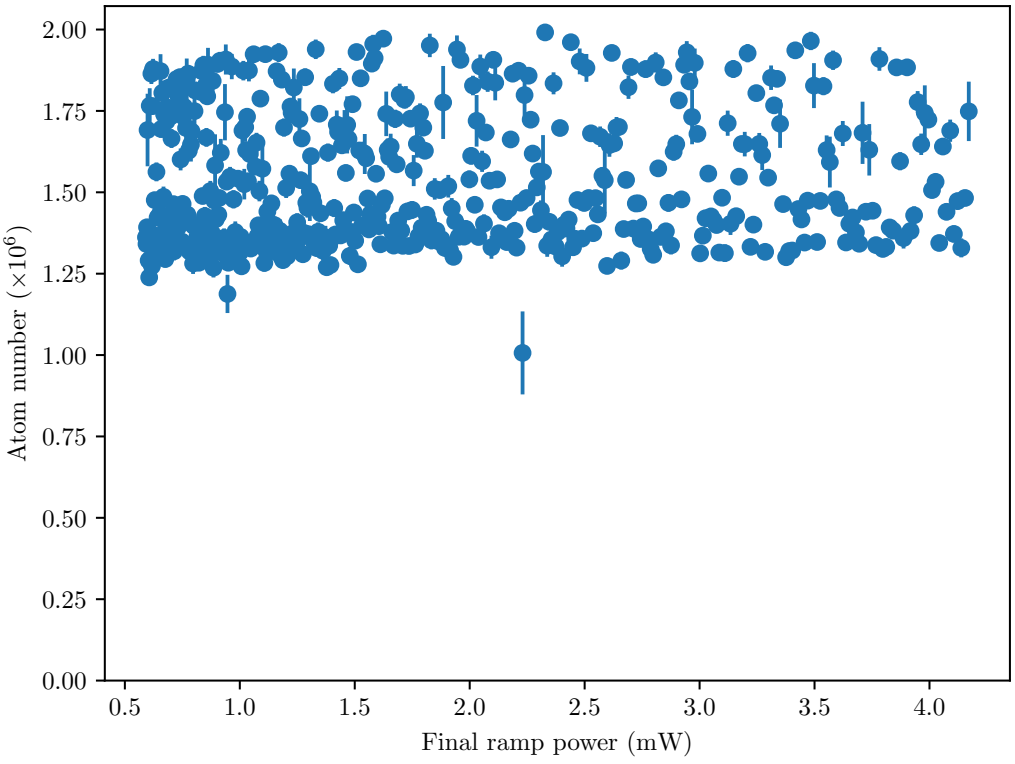

Figure 6.14: Atom number of the cloud as the cooling beam's power ramp end point is varied during the molasses stage.

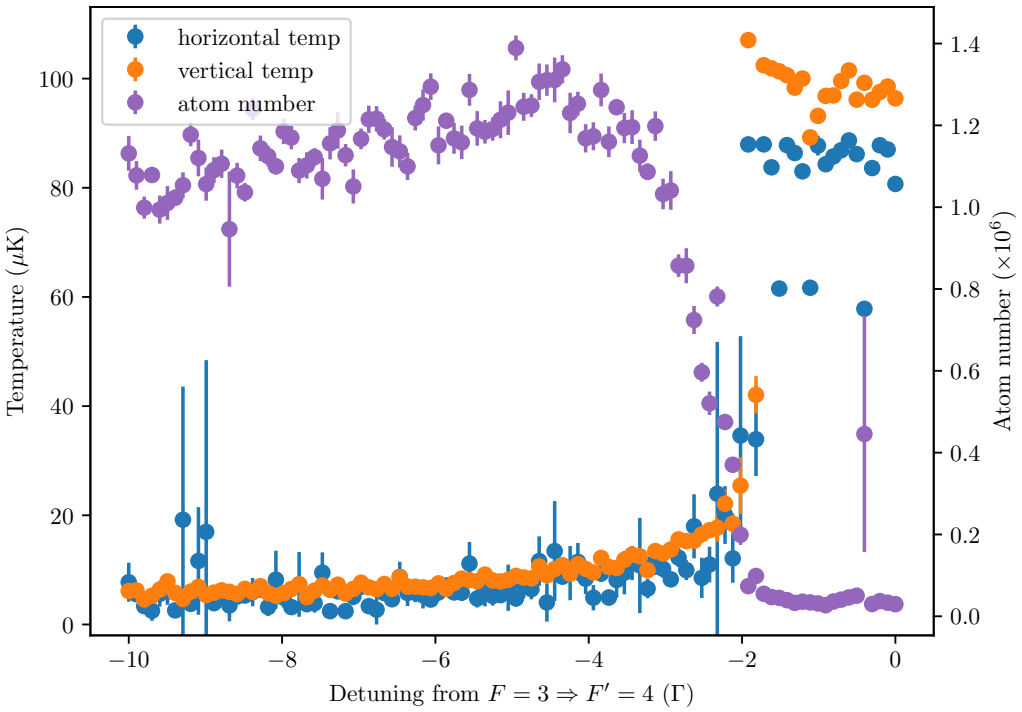

Figure 6.15: Graph showing how the temperature and atom number of the cloud varies as the cooling beam detuning is varied during the molasses stage. The temperature is represented by the blue and orange series and the left vertical axis. The atom number is described by the purple series and the right vertical axis.

find the optimal power the ramp finishes at to be 0.72 mW.

Figure 6.15 shows how the cooling laser's frequency effects the atom cloud's temperature. The cooling laser's frequency is immediately stepped from the frequency used during the MOT stage to the frequency shown on the graph once we begin the molasses stage. At detunings closer to resonance than $-2\,\Gamma$, the temperatures appear not be changed much (or at all) after the MOT. This is expected as the Sisyphus effect is only dominant with large red detunings. At $\approx -2\,\Gamma$ there is a very sharp step to significantly lower temperatures, where larger red detunings are able to cool atoms to temperatures $< 10\,\mu$K. We see in Figure 6.1 that we can no longer trap atoms in the MOT when the cooling laser has a frequency detuning $< -2\,\Gamma$. We can see in Equation 4.4, that the scattering force decreases as the detuning is increased. Once the scattering force—which cools the atoms to Doppler limited temperatures—is no longer dominant, the sub-Doppler mechanisms (e.g. the Sisyphus cooling effect) are able to be the dominant mechanism in cooling the atoms. The energy lost by the

atoms in each absorption-emission event in the Sisyphus effect is proportional to the light shift the atom experiences; this light shift is inversely proportional to the magnitude of the detuning [41]. This matches the trend of our results at larger red detunings beyond $\approx -2\,\Gamma$. This behaviour can also be seen in Lett et al. [92]. We can see that the effect of changing detuning is very similar to that of changing laser power as they both effect the magnitude of the light shift.

Figure 6.15 also shows how the cooling laser's frequency affects the total atom number of the cloud. Here we observe a similar shape to the temperature measurements, where there is a sudden change in response around $-2\,\Gamma$. Notably, the atom number is close to zero in the region $> -2\Gamma$. This explains the lack of (significant) error bars on the temperature measurements within this region. Here the Gaussian fitting would not be fitting to any significant amount of atoms, and then fitting Equation 6.12 would remain close to the initial guess used. While this may be caused by similar effects to the temperature response, at the near resonant detunings ($> -2\,\Gamma$) because there is not such a strong cooling effect it is possible that the atom cloud had become too diffuse to detect the total atom number properly. Once the molasses cooling became effective ($< -2\,\Gamma$) the atoms were able to remain dense enough for the absorption imaging to detect the cloud properly. Because the Gaussian fitting for measuring the radius of the atom cloud is able to use a large number of pixels to fit, it would still be able to fit to a low number of atoms to show the temperature accurately. We would also expect the near resonant light—where the scattering force is dominant—to continue to cool atoms at temperatures near the Doppler cooling limit. The absence of the quadrupole magnetic field would result in no new atoms being trapped. Since there is no mechanism for adding more atoms into the cold atom cloud—as would usually be the case for the MOT—only the loss mechanisms remain and therefore atoms are lost from the MOT. At $\approx -4.5\,\Gamma$, the maximum number of atoms are able to remain in the trap. At larger red detunings ($< -4.5\,\Gamma$), there is a steady increase in the loss of atoms. We choose to use a frequency detuning of $-4.5\,\Gamma$ during the experiment to maximise the atom number. Whilst this does not necessarily provide the coldest atoms, the loss of more atoms in this regime would cause a more significant loss of SNR compared to the small change in temperature.

Figure 6.16 shows how the period of time the cooling and repump beams are left on after the molasses ramp period affects the temperature of the cold atom cloud. Here we can see a small decrease in temperature from $\approx 10\,\mu$K to $\approx 5\,\mu$K until about 5 ms, as the atoms are able to continue to undergo cooling through the Sisyphus effect. Beyond the period of time shown on the graph, the atoms appear to undergo an extremely large heating effect. We have not shown this to instead have more clarity on the data shown as the measured temperatures were on the scale of > 1 mK, accompanied with errors proportional to the data

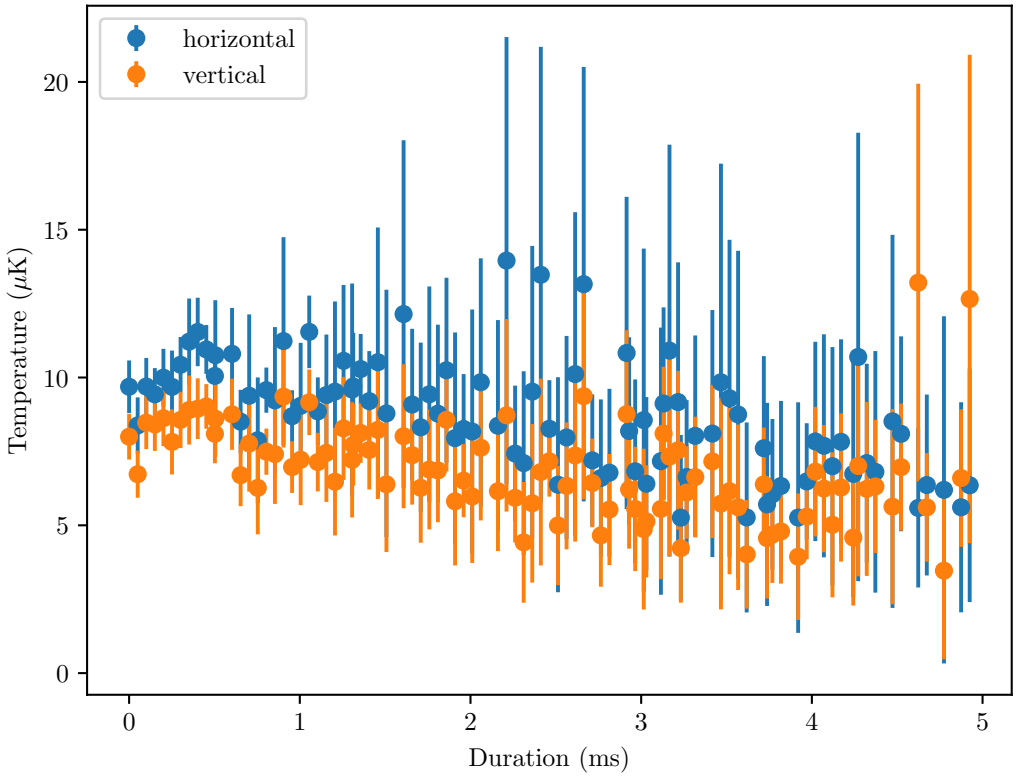

Figure 6.16: Graph showing the temperature of the cold atom cloud as a function of the period the cooling and repump lasers are left on after the cooling power is ramped down during the molasses stage.

point's temperature. We do not believe that this is an actual heating effect, but rather erroneous measurements caused by loss of signal through loss of detectable atoms. To combat this loss of atoms we use a period of 2.5 ms in the experiment; during this period the laser beams are able to cool the atoms down further while not losing too many atoms. The errors appear to increase as the duration is increased and the temperature is decreased; this may be due to small fluctuations of experimental parameters, such as laser powers, however we were able to consistently obtain these measurements. This may be due to a similar effect to the large variance in atom number measurements seen in Figures 6.12 and 6.14, as lower atom numbers would lead to a lower SNR and fluctuations would also affect the measurement's error.

Despite the molasses stage not being able to exhibit a trapping force like that seen in the MOT, we observed that the atom cloud would not begin expanding until being released from the molasses stage. If this were not the case we would expect to see the cloud to have already undergone expansion and seen a small increase in radius, and a shape closer resembling a Gaussian distribution as opposed to the 'squashed' cloud we see initially. As seen in Figure 6.9, we can observe the expansion clearly, even for a very cold cloud, within the time-scales used for the molasses stage (≈ 5 ms). This would also be accompanied by the atoms falling due to gravity—seen by the position of the atom cloud moving across the image. However, we observed neither of these effects even when testing long molasses stage periods of ≈ 20 ms. While not obvious from Chapter 4, the viscous force during the molasses stage prevents the atoms from moving quickly and provides confinement [120].

6.4 Finding the needle

Once the cold atoms are released from the cooling stages, they fall due to gravity towards the window of the vacuum chamber. Here, the pair of periscopes direct the absorption laser through a section of the atom's trajectory and then onto the PD. After a free fall period of ≈ 120 ms, the cold atoms fall into the path of the absorption beam. Figure 6.17 shows the decrease in laser beam power detected by the PD as the atom cloud passes through the resonant light. This shows that the MOT loading and the molasses cooling stages are effective in creating a dense enough atom cloud to be detected at the bottom of the chamber. Hence, it may be possible to *eventually* perform atom interferometry for gravimetry within this chamber. In order to analyse the magnitude of this dip in signal, assuming the ramp of the laser beam's power is constant during the period where the atom cloud intersects the beam, we fit a Gaussian—representing the

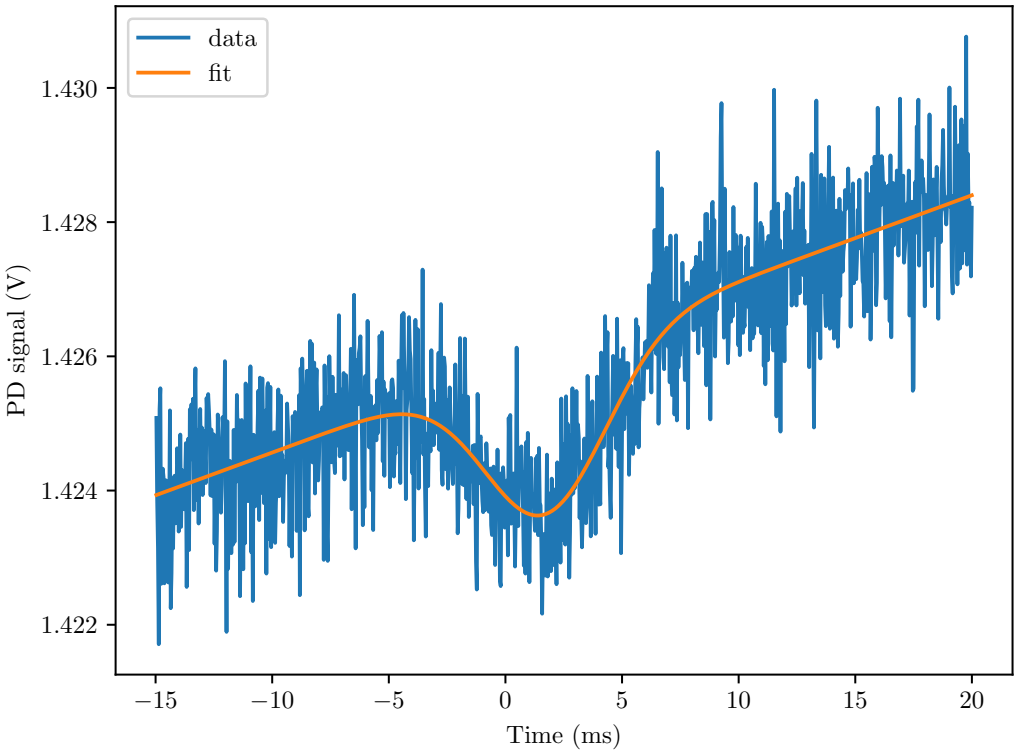

Figure 6.17: Absorption signal of atoms falling through the vacuum chamber detection area. The time axis is measured at 120 ms from the end of the molasses stage.

distribution of the atoms—on a linear ramp:

$$y(x) = A\exp\left(\frac{-(x-x_0)^2}{2\sigma^2}\right) + Bx + y_0, \tag{6.13}$$

where B is the gradient of the ramp. This ramp is required as the small fluctuations in the laser power cause a small gradient to be present on the signal. Usually these fluctuations would not affect measurements; however, because the absorption dip is $\approx 0.2\%$ of the total PD signal this instability becomes significant. This gradient varies in magnitude and sign and is low frequency enough to not show any sharp features such as points of inflection. Using the residuals of the data and the fit we can find an estimate of the standard deviation of the noise. The ratio between this and the amplitude of the dip in the signal, A, can provide us with an SNR of ≈ 3. Using reasonable experimental values for the atom cloud temperature of $10\,\mu$K and 1×10^6 atoms, we arrive at the same SNR. While we have measured larger number of atoms, it is possible that some are lost—possibly through collisions with background atoms—which reduces the number of atoms that reach the detection area. We have also measured lower temperatures; however, the errors associated with many of the TOF measurements are on the order of a few μK. This could indicate there is a temperature instability in our system; this is possibly caused by laser beam power fluctuations during the molasses cooling stage.

From this absorption signal we can determine some properties of the detected atom cloud. The amount of absorption is related to the number of atoms, we can quantify the relative size of the dip in the signal with

$$D = \frac{-A}{Bx_0 + y_0} = 1 - \frac{I_0}{I}, \tag{6.14}$$

where A, B, x_0, y_0 are the amplitude, ramp, central position, and offset of the fit in Equation 6.13. From this, we can approximate the number of atoms detected using Equation 4.24; from the dip in Figure 6.17 we obtain an atom number of $N \approx 0.5 \times 10^6$. This is a reasonable number of atom that agree with the lower end of atom numbers we have detected previously. We have measured relative dip sizes of $\approx 0.5\%$ which gives us an atom number of $N \approx 1.5 \times 10^6$ This matches atom numbers commonly detected by the absorption imaging. The discrepancy between the two could be the result of the atom number fluctuations seen throughout the molasses stage, or from inefficient hyperfine state pumping.

TOF measurements for temperature are often performed with a probe beam beneath the atomic cloud. As the atoms fall through the beam—and cause absorption—the size of the cloud can be determined and hence the temperature. This is commonly performed with either a small diameter Gaussian beam or a

'light sheet' [88, 108, 120, 121]. We can perform this same TOF measurement using our absorption signal. Here we find the radius of the cloud after free fall to be $\sigma(0.12) = 3\,\text{mm}$. Assuming the cloud started at a radius of $\sigma(0) = 0.3\,\text{mm}$, from Equation 4.28 we arrive at a temperature of $T \approx 5\,\mu\text{K}$. Which is amongst the coldest of the temperatures we have detected. It is worth noting that we can only gain information about the vertical temperature of the cloud due to it falling through the beam.

Increasing the SNR of this measurement would require increasing the number of atoms detected; the signal is proportional to the atom number whereas the noise is proportional to the square root of the atom number. One method of detecting more atoms is to ensure that they are all in the appropriate state to be measured. In our case, atoms in the $F = 2$ state are transparent to the wavelength used here, as such we can pump atoms into the 'bright' $F = 3$ state where we can drive this resonant transition. We also perform hyperfine state pumping of the atom cloud with the MOT beams as a precursor to the effect the Raman lasers would present. Figure 6.18 shows how the magnitude of the absorption dip is affected by the pumping time of the cooling laser. This is performed by leaving only the cooling beam on, with the frequency ($-4.5\,\Gamma$) and power ($0.5\,\text{mW}$) used during the molasses stage, after the molasses stage. We fit the exponential function to find the rate of this decay:

$$y(x) = A\exp(\lambda(x - x_0)), \tag{6.15}$$

where A is the amplitude and λ is the scale constant. Here we can see the cooling laser quickly pumps the cold atoms into the dark $F = 2$ state; preventing the resonant absorption laser interacting with the atoms. From the fit, we find this pumping rate to be $\lambda = -2.5 \pm 0.3\,\text{kHz}$, which is close to the scattering rate of $\approx 4\,\text{kHz}$. The data with values > 0 after $\approx 1.5\,\text{ms}$ are likely caused by the absorption dip fit (Equation 6.13) fitting to fluctuations in the signal that may appear similar to a decrease in signal due to absorption of the falling cloud.

Figure 6.19 shows how the magnitude of the absorption dip is affected by the pumping time of the repump laser. This is performed by leaving both the cooling—with the frequency and power used during the molasses stage—and repump beams on after the molasses stage ends. The time axis represents the time the repump beam is turned off relative to the time the cooling beam is switched off (at $t = 0$). Here we can see a rapid increase in the size of the signal's dip size before the cooling beam is switched off while the repump beam is left on. Both the effects of the cooling and repump state pumping can be seen here; in the negative time domain where the cooling beam is dominant, the atoms are pumped into the dark $F = 2$ state (as in Figure 6.18), whereas when only the repump is active the atoms are pumped into the $F = 3$ state which would give the maximum absorption signal. From the fit, we find the pumping rate to

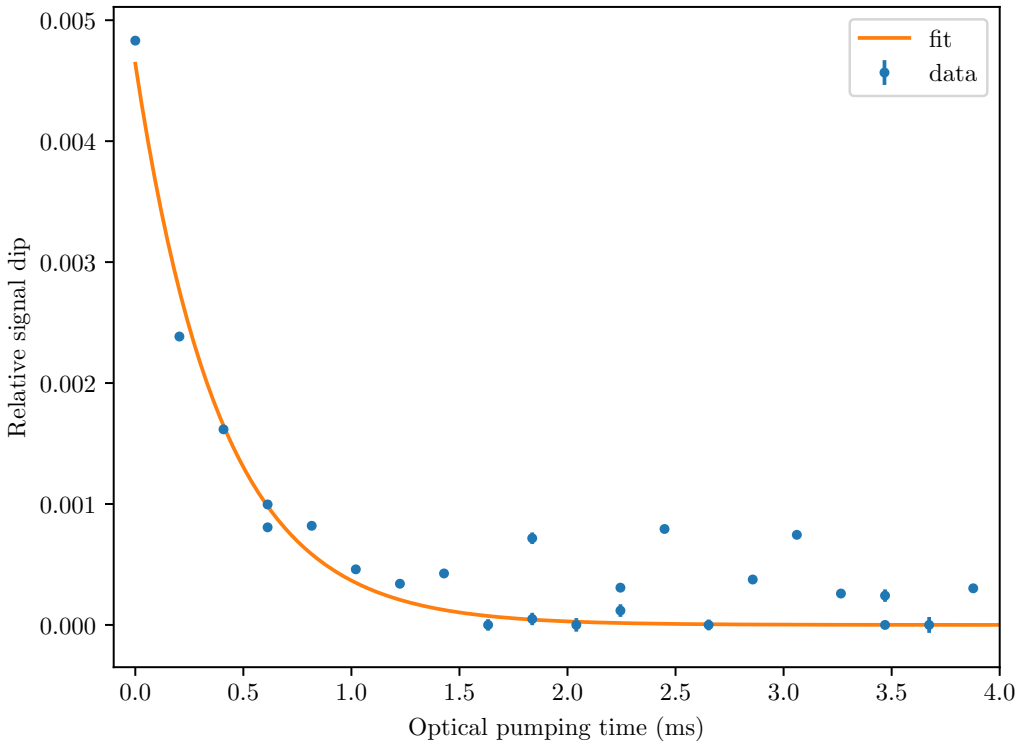

Figure 6.18: Periscope signal absorption dip size (Equation 6.13) as the optical pumping time—using the cooling beam—is varied. The exponential (Equation 6.15) is fitted to the data. Before the pumping with the cooling laser beam, only the molasses lasers had been active. The size of the signal dip is calculated with Equation 6.14. From the exponential fit, we find the time constant $\lambda = -2.5 \pm 0.3\,\mathrm{kHz}$.

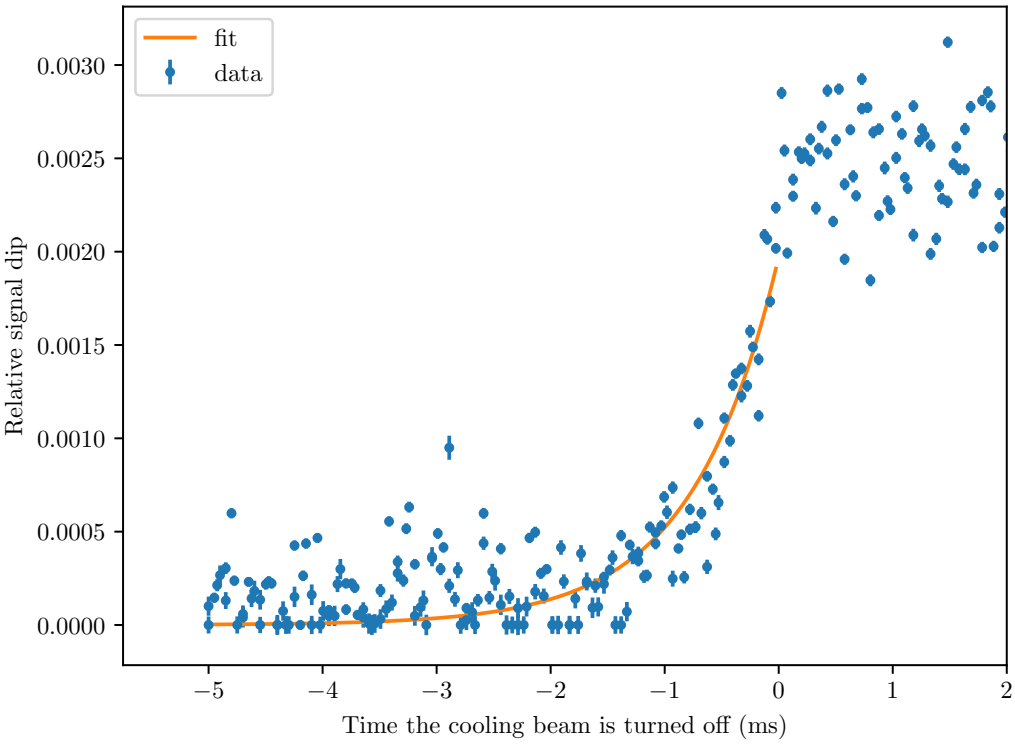

Figure 6.19: Periscope signal absorption dip size (Equation 6.13) as the time the repump beam is on for is varied relative to when the cooling beam is turned off. The exponential (Equation 6.15) is fitted to only the data points in the negative time period. In the negative time period both the repump and cooling beam are on, in the positive time period only the repump is left active. The size of the signal dip is calculated with Equation 6.14. From the exponential fit, we find the time constant $\lambda = 1.33 \pm 0.09\,\mathrm{kHz}$.

be $\lambda = 1.33 \pm 0.09\,\text{kHz}$; this differs from our calculated on resonance scattering rate of $\approx 205\,\text{kHz}$. This difference is most likely due to the saturation intensity, I_{sat}, being hard to calculate when multiple decay routes exist [122].[5] The large distribution of data points may be due to fluctuations in the temperature and atom number of the atom cloud affecting the number of atoms being detected by the absorption laser. The transition period in the centre, between the two regimes, can be interpreted as these points being samples of the decay seen in Figure 6.18. As the time the cooling is left on for after the repump is turned off is decreased, there is less time for the cooling laser to be able to pump the atoms into the dark state. Eventually both lasers are turned off together and no atoms are pumped into the dark state.

Successfully observing atoms at the bottom of the chamber, and the *hyperfine* state pumping effect of both individual MOT beams, shows the ability for this system to be able to successfully perform and observe Raman transitions of the cold atom cloud; and therefore, eventually atom interferometry for measurements of gravity in the PLAIN-GG system. For an atom interferometry experiment, one would ideally perform state pumping into specific Zeeman sub-levels—ideally the magnetically insensitive $m_F = 0$ state(s). To make the steps to atom interferometry would first require observing Raman transitions and Rabi oscillations. This requires a new laser system to be implemented into our current experimental apparatus.

[5]This was calculated with resonant light and $I_{\text{sat}} = c\epsilon_0\Gamma^2\hbar^2/4|\hat{\epsilon}\cdot\mathbf{d}|^2$, where c is the speed of light, ϵ_0 is the permittivity of free space, $\hat{\epsilon}$ is the unit polarisation vector of the light field, and $\mathbf{d}$ is the atomic dipole moment. [49].

Chapter 7

Progress towards Raman interferometry

This chapter documents the progress made towards realising a laser system for driving Raman transitions and the fibre stabilisation system to stabilise the phase of the Raman beams for the PLAIN-GG project. Both of these areas of development are incomplete and the results shown are preliminary. We begin this chapter by describing the Raman laser system that was built for use with the apparatus described in Chapter 5. We then describe the development of the optical fibre interferometer designed to stabilise the phase of the Raman beams between the sensor heads of the PLAIN-GG project.

7.1 Raman interaction laser

Figure 7.1 shows the optical arrangement used for the Raman laser system. This system uses seed light from a Toptica[1] DL pro and generates the sidebands used for the Raman transitions with a iX blue[2] NIR-MPX800-LN-10 fibre EOM. The EOM is driven by a Rohde & Schwarz[3] SMC100A signal generator whose signal is amplified by a Qubig[4] RF amplifier. We use the carrier and a sideband as the pair of Raman beams to stimulate the Raman transitions described in Chapter 2. The modulated light is then amplified by a TA. Using high laser beam powers increases the Rabi frequency, allowing for shorter interferometry pulses, which

[1] www.toptica.com
[2] photonics.ixblue.com
[3] www.rohde-schwarz.com
[4] www.qubig.com

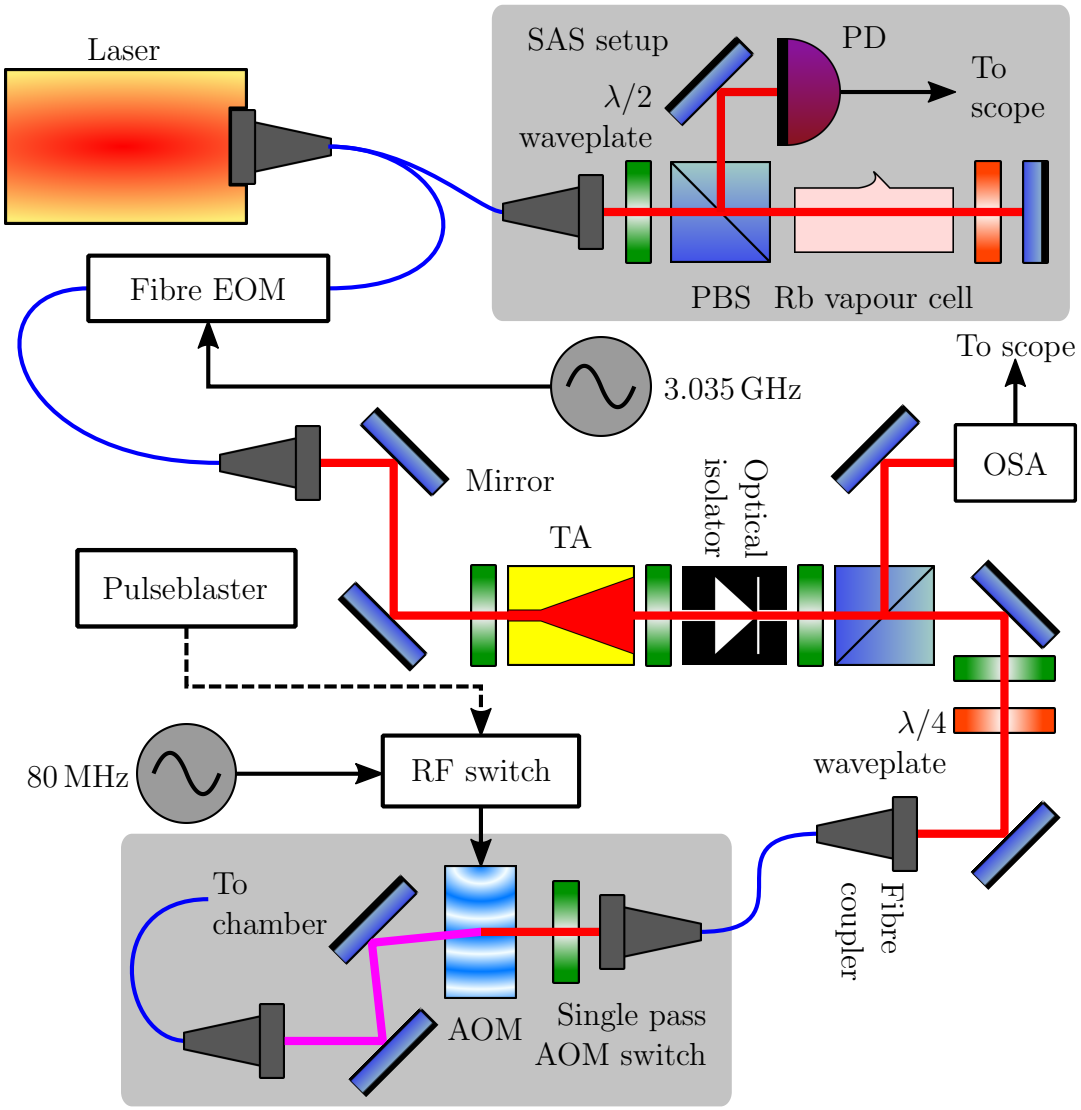

Figure 7.1: Raman laser experimental arrangement. The seed laser sends light to a SAS setup and through a fibre EOM. After passing through the EOM, a tapered amplifier (TA) then amplifies the laser beam. A small portion of this amplified light is coupled into an optical spectrum analyser (OSA) and the rest is fibre coupled into a PM fibre. The fibre coupled light then passes through a AOM switch before being sent to the vacuum chamber. This Raman light enters the vacuum chamber in Figure 5.1 at the camera's position. This system was designed and built by Max Carey.

approximate closer to the ideal instantaneous pulses. Before sending this light to the vacuum chamber—where the Raman transitions take place—we use an AOM switch to quickly shutter the light. The AOM used is a Gooch & Housego R23080-1-LTD and driven by an AA Opto-Electronic MODA80-B4-33. The AOM's RF signal is digitally controlled by TTL signals from the pulseblaster through a Mini-Circuits ZX80-DR230-S+ RF switch. By using a flip mirror in the camera's position in Figure 5.1 we are able to alternate optical access between the camera and the Raman laser to the vacuum chamber.

The SAS system is used to make sure the Raman carrier frequency is far detuned from the $F = 2, 3 \Rightarrow F' = 2, 3$ transitions. We use a Fabry-Pérot cavity as an OSA after the laser light has been modulated to observe the successful generation of the sidebands. We do not bother with suppression of the unused sideband as it would have minimal effect on the interferometry pulses [123].

Unfortunately, we were unable to observe any Raman transitions successfully due to equipment failure. We discovered a small fleck of dust on the surface of the optical fibre leading to the EOM. This had caused heating of the fibre optic and which gradually damaged the fibre. The gradual damage of the fibre reduced the fraction of light able to transmit through the fibre and seed the TA. This unnoticed drop of seed power then lead to damage of the TA's gain chip while we continued to run the TA at high current. This left the setup unusable without replacement components, which we were unable to obtain in a timely manner.

Our initial experiments would have involved FM of the EOM's driving frequency as the size of the absorption signal after the atoms undergo free fall is measured (Figure 6.17). By using long Raman pulses ($100\,\mu$s) we pump the ensemble's average population into a state depending on the frequency difference between the carrier and the sidebands from the ground level's hyperfine energy splitting (as described in Section 2.2.1). From this we would expect to observe spectroscopic features of a resonant Raman transition or, in the case of weak magnetic fields existing in the chamber, any m_F sub-level spitting. In order for the the carrier and sideband to interact with the atoms when the beams are counter-propagating, we allow the atoms to fall a short time to increase the frequency difference required between the carrier and the sideband. This ensures that the carrier cannot excite the transition we want the sideband to excite and vice verse. Hence the detected Raman transition resonance depends on the TOF between releasing the atoms from the MOT and turning on the Raman laser.

Once the correct frequency difference between the carrier and the sideband are found, work towards observing Rabi flopping can then begin. This would involve varying the period the Raman laser is switched on for and measuring the

size of the absorption signal in the detection area. This leads towards realising atom interferometry, and would likely require mechanical stabilisation/damping apparatus to observe the interferometry fringes that may otherwise be dominated by noise.

7.2 Fibre phase lock interferometer

The principles of gradiometry (described in Section 3.2.2) rely on the two atom ensembles experiencing identical phase noise of the Raman beams. Usually this is achieved through line-of-sight between the two ensembles, where the same Raman beam can drive transitions in both ensembles. In the PLAIN-GG project we cannot use line-of-sight to maintain the Raman beam's phase coherence between the two ensembles. We have chosen to use a Michelson interferometer whose arms are actively phase stabilised by an AOM in order to maintain the phase coherence of the Raman beams between the two chambers. At the ends of the interferometer arms would be the atom ensembles, and the retro-reflecting mirrors of the chambers where mechanical noise of the environment would manifest as phase noise. The aim of this system is not to eliminate the phase noise, but rather to imprint the phase noise from the passive arm/chamber onto the actively stabilised arm/chamber whilst also cancelling this arm's noise. This would mean the two atom ensembles would experience identical Raman phase noise as if they had line-of-sight. As mentioned in Section 3.2.2, for a sensitivity of 30 Eötvös we require a maximum phase difference of 3 mrad; hence this is the stability we aim for. A similar method of phase stabilisation has already been shown to reach much better stability and over much larger distances [36, 124, 125], indicating that this endeavour is feasible.

Because the Raman beams can only be active for very short periods during the experiment, direct phase stabilisation of the Raman beams themselves would be impractical. Instead, we stabilise the phase of the light from a HeNe—whose wavelength (633 nm) does not interact with Rubidium—travelling the same path as the Raman beams. We require to be able transfer the phase stability of the HeNe's light to the Raman beams for this stabilisation method to function; however, we have not yet demonstrated this. We hypothesise this to be possible as the AOMs constantly maintain the phase coherence of the two arms through measurements of the phase of the HeNe's light. Once the Raman beams are activated, they pass through the same path of the HeNe's beam which is being phase stabilised. The HeNe can be seen as a phase measurement laser in this aspect.

Figure 7.2 shows the design of the fibre Michelson interferometer for stabilising the phase of the HeNe's laser beam. We perform this stabilisation through FM of one of the AOMs that are present on each arm of the interferometer. To monitor the effect of this stabilisation where the phase of the Raman light is important, we also form an optical Mach-Zehnder interferometer. The signal from the optical Mach-Zehnder interferometer simulates the optical phase difference between the two PLAIN-GG sensor heads. In order to detect the phase of the light, we use different RF frequencies to drive the AOMs and perform heterodyne interferometry. We used Gooch & Housego 3200-125 for the AOMs and the Moglabs RF source was used to drive both of them. The Moglabs RF source has built-in PID controllers to allow for feedback control of the driving RF signals. To measure the phase of the beat notes, we use a Liquid instruments[5] Moku:Lab phasemeter which uses a digital phase-locked loop to monitor the phase of an input frequency; which, at 40 MHz, has a precision of $10\,\mu\text{rad}/\sqrt{\text{Hz}}$.

The optical fibre interferometer produces two signals: one which takes a path of a Michelson interferometer, and one which takes the path of a Mach-Zehnder interferometer.[6] The signal of the Mach-Zehnder interferometer is used to find the difference in the light's phase at the position where the atom ensembles would be in the PLAIN-GG project. Therefore, we aim to reduce the noise of the beat note's phase at the Mach-Zehnder's PD. The signal of the Michelson interferometer is used as a feedback signal to stabilise the light's phase.

We use a double-passed AOM setup to prevent any decrease of fibre coupling efficiency when modulating frequency of the AOMs [126].[7] Counter-intuitively, we stabilise the interferometer through FM of the AOM's RF signal as opposed to modulating the phase of the RF signal. We do this as we found phase modulation using the Moglabs RF source built-in PID to not produce any stabilising effect.[8] We suspect phase modulation did not work due to quirks with the Moglabs RF source's PID as firmware updates changed other behaviours of the PID. Implementing an external PID circuit may allow us to use phase modulation, however, at the cost of the convenience and flexibility of the buit-in PID. We use AOMs that require higher driving frequencies to increase the spatial separation

[5] `www.liquidinstruments.com`

[6] This is an *optical* Mach-Zehnder, not to be confused with the matter-wave Mach-Zehnder in Chapter 3.

[7] We plan to eventually propagate 780 nm light down this same optical path. However, the angle that AOMs diffract light at is wavelength dependent. Luckily, the difference in angular deflection between 633 nm and 780 nm light is ≈ 2 mrad. Furthermore, we can use small free space path lengths to further reduce the small path deviation from the slight angle difference. We assume that this small path deviation would be negligible in the operation of the stabilisation interferometer.

[8] A change of frequency, f, is also a change of phase, ϕ: $\phi = \int f(t)\,\mathrm{d}t$ and vice verse $f = f_0 + \frac{\mathrm{d}\phi}{\mathrm{d}t}$.

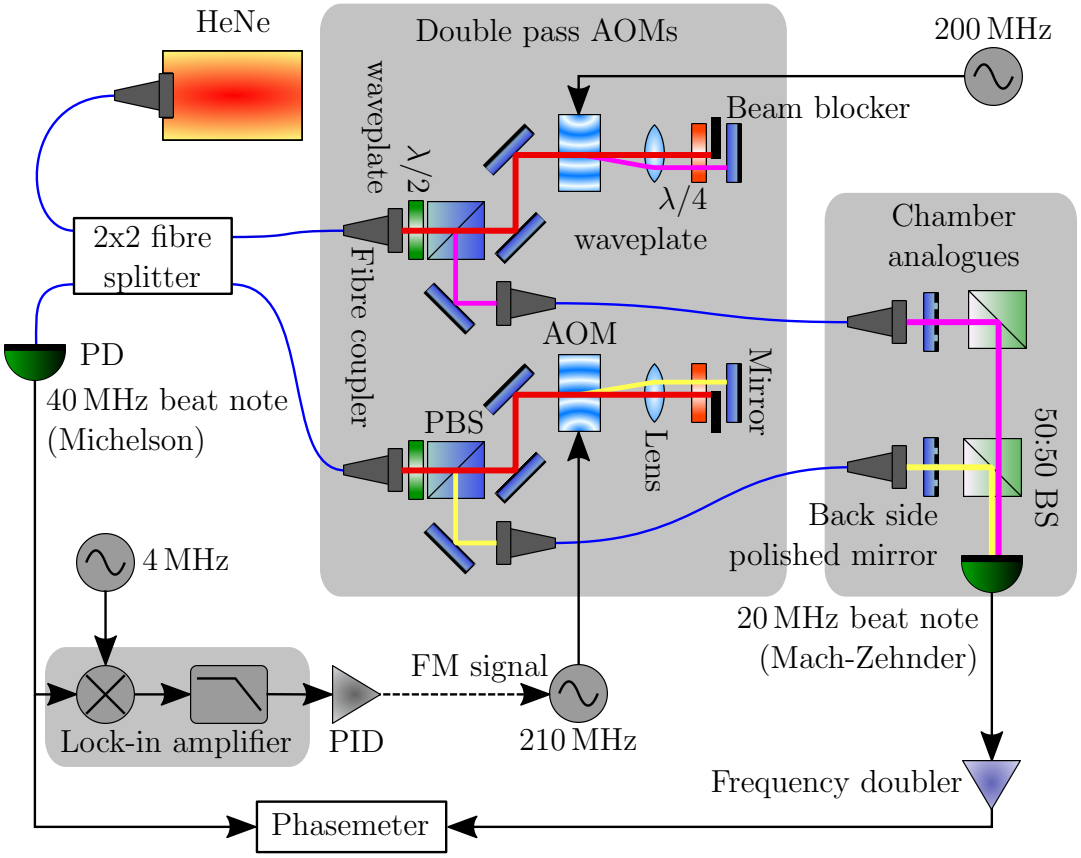

Figure 7.2: Current experimental arrangement of the optical fibre phase stabilisation interferometer. Light from the HeNe is split down two arms of interferometer. Along the paths are double passed AOM setups. The light is then coupled back into fibre and it is then directed towards setups which mimic the retro-reflecting mirror in the vacuum chamber (Figure 5.1). Some of this light is allowed to pass through the retro-reflecting mirrors and this light from both of the interferometer arms is then combined to form a Mach-Zehnder optical interferometer. The retro-reflected light passes back through the fibres and through the AOMs where its frequency is further shifted. This light is then combined in fibre and directed onto a PD. A phasemeter is used to measure the phase of the beat notes detected by the PDs. The top arm of the interferometer can be seen as a master reference arm that the lower slave arm is a locked to through the feedback loop. The light from the HeNe passes through an optical isolator (not shown) before being fibre coupled. We use a 50:50 Beam Splitter (50:50 BS) on both the Mach-Zehnder interferometer arms despite only requiring one because we plan to use AM to stabilise the amplitude of the beams—this is not yet implemented.

between the diffracted order and the zeroth diffracted order. This helps in blocking out the zeroth order beam without reducing the power in the diffracted order. The frequency shift caused by the AOMs would not be a problem for the Raman beams as their exact frequency is largely unimportant; only the frequency difference between the two Raman beams is important and both the carrier and sideband would experience the same shift. The choice of a 10 MHz difference between the RF driving the AOMs is mostly arbitrary, a large shift is used to be able to distinguish and filter the different frequencies detected however this could be performed at higher or lower frequencies.

7.2.1 Preliminary results

Figure 7.3 shows the phase of the two beat note signals when the feedback control is active and after it has been deactivated. Here it can be seen that the Michelson signal, the signal used to lock to, remains stable while locked. The Mach-Zehnder signal, while not as stable as the Michelson, does not wander freely and mainly stays centred around the Michelson signal. This could be caused by noise introduced by the 50:50 BS cubes. After the PID has been deactivated both signals freely roam. The difference between the signals remains generally the same regardless of the PID being active or not.

We can divide the apparatus into sections of noise sources; in particular the fibres and 'chamber' mirrors. The beat note generated from the light that has taken the Mach-Zehnder interferometer's path is affected by the difference of fibre noise and the 50:50 BS noise between the two arms. Whereas the light that has taken the Michelson interferometer's path contains twice the fibre noise difference and the chamber mirror noise difference. We will refer to the signals generated by the light that takes the different interferometer paths the Mach-Zehnder and Michelson signals respectively. The difference between these two signals is therefore comprised of the fibre noise and the mirror noise differences. An improvement to this system is already clear; the mechanical vibrations of the chamber mirrors is usually the mechanism of introducing Raman phase noise within a matter-wave interferometer, however the Mach-Zehnder signal currently does not contain this information. Altering the experimental design for the Mach-Zehnder signal to contain this information is required. However, the current Mach-Zender signal is still able to provide information about the effectiveness of this method for stabilising the noise from the *fibres* between the two chambers.

It can be seen that while the PID lock is engaged there appear to be more high frequency fluctuations of both phases. This may be caused by 'ringing' of the

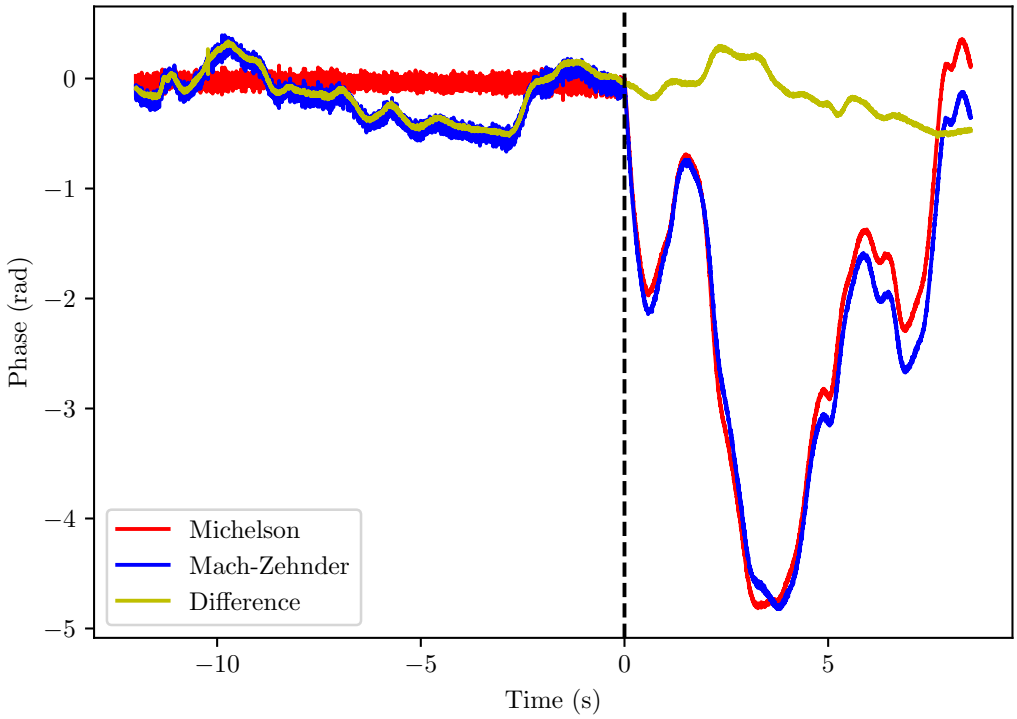

Figure 7.3: Time evolution of the phase of the beat notes when locked and unlocked. The signals are named after the optical interferometer path the light that generated the signal took. The region to the left of the dashed vertical line is when the phase lock was engaged. The region to the right of the dashed vertical line is when the phase lock was disengaged. This lock was achieved with a PID gain of 100.

PID loop where over-corrections of the signal prevent the signal ever reaching a point of stability. However, changes to the gain of the PID made little to no easily observable changes to this signal. A better set of tools to view the noise and stability of this signal is the noise spectra and Allan deviation [72].

Figure 7.4 shows the phase noise spectra of the signals at varying PID gains. This is essentially the Fourier transform of the phase signal (Figure 7.3) and can be used to find particular physical processes that effect the signal.[9] We will refer to the PID gain's magnitude here, the sign of the gain is largely irrelevant and affects the sign of the error signal's gradient that the PID locks

[9]The power spectral density is often used to describe the frequency components of a signal in the same manner. We have chosen to show the amplitude spectral density as its units are more intuitive to work with here. In any case, the power spectral density and the amplitude spectral density show the same information: the power spectral density is the square of the amplitude spectral density.

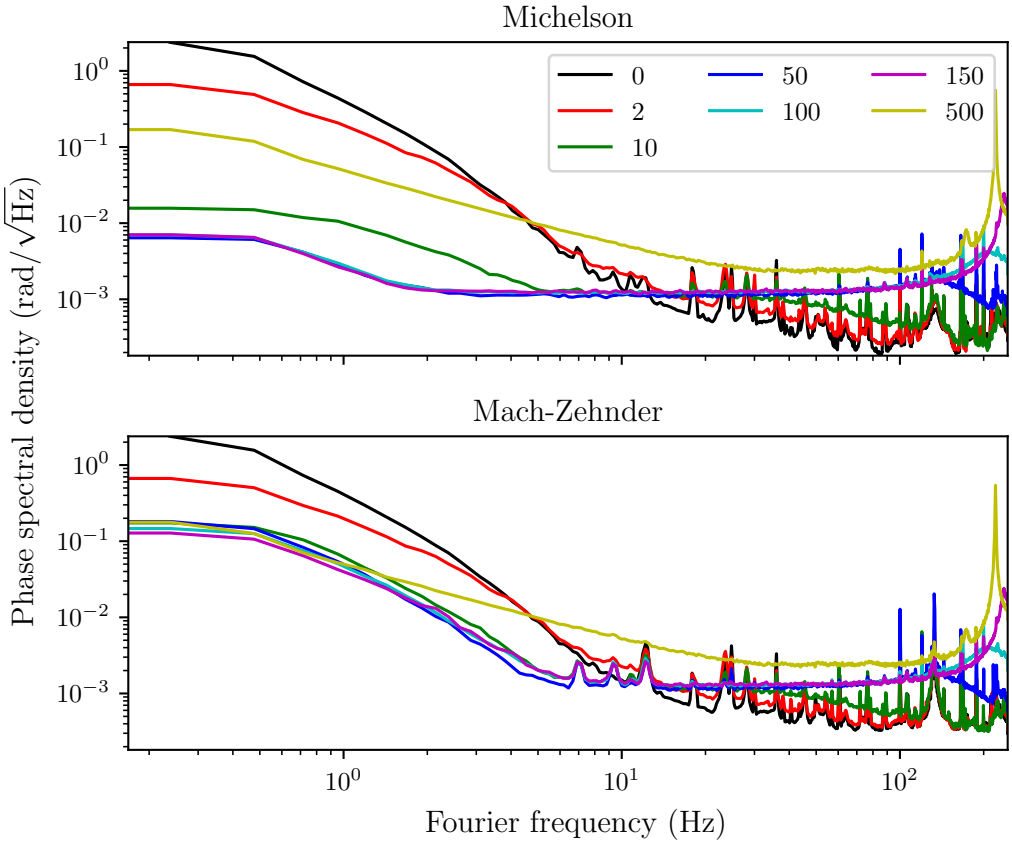

Figure 7.4: Measurements of the phase spectral power density at different PID gains labelled in the legend.

to. This gain is a global gain setting that effects the proportional, integral, and differential gains simultaneously. A PID gain of 0 is the unlocked case. Here we can see the effect different PID gains have on suppressing or creating different frequencies contributing to the phase difference between the two interferometer arms. In particular, we can see the low frequency ($< 10\,\mathrm{Hz}$) noise tends to become suppressed at higher gains. We can also observe the ringing effect of the PID as the noise increases at higher frequencies ($> 10\,\mathrm{Hz}$) with increasing gains; in particular the peak at 220 Hz at a gain of -500. Gains of -100 and larger appear to give this ringing effect which can also be seen by the flattening of the spectra at frequencies $\gtrsim 10\,\mathrm{Hz}$. The spectrum of the difference signal is not included as the PID had no significant effect on its spectra.

Using Equation 3.29 we can arrive at an estimate for the performance of a gradiometer with the phase noise presented by this optical interferometer. The PID gain of -50 does not produce a high frequency 'ringing' peak seen in the higher gain series and produces a maximum phase noise, at higher frequencies, of $20\,\mathrm{mrad}/\sqrt{\mathrm{Hz}}$ on the Mach-Zehnder signal—the signal that represents the phase noise between the two chambers. Using Equation 3.29 we can estimate how this value of phase noise would affect the sensitivity of a gravity gradiometer: for a baseline of 4 m, 780 nm light, and $T = 40\,\mathrm{ms}$ we estimate an ideal sensitivity of $200\,\mathrm{E}/\sqrt{\mathrm{Hz}}$.

This would only meet the 30 E sensitivity target described in Sections 1.1 and 3.2.2 after an integration time of 11 hours.[10] This is not practical for obtaining a large number of measurements in a reasonable time frame. It is clear that the phase noise difference must be further reduced in order to obtain a practical gravity gradiometer.

To avoid the effect of these peaks the transfer function of the atom interferometer could be engineered so that the regular oscillations of the transfer function that lead to zeroes sit on the frequencies that have the most significant contributions to noise. Another possibility to reduce the effect of this noise is by reducing the Rabi frequency, thus reducing the transfer function's corner frequency and allowing for the effect of the high frequency noise to be attenuated. However, higher Rabi frequencies tend to be ideal in most interferometers as longer interferometry pulses introduce other sources of errors into the measurement [38]. Higher Rabi frequencies allow the atom interferometry pulses to more closely approximate to the ideal instantaneous pulse.

The Allan deviation, σ_y, is also a useful tool for characterising the stability of a signal [127]. This is performed by monitoring the signal for an extended

[10] 40×10^3 seconds

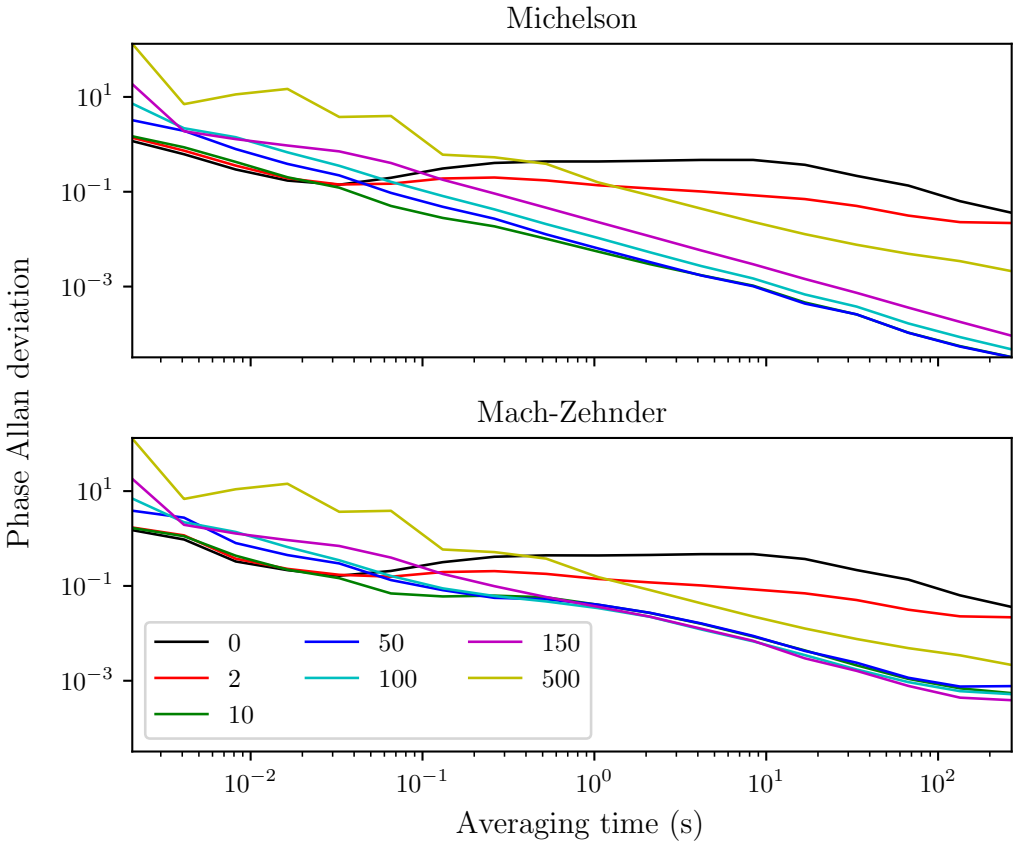

Figure 7.5: Measurements of the phase Allan deviation at different PID gains labelled in the legend.

period of time. The signal is then divided into varying lengths of time τ where statistics of the signal at varying time intervals can be determined. We use the overlapped variable τ estimator to calculate the Allan deviation [72, 128]:

$$\sigma_y^2(n\tau_0, N) = \frac{1}{2n^2\tau_0^2(N-2n)} \sum_{t=0}^{N-2n-1} (x_{i+2n} - 2x_{i+n} + x_i)^2 , \tag{7.1}$$

where x_i is the phase at time $i\tau$, $1/\tau_0$ is the sampling rate of the instrument, N is the number or measurements, and n is a factor that determines how many samples are overlapped.

Figure 7.5 shows the Allan deviation of the phase of the interferometery signals with varying PID gains. The Allan deviation shows how much the signal is likely to change after the indicated time period. For example, an Allan deviation—or instability—of 10^{-1} at an averaging time of 1 s means the phase will change by 10^{-1} rad after a second.

In the $< 0.02\,\mathrm{s}$ timescales the unlocked signal's Allan deviation is lower than the signals with a high PID gain. This shows how the phase of the unlocked signal does not contain the short timescale noise that the locked signals follow seen in Figure 7.3. Because the unlocked signal is able to wander freely, the longer timescale Allan deviation is significantly larger that its locked counterparts. This is as expected as only a shift in lockpoints would change the locked signals. We can also see the PID ringing effect when the gain is too high; in particular the -500 gain setting which also seems to cause lockpoint jumping at longer timescales. The -10 gain setting appears to follow most closely the short timescale Allan deviation, implying no PID ringing is present, and still reaches the lowest Allan deviations measured at the longest timescales.

The Allan deviation is not as applicable here to interpreting the effect of Raman phase noise on an atom interferometry sequence compared to the phase noise spectra, however it does provide some valuable insights. During the periods in between the interferometry pulses during the atom interferometry sequence, where the Raman beams are turned off, any phase shift does not *yet* become imprinted onto the atom's state. During this period the Raman beam's phase is able to change without affecting the interferometry fringe provided the phase returns to its original value before the next interferometry pulse is performed. However we only see these improvements of stability at periods $\gtrsim 100\,\mathrm{ms}$ when locked; and the maximum period the atom interferometry that can be performed over in our system is $2T = 120\,\mathrm{ms}$. As discussed in Section 3.2.2, for this locking mechanism to provide suitable performance for atom interferometry the instability at periods less than the $2T$ time must be reduced to $10^{-3}\,\mathrm{rad}$; which we have not achieved here.

From these results the current iteration of the optical fibre interferometer for stabilising the phase of the light is unsuitable for meeting the requirements of the PLAIN-GG project—even if we assume that we can transfer the phase stability imparted to the HeNe light to the Raman light. However, we have demonstrated that it is capable of manipulating the phase coherence of the light passing through the interferometer to varying degrees. This system still requires a large amount of optimisation in order to reach the desired lower stability levels such as seen in Foreman et al. [36].

7.2.2 Improvements required

Currently the chamber analogues do not fully imitate the PLAIN-GG chambers. The mirrors are currently only coupled together through the optical bench, however the gradiometer's chambers would be coupled together directly and

mounted vertically. Different noise sources might be present or absent in this arrangement and this should be represented in the analogues. As previously mentioned, the design of the analogues also needs to be altered slightly to enable us to detect the phase noise the chamber mirrors can introduce. This would also allow us to investigate the effect of the fibres and chamber mirrors on the phase noise separately.

The frequency separation of the AOM's driving RF will also require investigation. Currently the 10 MHz frequency shift is largely arbitrary. However, there could be a frequency separation which provides a more stable system.

A possible reason we observe a large amount of PID 'ringing' is that we are over-correcting for the fibre noise. The noise of the Michelson signal consists of twice the noise the fibre introduces into the system, however the Mach-Zehnder signal is only affected by this noise once. The locking feedback loop then acts 'twice' to correct for the fibre noise; creating more noise in the process. We suspect a frequency divider circuit can be implemented to half the Michelson beat note signal to remove this overcorrection. Furthermore, the PID behaviour of the Moglabs RF source requires further investigation. Firmware updates of this device would often change the PID behaviour and moving to an external PID, whose behaviour is more well known, would be ideal.

The final test of this system is to observe transferring the phase stability of the optical interferometer to the Raman light while detecting the phase noise of the HeNe's light. Until this is successfully observed, the feasibility of the current design of the PLAIN-GG project is uncertain. It is also possible that this scheme of creating common mode Raman phase noise in the between the two atom interferometers is not feasible. Further investigation into this would be required.

Chapter 8

Conclusion

The current design of atom interferometric gravity gradiometers requires line-of-sight between the atomic test masses [4, 18, 65]. Line-of-sight allows the same laser beams that perform the interferometry to impart identical noise profiles to both atomic test masses; allowing this noise to be eliminated in the differential measurement—this is the working principle behind a gradiometric measurement. This noise rejection makes a gradiometer ideal for field applications; where mechanical noise from the environment might prevent accurate measurement by an absolute measurement device. Unfortunately several factors limit the portability of atomic interferometric gravity gradiometers, such as the stability of the lasers and optical systems, and of the bulk arising from the vacuum chambers used. The sensitivity of a gradiometer is dependent on the separation between the atomic test masses and therefore a large vacuum chamber arrangement is usually favoured—usually leading to increased bulk from a larger vacuum chamber. Therefore, there is a trade-off between portability and sensitivity. Efforts have been made to create a portable atom interferometry system for gravity gradiometry that is suitable for field applications [15, 25, 26, 27, 77]. Most recently and notably, a measurement outside the lab has been achieved by a portable system [28]. Usually, these systems have tended to find use in fundamental—lab based—endeavours where the sensitivity of the device is focused on [2, 12, 129, 130, 131, 132]. Somewhat ironically, atom interferometers for absolute gravity measurement have found more success in field applications [29, 32, 34, 133, 134].

To retain the sensitivity a large baseline gradiometer can provide while reducing bulk from the vacuum chamber, we take a different approach to atom interferometric gravity gradiometry in the PLAIN-GG project. We separate the two atomic test masses onto two identical separate vacuum chambers, effectively

creating two absolute gravimeters, however this breaks the line-of-sight that maintains the phase coherence of the interacting laser beams. To facilitate the laser phase coherence between the atomic test masses an optical fibre Michelson interferometer is proposed to correct for any differences in laser phase between the two chambers—maintaining the condition for common noise rejection. In this thesis we have demonstrated a compact and commercially available vacuum chamber with integrated optics to be viable for atom interferometric gravity measurements and for use in the PLAIN-GG project. We have also briefly explored the optical fibre interferometer design for stabilising the Raman beams for the PLAIN-GG project.

In Part I, we introduced the theory behind atom interferometry and how it is used for measurements of a gravity gradient. In Chapter 2 we described how a multi-level atom can be turned into an ideal two-level atom with long state lifetimes through Raman transitions. Using these Raman transitions, we showed in Chapter 3 how one can perform atom interferometry. We then described how we can use atom interferometry to perform measurements of local gravity, and then measurements of the gravity gradient. To perform atom interferometry we require cold and trapped atoms, in Chapter 4 we detailed how this could be achieved with a MOT. Here we also described tools to characterise the MOT and the atoms trapped by it; specifically, how to perform measurements of the number of atoms in the cold atom cloud, and measurements of the cloud's average temperature.

Part II begins with Chapter 5 which details the apparatus and experimental methods used for creating such a MOT and cold atoms. This apparatus is the foundation for which the PLAIN-GG sensor head is to eventually be built with. In this chapter we described the first commercially available vacuum chamber with integrated optics designed for atom interferometric gravity measurements. This chamber contains mirrors and a waveplate arranged to create MOT beams, space for 120 ms drop time, and mirrors to collect light for state readout after the drop. In this chapter we also detail a laser system capable of generating light for atom trapping and for performing absorption imaging of the cold atom cloud. This absorption imaging system is used extensively in the characterisation of the MOT for both measurements of atom number and temperature.

Chapter 6 shows the results of the characterisation of the MOT. We first characterised the effect that several of the MOT parameters have on the atom cloud's total atom number. This is then followed by the characterisation of the effect the molasses cooling stage has on the atom cloud's temperature. Here we find we are able to generate an atom cloud of $\approx 1.5 \times 10^6$ atoms and of temperatures $\approx 7\,\mu$K. This cloud is sufficiently dense enough to then be detectable by an absorption beam after the 120 ms free fall. Fundamentally there

is little difference between this detection and the state detection after performing atom interferometry with the Raman beams. Therefore, this system is capable of performing atom interferometry and hence measurements of gravity. In order to perform inertial measurements through atom interferometry, implementation of the interferometry pulses via Raman transitions is necessary.

In Chapter 7 we briefly described the Raman laser system that was built and the immediate plans for using that system to build towards realising atom interferometry. Unfortunately, we were unable to observe any Raman transitions. Failure of several items of equipment hindered progress and prevented successful observation of any Raman transitions. Finally, we described a prototype optical fiber interferometer system for phase stabilising the Raman beams between the sensor heads of the PLAIN-GG project. Here we showed some preliminary results which indicate we currently do not meet the criteria for providing sufficient phase stabilisation and further work is required.

Bibliography

[1] Achim Peters, Keng Yeow Chung, and Steven Chu. Measurement of gravitational acceleration by dropping atoms. *Nature*, 400(6747):849, aug 1999.

[2] Jeffrey Michael McGuirk, G T Foster, J B Fixler, M J Snadden, and M A Kasevich. Sensitive absolute-gravity gradiometry using atom interferometry. *Physical Review A*, 65(3):33608, feb 2002.

[3] Zoltán Szabó. The history of the 125 year old Eötvös torsion balance. *Acta Geodaetica et Geophysica*, 51(2):273–293, jun 2016.

[4] Alexey V Veryaskin. *Gravity gradiometry.* 2053-2571. IOP Publishing, 2018.

[5] Robert L Forward, R M Lemmen, R W Lowe, R W Peterson, I Tonai, and W E Williams. Rotating gravity gradiometer study. *Hughes research laboratories. Malibu*, page 174, 1976.

[6] E Metzger. Recent gravity gradiometer developments. In *Guidance and control conference*, page 1081, 1977.

[7] M V Moody, H A Chan, and H J Paik. Superconducting gravity gradiometer for space and terrestrial applications. *Journal of Applied Physics*, 60(12):4308–4315, dec 1986.

[8] Jakob Flokstra, R Cuperus, R.J. Wiegerink, and M.C. van Essen. A MEMS-based gravity gradiometer for future planetary missions. *Cryogenics*, 49(11):665–668, nov 2009.

[9] Richard P Kornfeld, Bradford W Arnold, Michael A Gross, Neil T Dahya, William M Klipstein, Peter F Gath, and Srinivas Bettadpur. GRACE-FO: The Gravity Recovery and Climate Experiment Follow-On Mission. *Journal of Spacecraft and Rockets*, 56(3):931–951, may 2019.

[10] Frank Flechtner, Karl-Hans Neumayer, Christoph Dahle, Henryk Dobslaw, Elisa Fagiolini, Jean-Claude Raimondo, and Andreas Güntner. What Can be Expected from the GRACE-FO Laser Ranging Interferometer for Earth Science Applications? *Surveys in Geophysics*, 37(2):453–470, mar 2016.

[11] B Christophe, D Boulanger, B Foulon, P-A Huynh, V Lebat, F Liorzou, and E Perrot. A new generation of ultra-sensitive electrostatic accelerometers for GRACE follow-on and towards the next generation gravity missions. *Acta Astronautica*, 117:1–7, 2015.

[12] Jeffrey M. McGuirk. *High precision absolute gravity gradiometry with atom interferometry*. PhD thesis, Stanford University, 2001.

[13] Philip R. Bevington and D. Keith Robinson. *Data Reduction and Error Analysis for the Physical Sciences*. McGraw-Hill Education, third edition, 2002.

[14] Michel Van Camp, Olivier Viron, Arnaud Watlet, Bruno Meurers, Olivier Francis, and Corentin Caudron. Geophysics From Terrestrial Time-Variable Gravity Measurements. *Reviews of Geophysics*, 2017.

[15] Andrew George Hinton. *Development of a transportable cold atom gradiometer*. PhD thesis, University of Birmingham, dec 2016.

[16] Achim Peters, Keng Yeow Chung, and Steven Chu. High-precision gravity measurements using atom interferometry. *Metrologia*, 38(1):25–61, feb 2001.

[17] M. Snadden, J. McGuirk, P Bouyer, K. Haritos, and M. Kasevich. Measurement of the Earth's Gravity Gradient with an Atom Interferometer-Based Gravity Gradiometer. *Physical Review Letters*, 81(5):971–974, aug 1998.

[18] F Sorrentino, Y H Lien, G Rosi, L Cacciapuoti, M Prevedelli, and G M Tino. Sensitive gravity-gradiometry with atom interferometry: progress towards an improved determination of the gravitational constant. *New Journal of Physics*, 12(9):95009, 2010.

[19] Florence Yver-Leduc, Patrick Cheinet, Jérôme Fils, André Clairon, Noël Dimarcq, David Holleville, Philippe Bouyer, and Arnaud Landragin. Reaching the quantum noise limit in a high-sensitivity cold-atom inertial sensor. *Journal of Optics B: Quantum and Semiclassical Optics*, 5(2):S136, 2003.

[20] F Sorrentino, Q Bodart, L Cacciapuoti, Y.-H. Lien, M Prevedelli, G Rosi, L Salvi, and G M Tino. Sensitivity limits of a Raman atom interferometer as a gravity gradiometer. *Phys. Rev. A*, 89(2):23607, feb 2014.

[21] A Bertoldi, G Lamporesi, L Cacciapuoti, M De Angelis, M Fattori, T Petelski, A Peters, M Prevedelli, J Stuhler, and G M Tino. Atom interferometry gravity-gradiometer for the determination of the Newtonian gravitational constant G. *The European Physical Journal D-Atomic, Molecular, Optical and Plasma Physics*, 40(2):271–279, 2006.

[22] Nan Yu, J M Kohel, J R Kellogg, and L Maleki. Development of an atom-interferometer gravity gradiometer for gravity measurement from space. *Applied Physics B*, 84(4):647–652, 2006.

[23] G Rosi, G D'Amico, L Cacciapuoti, F Sorrentino, M Prevedelli, M Zych, Č Brukner, and G M Tino. Quantum test of the equivalence principle for atoms in coherent superposition of internal energy states. *Nature communications*, 8:15529, 2017.

[24] Kai Bongs, Michael Holynski, Jamie Vovrosh, Philippe Bouyer, Gabriel Condon, Ernst Rasel, Christian Schubert, Wolfgang P Schleich, and Albert Roura. Taking atom interferometric quantum sensors from the laboratory to real-world applications. *Nature Reviews Physics*, 1(12):731–739, dec 2019.

[25] A Hinton, M Perea-Ortiz, J Winch, J Briggs, S Freer, D Moustoukas, S Powell-Gill, C Squire, A Lamb, C Rammeloo, B. Stray, G. Voulazeris, L. Zhu, A. Kaushik, Y.-H. Lien, A. Niggebaum, A. Rodgers, A. Stabrawa, D. Boddice, S. R. Plant, G. W. Tuckwell, K. Bongs, N. Metje, and M. Holynski. A portable magneto-optical trap with prospects for atom interferometry in civil engineering. *Philosophical Transactions of the Royal Society A: Mathematical, Physical and Engineering Sciences*, 375(2099):20160238, aug 2017.

[26] Camille Janvier, Vincent Ménoret, Bruno Desruelle, Sébastien Merlet, Arnaud Landragin, and Franck Pereira dos Santos. Compact differential gravimeter at the quantum projection-noise limit. *Physical Review A*, 105(2):022801, feb 2022.

[27] Wei Lyu, Jia-Qi Zhong, Xiao-Wei Zhang, Wu Liu, Lei Zhu, Wei-Hao Xu, Xi Chen, Biao Tang, Jin Wang, and Ming-Sheng Zhan. Development of a compact high-resolution absolute gravity gradiometer based on atom interferometers. *arXiv preprint arXiv:2202.12021*, 2022.

[28] Ben Stray, Andrew Lamb, Aisha Kaushik, Jamie Vovrosh, Anthony Rodgers, Jonathan Winch, Farzad Hayati, Daniel Boddice, Artur Stabrawa, Alexander Niggebaum, Mehdi Langlois, Yu-Hung Lien, Samuel Lellouch, Sanaz Roshanmanesh, Kevin Ridley, Geoffrey de Villiers, Gareth Brown, Trevor Cross, George Tuckwell, Asaad Faramarzi, Nicole Metje, Kai Bongs,

and Michael Holynski. Quantum sensing for gravity cartography. *Nature*, 602(7898):590–594, feb 2022.

[29] M Hauth, C Freier, V Schkolnik, A Senger, M Schmidt, and A Peters. First gravity measurements using the mobile atom interferometer GAIN. *Applied Physics B*, 113(1):49–55, oct 2013.

[30] J Le Gouët, T E Mehlstäubler, Jaewan Kim, Sébastien Merlet, Andre Clairon, Arnaud Landragin, and F Pereira Dos Santos. Limits to the sensitivity of a low noise compact atomic gravimeter. *Applied Physics B*, 92(2):133–144, 2008.

[31] Malte Schmidt, A Senger, M Hauth, C Freier, V Schkolnik, and Achim Peters. A mobile high-precision absolute gravimeter based on atom interferometry. *Gyroscopy and Navigation*, 2(3):170–177, jul 2011.

[32] Xuejian Wu, Zachary Pagel, Bola S Malek, Timothy H Nguyen, Fei Zi, Daniel S Scheirer, and Holger Müller. Gravity surveys using a mobile atom interferometer. *Science Advances*, 5(9):eaax0800, sep 2019.

[33] Yannick Bidel, Olivier Carraz, Renée Charriere, Malo Cadoret, Nassim Zahzam, and Alexandre Bresson. Compact cold atom gravimeter for field applications. *Applied Physics Letters*, 102(14):144107, 2013.

[34] Yannick Bidel, N. Zahzam, C. Blanchard, A. Bonnin, M. Cadoret, Alexandre Bresson, D. Rouxel, and M. F. Lequentrec-Lalancette. Absolute marine gravimetry with matter-wave interferometry. *Nature communications*, 9(1):627, 2018.

[35] Long-Sheng Ma, Peter Jungner, Jun Ye, and John L Hall. Delivering the same optical frequency at two places: accurate cancellation of phase noise introduced by an optical fiber or other time-varying path. *Optics Letters*, 19(21):1777, nov 1994.

[36] Seth M Foreman, Andrew D Ludlow, Marcio H G de Miranda, Jason E Stalnaker, Scott A Diddams, and Jun Ye. Coherent Optical Phase Transfer over a 32-km Fiber with 1 s Instability at 10^{-17}. *Physical Review Letters*, 99(15):153601, oct 2007.

[37] Mark Kasevich and Steven Chu. Atomic interferometry using stimulated Raman transitions. *Phys. Rev. Lett.*, 67(2):181–184, jul 1991.

[38] Jack Cameron Saywell. *Optimal control of cold atoms for ultra-precise quantum sensors*. PhD thesis, University of Southampton, 2020.

[39] Kathryn Moler, David S Weiss, Mark Kasevich, and Steven Chu. Theoretical analysis of velocity-selective Raman transitions. *Physical Review A*, 45(1):342–348, jan 1992.

[40] Alexander J Dunning. *Coherent atomic manipulation and cooling using composite optical pulse sequences*. PhD thesis, University of Southampton, mar 2014.

[41] Christopher J Foot. *Atomic physics*, volume 7. Oxford University Press, 2005.

[42] F Bloch. Nuclear induction. *Physica*, 17(3-4):272–281, mar 1951.

[43] J.R. Johansson, P.D. Nation, and Franco Nori. QuTiP: An open-source Python framework for the dynamics of open quantum systems. *Computer Physics Communications*, 183(8):1760–1772, aug 2012.

[44] J.R. Johansson, P.D. Nation, and Franco Nori. QuTiP 2: A Python framework for the dynamics of open quantum systems. *Computer Physics Communications*, 184(4):1234–1240, apr 2013.

[45] Richard Stoner, David Butts, Joseph Kinast, and Brian Timmons. Analytical framework for dynamic light pulse atom interferometry at short interrogation times. *JOSA B*, 28(10):2418–2429, oct 2011.

[46] John D Hunter. Matplotlib: A 2D Graphics Environment. *Computing in Science & Engineering*, 9(3):90–95, 2007.

[47] Max Sebastian Carey. *Velocimetry, trapping and optimal coherent manipulation of atomic rubidium*. PhD thesis, University of Southampton, 2020.

[48] Mark Fox. *Quantum optics: an introduction*, volume 15. OUP Oxford, 2006.

[49] Daniel A. Steck. Rubidium 85 D Line Data, 2019.

[50] K J R Rosman and P D P Taylor. Isotopic compositions of the elements 1997 (Technical Report). *Pure and Applied Chemistry*, 70(1):217–235, jan 1998.

[51] Olivier Carnal and Jürgen Mlynek. Young's double-slit experiment with atoms: A simple atom interferometer. *Physical review letters*, 66(21):2689, 1991.

[52] Mark Kasevich and Steven Chu. Measurement of the gravitational acceleration of an atom with a light-pulse atom interferometer. *Applied Physics B Photophysics and Laser Chemistry*, 54(5):321–332, may 1992.

[53] Stephen M Barnett. On the recoil and Doppler shifts. *Journal of Modern Optics*, 57(14-15):1445–1447, aug 2010.

[54] Chris Overstreet, Peter Asenbaum, and Mark A Kasevich. Physically significant phase shifts in matter-wave interferometry. *American Journal of Physics*, 89(3):324–332, mar 2021.

[55] B Canuel, F Leduc, D Holleville, Alexandre Gauguet, J Fils, A Virdis, A Clairon, N Dimarcq, Ch J Bordé, A Landragin, and P. Bouyer. Six-Axis Inertial Sensor Using Cold-Atom Interferometry. *Physical Review Letters*, 97(1):010402, jul 2006.

[56] J K Stockton, K Takase, and M A Kasevich. Absolute Geodetic Rotation Measurement Using Atom Interferometry. *Physical Review Letters*, 107(13):133001, sep 2011.

[57] D Savoie, M Altorio, B Fang, L A Sidorenkov, R Geiger, and A Landragin. Interleaved atom interferometry for high-sensitivity inertial measurements. *Science Advances*, 4(12):eaau7948, dec 2018.

[58] Remi Geiger, Vincent Ménoret, Guillaume Stern, Nassim Zahzam, Patrick Cheinet, Baptiste Battelier, André Villing, Frédéric Moron, Michel Lours, Yannick Bidel, A. Bresson, A. Landragin, and P. Bouyer. Detecting inertial effects with airborne matter-wave interferometry. *Nature Communications*, 2(1):474, sep 2011.

[59] B Barrett, A Bertoldi, and P Bouyer. Inertial quantum sensors using light and matter. *Physica Scripta*, 91(5):053006, may 2016.

[60] Todd Lyndell Gustavson. *Precision rotation sensing using atom interferometry*. PhD thesis, Stanford University, 2000.

[61] T L Gustavson, A Landragin, and M A Kasevich. Rotation sensing with a dual atom-interferometer Sagnac gyroscope. *Classical and Quantum Gravity*, 17(12):2385, 2000.

[62] B Dubetsky and M A Kasevich. Atom interferometer as a selective sensor of rotation or gravity. *Physical Review A*, 74(2):023615, aug 2006.

[63] Brynle Barrett, Rémy Geiger, Indranil Dutta, Matthieu Meunier, Benjamin Canuel, Alexandre Gauguet, Philippe Bouyer, and Arnaud Landragin. The Sagnac effect: 20 years of development in matter-wave interferometry. *Comptes Rendus Physique*, 15(10):875–883, dec 2014.

[64] Malte Schmidt. *A mobile high-precision gravimeter based on atom interferometry*. PhD thesis, Humboldt-Universität zu Berlin, 2011.

[65] Brenton Young, Mark Kasevich, and Steven Chu. Precision atom interferometry with light pulses. In Paul R Berman, editor, *Atom Interferometry*, pages 363–406. Elsevier, San Diego, 1997.

[66] Grant Biedermann. *Gravity tests, differential accelerometry and interleaved clocks with cold atom interferometers*. PhD thesis, Stanford University, 2008.

[67] Achim Peters. *High precision gravity measurements using atom interferometry*. PhD thesis, Stanford University, 1998.

[68] Pierrick Cheiney, Lauriane Fouché, Simon Templier, Fabien Napolitano, Baptiste Battelier, Philippe Bouyer, and Brynle Barrett. Navigation-compatible hybrid quantum accelerometer using a Kalman filter. *Physical Review Applied*, 10(3):34030, 2018.

[69] Lingziao Zhu. *A cold atoms gravimeter for use in absolute gravity comparisons*. PhD thesis, University of Birmingham, 2018.

[70] Patrick Cheinet, Benjamin Canuel, F. Pereira Dos Santos, Alexandre Gauguet, Florence Yver-Leduc, and Arnaud Landragin. Measurement of the Sensitivity Function in a Time-Domain Atomic Interferometer. *IEEE Transactions on Instrumentation and Measurement*, 57(6):1141–1148, jun 2008.

[71] David W Allan. Statistics of atomic frequency standards. *Proceedings of the IEEE*, 54(2):221–230, 1966.

[72] David A Howe, David W Allan, and J A Barnes. Properties of signal sources and measurement methods. In *Thirty Fifth Annual Frequency Control Symposium*, pages 669–716. IEEE, 1981.

[73] John K Stockton, Xinan Wu, and Mark A Kasevich. Bayesian estimation of differential interferometer phase. *Physical Review A*, 76(3):033613, sep 2007.

[74] Holger Müller, Sheng-wey Chiow, Quan Long, Sven Herrmann, and Steven Chu. Atom Interferometry with up to 24-Photon-Momentum-Transfer Beam Splitters. *Physical Review Letters*, 100(18):180405, may 2008.

[75] Mauro Chiarotti, Jonathan N Tinsley, Satvika Bandarupally, Shamaila Manzoor, Michele Sacco, Leonardo Salvi, and Nicola Poli. Practical limits for large-momentum-transfer clock atom interferometers. *arXiv preprint arXiv:2206.05145*, jun 2022.

[76] Jack C Saywell, Ilya Kuprov, David Goodwin, Max Carey, and Tim Freegarde. Optimal control of mirror pulses for cold-atom interferometry. *Physical Review A*, 98(2):023625, aug 2018.

[77] Xinan Wu. *Gravity gradient survey with a mobile atom interferometer*. PhD thesis, Stanford University, 2009.

[78] Matthew Himsworth. *Coherent manipulation of ultracold rubidium*. PhD thesis, University of Southmpton, 2009.

[79] William D Phillips, John V Prodan, and Harold J Metcalf. Laser cooling and electromagnetic trapping of neutral atoms. *J. Opt. Soc. Am. B*, 2(11):1751–1767, nov 1985.

[80] Steven Chu, Leo Hollberg, John E Bjorkholm, Alex Cable, and Arthur Ashkin. Three-dimensional viscous confinement and cooling of atoms by resonance radiation pressure. *Physical review letters*, 55(1):48, 1985.

[81] Arthur Ashkin and James P Gordon. Stability of radiation-pressure particle traps: an optical Earnshaw theorem. *Optics Letters*, 8(10):511, oct 1983.

[82] Andrei-Aurel Dragomir. *Cold atoms in your pocket-Enabling technologies*. PhD thesis, University of Southampton, 2018.

[83] J.J. Arlt, O. Maragò, Stephen Webster, S Hopkins, and C.J. Foot. A pyramidal magneto-optical trap as a source of slow atoms. *Optics Communications*, 157(1-6):303–309, dec 1998.

[84] Matthieu Vangeleyn, Paul F Griffin, Erling Riis, and Aidan S Arnold. Single-laser, one beam, tetrahedral magneto-optical trap. *Optics Express*, 17(16):13601, aug 2009.

[85] B.M. Xu, X Chen, J Wang, and M.S. Zhan. Realization of a single-beam mini magneto-optical trap: A candidate for compact CPT cold atom-clocks. *Optics Communications*, 281(23):5819–5823, dec 2008.

[86] Daniel A Steck. Rubidium 87 D line data, 2019.

[87] Y Castin, H Wallis, and Jean Dalibard. Limit of Doppler cooling. *Journal of the Optical Society of America B*, 6(11):2046, nov 1989.

[88] Paul D Lett, Richard N Watts, Christoph I Westbrook, William D Phillips, Phillip L Gould, and Harold J Metcalf. Observation of Atoms Laser Cooled below the Doppler Limit. *Physical Review Letters*, 61(2):169–172, jul 1988.

[89] Jean Dalibard and Claude Cohen-Tannoudji. Laser cooling below the Doppler limit by polarization gradients: simple theoretical models. *Journal of the Optical Society of America B*, 6(11):2023, nov 1989.

[90] Zhong-Hua Ji, Jin-Peng Yuan, Yan-Ting Zhao, Xue-Fang Chang, Lian-Tuan Xiao, and Suo-Tang Jia. Systematically investigating the polarization gradient cooling in an optical molasses of ultracold cesium atoms. *Chinese Physics B*, 23(11):113702, nov 2014.

[91] F Lienhart, S Boussen, O Carraz, N Zahzam, Y Bidel, and AJAPB Bresson. Compact and robust laser system for rubidium laser cooling based on the frequency doubling of a fiber bench at 1560 nm. *Applied Physics B*, 89(2-3):177–180, nov 2007.

[92] Paul D Lett, William D Phillips, S L Rolston, Carol E Tanner, R N Watts, and C I Westbrook. Optical molasses. *Journal of the Optical Society of America B*, 6(11):2084, nov 1989.

[93] Mariusz Gajda and Jan Mostowski. Three-dimensional theory of the magneto-optical trap: Doppler cooling in the low-intensity limit. *Physical Review A*, 49(6):4864–4875, jun 1994.

[94] Yvan Castin and Klaus Mølmer. Monte Carlo Wave-Function Analysis of 3D Optical Molasses. *Physical Review Letters*, 74(19):3772–3775, may 1995.

[95] A M Steane, M Chowdhury, and C J Foot. Radiation force in the magneto-optical trap. *Journal of the Optical Society of America B*, 9(12):2142–2158, dec 1992.

[96] T. Arpornthip, C. A. Sackett, and K. J. Hughes. Vacuum-pressure measurement using a magneto-optical trap. *Physical Review A*, 85(3):033420, mar 2012.

[97] K Lindquist, M Stephens, and C Wieman. Experimental and theoretical study of the vapor-cell Zeeman optical trap. *Physical Review A*, 46(7):4082–4090, oct 1992.

[98] James P. Burke, John L Bohn, B D Esry, and Chris H Greene. Prospects for Mixed-Isotope Bose-Einstein Condensates in Rubidium. *Physical Review Letters*, 80(10):2097–2100, mar 1998.

[99] C Monroe, W Swann, H Robinson, and C Wieman. Very cold trapped atoms in a vapor cell. *Physical Review Letters*, 65(13):1571–1574, sep 1990.

[100] Xiao-Long Wang, Bing Cheng, Bin Wu, Zhao-Ying Wang, and Qiang Lin. A Simplified Cold Atom Source for 3-D MOT Loading. *Chinese Physics Letters*, 28(5):053701, may 2011.

[101] Sören Dörscher, Alexander Thobe, Bastian Hundt, André Kochanke, Rodolphe Le Targat, Patrick Windpassinger, Christoph Becker, and Klaus Sengstock. Creation of quantum-degenerate gases of ytterbium in a compact 2D-/3D-magneto-optical trap setup. *Review of Scientific Instruments*, 84(4):043109, apr 2013.

[102] Wolfgang Ketterle, Dallin S Durfee, and D M Stamper-Kurn. Making, probing and understanding Bose-Einstein condensates. *arXiv preprint cond-mat/9904034*, apr 1999.

[103] David A Smith, Simon Aigner, Sebastian Hofferberth, Michael Gring, Mauritz Andersson, Stefan Wildermuth, Peter Krüger, Stephan Schneider, Thorsten Schumm, and Jörg Schmiedmayer. Absorption imaging of ultracold atoms on atom chips. *Optics Express*, 19(9):8471, apr 2011.

[104] Andrejs Vorozcovs, Matthew Weel, Scott Beattie, Saviour Cauchi, and A Kumarakrishnan. Measurements of temperature scaling laws in an optically dense magneto-optical trap. *Journal of the Optical Society of America B*, 22(5):943, may 2005.

[105] William D Phillips. Nobel Lecture: Laser cooling and trapping of neutral atoms. *Reviews of Modern Physics*, 70(3):721–741, jul 1998.

[106] Dennis Becker, Maike D Lachmann, Stephan T Seidel, Holger Ahlers, Aline N Dinkelaker, Jens Grosse, Ortwin Hellmig, Hauke Müntinga, Vladimir Schkolnik, Thijs Wendrich, and Others. Space-borne Bose–Einstein condensation for precision interferometry. *Nature*, 562(7727):391–395, oct 2018.

[107] S Pradhan and B N Jagatap. Measurement of temperature of laser cooled atoms by one-dimensional expansion in a magneto-optical trap. *Review of Scientific Instruments*, 79(1):013101, jan 2008.

[108] David S Weiss, Erling Riis, Yaakov Shevy, P. Jeffrey Ungar, and Steven Chu. Optical molasses and multilevel atoms: experiment. *Journal of the Optical Society of America B*, 6(11):2072, nov 1989.

[109] Gary C Bjorklund. Frequency-modulation spectroscopy: a new method for measuring weak absorptions and dispersions. *Optics Letters*, 5(1):15, jan 1980.

[110] Jürgen Appel, Andrew MacRae, and Alexander I Lvovsky. A versatile digital GHz phase lock for external cavity diode lasers. *Measurement Science and Technology*, 20(5):55302, may 2009.

[111] Paul Siddons, Charles S Adams, Chang Ge, and Ifan G Hughes. Absolute absorption on rubidium D lines: comparison between theory and experiment. *Journal of Physics B: Atomic, Molecular and Optical Physics*, 41(15):155004, aug 2008.

[112] Takafumi Chiba, Yasuo Ohtera, and Shojiro Kawakami. Polarization stabilizer using liquid crystal rotatable waveplates. *Journal of Lightwave Technology*, 17(5):885–890, may 1999.

[113] Katsuhiko Hirabayashi. Electrically controllable liquid-crystal rotatable wave plate with variable phase retardation. *Applied Optics*, 44(17):3552, jun 2005.

[114] Andrii B Golovin, Sergij V Shiyanovskii, and Oleg D Lavrentovich. Fast switching dual-frequency liquid crystal optical retarder, driven by an amplitude and frequency modulated voltage. *Applied Physics Letters*, 83(19):3864–3866, nov 2003.

[115] HsienHui Cheng, Achintya Bhowmik, and Philip J Bos. Fast-response liquid crystal variable optical retarder and multilevel attenuator. *Optical Engineering*, 52(10):107105, oct 2013.

[116] Shin-Tson Wu and Chiung-Sheng Wu. High-speed liquid-crystal modulators using transient nematic effect. *Journal of Applied Physics*, 65(2):527–532, jan 1989.

[117] Shin-Tson Wu. Nematic liquid crystal modulator with response time less than 100 μs at room temperature. *Applied Physics Letters*, 57(10):986–988, sep 1990.

[118] Scot W McDermott, Samuel C Rogers, John D Gonglewski, and Stephen L Browne. Electronic control system exploiting both the dual-frequency effect and the transient nematic effect for a fast 127-element nematic liquid crystal spatial light modulator. In Domenico Bonaccini and Robert K. Tyson, editors, *Adaptive Optical System Technologies*, volume 3353, page 782. International Society for Optics and Photonics, sep 1998.

[119] O Carraz, F Lienhart, R Charrière, M Cadoret, N Zahzam, Y Bidel, and AJAPB Bresson. Compact and robust laser system for onboard atom interferometry. *Applied Physics B*, 97(2):405–411, oct 2009.

[120] Ch Salomon, J Dalibard, W D Phillips, A Clairon, and S Guellati. Laser Cooling of Cesium Atoms Below 3 μK. *Europhysics Letters (EPL)*, 12(8):683–688, aug 1990.

[121] Tomasz M Brzozowski, Maria Maczynska, Michal Zawada, Jerzy Zachorowski, and Wojciech Gawlik. Time-of-flight measurement of the temperature of cold atoms for short trap-probe beam distances. *Journal of Optics B: Quantum and Semiclassical Optics*, 4(1):62–66, feb 2002.

[122] Wolfgang Demtröder. *Laser Spectroscopy*. Advanced Texts in Physics. Springer Berlin Heidelberg, Berlin, Heidelberg, 2003.

[123] Olivier Carraz, Renée Charrière, Malo Cadoret, Nassim Zahzam, Yannick Bidel, and Alexandre Bresson. Phase shift in an atom interferometer induced by the additional laser lines of a Raman laser generated by modulation. *Physical Review A*, 86(3):033605, sep 2012.

[124] Paul A Williams, William C Swann, and Nathan R Newbury. High-stability transfer of an optical frequency over long fiber-optic links. *Journal of the Optical Society of America B*, 25(8):1284, aug 2008.

[125] N R Newbury, P A Williams, and W C Swann. Coherent transfer of an optical carrier over 251 km. *Optics Letters*, 32(21):3056, nov 2007.

[126] Elizabeth A Donley, Thomas P Heavner, F Levi, M O Tataw, and Steven R Jefferts. Double-pass acousto-optic modulator system. *Review of Scientific Instruments*, 76(6):63112, 2005.

[127] David W Allan, Marc A Weiss, and James L Jespersen. A frequency-domain view of time-domain characterization of clocks and time and frequency distribution systems. In *Proceedings of the 45th Annual Symposium on Frequency Control 1991*, pages 667–678. IEEE, 1991.

[128] J J Snyder. An ultra-high resolution frequency meter. In *Thirty Fifth Annual Frequency Control Symposium*, pages 464–469. IEEE, 1981.

[129] Chris Overstreet. *Atom-interferometric test of the equivalence principle and observation of a quantum system in curved spacetime*. PhD thesis, Stanford University, 2020.

[130] Savas Dimopoulos, Peter W Graham, Jason M Hogan, Mark A Kasevich, and Surjeet Rajendran. Atomic gravitational wave interferometric sensor. *Physical Review D*, 78(12):122002, dec 2008.

[131] Henning Albers, Alexander Herbst, Logan L Richardson, Hendrik Heine, Dipankar Nath, Jonas Hartwig, Christian Schubert, Christian Vogt, Marian Woltmann, Claus Lämmerzahl, Sven Herrmann, Wolfgang Ertmer, Ernst M. Rasel, and Dennis Schlippert. Quantum test of the Universality of Free Fall using rubidium and potassium. *The European Physical Journal D*, 74(7):145, jul 2020.

[132] Alex Sugarbaker. *Atom interferometry in a 10 m fountain.* Stanford University, 2014.

[133] Diviya Devani, Stephen Maddox, Ryan Renshaw, Nigel Cox, Helen Sweeney, Trevor Cross, Michael Holynski, Raffaele Nolli, Jonathan Winch, Kai Bongs, Karen Holland, David Colebrook, Neil Adams, Kevin Quillien, James Buckle, Anupe Karde, Mark Farries, Tom Legg, Richard Webb, Corin Gawith, Sam A. Berry, and Lewis Carpenter. Gravity sensing: cold atom trap onboard a 6U CubeSat. *CEAS Space Journal*, 12(4):539–549, dec 2020.

[134] Bin Wu, Zhaoying Wang, Bing Cheng, Qiyu Wang, Aopeng Xu, and Qiang Lin. The investigation of a μGal-level cold atom gravimeter for field applications. *Metrologia*, 51(5):452–458, oct 2014.

Appendix A

Additional algebra

A common annoyance among students of maths and physics is the ominous phrase "this is left as an exercise for the reader". As a perpetual student myself, and having felt annoyance at that phrase many times, I felt it unfair to risk providing the same emotion to a reader. While I now know what I have derived in this thesis; there was once a time when I did not. The following is mostly my own working-outs and small algebraic steps between equations that helped me understand the broad brush-strokes of derivations in previous chapters. There is nothing particularly spectacular hidden in these pages and this section can be skipped without any loss of content. My hope is that this may provide assistance to a someone attempting and struggling to wrap their head around these concepts as I once did. Some steps may be small and inconsequential to the broader picture but are left in for clarity.

A.1 Raman Transitions

A.1.1 Applying transformation to the time-dependent Schrödinger equation

Apply transformation substitution, $|\Psi'(t)\rangle = \hat{T}\,|\Psi(t)\rangle \Rightarrow |\Psi(t)\rangle = \hat{T}^\dagger\,|\Psi'(t)\rangle$, to the TDSE:

$$i\hbar\frac{\partial}{\partial t}\left(\hat{T}^\dagger\,|\Psi'(t)\rangle\right) = \hat{H}\left(\hat{T}^\dagger\,|\Psi'(t)\rangle\right). \tag{A.1}$$

The product rule on the left-hand side of the equation gives

$$i\hbar\left(\frac{\partial}{\partial t}\hat{T}^\dagger\left|\Psi'(t)\right\rangle+\hat{T}^\dagger\frac{\partial}{\partial t}\left|\Psi'(t)\right\rangle\right)=\hat{H}\left(\hat{T}^\dagger\left|\Psi'(t)\right\rangle\right) \tag{A.2}$$

Premultiplying by $\hat{T}$ and performing some algebra:

$$i\hbar\left(\underbrace{\hat{T}\frac{\partial}{\partial t}\hat{T}^\dagger\left|\Psi'(t)\right\rangle}_{\text{move to other side}}+\underbrace{\hat{T}\hat{T}^\dagger}_{=I}\frac{\partial}{\partial t}\left|\Psi'(t)\right\rangle\right)=\hat{T}\hat{H}\hat{T}^\dagger\left|\Psi'(t)\right\rangle \tag{A.3}$$

$$i\hbar\frac{\partial}{\partial t}\left|\Psi'(t)\right\rangle=\hat{T}\hat{H}\hat{T}^\dagger\left|\Psi'(t)\right\rangle-i\hbar\hat{T}\frac{\partial}{\partial t}\hat{T}^\dagger\left|\Psi'(t)\right\rangle \tag{A.4}$$

$$i\hbar\left|\Psi'(t)\right\rangle=\underbrace{\left(\hat{T}\hat{H}\hat{T}^\dagger-i\hbar\hat{T}\frac{\partial}{\partial t}\hat{T}^\dagger\right)}_{\text{Transformed Hamiltonian, }\hat{H}'}\left|\Psi'(t)\right\rangle \tag{A.5}$$

A.2 The Bloch sphere picture

We begin by introducing the density matrix,

$$\rho=\left|\Psi\right\rangle\left\langle\Psi\right|=\begin{pmatrix}c_1\\c_2\end{pmatrix}\begin{pmatrix}c_1^*&c_2^*\end{pmatrix}=\begin{pmatrix}\left|c_1\right|^2&c_1c_2^*\\c_2c_1^*&\left|c_2\right|^2\end{pmatrix}=\begin{pmatrix}\rho_{11}&\rho_{12}\\\rho_{21}&\rho_{22}\end{pmatrix}, \tag{A.6}$$

where the off diagonal elements are the coherences of the system. The following closely follows the derivation found in Himsworth [78] and another derivation can be found in Foot [41]. Dunning [40] contains a full derivation including the laser phase terms. We have chosen to ignore the laser phase terms here for brevity. The Hamiltonian (Equation 2.3) can be represented in its matrix form[1],

$$\hat{H}=\hbar\begin{pmatrix}\omega_1&\frac{\Omega^*}{2}e^{i\omega_{\mathrm{EM}}t}\\\frac{\Omega}{2}e^{-i\omega_{\mathrm{EM}}t}&\omega_2\end{pmatrix}, \tag{A.7}$$

where the diagonal elements are from the unperturbed Hamiltonian, $\hat{H}_0$, and the off-diagonal elements from the perturbation, $\hat{V}(t)$. Substituting this Hamiltonian and the density matrix, ρ, into the Liouville form of the TDSE,

$$i\hbar\dot{\rho}=\Big[\hat{H},\rho\Big], \tag{A.8}$$

[1]Here we have also used the rotating wave approximation to ignore any fast oscillating terms

we obtain the rate of change for the density matrix populations:

$$\dot{\rho_{11}} = \frac{i}{2}\Omega\rho_{12}e^{-i\omega_{\mathrm{EM}}t} - \frac{i}{2}\Omega^*\rho_{21}e^{-i\omega_{\mathrm{EM}}t} + \gamma\rho_{22} \tag{A.9a}$$

$$\dot{\rho_{22}} = \frac{i}{2}\Omega^*\rho_{21}e^{-i\omega_{\mathrm{EM}}t} - \frac{i}{2}\Omega\rho_{12}e^{-i\omega_{\mathrm{EM}}t} - \gamma\rho_{22} \tag{A.9b}$$

$$\dot{\rho_{12}} = i\rho_{12}\omega - \frac{i}{2}\Omega^*e^{-i\omega_{\mathrm{EM}}t}(\rho_{11} - \rho_{22}) - \frac{\gamma}{2}\rho_{12} \tag{A.9c}$$

$$\dot{\rho_{21}} = -i\rho_{21}\omega + \frac{i}{2}\Omega^*e^{-i\omega_{\mathrm{EM}}t}(\rho_{11} - \rho_{22}) - \frac{\gamma}{2}\rho_{21}, \tag{A.9d}$$

where γ is the natural decay rate of $|2\rangle$ to $|1\rangle$ through spontaneous emission[2] and the $\gamma/2$ terms are known as the transverse relaxation rates [78]. By transforming into a rotating frame by making the following substitutions,

$$\tilde{\rho_{12}} = \rho_{12}e^{-i\omega_{\mathrm{EM}}t} \tag{A.10a}$$

$$\tilde{\rho_{21}} = \rho_{21}e^{-\omega_{\mathrm{EM}}t} \tag{A.10b}$$

$$\tilde{\rho_{11}} = \rho_{11} \tag{A.10c}$$

$$\tilde{\rho_{22}} = \rho_{22}, \tag{A.10d}$$

we can remove any fast oscillating terms and arrive at the following equations:

$$\dot{\tilde{\rho_{11}}} = -\frac{i\Omega}{2}\left(\tilde{\rho_{21}} - \tilde{\rho_{12}}\right) + \gamma\tilde{\rho_{22}} \tag{A.11a}$$

$$\dot{\tilde{\rho_{22}}} = +\frac{i\Omega}{2}\left(\tilde{\rho_{21}} - \tilde{\rho_{12}}\right) - \gamma\tilde{\rho_{22}} \tag{A.11b}$$

$$\dot{\tilde{\rho_{12}}} = -i\tilde{\rho_{12}}\delta - \frac{i\Omega}{2}\left(\tilde{\rho_{22}} - \tilde{\rho_{11}}\right) - \frac{\gamma}{2}\tilde{\rho_{12}} \tag{A.11c}$$

$$\dot{\tilde{\rho_{21}}} = +i\tilde{\rho_{21}}\delta + \frac{i\Omega}{2}\left(\tilde{\rho_{22}} - \tilde{\rho_{11}}\right) - \frac{\gamma}{2}\tilde{\rho_{21}}, \tag{A.11d}$$

where $\delta = \omega_{\mathrm{EM}} - \omega_{12}$ is the laser detuning from the transition resonance, ω_{12}.

To map these onto the Bloch sphere we use can use the Pauli spin matrices

$$u = \begin{pmatrix} 0 & 1 \\ 1 & 0 \end{pmatrix}\tilde{\rho} \quad = \tilde{\rho_{12}} + \tilde{\rho_{21}} \tag{A.12a}$$

$$v = \begin{pmatrix} 0 & -i \\ i & 0 \end{pmatrix}\tilde{\rho} = -i\left(\tilde{\rho_{12}} - \tilde{\rho_{21}}\right) \tag{A.12b}$$

$$w = \begin{pmatrix} 1 & 0 \\ 0 & -1 \end{pmatrix}\tilde{\rho} = \tilde{\rho_{11}} - \tilde{\rho_{22}}. \tag{A.12c}$$

[2] $|1\rangle$ is assumed to be the lowest ground state of the system and hence cannot spontaneously decay. We therefore have no decay term associated with it.

By substituting Equations A.11 into the time derivative of these equations we arrive at the OBEs

$$\dot{u} = \delta v - \frac{\gamma}{2}u \tag{A.13a}$$

$$\dot{v} = -\delta u + \Omega w - \frac{\gamma}{2}v \tag{A.13b}$$

$$\dot{w} = -\Omega v + \gamma(1 - w). \tag{A.13c}$$

We can now define the optical Bloch vector by ignoring the decay terms ($\gamma = 0$):

$$\mathbf{R} = u\hat{\mathbf{x}} + v\hat{\mathbf{y}} + w\hat{\mathbf{z}}, \tag{A.14}$$

where $\hat{\mathbf{x}}$, $\hat{\mathbf{y}}$, and $\hat{\mathbf{z}}$ are the unit vectors on the Bloch sphere. Equations A.13 can then be written as

$$\dot{\mathbf{R}} = \mathbf{R} \times (\Omega\hat{\mathbf{x}} + \delta\hat{\mathbf{z}}). \tag{A.15}$$

Here we can see that the Rabi frequency, modified by the laser detuning, behaves as a torque on the current state of the atom. Therefore the laser pulses shown previously can be represented as rotations on the Bloch sphere.

A.3 Atom interferometry

This section describes certain mathematical details of the matter-wave Mach-Zehnder interferometer sequence shown in Chapter 3. It is useful to have in mind the Bloch sphere (Section 2.2) picture in mind throughout these steps. This geometrical representation helped me greatly in building an intuitive understanding of the interferometry sequence.

Here we will first build tools for propagating the atomic wavefunction, $|\Psi(t)\rangle$, through the interferometry sequence. Followed by a run through of the whole sequence to see that we arrive at the expected phase dependent interferometer output: Equation 3.13. This has been adapted mainly from Saywell [38].

A.3.1 Solving the Shrödinger equation with matrix exponentials

Assuming a general time *independent* Hamiltonian, $\hat{H}$, the following equation

$$|\Psi(t)\rangle = \exp\left[\frac{-i}{\hbar}\hat{H} \cdot (t - t_0)\right] |\Psi(t_0)\rangle \tag{A.16}$$

is a solution to the TDSE. We check this by substituting it into the TDSE:

$$\frac{\partial}{\partial t}\left|\Psi(t)\right\rangle = \frac{-i}{\hbar}\hat{H}\left|\Psi(t)\right\rangle. \tag{A.17}$$

Beginning with the left hand side of the equation; we can expand the exponential[3]

$$\begin{aligned}\left|\Psi(t)\right\rangle = \Bigg[I + \left(\frac{-i}{\hbar}\hat{H}\cdot(t-t_0)\right) + \frac{1}{2!}\left(\frac{-i}{\hbar}\hat{H}\cdot(t-t_0)\right)^2 \\ + \ldots + \frac{1}{n!}\left(\frac{-i}{\hbar}\hat{H}\cdot(t-t_0)\right)^n\Bigg]\left|\Psi(t_0)\right\rangle\end{aligned} \tag{A.18}$$

We then differentiate with respect to time, remembering $\left|\Psi(t_0)\right\rangle$ is constant,

$$\begin{aligned}\frac{\partial}{\partial t}\left|\Psi(t)\right\rangle &= \Bigg[\left(\frac{-i}{\hbar}\hat{H}\right) + \frac{\partial}{\partial t}\frac{1}{2!}\left(\frac{-i}{\hbar}\hat{H}\cdot(t-t_0)\right)^2 \\ &\quad + \frac{\partial}{\partial t}\frac{1}{3!}\left(\frac{-i}{\hbar}\hat{H}\cdot(t-t_0)\right)^3 + \ldots \\ &\quad + \frac{\partial}{\partial t}\frac{1}{n!}\left(\frac{-i}{\hbar}\hat{H}\cdot(t-t_0)\right)^n\Bigg]\left|\Psi(t_0)\right\rangle \qquad \text{(A.19)} \\ &= \Bigg[\left(\frac{-i}{\hbar}\hat{H}\right) + \frac{2}{2!}\left(\frac{-i}{\hbar}\hat{H}\cdot(t-t_0)\right)\cdot\frac{-i}{\hbar}\hat{H} \\ &\quad + \frac{3}{3!}\left(\frac{-i}{\hbar}\hat{H}\cdot(t-t_0)\right)^2\cdot\frac{-i}{\hbar}\hat{H} + \ldots \\ &\quad + \frac{n}{n!}\left(\frac{-i}{\hbar}\hat{H}\cdot(t-t_0)\right)^{n-1}\cdot\frac{-i}{\hbar}\hat{H}\Bigg]\left|\Psi(t_0)\right\rangle. \qquad \text{(A.20)}\end{aligned}$$

Factoring out $\frac{-i}{\hbar}\hat{H}$ and tiding up the factorials we arrive at

$$\begin{aligned}\frac{\partial}{\partial t}\left|\Psi(t)\right\rangle = \frac{-i}{\hbar}\hat{H}\Bigg[I + \left(\frac{-i}{\hbar}\hat{H}\cdot(t-t_0)\right) + \frac{1}{2!}\left(\frac{-i}{\hbar}\hat{H}\cdot(t-t_0)\right)^2 \\ + \ldots + \frac{1}{n!}\left(\frac{-i}{\hbar}\hat{H}\cdot(t-t_0)\right)^n\Bigg]\left|\Psi(t_0)\right\rangle.\end{aligned} \tag{A.21}$$

Which can then be described succinctly with a familiar matrix exponential,

$$\frac{\partial}{\partial t}\left|\Psi(t)\right\rangle = \frac{-i}{\hbar}\hat{H}\exp\left[\frac{-i}{\hbar}\hat{H}\cdot(t-t_0)\right]\left|\Psi(t_0)\right\rangle, \tag{A.22}$$

[3] $\exp(x)$ is, rather misleadingly, shorthand for the infinite sum of $x^0 + x^1 + x^2/2! + x^3/3! + \ldots + x^n/n!$. Turns out real numbers aren't the only thing you can substitute for x. In our case we even put a matrix in there!

which is identical to the TDSE, Equation A.17, when substituting in the wavefunction, Equation A.16, into the right hand side.

We can then call the exponential in Equation A.16 the propagator operator:

$$\hat{U}(t,t_0) = \exp\left[\frac{-i}{\hbar}\hat{H}\cdot(t-t_0)\right], \tag{A.23}$$

which propagates an initial state, $|\Psi t_0\rangle$, through time to the final state, $|\Psi(t)\rangle$.

Equation A.16 is only valid when the Hamiltonian is constant. As we will see in Appendix A.3.2 this assumption breaks down and we need to solve the TDSE again.

Now lets use the rotating frame Hamiltonian:

$$\hat{H}_R = \frac{\hbar}{2}\begin{pmatrix}\delta & \Omega_R e^{-i\phi_L}\\ \Omega_R e^{i\phi_L} & -\delta\end{pmatrix} = \frac{\hbar}{2}\mathbf{\Omega}\cdot\hat{\sigma} \tag{A.24}$$

and express it as the product of the field vector, $\mathbf{\Omega} = \Omega_R\cos(\phi_L)\hat{\mathbf{x}} + \Omega_R\sin(\phi_L)\hat{\mathbf{y}} + \delta\hat{\mathbf{z}}$, and the vector of Pauli matrices, $\hat{\sigma} = (\hat{\sigma_x},\hat{\sigma_y},\hat{\sigma_z})^{\mathsf{T}}$, where ϕ_L is the laser phase, Ω_R is the two photon Rabi frequency, and δ is the laser detuning. Those familiar with the Bloch sphere will recognise these vectors. We will not derive these vectors here as they are only used as a shortcut to the result we are looking for — this will make more sense in a couple of steps. If you are confused of the derivation or physical meaning of Omega please refer to Section 2.2 in the main body of the text.

As a quick proof that $\hat{H}_R$ can be expressed this way we simply perform the dot product:

$$\mathbf{\Omega}\cdot\hat{\sigma} = \Omega_R\cos(\phi_L)\hat{\sigma_x} + \Omega_R\sin(\phi_L)\hat{\sigma_y} + \delta\hat{\sigma_z} \tag{A.25}$$

$$= \Omega_R\cos(\phi_L)\begin{pmatrix}0 & 1\\ 1 & 0\end{pmatrix} + \Omega_R\sin(\phi_L)\begin{pmatrix}0 & -i\\ i & 0\end{pmatrix} + \delta\begin{pmatrix}1 & 0\\ 0 & -1\end{pmatrix} \tag{A.26}$$

$$= \begin{pmatrix}\delta & \Omega_R\cos(\phi_L) - i\Omega_R\sin(\phi_L)\\ \Omega_R\cos(\phi_L) + i\Omega_R\sin(\phi_L) & -\delta\end{pmatrix} \tag{A.27}$$

$$\mathbf{\Omega}\cdot\hat{\sigma} = \begin{pmatrix}\delta & \Omega_R e^{-i\phi_L}\\ \Omega_R e^{i\phi_L} & -\delta\end{pmatrix}. \tag{A.28}$$

Which satisfies the Hamiltonian.

We can now represent the propagator operator as such:

$$\hat{U} = \exp\left[\frac{-i}{\hbar}\frac{\hbar}{2}\mathbf{\Omega}\cdot\hat{\sigma}\cdot(t-t_0)\right] = \exp\left[\frac{-i\mathbf{\Omega}\cdot\hat{\sigma}}{2}(t-t_0)\right]. \tag{A.29}$$

We can then apply the identity $\exp(i\alpha\hat{\mathbf{n}}\cdot\hat{\sigma}) = I\cos(\alpha) + i\hat{\mathbf{n}}\cdot\hat{\sigma}\sin(\alpha)$, where I is the identity matrix, to retrieve a computable matrix. First lets clearly define the different variables used in the identity:

$$\alpha = \frac{-|\mathbf{\Omega}|}{2}(t-t_0) = \frac{-\sqrt{\Omega_R^2+\delta^2}}{2}(t-t_0) \quad \text{and} \quad \hat{\mathbf{n}} = \frac{\mathbf{\Omega}}{\sqrt{\Omega_R^2+\delta^2}}. \tag{A.30}$$

Substituting these into the identity results in

$$\hat{U} = I\cos(\alpha) + \frac{i}{\sqrt{\Omega_R^2+\delta^2}}\begin{pmatrix}\Omega_R\cos(\phi_L)\\ \Omega_R\sin(\phi_L)\\ \delta\end{pmatrix}\cdot\begin{pmatrix}\hat{\sigma_x}\\ \hat{\sigma_y}\\ \hat{\sigma_z}\end{pmatrix}\sin(\alpha) \tag{A.31}$$

$$= I\cos(\alpha) + \frac{i}{\sqrt{\Omega_R^2+\delta^2}}\left(\Omega_R\cos(\phi_L)\hat{\sigma_x} + \Omega_R\sin(\phi_L)\hat{\sigma_y} + \delta\hat{\sigma_z}\right)\sin(\alpha) \tag{A.32}$$

$$\begin{aligned}= I\cos(\alpha) + \frac{i}{\sqrt{\Omega_R^2+\delta^2}}\Bigg[&\begin{pmatrix}0 & \Omega_R\cos(\phi_L)\\ \Omega_R\cos(\phi_L) & 0\end{pmatrix}\\ &+\begin{pmatrix}0 & -i\Omega_R\sin(\phi_L)\\ i\Omega_R\sin(\phi_L) & 0\end{pmatrix} + \begin{pmatrix}\delta & 0\\ 0 & -\delta\end{pmatrix}\Bigg]\sin(\alpha)\end{aligned} \tag{A.33}$$

$$= \begin{pmatrix}\cos(\alpha) + \frac{i\delta}{\sqrt{\Omega_R^2+\delta^2}}\sin(\alpha) & \frac{i\Omega_R}{\sqrt{\Omega_R^2+\delta^2}}(\cos(\phi_L) - i\sin(\phi_L))\sin(\alpha)\\ \frac{i\Omega_R}{\sqrt{\Omega_R^2+\delta^2}}(\cos(\phi_L) + i\sin(\phi_L))\sin(\alpha) & \cos(\alpha) - \frac{i\delta}{\sqrt{\Omega_R^2+\delta^2}}\sin(\alpha)\end{pmatrix} \tag{A.34}$$

$$\hat{U} = \begin{pmatrix}\cos(\alpha) + \frac{i\delta}{\sqrt{\Omega_R^2+\delta^2}}\sin(\alpha) & \frac{i\Omega_R}{\sqrt{\Omega_R^2+\delta^2}}e^{-i\phi_L}\sin(\alpha)\\ \frac{i\Omega_R}{\sqrt{\Omega_R^2+\delta^2}}e^{i\phi_L}\sin(\alpha) & \cos(\alpha) - \frac{i\delta}{\sqrt{\Omega_R^2+\delta^2}}\sin(\alpha)\end{pmatrix}. \tag{A.35}$$

Some symmetry can be seen here. We then can make the necessary substitutions to obtain $\hat{U}$ in the form:

$$\hat{U} = \begin{pmatrix}C^* & -iS^*\\ -iS & C\end{pmatrix}. \tag{A.36}$$

The reasoning for the choice of the off-diagonal terms will become apparent when we eventually use this operator. We define these terms as so:

$$C = \cos\left(\frac{-\sqrt{\Omega_R^2+\delta^2}}{2}(t-t_0)\right) - \frac{i\delta}{\sqrt{\Omega_R^2+\delta^2}}\sin\left(\frac{-\sqrt{\Omega_R^2+\delta^2}}{2}(t-t_0)\right) \tag{A.37}$$

$$\Rightarrow C = \cos\left(\frac{\sqrt{\Omega_R^2+\delta^2}}{2}(t-t_0)\right) + \frac{i\delta}{\sqrt{\Omega_R^2+\delta^2}}\sin\left(\frac{\sqrt{\Omega_R^2+\delta^2}}{2}(t-t_0)\right) \tag{A.38}$$

$$-iS = \frac{i\Omega_R}{\sqrt{\Omega_R^2 + \delta^2}} e^{i\phi_L} \sin(\alpha) \tag{A.39}$$

$$S = \frac{-\Omega_R}{\sqrt{\Omega_R^2 + \delta^2}} e^{i\phi_L} \sin(\alpha) \tag{A.40}$$

$$= \frac{\Omega_R}{\sqrt{\Omega_R^2 + \delta^2}} e^{i\phi_L} \sin(-\alpha) \tag{A.41}$$

$$\Rightarrow S = e^{i\phi_L} \frac{\Omega_R}{\sqrt{\Omega_R^2 + \delta^2}} \sin\left(\frac{\sqrt{\Omega_R^2 + \delta^2}}{2} (t - t_0) \right) \tag{A.42}$$

Using $\hat{U}$ and applying appropriate values for the various variables, now absorbed within C and S, we can obtain operators for the beam-splitter and mirror pulses in the interferometer sequence. As previously alluded to, when the Hamiltonian is time dependent such as in free evolution, we will need a slightly different formulation seen in Appendix A.3.2.

A.3.2 Free evolution operator

From Equation 2.22, we introduce time dependence into the Hamiltonian through the Doppler shift:

$$\delta_{\text{Doppler}}(t) = \mathbf{k}_{\text{eff}} \cdot \mathbf{v}(t) = \mathbf{k}_{\text{eff}} \cdot (\mathbf{v}_0 + \mathbf{a}t)\,, \tag{A.43}$$

where $\mathbf{v}_0$ it the initial velocity of the atom at time $t = t_0$, and $\mathbf{a}$ is the acceleration the atom is experiencing. The rotating frame Hamiltonian (Equation 2.33) therefore becomes

$$\begin{aligned} \hat{H}_R &= \frac{\hbar}{2} \begin{pmatrix} \delta(t) & \Omega_R e^{-i\phi_L} \\ \Omega_R^* e^{+i\phi_L} & -\delta(t) \end{pmatrix} \\ &= \frac{\hbar}{2} \begin{pmatrix} \mathbf{k}_{\text{eff}} \cdot (\mathbf{v}_0 + \mathbf{a}t) & \Omega_R e^{-i\phi_L} \\ \Omega_R^* e^{+i\phi_L} & -\mathbf{k}_{\text{eff}} \cdot (\mathbf{v}_0 + \mathbf{a}t) \end{pmatrix}. \end{aligned} \tag{A.44}$$

During free evolution, there is no light field to interact with i.e. $\Omega_R = 0$. The Hamiltonian is therefore

$$\hat{H}_R = \frac{\hbar}{2} \begin{pmatrix} \delta(t) & 0 \\ 0 & -\delta(t) \end{pmatrix}. \tag{A.45}$$

Substituting this into the TDSE gives

$$i\hbar\frac{\partial}{\partial t}\begin{pmatrix}c_1(t)\\c_2(t)\end{pmatrix} = \frac{\hbar}{2}\begin{pmatrix}\delta(t) & 0\\0 & -\delta(t)\end{pmatrix}\begin{pmatrix}c_1(t)\\c_2(t)\end{pmatrix} \tag{A.46}$$

$$i\hbar\frac{\partial}{\partial t}\begin{pmatrix}c_1(t)\\c_2(t)\end{pmatrix} = \frac{\hbar}{2}\begin{pmatrix}\delta(t)c_1(t)\\-\delta(t)c_2(t)\end{pmatrix} \tag{A.47}$$

$$i\hbar\frac{\partial}{\partial t}\begin{pmatrix}c_1(t)\\c_2(t)\end{pmatrix} = \frac{\hbar}{2}\begin{pmatrix}\mathbf{k}_{\text{eff}}\cdot(\mathbf{v}_0+\mathbf{a}t)\,c_1(t)\\-\mathbf{k}_{\text{eff}}\cdot(\mathbf{v}_0+\mathbf{a}t)\,c_2(t)\end{pmatrix}. \tag{A.48}$$

This has solutions

$$c_1(t) = c_1(t_0)\exp\left(-\frac{i}{2}\int_{t_0}^{t+t_0}\delta(\tau)\,\mathrm{d}\tau\right) = c_1(t_0)\exp\left(-\frac{i}{2}\int_{t_0}^{t+t_0}\mathbf{k}_{\text{eff}}\cdot(\mathbf{v}_0+\mathbf{a}\tau)\,\mathrm{d}\tau\right) \tag{A.49a}$$

$$c_2(t) = c_2(t_0)\exp\left(+\frac{i}{2}\int_{t_0}^{t+t_0}\delta(\tau)\,\mathrm{d}\tau\right) = c_2(t_0)\exp\left(+\frac{i}{2}\int_{t_0}^{t+t_0}\mathbf{k}_{\text{eff}}\cdot(\mathbf{v}_0+\mathbf{a}\tau)\,\mathrm{d}\tau\right). \tag{A.49b}$$

Performing the integration:

$$\begin{pmatrix}c_1(t)\\c_2(t)\end{pmatrix} = \begin{pmatrix}\exp\left(-\frac{i}{2}\mathbf{k}_{\text{eff}}\cdot\left[\mathbf{v}_0\tau+\frac{1}{2}\mathbf{a}\tau^2\right]_{t_0}^{t+t_0}\right)c_1(t_0)\\\exp\left(+\frac{i}{2}\mathbf{k}_{\text{eff}}\cdot\left[\mathbf{v}_0\tau+\frac{1}{2}\mathbf{a}\tau^2\right]_{t_0}^{t+t_0}\right)c_2(t_0)\end{pmatrix} \tag{A.50}$$

$$= \begin{pmatrix}\exp\left(-\frac{i}{2}\mathbf{k}_{\text{eff}}\cdot\left[\mathbf{v}_0(t+t_0)+\frac{1}{2}\mathbf{a}(t+t_0)^2-\mathbf{v}_0t_0-\frac{1}{2}\mathbf{a}t_0^2\right]\right)c_1(t_0)\\\exp\left(+\frac{i}{2}\mathbf{k}_{\text{eff}}\cdot\left[\mathbf{v}_0(t+t_0)+\frac{1}{2}\mathbf{a}(t+t_0)^2-\mathbf{v}_0t_0-\frac{1}{2}\mathbf{a}t_0^2\right]\right)c_2(t_0)\end{pmatrix} \tag{A.51}$$

$$= \begin{pmatrix}\exp\left(-\frac{i}{2}\mathbf{k}_{\text{eff}}\cdot\left[\mathbf{v}_0t+\frac{1}{2}\mathbf{a}\left(t^2+2tt_0\right)\right]\right)c_1(t_0)\\\exp\left(+\frac{i}{2}\mathbf{k}_{\text{eff}}\cdot\left[\mathbf{v}_0t+\frac{1}{2}\mathbf{a}\left(t^2+2tt_0\right)\right]\right)c_2(t_0)\end{pmatrix}. \tag{A.52}$$

Something to keep in mind; since we have integrated between t_0 and $t+t_0$, when using this result the period of free evolution t will be already offset from t_0.

For the first period of free evolution: $t = T_1$. This gives the wavefunction as

$$|\Psi\rangle_{\text{FE1}} = \begin{pmatrix}\exp\left(-\frac{i}{2}\mathbf{k}_{\text{eff}}\cdot\left[\mathbf{v}_0T_1+\frac{1}{2}\mathbf{a}\left(T_1^2+2T_1t_0\right)\right]\right)c_1(t_0)\\\exp\left(+\frac{i}{2}\mathbf{k}_{\text{eff}}\cdot\left[\mathbf{v}_0T_1+\frac{1}{2}\mathbf{a}\left(T_1^2+2T_1t_0\right)\right]\right)c_2(t_0)\end{pmatrix}. \tag{A.53}$$

Similarly, for the second period of free evolution: $t = T_2$ and $t_0 \Rightarrow T_1 + t_0$.

$$|\Psi\rangle_{\text{FE2}} = \begin{pmatrix}\exp\left(-\frac{i}{2}\mathbf{k}_{\text{eff}}\cdot\left[\mathbf{v}_0T_2+\frac{1}{2}\mathbf{a}\left(T_2^2+2T_2(T_1+t_0)\right)\right]\right)c_1(T_1+t_0)\\\exp\left(+\frac{i}{2}\mathbf{k}_{\text{eff}}\cdot\left[\mathbf{v}_0T_2+\frac{1}{2}\mathbf{a}\left(T_2^2+2T_2(T_1+t_0)\right)\right]\right)c_2(T_1+t_0)\end{pmatrix}. \tag{A.54}$$

For completeness we have also applied the change of t_0 to the state populations, however these are largely unimportant here as we are mainly interested in the

phases of the populations. The value of these populations will also be dependent on the previous sequences of interferometer.

From Equations A.53 and A.54, we find the phases of the atomic states to be

$$\frac{1}{2}\phi_{T_1} = \frac{1}{2}\mathbf{k}_{\text{eff}} \cdot \left(\mathbf{v}_0 T_1 + \frac{1}{2}\mathbf{a}\left[T_1^2 + 2T_1 t_0\right]\right) \tag{A.55}$$

$$\frac{1}{2}\phi_{T_2} = \frac{1}{2}\mathbf{k}_{\text{eff}} \cdot \left(\mathbf{v}_0 T_2 + \frac{1}{2}\mathbf{a}\left[T_2^2 + 2T_2(T_1 + t_0)\right]\right), \tag{A.56}$$

which we can see are identical to Equations 3.12.

A.3.3 Total interferometer phase

Steps between Equation 3.10 and Equation 3.13. We shall do this step by step. Initial state:

$$|\Psi(t_0)\rangle = \begin{pmatrix} c_1(t_0) \\ c_2(t_0) \end{pmatrix} = \begin{pmatrix} 1 \\ 0 \end{pmatrix}. \tag{A.57}$$

It may be worth to note that we will use t_0 quite liberally here. It does not mean the start of the sequence, as we have implied here, but rather the start of the pulse or period we are transforming the state with. We begin with the initial beam-splitter operation:

$$|\Psi\rangle_{\pi/2} = \hat{U}_{\pi/2}\,|\Psi(t_0)\rangle \tag{A.58}$$

$$= \frac{1}{\sqrt{2}} \begin{pmatrix} 1 & -ie^{-i\phi_L} \\ -ie^{i\phi_L} & 1 \end{pmatrix} \begin{pmatrix} 1 \\ 0 \end{pmatrix} \tag{A.59}$$

$$= \frac{1}{\sqrt{2}} \begin{pmatrix} 1 - ie^{-i\phi_L} \times 0 \\ 0 - ie^{+i\phi_L} \times 1 \end{pmatrix} \tag{A.60}$$

$$= \frac{1}{\sqrt{2}} \begin{pmatrix} 1 \\ -ie^{i\phi_L} \end{pmatrix} = \frac{1}{\sqrt{2}} \begin{pmatrix} 1 \\ e^{i\left(\phi_L - \frac{\pi}{2}\right)} \end{pmatrix}. \tag{A.61}$$

We then apply the first period of free evolution. For simplicity we will use the phase terms defined in Equations 3.12 for the phase gained during the free

evolutions.

$$|\Psi\rangle_{\mathrm{FE1}} = \hat{U}_{\mathrm{FE}}\hat{U}_{\pi/2}\,|\Psi(t_0)\rangle = \hat{U}_{\mathrm{FE}}\,|\Psi\rangle_{\pi/2} \tag{A.62}$$

$$= \begin{pmatrix} e^{-\frac{i}{2}\phi_{T_1}} & 0 \\ 0 & e^{+\frac{i}{2}\phi_{T_1}} \end{pmatrix} \frac{1}{\sqrt{2}} \begin{pmatrix} 1 \\ -ie^{i\phi_L} \end{pmatrix} \tag{A.63}$$

$$= \frac{1}{\sqrt{2}} \begin{pmatrix} e^{-\frac{i}{2}\phi_{T_1}} \\ -ie^{i\phi_L}e^{+\frac{i}{2}\phi_{T_1}} \end{pmatrix} \tag{A.64}$$

$$= \frac{1}{\sqrt{2}} \begin{pmatrix} e^{-\frac{i}{2}\phi_{T_1}} \\ -ie^{i\left(\phi_L+\frac{\phi_{T_1}}{2}\right)} \end{pmatrix} = \frac{1}{\sqrt{2}} \begin{pmatrix} e^{-\frac{i}{2}\phi_{T_1}} \\ e^{i\left(\phi_L-\frac{\pi}{2}+\frac{\phi_{T_1}}{2}\right)} \end{pmatrix} \tag{A.65}$$

Apply mirror pulse.

$$|\Psi\rangle_{\pi} = \hat{U}_{\pi}\hat{U}_{\mathrm{FE}}\hat{U}_{\pi/2}\,|\Psi(t_0)\rangle = \hat{U}_{\pi}\,|\Psi\rangle_{\mathrm{FE1}} \tag{A.66}$$

$$= \begin{pmatrix} 0 & -ie^{-i\phi_L} \\ -ie^{i\phi_L} & 0 \end{pmatrix} \frac{1}{\sqrt{2}} \begin{pmatrix} e^{-\frac{i}{2}\phi_{T_1}} \\ -ie^{i\left(\phi_L+\frac{\phi_{T_1}}{2}\right)} \end{pmatrix} \tag{A.67}$$

$$= \frac{-i}{\sqrt{2}} \begin{pmatrix} e^{-i\phi_L}(-i)e^{i\left(\phi_L+\frac{\phi_{T_1}}{2}\right)} \\ e^{i\phi_L}e^{-\frac{i}{2}\phi_{T_1}} \end{pmatrix} \tag{A.68}$$

$$= \frac{-i}{\sqrt{2}} \begin{pmatrix} -ie^{i\frac{\phi_{T_1}}{2}} \\ e^{i\left(\phi_L-\frac{1}{2}\phi_{T_1}\right)} \end{pmatrix} \tag{A.69}$$

$$= \frac{1}{\sqrt{2}} \begin{pmatrix} -e^{i\frac{\phi_{T_1}}{2}} \\ -ie^{i\left(\phi_L-\frac{1}{2}\phi_{T_1}\right)} \end{pmatrix} = \frac{1}{\sqrt{2}} \begin{pmatrix} -e^{i\frac{\phi_{T_1}}{2}} \\ e^{i\left(\phi_L-\frac{\pi}{2}-\frac{1}{2}\phi_{T_1}\right)} \end{pmatrix} \tag{A.70}$$

Second period of free evolution.

$$|\Psi\rangle_{\mathrm{FE2}} = \hat{U}_{\mathrm{FE}}\hat{U}_{\pi}\hat{U}_{\mathrm{FE}}\hat{U}_{\pi/2}\,|\Psi(t_0)\rangle = \hat{U}_{\mathrm{FE}}\,|\Psi\rangle_{\pi} \tag{A.71}$$

$$= \begin{pmatrix} e^{-\frac{i}{2}\phi_{T_2}} & 0 \\ 0 & e^{+\frac{i}{2}\phi_{T_2}} \end{pmatrix} \frac{1}{\sqrt{2}} \begin{pmatrix} -e^{i\frac{\phi_{T_1}}{2}} \\ -ie^{i\left(\phi_L-\frac{1}{2}\phi_{T_1}\right)} \end{pmatrix} \tag{A.72}$$

$$= \frac{1}{\sqrt{2}} \begin{pmatrix} -e^{i\frac{\phi_{T_1}}{2}}e^{-\frac{i}{2}\phi_{T_2}} \\ -ie^{i\left(\phi_L-\frac{1}{2}\phi_{T_1}\right)}e^{+\frac{i}{2}\phi_{T_2}} \end{pmatrix} \tag{A.73}$$

$$= \frac{1}{\sqrt{2}} \begin{pmatrix} -e^{i\left(\frac{1}{2}\phi_{T_1}-\frac{1}{2}\phi_{T_2}\right)} \\ -ie^{i\left(\phi_L-\frac{1}{2}\phi_{T_1}+\frac{1}{2}\phi_{T_2}\right)} \end{pmatrix} = \frac{1}{\sqrt{2}} \begin{pmatrix} -e^{i\left(\frac{1}{2}\phi_{T_1}-\frac{1}{2}\phi_{T_2}\right)} \\ e^{i\left(\phi_L-\frac{\pi}{2}-\frac{1}{2}\phi_{T_1}+\frac{1}{2}\phi_{T_2}\right)} \end{pmatrix} \tag{A.74}$$

Final beam-splitter pulse.

$$|\Psi\rangle_{\text{final}} = \hat{U}_{\pi/2}\hat{U}_{\text{FE}}\hat{U}_{\pi}\hat{U}_{\text{FE}}\hat{U}_{\pi/2}\,|\Psi(t_0)\rangle = \hat{U}_{\pi/2}\,|\Psi\rangle_{\text{FE2}} \tag{A.75}$$

$$= \frac{1}{\sqrt{2}}\begin{pmatrix} 1 & -ie^{-i\phi_L} \\ -ie^{i\phi_L} & 1 \end{pmatrix}\frac{1}{\sqrt{2}}\begin{pmatrix} -e^{i\left(\frac{1}{2}\phi_{T_1}-\frac{1}{2}\phi_{T_2}\right)} \\ -ie^{i\left(\phi_L-\frac{1}{2}\phi_{T_1}+\frac{1}{2}\phi_{T_2}\right)} \end{pmatrix} \tag{A.76}$$

$$= \frac{1}{2}\begin{pmatrix} -e^{i\left(\frac{1}{2}\phi_{T_1}-\frac{1}{2}\phi_{T_2}\right)} - ie^{-i\phi_L}(-i)e^{i\left(\phi_L-\frac{1}{2}\phi_{T_1}+\frac{1}{2}\phi_{T_2}\right)} \\ -ie^{i\left(\phi_L-\frac{1}{2}\phi_{T_1}+\frac{1}{2}\phi_{T_2}\right)} - ie^{i\phi_L}(-1)e^{i\left(\frac{1}{2}\phi_{T_1}-\frac{1}{2}\phi_{T_2}\right)} \end{pmatrix} \tag{A.77}$$

$$= \frac{1}{2}\begin{pmatrix} -e^{i\left(\frac{1}{2}\phi_{T_1}-\frac{1}{2}\phi_{T_2}\right)} - e^{-i\phi_L}e^{i\left(\phi_L-\frac{1}{2}\phi_{T_1}+\frac{1}{2}\phi_{T_2}\right)} \\ -ie^{i\left(\phi_L-\frac{1}{2}\phi_{T_1}+\frac{1}{2}\phi_{T_2}\right)} + ie^{i\phi_L}e^{i\left(\frac{1}{2}\phi_{T_1}-\frac{1}{2}\phi_{T_2}\right)} \end{pmatrix} \tag{A.78}$$

$$= -\frac{1}{2}\begin{pmatrix} e^{i\left(\frac{1}{2}\phi_{T_1}-\frac{1}{2}\phi_{T_2}\right)} + e^{-i\phi_L}e^{i\left(\phi_L-\frac{1}{2}\phi_{T_1}+\frac{1}{2}\phi_{T_2}\right)} \\ ie^{i\left(\phi_L-\frac{1}{2}\phi_{T_1}+\frac{1}{2}\phi_{T_2}\right)} - ie^{i\phi_L}e^{i\left(\frac{1}{2}\phi_{T_1}-\frac{1}{2}\phi_{T_2}\right)} \end{pmatrix} \tag{A.79}$$

$$= -\frac{1}{2}\begin{pmatrix} e^{i\left(\frac{1}{2}\phi_{T_1}-\frac{1}{2}\phi_{T_2}\right)} + e^{i\left(\frac{1}{2}\phi_{T_2}-\frac{1}{2}\phi_{T_1}\right)} \\ e^{i\phi_L}\left(ie^{i\left(\frac{1}{2}\phi_{T_2}-\frac{1}{2}\phi_{T_1}\right)} - ie^{-i\left(\frac{1}{2}\phi_{T_2}-\frac{1}{2}\phi_{T_1}\right)}\right) \end{pmatrix} \tag{A.80}$$

We can then apply the following trigonometric identities:

$$\cos(x) = \frac{e^{ix}+e^{-ix}}{2} \tag{A.81}$$

to c_1, and

$$\sin(x) = \frac{e^{ix}-e^{-ix}}{2i} = -\frac{ie^{ix}-ie^{-ix}}{2} \tag{A.82}$$

to c_2. We obtain the final wave-function

$$|\Psi\rangle_{\text{final}} = \begin{pmatrix} -\cos\left(\frac{1}{2}\phi_{T_1}-\frac{1}{2}\phi_{T_2}\right) \\ e^{i\phi_L}\sin\left(\frac{1}{2}\phi_{T_2}-\frac{1}{2}\phi_{T_1}\right) \end{pmatrix} = \begin{pmatrix} -\cos\left(\frac{1}{2}\phi_{T_2}-\frac{1}{2}\phi_{T_1}\right) \\ e^{i\phi_L}\sin\left(\frac{1}{2}\phi_{T_2}-\frac{1}{2}\phi_{T_1}\right) \end{pmatrix}. \tag{A.83}$$

The population of the excited level of the atom is therefore

$$P_2 = \sin^2\left(\frac{1}{2}\phi_{T_2}-\frac{1}{2}\phi_{T_1}\right) \tag{A.84}$$

Using the trigonometric identity

$$\sin^2(x) = \frac{1}{2}-\frac{1}{2}\cos(2x), \tag{A.85}$$

we arrive at Equation 3.13:

$$P_2 = \frac{1}{2}-\frac{1}{2}\cos(\phi_{T_2}-\phi_{T_1}) = \frac{1}{2}-\frac{1}{2}\cos(\Phi). \tag{A.86}$$

A.3.4 Bloch sphere phases

The atomic state on the Bloch sphere can also be represented by polar coordinates:

$$|\Psi\rangle = \cos\left(\frac{\theta}{2}\right)|1\rangle + e^{i\phi}\sin\left(\frac{\theta}{2}\right)|2\rangle\,, \tag{A.87}$$

where θ is the polar angle, angle from $\hat{\mathbf{z}} \equiv |1\rangle$ and $\mathbf{R}$, and ϕ is a azimuthal angle, the angle of $\mathbf{R}$ along the $\hat{\mathbf{x}}$–$\hat{\mathbf{y}}$ plane. Here ϕ represents the phase difference between the two atomic states: Therefore we can calculate the phase at each stage of the interferometry sequence:

$$e^{i\phi} = e^{i\phi_{|2\rangle}}/e^{i\phi_{|1\rangle}} \tag{A.88}$$

where $\phi_{|1,2\rangle}$ is the phase of the respective state.

The atom's phase after the first beam-splitter pulse is

$$e^{i\phi} = e^{i\left(\phi_L - \frac{\pi}{2}\right)}/e^{i\times 0} \tag{A.89}$$

$$\phi = \phi_L - \frac{\pi}{2}. \tag{A.90}$$

First free evolution phase:

$$e^{i\phi} = e^{i\left(\phi_L - \frac{\pi}{2} + \frac{1}{2}\phi_{T_1}\right)}/e^{-i\frac{1}{2}\phi_{T_1}} \tag{A.91}$$

$$\phi = \phi_L - \frac{\pi}{2} + \phi_{T_1}. \tag{A.92}$$

Mirror pulse:

$$e^{i\phi} = e^{i\left(\phi_L - \frac{\pi}{2} - \frac{1}{2}\phi_{T_1}\right)}/ - e^{i\frac{1}{2}\phi_{T_1}} \tag{A.93}$$

$$= e^{i\left(\phi_L - \frac{\pi}{2} - \frac{1}{2}\phi_{T_1}\right)}/e^{i\frac{1}{2}\phi_{T_1}\pm\pi} \tag{A.94}$$

$$\phi = \phi_L - \frac{\pi}{2} - \phi_{T_1} \mp \pi. \tag{A.95}$$

Second period of free evolution:

$$e^{i\phi} = e^{i\left(\phi_L - \frac{\pi}{2} - \frac{1}{2}\phi_{T_1} + \frac{1}{2}\phi_{T_2}\right)}/ - e^{i\left(\frac{1}{2}\phi_{T_1} - \frac{1}{2}\phi_{T_2}\right)} \tag{A.96}$$

$$= e^{i\left(\phi_L - \frac{\pi}{2} - \frac{1}{2}\phi_{T_1} + \frac{1}{2}\phi_{T_2}\right)}/e^{i\left(\frac{1}{2}\phi_{T_1} - \frac{1}{2}\phi_{T_2}\pm\pi\right)} \tag{A.97}$$

$$\phi = \left(\phi_L - \frac{\pi}{2} - \frac{1}{2}\phi_{T_1} + \frac{1}{2}\phi_{T_2}\right) - \left(\frac{1}{2}\phi_{T_1} - \frac{1}{2}\phi_{T_2} \pm \pi\right) \tag{A.98}$$

$$= \phi_L - \frac{\pi}{2} - \frac{1}{2}\phi_{T_1} + \frac{1}{2}\phi_{T_2} - \frac{1}{2}\phi_{T_1} + \frac{1}{2}\phi_{T_2} \mp \pi \tag{A.99}$$

$$= \phi_L - \frac{\pi}{2} - \phi_{T_1} + \phi_{T_2} \mp \pi \tag{A.100}$$

$$= \phi_L - \frac{\pi}{2} + \phi_{T_2} - \phi_{T_1} \mp \pi. \tag{A.101}$$

And final atomic phase after the final beam-splitter:

$$e^{i\phi} = e^{i\phi_L}/e^{\pm i\pi} \tag{A.102}$$
$$\phi = \phi_L \mp \pi. \tag{A.103}$$

A.4 Interferometry with varying laser phase

Same method as Appendix A.3.3 however using ϕ_1, ϕ_2, and ϕ_3 for the phases of the beam-splitter, mirror, and final beam-splitter pulses respectively.

$$|\Psi\rangle_{\pi/2} = \hat{U}_{\pi/2}\,|\Psi(t_0)\rangle \tag{A.104}$$
$$= \frac{1}{\sqrt{2}}\begin{pmatrix} 1 & -ie^{-i\phi_1} \\ -ie^{i\phi_1} & 1 \end{pmatrix}\begin{pmatrix} 1 \\ 0 \end{pmatrix} \tag{A.105}$$
$$= \frac{1}{\sqrt{2}}\begin{pmatrix} 1 \\ -ie^{i\phi_1} \end{pmatrix} \tag{A.106}$$

Apply free evolution:

$$|\Psi\rangle_{\mathrm{FE1}} = \hat{U}_{\mathrm{FE}}\,|\Psi\rangle_{\pi/2} \tag{A.107}$$
$$= \begin{pmatrix} e^{-\frac{i}{2}\phi_{T_1}} & 0 \\ 0 & e^{+\frac{i}{2}\phi_{T_1}} \end{pmatrix}\frac{1}{\sqrt{2}}\begin{pmatrix} 1 \\ -ie^{i\phi_1} \end{pmatrix} \tag{A.108}$$
$$= \frac{1}{\sqrt{2}}\begin{pmatrix} e^{-\frac{i}{2}\phi_{T_1}} \\ -ie^{i\left(\phi_1+\frac{1}{2}\phi_{T_1}\right)} \end{pmatrix}. \tag{A.109}$$

So far same as previous calculations. It will now begin to deviate slightly with the mirror pulse:

$$|\Psi\rangle_{\pi} = \hat{U}_{\pi}\,|\Psi\rangle_{\mathrm{FE1}} \tag{A.110}$$
$$= \begin{pmatrix} e^{-\frac{i}{2}\phi_{T_2}} & 0 \\ 0 & e^{+\frac{i}{2}\phi_{T_2}} \end{pmatrix}\frac{1}{\sqrt{2}}\begin{pmatrix} e^{-\frac{i}{2}\phi_{T_1}} \\ -ie^{i\left(\phi_1+\frac{1}{2}\phi_{T_1}\right)} \end{pmatrix} \tag{A.111}$$
$$= \frac{1}{\sqrt{2}}\begin{pmatrix} \left(-ie^{-i\phi_2}\right)\left(-ie^{i\left(\phi_1+\frac{1}{2}\phi_{T_1}\right)}\right) \\ -ie^{i\phi_2}e^{-i\frac{1}{2}\phi_{T_1}} \end{pmatrix} \tag{A.112}$$
$$= \frac{1}{\sqrt{2}}\begin{pmatrix} -e^{i\left(\phi_1-\phi_2+\frac{1}{2}\phi_{T_1}\right)} \\ -ie^{i\left(\phi_2-\frac{1}{2}\phi_{T_1}\right)} \end{pmatrix}. \tag{A.113}$$

Second free evolution:

$$|\Psi\rangle_{\text{FE2}} = \hat{U}_{\text{FE}} |\Psi\rangle_{\pi} \tag{A.114}$$

$$= \begin{pmatrix} e^{-\frac{i}{2}\phi_{T_1}} & 0 \\ 0 & e^{+\frac{i}{2}\phi_{T_1}} \end{pmatrix} \frac{1}{\sqrt{2}} \begin{pmatrix} -e^{i\left(\phi_1-\phi_2+\frac{1}{2}\phi_{T_1}\right)} \\ -ie^{i\left(\phi_2-\frac{1}{2}\phi_{T_1}\right)} \end{pmatrix} \tag{A.115}$$

$$= \frac{1}{\sqrt{2}} \begin{pmatrix} -e^{-i\frac{1}{2}\phi_{T_2}} e^{i\left(\phi_1-\phi_2+\frac{1}{2}\phi_{T_1}\right)} \\ -ie^{+i\frac{1}{2}\phi_{T_2}} e^{i\left(\frac{1}{2}\phi_{T_1}+\phi_2\right)} \end{pmatrix} \tag{A.116}$$

$$= \frac{1}{\sqrt{2}} \begin{pmatrix} -e^{i\left(\phi_1-\phi_2+\frac{1}{2}\phi_{T_1}-\frac{1}{2}\phi_{T_2}\right)} \\ -ie^{i\left(\frac{1}{2}\phi_{T_2}-\frac{1}{2}\phi_{T_1}+\phi_2\right)} \end{pmatrix}. \tag{A.117}$$

Final beamsplitter:

$$|\Psi\rangle_{\text{final}} = \hat{U}_{\pi/2} |\Psi\rangle_{\text{FE2}} \tag{A.118}$$

$$= \frac{1}{\sqrt{2}} \begin{pmatrix} 1 & -ie^{-i\phi_3} \\ -ie^{i\phi_3} & 1 \end{pmatrix} \frac{1}{\sqrt{2}} \begin{pmatrix} -e^{i\left(\phi_1-\phi_2+\frac{1}{2}\phi_{T_1}-\frac{1}{2}\phi_{T_2}\right)} \\ -ie^{i\left(\frac{1}{2}\phi_{T_2}-\frac{1}{2}\phi_{T_1}+\phi_2\right)} \end{pmatrix} \tag{A.119}$$

$$= \frac{1}{2} \begin{pmatrix} -e^{i\left(\phi_1-\phi_2+\frac{1}{2}\phi_{T_1}-\frac{1}{2}\phi_{T_2}\right)} + \left(-ie^{-i\phi_3}\right)\left(-ie^{i\left(\frac{1}{2}\phi_{T_2}-\frac{1}{2}\phi_{T_1}+\phi_2\right)}\right) \\ -ie^{i\left(\frac{1}{2}\phi_{T_2}-\frac{1}{2}\phi_{T_1}+\phi_2\right)} + \left(-ie^{+i\phi_3}\right)\left(-e^{i\left(\phi_1-\phi_2+\frac{1}{2}\phi_{T_1}-\frac{1}{2}\phi_{T_2}\right)}\right) \end{pmatrix} \tag{A.120}$$

$$= \frac{1}{2} \begin{pmatrix} -e^{i\left(\phi_1-\phi_2+\frac{1}{2}\phi_{T_1}-\frac{1}{2}\phi_{T_2}\right)} - e^{i\left(\frac{1}{2}\phi_{T_2}-\frac{1}{2}\phi_{T_1}+\phi_2-\phi_3\right)} \\ -ie^{i\left(\frac{1}{2}\phi_{T_2}-\frac{1}{2}\phi_{T_1}+\phi_2\right)} + ie^{i\left(\phi_1-\phi_2+\phi_3+\frac{1}{2}\phi_{T_1}-\frac{1}{2}\phi_{T_2}\right)} \end{pmatrix}. \tag{A.121}$$

To make sense of this we can find the population of state two:

$$P_2 = c_2^* c_2 \tag{A.122}$$

$$= \begin{array}{l} \frac{1}{4}\left(-ie^{i\left(\frac{1}{2}\phi_{T_2}-\frac{1}{2}\phi_{T_1}+\phi_2\right)} + ie^{-i\left(\phi_1-\phi_2+\phi_3+\frac{1}{2}\phi_{T_1}-\frac{1}{2}\phi_{T_2}\right)}\right) \\ \times \left(+ie^{-i\left(\frac{1}{2}\phi_{T_2}-\frac{1}{2}\phi_{T_1}+\phi_2\right)} - ie^{-i\left(\phi_1-\phi_2+\phi_3+\frac{1}{2}\phi_{T_1}-\frac{1}{2}\phi_{T_2}\right)}\right) \end{array} \tag{A.123}$$

$$= \frac{1}{4}(a+b)\times(c+d) = \frac{1}{4}\left(ac+ad+bc+bd\right) \tag{A.124}$$

where

$$a = -ie^{i\left(\frac{1}{2}\phi_{T_2}-\frac{1}{2}\phi_{T_1}+\phi_2\right)} \tag{A.125a}$$

$$b = ie^{-i\left(\phi_1-\phi_2+\phi_3+\frac{1}{2}\phi_{T_1}-\frac{1}{2}\phi_{T_2}\right)} \tag{A.125b}$$

$$c = ie^{-i\left(\frac{1}{2}\phi_{T_2}-\frac{1}{2}\phi_{T_1}+\phi_2\right)} \tag{A.125c}$$

$$d = -ie^{-i\left(\phi_1-\phi_2+\phi_3+\frac{1}{2}\phi_{T_1}-\frac{1}{2}\phi_{T_2}\right)}. \tag{A.125d}$$

$$ac = -ie^{i\left(\frac{1}{2}\phi_{T_2} - \frac{1}{2}\phi_{T_1} + \phi_2\right)} ie^{-i\left(\frac{1}{2}\phi_{T_2} - \frac{1}{2}\phi_{T_1} + \phi_2\right)} \tag{A.126}$$
$$= +1 \tag{A.127}$$

$$ad = -ie^{i\left(\frac{1}{2}\phi_{T_2} - \frac{1}{2}\phi_{T_1} + \phi_2\right)}(-i)e^{-i\left(\phi_1 - \phi_2 + \phi_3 + \frac{1}{2}\phi_{T_1} - \frac{1}{2}\phi_{T_2}\right)} \tag{A.128}$$
$$= -e^{i\left(\frac{1}{2}\phi_{T_2} - \frac{1}{2}\phi_{T_1} + \phi_2 - \phi_1 + \phi_2 - \phi_3 - \frac{1}{2}\phi_{T_1} + \frac{1}{2}\phi_{T_2}\right)} \tag{A.129}$$
$$= -e^{i\left(\phi_{T_2} - \phi_{T_1} - \phi_1 + 2\phi_2 - \phi_3\right)} \tag{A.130}$$

$$bc = ie^{-i\left(\phi_1 - \phi_2 + \phi_3 + \frac{1}{2}\phi_{T_1} - \frac{1}{2}\phi_{T_2}\right)} ie^{-i\left(\frac{1}{2}\phi_{T_2} - \frac{1}{2}\phi_{T_1} + \phi_2\right)} \tag{A.131}$$
$$= -e^{i\left(\phi_1 - \phi_2 + \phi_3 + \frac{1}{2}\phi_{T_1} - \frac{1}{2}\phi_{T_2} - \frac{1}{2}\phi_{T_2} + \frac{1}{2}\phi_{T_1} - \phi_2\right)} \tag{A.132}$$
$$= -e^{i\left(\phi_1 - 2\phi_2 + \phi_3 + \phi_{T_1} - \phi_{T_2}\right)} \tag{A.133}$$

$$bd = ie^{-i\left(\phi_1 - \phi_2 + \phi_3 + \frac{1}{2}\phi_{T_1} - \frac{1}{2}\phi_{T_2}\right)}(-i)e^{-i\left(\phi_1 - \phi_2 + \phi_3 + \frac{1}{2}\phi_{T_1} - \frac{1}{2}\phi_{T_2}\right)} \tag{A.134}$$
$$= +1 \tag{A.135}$$

$$\Rightarrow P_2 = \frac{1}{4}\left(ac + ad + bc + bd\right) \tag{A.136}$$
$$= \frac{1}{4}\left(1 - e^{i\left(\phi_{T_2} - \phi_{T_1} - \phi_1 + 2\phi_2 - \phi_3\right)} - e^{i\left(\phi_1 - 2\phi_2 + \phi_3 + \phi_{T_1} - \phi_{T_2}\right)} + 1\right) \tag{A.137}$$
$$= \frac{1}{4}\left(2 - 2\cos(\phi_{T_2} - \phi_{T_1} - \phi_1 + 2\phi_2 - \phi_3)\right) \tag{A.138}$$
$$= \frac{1}{2} - \frac{1}{2}\cos(\phi_{T_2} - \phi_{T_1} - \phi_1 + 2\phi_2 - \phi_3) \tag{A.139}$$
$$= \frac{1}{2} - \frac{1}{2}\cos(\Phi - \phi_{\text{offset}}) \tag{A.140}$$

where $\phi_{\text{offset}} = \phi_1 - 2\phi_2 + \phi_3$.

Appendix B

Scientific Posters

Figure B.1 shows the poster taken to the following events: QLM Summer School 2018, Young Atom Opticians 2018, International Conference on Atomic Physics 2018, and the Frontiers of Matter Wave Optics 2018 conference and summer school.

Phase Locked Atomic INterferometers for Gravity Gradiometry

Chester Camm*, Andrei Dragomir, and Matt Himsworth
Integrated Atom Chip Group, University of Southampton
*c.camm@soton.ac.uk

Gravity Gradiometry

- Gravity cannot be shielded, a device which can measure changes in gravity would be very useful
- Absolute measurements of gravity are problematic due to the equivalence principle
- A gradiometer measures the change of gravity between two points
- Such a device can measure density variations along a line intersecting the two chosen points
- This can be used to detect subterranean features such as unmapped underground tunnels
- Provides an invaluable tool for civil engineering
- Additional applications can be found in archaeology, deep sea exploration, and inertial navigation

Problems

- Current gradiometers are large and bulky
- Measurements take a long time
- Impractical for many applications
- Most gradiometers measure only one axis

Atom Interferometry

- Gravity measurements require using an inertial test mass
- Classical gravity measurements use weights of known mass but these are prone to degradation and manufacture tolerances
- Cold atoms also give the advantage of increased sensitivity from atom interferometry
- This gives unparalleled sensitivity in gravity and inertial measurements [1]

UK NATIONAL QUANTUM TECHNOLOGIES PROGRAMME

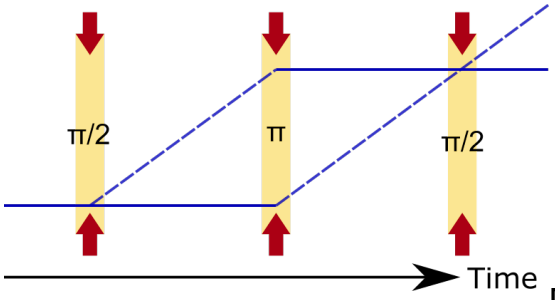

Current Gradiometers

- A requirement for this to work is that the atom clouds experience phase coherent Raman beams.
- This is solved by having line of sight between the clouds and a single beam is used to interrogate both clouds; limiting exibility of geometry
- The also requires the vacuum chamber to be large in order to accommodate drop distance, large enough separation of clouds, and line of sight [2]

Our Idea

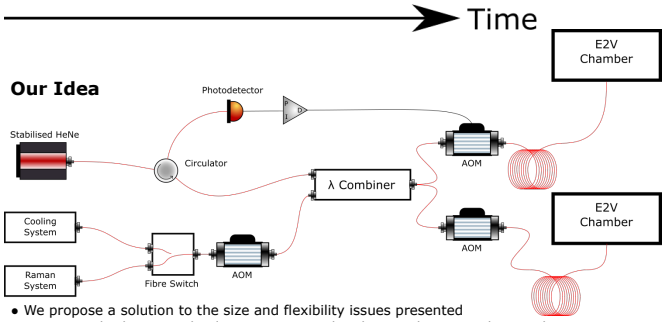

- We propose a solution to the size and flexibility issues presented
- Here we split the atom clouds into separate chambers and connect them with an optical fibre system
- This fibre system also acts as a stability mechanism to maintain phase coherence between the two vacuum chambers
- Now we are able to freely orientate the two measurement points to explore the desired gravitational axes
- Line of sight is no longer required which reduces weight and bulk making system more practical.
- We aim to ensure instability of the fibre arms not main noise and to maintain phase noise to <1 mrad
- Modular design enables simple integration of more sensor heads - leading to full tensor measurements

Exploration into whether the residual phase noise in the optical interometer and other common-mode noise sources are the limiting factors in using separate, but correlated, gravimeters.

Fibre Stabilisation

- The fibre arms act as an optical interferometer.
- Using AOMs to modulate the phase of the interferometer we can maintain correlation between the two atom clouds
- This technique used in atomic clocks for distributing optical phase and demonstrates the required stability levels for this endeavour [3]

Summary

- We aim to improve practicality of quantum gravity gradiometers
- This shall be achieved by separating the atom clouds into separate chambers
- The chambers will be connected by a fibre interferometer that will be used to maintain stability
- This will increase portability and flexibility
- However there will be a reduction of sensitivity of measurements due to shorter drop times
- Exploring residual phase noise in optical interferometer
- The regime between uncorrelated accelerometers, and the fully coherent single chamber gradiometers are to be explored.

References

[1] A. Peters, K. Y. Chung and S. Chu, Metrologia, **38**, 1 (2001).
[2] J. M. McGuirk, G. T. Foster, J. B. Fixler, M. J. Snadden, and M. A. Kasevich, Phys. Rev. A **65**, 3 (2002)
[3] S. M. Foreman, A. D. Ludlow, M. H. G. de Miranda, J. E. Stalnaker, S. A. Diddams, and J. Ye Phys. Rev. Lett. **99**, 15 (2007)

UNIVERSITY OF Southampton EPSRC Engineering and Physical Sciences Research Council

Figure B.1: Poster advertising the concept and aims of the Phase Locked Atomic Interferometers for Gravity Gradiometry project.